Analysis of Beams and Shells Using a Rotation - Free Finite Element - Finite Volume Formulation

J. Jovicevic
E. Oñate

Monograph CIMNE Nº 43, January 1999

Analysis of Beams and Shells Using a Rotation - Free Finite Element - Finite Volume Formulation

J. Jovicevic
E. Oñate

Monograph CIMNE Nº 43, January 1998

International Center for Numerical Methods in Engineering
Gran Capitán s/n, 08034 Barcelona, Spain

The cover designed by: Jordi Pallí

First published, January 1999

Edited by:
International Center for Numerical Methods in Engineering
C/ Gran Capitán, s/n
08034 Barcelona, Spain

ISBN: 84-89925-36-4
Deposito Legal: B-7726-99

CONTENTS

INTRODUCTION

MOTIVATION

A number of industrial problems in manufacturing, most notably sheet stamping problems, vehicle and crash worthiness, require a lot of computational effort for their numerical simulations. The main interest of an analyst is to try to reduce this computational effort to a practically affordable level. Different possibilities can be explored for this purpose. The most obvious possibility is to use more powerful computing devices (i.e. vector computers, parallel computers, etc.). However, there are other possible avenues to be explored in order to reduce the computational effort in which the computational mechanics specialist has even more to offer. More precisely, just by choosing the models which are appropriate for the majority of applications, such as the models of structural elements, beams, plates and shells, one can significantly reduce the amount of computational effort with respect to use the fully 3D solid models. Moreover, these structural models can be recast in a new way which does not allow explicitly the rotational degrees of freedom. Hence, one obtains so called "rotation-free" models for beams, plates and shells. These models lead to the beam, plate and shell elements with translational degrees of freedom only in the finite element implementation.

This idea has first been used by Nay and Utku for plate analysis [N-1], who used a least square quadratic approximation to describe the deflection field within the patch surrounding a node in terms of the deflections of the patch nodes. A similar idea was proposed by Barnes [B-4] who used an approximation for the curvatures at the mid side points determined from the nodal deflections of the adjacent plate elements. Later on, this method was also exploited by Hampshire *et al.* [H-1], who assumed that the elements were hinged together at their common boundaries and that the bending stiffness was represented by the torsional springs resisting the rotations about the hinge lines. A similar class of rotation-free triangles for plate and shell analysis was proposed by Phaal and Calladine [P-2], [P-3]. Yang *et al.* [Y-1] derived a family of elements based on bending energy augment membrane approach which reproduces the hinge bending stiffness procedure developed by Hampshire *et al.* Brunet and Sabourin [B-6], proposed a different approach to compute the constant curvature field within each element in terms of the six node displacements of a macroelement. The element was successfully applied to nonlinear shell analysis using an explicit dynamic approach. Rio *et al.* [R-1], used the concept of side hinge bending

stiffness to derive a thin shell triangle of translational kind for explicit dynamic analysis of sheet stamping problems.

However, it was only Oñate and Cervera [O-2], who clearly demonstrated that the systematic development of rotation-free structural finite elements could be carried out relying on the combined Finite Element (FE)/Finite Volume (FV) approach. Following these ideas, Oñate and Cervera (1993), developed a simple rotation-free three node thin plate element. This work was expanded by Zarate [Z-1], who developed new rotation-free plate and shell three node triangle elements for linear elastic analysis based on combining Cell Centered and Cell Vertex Finite Volume schemes with linear Finite Element approximations. The Cell Centered based shell triangle element was extended by Cendoya [C-1] for nonlinear dynamic analysis of shells and sheet metal forming process.

In this research work, the studies of the previous authors have been applied and expanded to other types of structural problems: Euler-Bernoulli beams, axisymmetric shells and arbitrary shape shells. The main novelty of the particular interest in this work is recasting the mentioned developments in the framework of the mixed Hu-Washizu type variational formulation. Different FE/EV approximations have been accommodated owing to such a variational formulation, in particular Cell Centered and Cell Vertex FV schemes combined with simple linear finite element interpolation have been studied.

The study of the simpler linear beam and axisymmetric problems has shown clearly that the Cell Vertex scheme is more accurate than the Cell Centered one. On the basis of this experience, new nonlinear axisymmetric and arbitrary shape shell elements have been developed in the framework of the Updated Lagrangian formulation and an explicit dynamic formulation. These elements are shown to be useful for the analysis of complex sheet stamping problems involving large strains, plasticity and frictional contact situations. Such an approach has resulted in enhanced computational efficiency to the extent that the analyses of complex industrial problems can be carried out on a personal computer.

OBJECTIVES

The main goal of this work is twofold: to develop the theoretical basis of the FE/FV technique in the framework of the mixed Hu-Washizu variational formulation and to construct efficient rotation-free finite elements for beam, plate and shell analyses. The study has been carried out in two subsequent phases dealing with linear and nonlinear problems, respectively. The facts obtained in each phase of the study have influenced and guided the development for each subsequent phase. In particular, the following principal objectives have been addressed:

- to construct the theoretical basis for the FE/FV approximations starting with the mixed Hu-Washizu type of variational principle.
- to develop rotation-free FE/FV approximations for beam, axisymmetric and arbitrary shape shell elements. The first developments have been carried out in simple one dimension problems of beams, showing that the results obtained by the developed FE/FV technique are the same as those obtained by more standard Finite Difference (FD) techniques. However, the development of more general problems as axisymmetric shells and arbitrary shape shells have clearly demonstrated the superiority of the presented FE/FV technique versus FD methods.
- to develop and compare two types of FE/FV approximations: Cell Vertex and Cell Centered approaches. The main difference between the two methods is based on the construction of the weighting function. With the Cell Centered scheme the support for the chosen weighting function is half of the element domains linked to a node, whereas the weighting function for the Cell Vertex scheme spans throughout the whole element. The Cell Centered scheme has given superior results in the most of the linear problems solved in the thesis and it has been used as only one for the nonlinear analysis.
- to extend the theoretical formulation of the rotation-free FE/FV methodology in the framework of the mixed Hu-Washizu variational principle to large displacements problems by using the Updated Lagrangian formulation and an explicit dynamic approach.
- to develop the FE/FV approximations for the axisymmetric and arbitrary shape shell elements for large displacement problems. For the reasons stated above, this has been accomplished only with rotation-free shell elements based on the Cell Centered scheme.
- to show the applications of the proposal rotation-free formulation for nonlinear dynamic analysis of shells as well as for the analysis of practical sheet stamping problems.

SUMMARY

The outline of this study is as follows:

Chapter 1 gives a brief introduction containing strong and weak forms of the classical linear elasticity in standard displacement-type, followed by more general Hu-Washizu mixed-type formulation of the same problem. Some basic properties of the discrete approximation are reviewed.

Chapter 2 addresses the discrete approximation of the beam bending problem. The basic equations of the strong and weak forms are first presented. The Finite Volume technique is then applied in order to construct the discrete approximations of Cell Centered and Cell Vertex FV schemes. Finally, it is also shown that the presented formulation is a particular case of a more general approach based on the combined FE/FV approximation starting with the mixed Hu-Washizu type of variational principle. The same discrete approximation can be recovered by applying Finite Difference method. A number of simple linear examples are presented in order to illustrate the performance of the rotation-free beam elements developed.

Chapter 3 deals with the same kind of consideration for axisymmetric shell problems. It is shown that the combined FE/FV technique leads to discrete approximation of high performance with the Cell Vertex version being somewhat superior to the Cell Centered one. This fact has been verified by an extensive set of numerical simulations of linear axisymmetric shell problems taken from the literature.

Chapter 4 focuses upon extending the Cell Vertex version of a linear rotation-free axisymmetric shell approximation to the nonlinear dynamic regime as this superiority has been established. This has been accomplished within the framework of the Updated Lagrangian formulation which allows to benefit directly from the expressions obtained in the previous chapter. The developed element is integrated within an explicit dynamic formulation and some benchmark sheet stamping problems are solved.

Chapter 5 proposes how to handle more general problems of the particular interest, a rotation-free 3D thin shell element also based on Cell Vertex scheme as well as its application to nonlinear analysis. The performance of the new element is compared with that of the BST element developed by Zarate [Z-1] and Cendoya [C-1] for the analysis of nonlinear shell problems using an explicit dynamic approach. Some of these problems include the well known benchmark tests for the dynamic analysis of shells including frictional contact situations as well as some rather complex sheet stamping problems.

Chapter 6 gives the conclusions and the future outlook of the current problems of the study.

CHAPTER 1

GENERAL CASE

1.1 STRONG FORM OF LINEAR ELASTICITY

In this section the basic equations necessary for describing the classical linear elasticity are reviewed. The reason for this is twofold. First of all, all of the model problems to be studied in the following chapters are derived consistently from this fundamental equations simply by using approximate kinematic assumptions. Second, this gives an opportunity to describe the difficulties in constructing discrete approximations in the presence of constraints.

The strong form of the boundary value problem in linear elasticity can be described by three groups of equations concerning kinematics, constitutive and equilibrium equations which are applied to each point of the domain under consideration, as well as the corresponding boundary conditions which are applied over the domain boundary.

The kinematic considerations in infinitesimal elasticity give rise to the definition of the deformation tensor $\boldsymbol{\varepsilon}$ as the symmetric part of the displacement gradient as

$$\boldsymbol{\varepsilon} = \begin{Bmatrix} \varepsilon_x \\ \varepsilon_y \\ \varepsilon_z \\ \gamma_{xy} \\ \gamma_{yz} \\ \gamma_{zx} \end{Bmatrix} = \begin{bmatrix} \frac{\partial}{\partial x} & 0 & 0 \\ 0 & \frac{\partial}{\partial y} & 0 \\ 0 & 0 & \frac{\partial}{\partial z} \\ \frac{\partial}{\partial y} & \frac{\partial}{\partial x} & 0 \\ 0 & \frac{\partial}{\partial z} & \frac{\partial}{\partial y} \\ \frac{\partial}{\partial z} & 0 & \frac{\partial}{\partial x} \end{bmatrix} \begin{Bmatrix} u \\ v \\ w \end{Bmatrix} \Leftrightarrow \boldsymbol{\varepsilon} = \mathbf{L}\mathbf{u} \tag{1.1}$$

where $\mathbf{u}$ is the displacement vector.

The key ingredient defining linear elasticity is Hook's law describing the constitutive equation as

$$\boldsymbol{\sigma} = \mathbf{D}\boldsymbol{\varepsilon} \tag{1.2}$$

where $\mathbf{D}$ is the elasticity tensor, which can be written explicitly in terms of Lamé parameters [Z-4].

The equilibrium equations in linear elasticity can be written in terms of the Cauchy (true) stress tensor $\boldsymbol{\sigma}$ as follows

$$\mathbf{L}^T\boldsymbol{\sigma} + \mathbf{f} = \mathbf{0} \tag{1.3}$$

where $\mathbf{f}$ is the body force, whereas the stress $\boldsymbol{\sigma}$ is

$$\boldsymbol{\sigma}^T = [\sigma_x, \sigma_y, \sigma_z, \sigma_{xy}, \sigma_{yz}, \sigma_{zx}]$$

In order to complete the description of the strong form of linear elasticity, it is necessary to specify the boundary conditions. Without loss of generality it is assumed that the total boundary is split into two parts, Γ_u where the displacements are prescribed and Γ_t where the traction vector is prescribed, i.e.

$$\mathbf{u} = \bar{\mathbf{u}} \quad \text{on} \quad \Gamma_u \tag{1.4a}$$

$$\mathbf{t} = \mathbf{T}^T\boldsymbol{\sigma} = \bar{\mathbf{t}} \quad \text{on} \quad \Gamma_t \tag{1.4b}$$

where the matrix $\mathbf{T}$ contains the components of the unit normal vector to the boundary Γ_t

$$\mathbf{T} = \begin{bmatrix} n_x & 0 & 0 \\ 0 & n_y & 0 \\ 0 & 0 & n_z \\ n_y & n_x & 0 \\ 0 & n_z & n_y \\ n_z & 0 & n_x \end{bmatrix} \tag{1.5}$$

and $\bar{\mathbf{u}}$ and $\bar{\mathbf{t}}$ are the prescribed displacements and tractions, respectively.

The boundary conditions concerning the imposed displacements are referred as essential, whereas the boundary condition on imposed traction are referred as natural [H-5].

By combining the kinematic and constitutive equations (1.1) and (1.2), and replacing them into the equilibrium equations (1.3) the strong form of linear elasticity can be simplified to a set of the second order differential equations in terms of the displacement vector components only. The exact solution of these equations is not easy to obtain for the most general case, and in most problems it is unavoidable to search for an approximate solution. In order to facilitate the construction of such approximate solution, the described strong form of linear elasticity is abandoned in favour of the weak form of the same problem.

1.2 WEAK FORM OF LINEAR ELASTICITY

The basic difference of the weak form with respect to the previously described strong form of linear elasticity concerns the manner in which the equilibrium equations are interpreted in the integral sense in the former and in the local sense (point wise) in the latter. Moreover, in the weak form it is not required for the natural boundary conditions to be imposed, they are simply included from the variational form.

The weak form of linear elasticity can be formulated in two ways: by a weighted residual method or as the integral equation corresponding to the minimum of the potential energy.

In the weighted residual approach, the set of weighting functions is chosen (virtual displacements) which shares the same regularity property as the real displacement field except that there is a set equal to zero on the boundary Γ_u

$$\delta \mathbf{u} = \mathbf{0} \quad \text{on} \quad \Gamma_u \tag{1.6}$$

The strong form of equilibrium equations in (1.3) is then replaced by the following integral form

$$\int_{\Omega} \delta \mathbf{u}^T (\mathbf{L}^T \boldsymbol{\sigma} + \mathbf{f}) d\Omega = \mathbf{0} \tag{1.7}$$

By using the standard integration by parts and the divergence theorem [H-5], the last equation can be rewritten in the following way

$$\int_{\Omega} [(\mathbf{L}\delta \mathbf{u})^T \boldsymbol{\sigma} - \delta \mathbf{u}^T \mathbf{f}] d\Omega - \int_{\Gamma_t} \delta \mathbf{u}^T \mathbf{t} d\Gamma = \mathbf{0} \tag{1.8}$$

In the case of linear elasticity the same equation can be recovered as the condition for the minimum of potential energy $\mathbf{\Pi}$, which can be written as

$$\mathbf{\Pi} = \int_{\Omega} [\frac{1}{2} (\mathbf{Lu})^T \mathbf{D} (\mathbf{Lu}) - \mathbf{u}^T \mathbf{f}] d\Omega \rightarrow min \tag{1.9}$$

It is easy to verify that the first variation of the potential energy above, $\delta \mathbf{\Pi} = 0$, leads exactly to the weak form of the equilibrium equations presented in (1.8). By replacing the kinematic equations (1.1) and constitutive equations (1.2) into equation (1.3) the weak form of the equilibrium equations is recovered in terms of displacement vector components only.

It is important to note that in the weak form of linear elasticity, only the first order derivatives appear. If the solution for the displacements field is

sufficiently regular, the weak and the strong form give, nonetheless, the same results. Moreover, the reduced order of the displacements derivatives helps to construct the discrete approximation of the solution more easily and this is discussed in the following section.

1.3 DISCRETE APPROXIMATION

In the discrete approximation of the weak form, the approximate solution of the displacement field is constructed as

$$\mathbf{u} = \mathbf{N}\mathbf{a} \tag{1.10}$$

where $\mathbf{N}$ are so called shape functions and $\mathbf{a}$ are the displacement interpolation parameters [Z-4].

If standard Galerkin approximation is used, the same shape functions are chosen in order to construct the virtual displacement field,

$$\delta\mathbf{u} = \mathbf{N}\delta\mathbf{a} \tag{1.11}$$

where $\delta\mathbf{a}$ are the virtual displacement interpolation parameters.

In the Finite Element (FE) method [Z-4], the shape functions $\mathbf{N}$ are defined locally on every element so that they take a unit value at a node and zero in all other nodes in the mesh. The $\mathbf{a}$ parameters coincide with the nodal displacement values in this case.

The present displacement type formulation is the most appropriate way to obtain an approximate solution to the linear elasticity problem. It can be shown [H-5], that the error of such an approximate displacement field is orthogonal-in-energy to any weighting function (virtual displacement) and moreover, that the energy norm of such an error is minimized. This is referred to as the best approximation property [H-5].

1.4 FINITE VOLUME METHOD - DERIVATION OF DISCRETIZED EQUATIONS VIA MINIMUM POTENTIAL ENERGY

In Finite Volume (FV) methods, the same displacement type variational formulation is kept and the manner for constructing the discrete approximation is also unchanged. However, a particular class of weighting functions is chosen which allows to replace the domain integrals by boundary integrals [O-1] over specific control domains or volumes.

The FV method can be considered as a particular case of FE method with a non Galerkin weighting [O-1], [Z-4]. Starting from the same strong form of the kinematic equations (1.1), constitutive equations (1.2), equilibrium equations (1.3) and the boundary conditions (1.4a) and (1.4b), the weighted residual form of the equilibrium equations can be written as

$$\int_{\Omega} \mathbf{W}^T[\mathbf{L}^T\mathbf{DLu} + \mathbf{b}]d\Omega + \oint_{\Gamma_u} \mathbf{W}_u{}^T\mathbf{u}d\Gamma + \oint_{\Gamma_t} \mathbf{W}_t{}^T[\mathbf{TDLu} - \mathbf{t}]d\Gamma = \mathbf{0} \quad (1.12)$$

By using the assumption that the weighting functions $\mathbf{W}_u = 0$ on Γ_u the satisfaction of the kinematic boundary conditions is enforced. Integrating by parts the first integral of (1.12) and choosing $\mathbf{W}_t = -\mathbf{W}$, the last equation can be rewritten in the following way

$$-\int_{\Omega} [\mathbf{LW}]^T\mathbf{DLu}d\Omega + \int_{\Omega} \mathbf{W}^T\mathbf{b}d\Omega + \oint_{\Gamma_t} \mathbf{W}^T\mathbf{TDLu}d\Gamma + \oint_{\Gamma_t} \mathbf{W}^T\mathbf{t}d\Gamma = \mathbf{0} \quad (1.13)$$

The independent unknowns in both, FE and FV methods are approximated as

$$\mathbf{u} = \hat{\mathbf{u}} = \mathbf{N}\bar{\mathbf{u}} \quad (1.14)$$

where $\bar{\mathbf{u}}$ is the nodal displacement vector and $\mathbf{N}$ is the shape function matrix for the displacement approximation. Substituting equation (1.14) into (1.13), the following set of algebraic equations is obtained

$$-\int_{\Omega} [\mathbf{LW}_i]^T\mathbf{DL}\hat{\mathbf{u}}d\Omega + \int_{\Omega} \mathbf{W}_i{}^T\mathbf{b}d\Omega + \oint_{\Gamma_t} \mathbf{W}_i{}^T\mathbf{TDL}\hat{\mathbf{u}}d\Gamma + \oint_{\Gamma_t} \mathbf{W}_i{}^T\mathbf{t}d\Gamma = \mathbf{0} \quad (1.15)$$

where $\mathbf{W}_i (i = 1, 2, ...n)$ are the appropriately selected weighting functions.

Equation (1.15) can be written in matrix form after the substitutions of the interpolation (1.14) as

$$\mathbf{K}\bar{\mathbf{u}} = \mathbf{f} \tag{1.16}$$

where $\mathbf{K}$ is the stiffness matrix

$$\mathbf{K}_{ij} = \int_{\Omega_i} [\mathbf{L}\mathbf{W}_i]^T \mathbf{D}\mathbf{L}\mathbf{N}_j d\Omega - \oint_{\Gamma_i} \mathbf{W}_i{}^T \mathbf{T}\mathbf{D}\mathbf{L}\mathbf{N}_j d\Gamma \tag{1.17}$$

and $\mathbf{f}$ is the equivalent nodal force vector

$$\mathbf{f}_i = \int_{\Omega_i} \mathbf{W}_i{}^T \mathbf{b} d\Omega + \oint_{\Gamma_{ti}} \mathbf{W}_i{}^T \mathbf{t} d\Gamma \tag{1.18}$$

In above, Ω_i is the control domain associated with node i, Γ_i is the boundary of the control domain excluding the part which may coincide with the external boundary of the total domain where tractions are prescribed and Γ_{ti} is the boundary part which coincides with the external boundary of the total domain where tractions are prescribed.

1.4.1 Finite Element and Finite Volume method

In the FE method, the Galerkin approach is typically used with the assumption that

$$\mathbf{W}_i = \mathbf{N}_i \tag{1.19}$$

In other words, the chosen weighting function implies the same approximation for the virtual displacements as for the actual ones. The weighting functions for the FE approximation is presented in Figure 1.1. It is essential that the symmetry of the stiffness matrix $\mathbf{K}$ is preserved and the surface integral in (1.17) vanishes as $\mathbf{N}_i$ is zero at the control domain boundary. So, the stiffness matrix is expressed as

$$\mathbf{K}_{ij} = \int_{\Omega_i} [\mathbf{L}\mathbf{N}_i]^T \mathbf{D}\mathbf{L}\mathbf{N}_j d\Omega \tag{1.20}$$

and the equivalent nodal forces are expressed as

$$\mathbf{f}_i = \int_{\Omega_i} \mathbf{N}_i{}^T \mathbf{b} d\Omega + \oint_{\Gamma_{ti}} \mathbf{N}_i{}^T \mathbf{t} d\Gamma \tag{1.21}$$

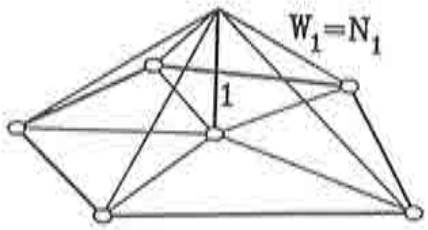

Figure 1.1 Weighting function for Finite Element approximation.

In the FV method, the following assumption is used

$$\mathbf{W}_i = \mathbf{I} \quad in \quad \Omega_i \quad and \quad \mathbf{W}_i = 0 \quad elsewhere \tag{1.22}$$

where $\mathbf{I}$ is the unity matrix. The weighting function for FV approximation is presented in Figure 1.23.

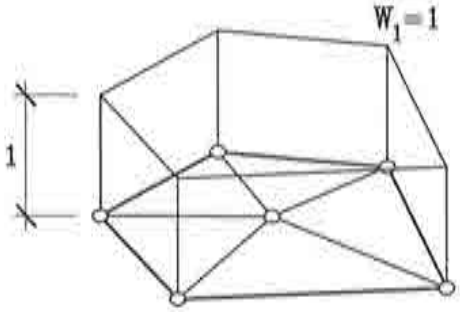

Figure 1.2 Weighting function for Finite Volume approximation.

Equation (1.15) can be interpreted as applying unit virtual displacements over each control domain [O-1]. Substituting (1.22) into (1.15) gives

$$\int_{\Omega_i} \mathbf{b} d\Omega + \oint_{\Gamma_{ti}} \mathbf{t} d\Gamma + \oint_{\Gamma_i} \mathbf{TDL}\hat{\mathbf{u}} d\Gamma = 0 \tag{1.23}$$

Substituting equation (1.14) into (1.23), the same can be rewritten in matrix form (1.16), where the stiffness matrix is expressed as

$$\mathbf{K}_{ij} = \oint_{\Gamma_i} \mathbf{TDLN}_j d\Gamma \tag{1.24}$$

and the equivalent nodal forces are

$$\mathbf{f}_i = \int_{\Omega_i} \mathbf{b} d\Omega + \oint_{\Gamma_{ti}} \mathbf{t} d\Gamma \tag{1.25}$$

The definition of Ω_i, Γ_t and Γ_{ti} are the same as for equation (1.18). It should be noted that the symmetry of the $\mathbf{K}$ matrix is not preserved and the volume integral in stiffness matrix $\mathbf{K}_{ij}$ vanishes.

Two different schemes can be used in FV method: Cell Centered scheme and Cell Vertex scheme which are similar but not identical. The main differences between both schemes are presented below.

1.4.2 Cell Centered scheme

In the Cell Centered scheme presented in Figure 1.3 weighting areas and control domains coincide with the elements, thus the difficulty of discontinuity of normal derivatives along boundaries appears. Figure 1.3 represents the field of arbitrary three node triangles with linear interpolations. Applying the same assumption (1.22) used for the FV method, all volume integrals involving derivatives of the constant weighting function disappear, as it is shown in equation (1.24) and only the boundary integrals in the stiffness matrix $\mathbf{K}_{ij}$ appear.

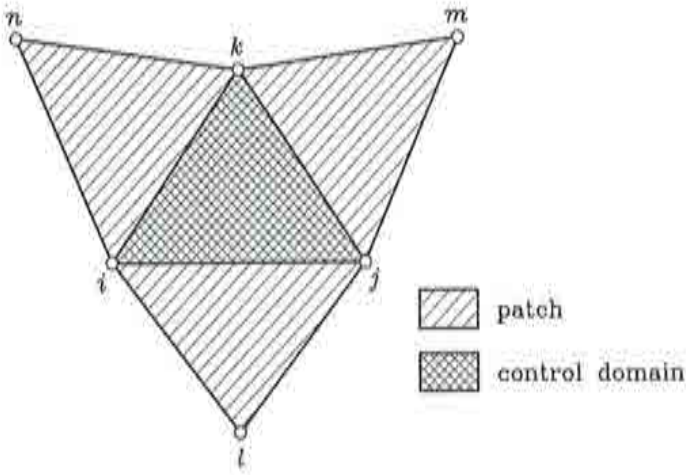

Figure 1.3 Cell Centered patch and control domain.

The displacement gradients involved in equation (1.23) are not continuous at the interfaces between the elements, and this makes some difficulties. The discontinuity in the normal direction n between two adjacent elements jumps from a value $\frac{1}{h1}$ to $\frac{1}{h2}$, as shown in Figure 1.4, where $h1$ and $h2$ are the heights of adjacent triangles.

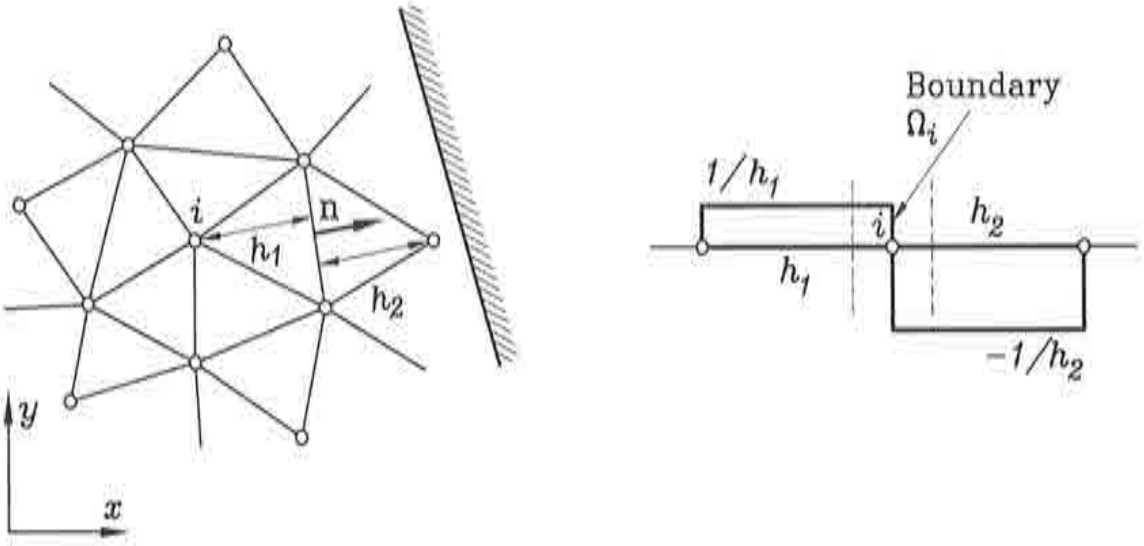

Figure 1.4 Finite element mesh of linear triangles and discontinuity of gradient at boundaries of control domain in Cell Centered scheme.

Using the theory of distributions, the jump in $\frac{\partial \hat{u}}{\partial n}$ across the boundary should be given as an average value, supposing that the mid value is optimal

$$\frac{\partial \hat{u}}{\partial n} = \frac{1}{2}\left(\frac{\partial \hat{u}}{\partial n}\Big|_1 + \frac{\partial \hat{u}}{\partial n}\Big|_2\right) \tag{1.26}$$

where $\frac{\partial \hat{u}}{\partial n}\Big|_1$ and $\frac{\partial \hat{u}}{\partial n}\Big|_2$ are the values of $\frac{\partial \hat{u}}{\partial n}$ over the elements 1 and 2, respectively. The last equation represents the jump in $\frac{\partial \hat{u}}{\partial n}$ across the boundaries, which leads to the discontinuity of tractions along the common boundary between two adjacent elements.

It can be shown [O-3], [I-1], that the stiffness term in the Cell Centered Finite Volume method has a wider bandwidth than the corresponding one in Finite Element method due to the contributions from the interface derivatives $\frac{\partial \hat{u}}{\partial n}$, as the external nodes of the adjacent elements are involved. Oñate, Cervera and Zienkiewicz [O-3] and Idelson and Oñate [I-1], have shown that the stiffness equations obtained with the Cell Vertex scheme coincide with those obtained with standard FEM for the case of structured triangular meshes of equal size elements.

1.4.3 Cell Vertex scheme

The Cell Vertex scheme is defined by assigning the control domain to each node without overlapping of the weighted area (i.e. an element shares several control domains), as presented in Figure 1.5.

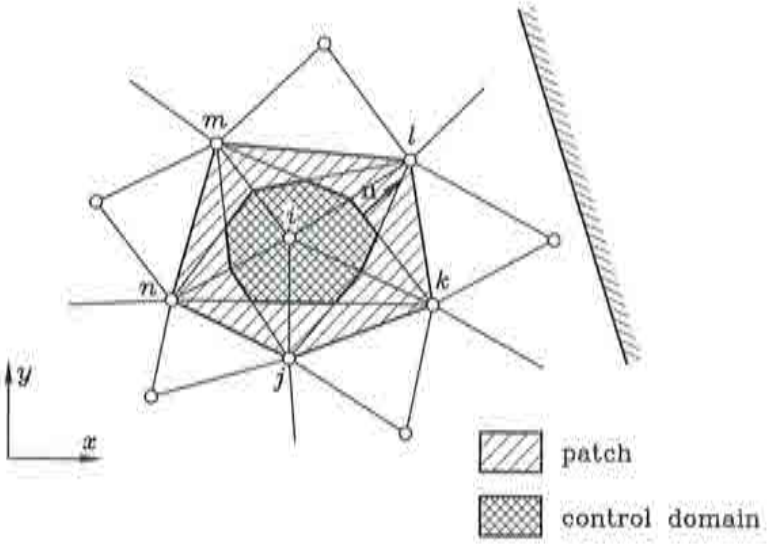

Figure 1.5 Cell Vertex patch and control domain.

Using the Cell Vertex scheme, the above mentioned gradient discontinuity difficulties are avoided as the displacement derivatives are constant within each element containing now part of the control domain boundary. Conversely, a more complicated element subdivision is involved, as shown in Figure 1.5.

1.5 MIXED FORMULATION. HU-WASHIZU PRINCIPLE

The second possibility to handle the elasticity problem with constraints is to abandon the displacement type variational formulation in favour of a mixed type approach in which not only displacements but also strains and stresses need to be interpolated. This type of formulation is obtained by defining separately the weighted residual form of the three fundamental groups of equations expressed in (1.1), (1.2) and (1.3). This leads to the weighted residual form of the kinematic equations

$$\int_{\Omega} \delta\boldsymbol{\sigma}^T (\mathbf{L}\mathbf{u} - \boldsymbol{\varepsilon}) d\Omega = \mathbf{0} \tag{1.27}$$

where $\delta\boldsymbol{\sigma}$ is the virtual stress. The analogous integral form of the constitutive equations is

$$\int_{\Omega} \delta\boldsymbol{\varepsilon}^T (\mathbf{D}\boldsymbol{\varepsilon} - \boldsymbol{\sigma}) d\Omega = \mathbf{0} \tag{1.28}$$

where $\delta\boldsymbol{\varepsilon}$ is the virtual strain. Finally, the weighted residual form of the equilibrium equations is

$$\int_{\Omega} (\mathbf{L}\delta\mathbf{u})^T \boldsymbol{\sigma} d\Omega - \int_{\Omega} \delta\mathbf{u}^T \mathbf{b} d\Omega - \int_{\Gamma_t} \delta\mathbf{u}^T \mathbf{t} d\Gamma = \mathbf{0} \tag{1.29}$$

It can be shown that these integral forms can be recovered as the variational equations of the so called Hu-Washizu variational principle [W-1], requiring the stationarity of

$$\boldsymbol{\Pi}_{HW} = \int_{\Omega} \frac{1}{2} \boldsymbol{\varepsilon}^T \mathbf{D}\boldsymbol{\varepsilon} d\varepsilon + \int_{\Omega} \boldsymbol{\sigma}^T (\mathbf{L}\mathbf{u} - \boldsymbol{\varepsilon}) d\Omega - \int_{\Omega} \mathbf{u}^T \mathbf{b} d\Omega - \int_{\Gamma_t} \mathbf{u}^T \mathbf{t} d\Gamma \tag{1.30}$$

where $\mathbf{u} = \bar{\mathbf{u}}$ on Γ_u is enforced.

It is important to note that in this case, it is necessary to choose not only the displacement approximations, but also the appropriate approximations for the strains and stresses, in other words to define

$$\begin{aligned} \mathbf{u} &= \mathbf{N}_u \bar{\mathbf{u}} \\ \boldsymbol{\varepsilon} &= \mathbf{N}_\varepsilon \bar{\boldsymbol{\varepsilon}} \\ \boldsymbol{\sigma} &= \mathbf{N}_\sigma \bar{\boldsymbol{\sigma}} \end{aligned} \tag{1.31}$$

where $\bar{\mathbf{u}}, \bar{\boldsymbol{\varepsilon}}$ and $\bar{\boldsymbol{\sigma}}$ are the nodal displacement, deformation and stress interpolation parameters respectively and $\mathbf{N}_u, \mathbf{N}_\varepsilon$ and $\mathbf{N}_\sigma$ denote the corresponding shape functions.

Replacing the approximations for the stresses, strains and displacements (1.31) into the weak form of the kinematic equations (1.27), constitutive equations (1.28) and equilibrium equations (1.29) respectively, the same can be rewritten as

$$\int_{\Omega} \mathbf{N}_\sigma^T [\mathbf{L}\mathbf{N}_u \bar{\mathbf{u}} - \mathbf{N}_\varepsilon \bar{\boldsymbol{\varepsilon}}] d\Omega = \mathbf{0} \tag{1.32}$$

$$\int_{\Omega} \mathbf{N}_\varepsilon^T [\mathbf{D}\mathbf{N}_\varepsilon \bar{\boldsymbol{\varepsilon}} - \mathbf{N}_\sigma \bar{\boldsymbol{\sigma}}] d\Omega = \mathbf{0} \tag{1.33}$$

$$\int_{\Omega} (\mathbf{L}\mathbf{N}_u)^T \mathbf{N}_\sigma \bar{\boldsymbol{\sigma}} d\Omega - \int_{\Omega} \mathbf{N}_u^T \mathbf{b} d\Omega - \int_{\Gamma_t} \mathbf{N}_u^T \mathbf{t} d\Gamma = \mathbf{0} \tag{1.34}$$

The system can be rewritten in matrix form as

$$\begin{bmatrix} \mathbf{K}_{\varepsilon\varepsilon} & \mathbf{K}_{\sigma\varepsilon} & \mathbf{0} \\ \mathbf{K}_{\sigma\varepsilon}^T & \mathbf{0} & \mathbf{K}_{u\sigma} \\ \mathbf{0} & \mathbf{K}_{u\sigma}^T & \mathbf{0} \end{bmatrix} \begin{Bmatrix} \bar{\boldsymbol{\varepsilon}} \\ \bar{\boldsymbol{\sigma}} \\ \bar{\mathbf{u}} \end{Bmatrix} = \begin{Bmatrix} \mathbf{0} \\ \mathbf{0} \\ \mathbf{f} \end{Bmatrix} \tag{1.35}$$

where

$$\mathbf{K}_{u\sigma} = \int_{\Omega} (\mathbf{L}\mathbf{N}_u)^T \mathbf{N}_\sigma d\Omega$$

$$\mathbf{K}_{\varepsilon\varepsilon} = \int_{\Omega} \mathbf{N}_\varepsilon^T \mathbf{D} \mathbf{N}_\varepsilon d\Omega$$

$$\mathbf{K}_{\sigma\varepsilon} = -\int_{\Omega} \mathbf{N}_\sigma^T \mathbf{N}_\varepsilon d\Omega$$

$$\mathbf{f} = -\int_{\Omega} \mathbf{N}_u^T \mathbf{b} d\Omega - \int_{\Gamma_t} \mathbf{N}_u^T \mathbf{t} d\Gamma \tag{1.36}$$

The criterion of necessary stability for any element assembly and boundary conditions is that [Z-4]

$$n_\varepsilon + n_u \geq n_\sigma \tag{1.37}$$

$$n_\sigma \geq n_u \tag{1.38}$$

where n_u, n_ε and n_σ are respectively the numbers of parameters defining the approximations of $\boldsymbol{\sigma}, \boldsymbol{\varepsilon}$ and $\mathbf{u}$ defined in the equation (1.31).

The reduced form of the mixed equations (1.35) can be derived and written as

$$\mathbf{K}_{\varepsilon\varepsilon}\bar{\boldsymbol{\varepsilon}} + \mathbf{K}_{\sigma\varepsilon}\bar{\boldsymbol{\sigma}} = \mathbf{0} \tag{1.39a}$$

$$\mathbf{K}_{\sigma\varepsilon}^T\bar{\boldsymbol{\varepsilon}} + \mathbf{K}_{u\sigma}\bar{\mathbf{u}} = \mathbf{0} \tag{1.39b}$$

$$\mathbf{K}_{u\sigma}^T\bar{\boldsymbol{\sigma}} = \mathbf{f} \tag{1.39c}$$

From equation (1.39a) follows

$$\bar{\varepsilon} = -\mathbf{K}_{\varepsilon\varepsilon}^{-1}\mathbf{K}_{\sigma\varepsilon}\bar{\boldsymbol{\sigma}} \tag{1.40}$$

and replacing $\bar{\varepsilon}$ into equation (1.39b) gives

$$\mathbf{K}_{u\sigma}\bar{\mathbf{u}} - [\mathbf{K}_{\sigma\varepsilon}^{T}\mathbf{K}_{\varepsilon\varepsilon}^{-1}\mathbf{K}_{\sigma\varepsilon}]\bar{\boldsymbol{\sigma}} = \mathbf{0} \tag{1.41}$$

The stresses $\bar{\boldsymbol{\sigma}}$ can be obtained as

$$\bar{\boldsymbol{\sigma}} = \mathbf{K}_{\sigma\sigma}^{-1}\mathbf{K}_{u\sigma}\bar{\mathbf{u}} \tag{1.42}$$

where $\mathbf{K}_{\sigma\sigma} = \mathbf{K}_{\sigma\varepsilon}^{T}\mathbf{K}_{\varepsilon\varepsilon}^{-1}\mathbf{K}_{\sigma\varepsilon}$.

Substituting equation (1.42) into (1.39c) gives the reduced matrix form

$$[\mathbf{K}_{u\sigma}^{T}\mathbf{K}_{\sigma\sigma}^{-1}\mathbf{K}_{u\sigma}]\bar{\mathbf{u}} = \mathbf{f} \tag{1.43}$$

i.e.

$$\mathbf{K}\bar{\mathbf{u}} = \mathbf{f} \tag{1.44}$$

with $\mathbf{K} = \mathbf{K}_{u\sigma}^{T}\mathbf{K}_{\sigma\sigma}^{-1}\mathbf{K}_{u\sigma}$.

In constructing the displacement approximation, the same shape functions as in equation (1.10) can be used. The shape functions for the strain and stress approximation $\mathbf{N}_{\varepsilon}$ and $\mathbf{N}_{\sigma}$ can possess more reduced regularity than $\mathbf{N}_{u}$ (i.e. C^{-1}), as no derivatives affect the stress and strain fields.

In other words, there is more flexibility in selecting these shape functions which could accommodate constraints and thus a better way to find an approximate solution. However, the choice of the approximations for $\boldsymbol{\varepsilon}$ and $\boldsymbol{\sigma}$ is not entirely arbitrary and it should be made in such a way that the so called Babuska-Brezzi (or LBB) conditions (1.37) and (1.38) are satisfied, which guarantees the necessary stability of the discrete solution.

1.5.1 Finite Volume scheme

The constant stress and strain fields are chosen within each control domain so that

$$\mathbf{N}_{\varepsilon} = \mathbf{N}_{\sigma} = \mathbf{I}_{\sigma} \tag{1.45}$$

$$\text{i.e.} \quad \boldsymbol{\sigma} = \boldsymbol{\sigma}_{i}, \quad \boldsymbol{\varepsilon} = \boldsymbol{\varepsilon}_{i}$$

$$n_\varepsilon = n_\sigma \tag{1.46}$$

where $\mathbf{I}_\sigma$ is the unit matrix and $(\cdot)_i$ denotes constant values over each control domain. Substituting equation (1.46) into (1.37) the first stability condition becomes

$$n_\varepsilon + n_u \geq n_\sigma \quad \Rightarrow \quad n_u \geq 0 \tag{1.47}$$

which is always satisfied. The only stability condition is

$$n_\sigma \geq n_u \tag{1.48}$$

It can be easily shown that this condition is satisfied for any Cell Centered and Cell Vertex patch using a linear approximation for $\mathbf{u}$. Taking into account the assumption (1.45) for the constant stress and strain fields leads to the following expressions

$$\int_\Omega (\mathbf{L}\delta\mathbf{u})^T \boldsymbol{\sigma} d\Omega = \sum_i [\int_{\Omega_i} (\mathbf{L}\delta\mathbf{u})^T \mathbf{I}_\sigma d\Omega] \bar{\boldsymbol{\sigma}}_i = \sum_i [\oint_{\Gamma_i} (\mathbf{T}\delta\mathbf{u})^T \mathbf{I}_\sigma d\Gamma] \bar{\boldsymbol{\sigma}}_i \tag{1.49a}$$

$$\int_\Omega \boldsymbol{\sigma}^T \mathbf{L}\mathbf{u} d\Omega = \sum_i \bar{\boldsymbol{\sigma}}_i^T \int_{\Omega_i} \mathbf{I}_\sigma \mathbf{L}\mathbf{u} d\Omega = \sum_i \bar{\boldsymbol{\sigma}}_i^T \oint_{\Gamma_i} \mathbf{I}_\sigma \mathbf{T}\mathbf{u} d\Gamma \tag{1.49b}$$

where the sum extends over the (non-overlapping) control domain covering the whole mesh. It should be noted that the right hand side of the above expressions has been obtained after integrating by parts the corresponding domain integrals.

Equation (1.49) is the basis for deriving Finite Volume schemes. Applying (1.49), the matrices in equation (1.36) become

$$\mathbf{K}_{u\sigma} = \oint_\Gamma [\mathbf{T}\mathbf{N}_u]^T \mathbf{I}_\sigma d\Gamma \tag{1.50a}$$

$$\mathbf{K}_{\varepsilon\varepsilon} = \int_\Omega \mathbf{I}_\sigma^T \mathbf{D} \mathbf{I}_\sigma d\Omega = \mathbf{D}\Omega \tag{1.50b}$$

$$\mathbf{K}_{\sigma\varepsilon} = -\int_\Omega \mathbf{I}_\sigma^T \mathbf{I}_\sigma d\Omega = -\mathbf{I}_\sigma \Omega \tag{1.50c}$$

and the expression for $\mathbf{K}_{\sigma\sigma}$ is as follows

$$\mathbf{K}_{\sigma\sigma} = -\Omega \mathbf{I}_\sigma^T \Omega^{-1} \mathbf{D}^{-1} - \Omega \mathbf{I}_\sigma = \Omega \mathbf{D}^{-1} \tag{1.51}$$

Replacing (1.50a) and (1.51) into equation (1.44) gives

$$[\mathbf{K}_{u\sigma}^T \frac{1}{\Omega} \mathbf{D} \mathbf{K}_{u\sigma}] \bar{\mathbf{u}} = \mathbf{f} \tag{1.52}$$

i.e.

$$\mathbf{K}\bar{\mathbf{u}} = \mathbf{f} \tag{1.53a}$$

with

$$\boxed{\mathbf{K} = \left[\oint_\Gamma [\mathbf{T}\mathbf{N}_u]^T \mathbf{I}_\sigma d\Gamma\right]^T \frac{1}{\Omega} \mathbf{D} \left[\oint_\Gamma [\mathbf{T}\mathbf{N}_u]^T \mathbf{I}_\sigma d\Gamma\right]} \tag{1.53b}$$

The global stiffness matrix $\mathbf{K}$ can be constructed by assembling the contribution of the different control domains in the standard manner. It should be noted again that if the Cell Centered scheme is used, the gradient terms $\mathbf{TN}_u$ are discontinuous at the element boundaries and some smoothing procedure is required as explained in Section 1.4.2. This problem disappears in the Cell Vertex scheme (see Section 1.4.3). The given ideas will be used to derive rotation-free beam and shell elements using Cell Centered and Cell Vertex schemes in the next chapters.

CHAPTER 2

ROTATION-FREE EULER-BERNOULLI BEAM ELEMENTS

2.1 INTRODUCTION

Classical Euler-Bernoulli beam theory is probably one of the simplest model problems of the constrained formulation of linear elasticity. The constraint in this case is in kinematic standard Euler-Bernoulli hypothesis restricting the cross section of the beam to remain plain and orthogonal to the neutral axis of the beam. This introduces the requirement of C_1 continuity of Finite Element interpolations. The classical choice of shape functions are Hermitian polynomials [O-1], leading to the coupling of the displacements and rotational degrees of freedom.

The main novelty in this study is to abandon this concept and to develop other types of discrete approximations for Euler-Bernoulli beams in the framework of the mixed Hu-Washizu formulation, using the concepts based on the rotation-free coupled FE/FV technique explained in the previous chapter. More precisely, two beam elements without rotational degrees of freedom are developed in this thesis. They are based on Cell Centered and Cell Vertex schemes by making use of the Euler-Bernoulli kinematic hypothesis and transferring the domain integral into a boundary integral. The corresponding beam elements are termed CCB and CVB elements, respectively.

It is also shown that the same discrete approximations can be recovered by applying the Finite Difference method, but the previous approach is much more general and easily extendable to other types of problems, as presented in the next chapter.

The outline of the chapter is as follows. First, the basic theory for Euler-Bernoulli beams is reviewed and then the set of governing equations is developed in integral form from the standard Hu-Washizu functional. This set of equations represents the basis of the coupled FE/FV discretization, discussed in detail further. The results obtained by the FE/FV technique are the same as those obtained by the Finite Difference method. The computation of the control domain curvature matrix is presented for both elements separately including the imposition of boundary conditions and the evaluation of stress resultants.

The extensive validation of the new developed rotation-free beam elements is carried out on simple linear problems, using uniform as well as nonuniform meshes. Finally, some conclusions are given.

2.2 BASIC THEORY

The governing equations of the Euler-Bernoulli beam problem presented in Figure 2.1, may be summarized as follows.

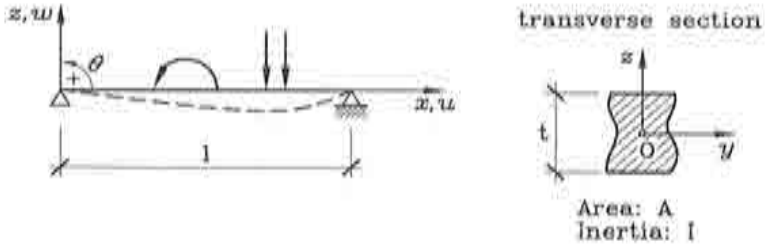

Figure 2.1 The Euler-Bernoulli beam problem.

The kinematic equation is

$$\chi = -\frac{\partial^2 w}{\partial x^2} \Rightarrow \chi = Lw \tag{2.1}$$

where $L = \left[\frac{\partial^2}{\partial x^2}\right]$, χ is the beam curvature and w is the vertical deflection.

The constitutive equation is

$$m = D\chi \tag{2.2}$$

where m is the bending moment, $D = [EI]$, E is the Young's modulus and I is the moment of inertia of the transverse section.

The equilibrium equation of the beam is

$$\frac{\partial^2 m}{\partial x^2} + q = 0 \Rightarrow Lm + q = 0 \tag{2.3}$$

where q is the distributed loading.

Substituting the constitutive equation (2.2) into the equilibrium equation (2.3) gives

$$D\frac{\partial^2 w}{\partial x^2} + q = 0 \tag{2.4}$$

Finally, substituting the kinematic equation (2.1) into (2.4), the well known equilibrium equation for Euler-Bernoulli beam is obtained

$$-D\frac{\partial^4 w}{\partial x^4} + q = 0 \quad \text{for} \quad \forall x \in [0, l] \tag{2.5}$$

The set of the governing equations in integral form can be obtained from the standard Hu-Washizu functional

$$\Pi = \frac{1}{2}\int_l \chi D\chi dx + \int_l m(Lw - \chi)dx - \int_l wqdx \tag{2.6}$$

where q is the distributed loading.

Variation of Π leads to the following set of kinematic, constitutive and equilibrium integral equations, respectively

$$\int_l \delta m(Lw - \chi)dx = 0 \tag{2.7a}$$

$$\int_l \delta\chi(D\chi - m)dx = 0 \tag{2.7b}$$

$$\int_l (L\delta w)^T m dx - \int_l \delta w q dx = 0 \tag{2.7c}$$

The set of equations (2.7) is the basis for the rotation-free coupled FE/FV discretization. It should be noted that as the virtual variables $\delta m, \delta\chi$ and δw are arbitrary, the strong form of the kinematic, constitutive and equilibrium equations can be recovered from (2.7).

2.3 FINITE ELEMENT - FINITE VOLUME DISCRETIZATION

The discretization of the beam into standard two node elements is first considered. The curvature χ and the bending moment m are assumed to be constant within the specific control domain to be defined later. Therefore

$$m, \delta m = m_p, \delta m_p \tag{2.8a}$$

$$\chi, \delta\chi = \chi_p, \delta\chi_p \tag{2.8b}$$

where $(.)_p$ denotes constant values over the control domain p. Using these assumptions, the kinematic, constitutive and equilibrium equations (2.7) are expressed as follows

$$\sum_p \delta m_p [\int_{l_p} Lw dx - \chi_p \int_{l_p} dx] = 0 \tag{2.9a}$$

$$\sum_p \delta\chi_p (D\chi_p - m_p) \int_{l_p} dx = 0 \tag{2.9b}$$

$$\sum_p \int_{l_p} (L\delta w)^T m_p dx - \sum_p \int_{l_p} \delta w q dx = 0 \tag{2.9c}$$

where the summation is extended over the number of control domains.

Integrating by parts equation (2.9a) in order to reduce the order of derivatives on w and taking into account that the virtual moments and curvatures are arbitrary, allows to obtain the patch curvature after some small algebra as

$$\chi_p = \frac{1}{l_p} \int_{l_p} \frac{\partial^2 w}{\partial x^2} dx = \frac{1}{l_p} [\frac{\partial w}{\partial x}]_{l_p^-}^{l_p^+} = \frac{1}{l_p} [\frac{\partial w}{\partial x}(l_p{}^+) - \frac{\partial w}{\partial x}(l_p{}^-)] \tag{2.10}$$

The last equation allows to compute the curvature over a control domain, as the difference of the slopes at the domain ends. In the above equation $l_p{}^+$ and $l_p{}^-$ denote the right and left ends of the domain of length l_p, respectively.

Replacing equation (2.10) into (2.9b) leads to the discrete approximation for the bending moment

$$m_p = D\chi_p = D\frac{1}{l_p} [\frac{\partial w}{\partial x}(l_p^+) - \frac{\partial w}{\partial x}(l_p^-)] \tag{2.11}$$

From equation (2.9c), using again the same procedure gives

$$\sum_p \int_{l_p} (\frac{\partial^2 w}{\partial x^2} dx) m_p = \sum_p [\frac{\partial w}{\partial x}]_{l_p^-}^{l_p^+} m_p = \sum_p [\frac{\partial w}{\partial x}(l_p^+) - \frac{\partial w}{\partial x}(l_p^-)] m_p \tag{2.12}$$

where the sum extends over the number of the control domains. Substituting equations (2.11) and (2.12) into (2.9c), the following expression for the equilibrium equation is found

$$\boxed{\sum_p [\frac{\partial w}{\partial x}(l_p^+) - \frac{\partial w}{\partial x}(l_p^-)]^T D \frac{1}{l_p} [\frac{\partial w}{\partial x}(l_p^+) - \frac{\partial w}{\partial x}(l_p^-)] = \sum_p \int_{l_p} \delta w q dx} \tag{2.13}$$

The deflection field is now interpolated within each element using standard linear shape functions N_i [O-1]

$$w = \sum_{i=1}^{2} N_i w_i = \mathbf{N}^e \bar{\mathbf{w}}^e \tag{2.14}$$

where w_i are the nodal deflection values, $\mathbf{N}^e = [N_1, N_2]$ and $\bar{\mathbf{w}}^e = [w_1, w_2]^T$.

Substituting equation (2.14) into (2.13) gives the final system of discretized equations

$$\mathbf{K}\bar{\mathbf{w}} = \mathbf{f} \tag{2.15}$$

where $\mathbf{K}$ is the stiffness matrix, $\bar{\mathbf{w}}$ is the vector containing the nodal deflections and $\mathbf{f}$ is the nodal force vector.

The global stiffness matrix can be obtained by the element contributions in the standard manner. Alternatively, it can also be obtained by assembling the contributions from the different control domains. The domain stiffness matrix $\mathbf{K}_p$ for the p-th control domain can be expressed as

$$\mathbf{K}_p = [\mathbf{B}_p]^T \mathbf{D} \mathbf{B}_p l_p \tag{2.16}$$

where $\mathbf{B}_p$ is the control domain curvature matrix and $\mathbf{D} = [EI]$. The details of the computation of this matrix are given in the next section. The components of the nodal force vector $\mathbf{f}$ for a uniformly distributed load are obtained as

$$f_i = q \frac{\sum_i A^{(e)}}{n_i} \tag{2.17}$$

where the sum extends over the number of elements sharing the i-th node and $A^{(e)}$ is the area of the element e.

2.4 COMPUTATION OF THE DOMAIN CURVATURE MATRIX

The computation of the control domain curvature matrix $\mathbf{B}_p$ is different for the Cell Centered and Cell Vertex schemes. The practical application of the new rotation-free beam element, requires the consideration of the various types of boundary conditions: free edges, simply supported edges and clamped edges. For each of them, the corresponding $\mathbf{B}_p$ matrix is calculated.

2.4.1 Cell Centered scheme - CCB element

Equation (2.13) requires the computation of the deflection gradient along the domain edges. This leads to difficulties in Cell Centered scheme, as the deflection is discontinuous at the element ends. The way to overcome this problem is to compute the deflection gradient at the element ends as the average value of the gradients contributed by the two elements sharing the end node.

The linear interpolation for displacements and the constant value for the curvature and bending moment within the control domain (i.e. the element) are assumed, as shown in Figure 2.2.

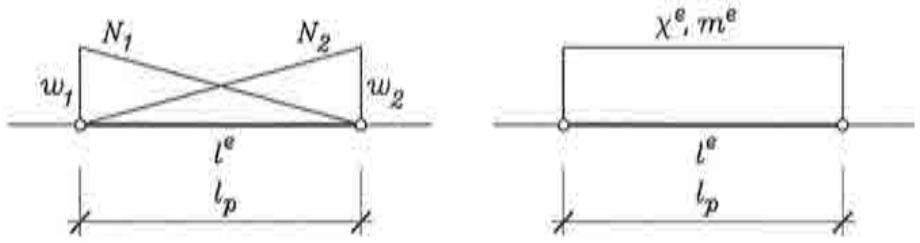

Figure 2.2 Interpolation functions for displacement, curvature and bending fields in Cell Centered domains.

2.4.1.1 General case

The elements adjacent to the chosen element l^e are connected together forming one patch, as presented in Figure 2.3. The boundary conditions are not applied.

The curvature over the control domain is obtained from equation (2.10) as

$$\chi_p = \frac{1}{l^e}\left[\left(\frac{\partial w}{\partial x}\right)_{i+1} - \left(\frac{\partial w}{\partial x}\right)_i\right] \tag{2.18}$$

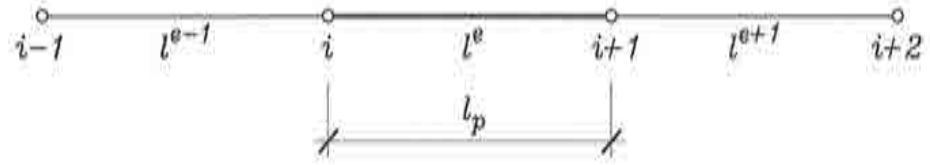

Figure 2.3 General element patch for the Cell Centered scheme.

It should be noted that in this case $l^e = l_p$. Using the theory of distributions, the values $(\frac{\partial w}{\partial x})_{i+1}$ and $(\frac{\partial w}{\partial x})_i$ across the element boundaries are computed as an average value

$$(\frac{\partial w}{\partial x})_{i+1} = \frac{1}{2}\Big[(\frac{\partial w}{\partial x})^e_{i+1} + (\frac{\partial w}{\partial x})^{e+1}_{i+1}\Big] = \frac{1}{2}\Big[\frac{w_{i+1} - w_i}{l^e} + \frac{w_{i+2} - w_{i+1}}{l^{e+1}}\Big] \tag{2.19}$$

$$(\frac{\partial w}{\partial x})_i = \frac{1}{2}\Big[(\frac{\partial w}{\partial x})^{e-1}_i + (\frac{\partial w}{\partial x})^e_i\Big] = \frac{1}{2}\Big[\frac{w_i - w_{i-1}}{l^{e-1}} + \frac{w_{i+1} - w_i}{l^e}\Big] \tag{2.20}$$

Substituting the last two equations into (2.18), yields

$$\chi_p = \frac{1}{2l^{e-1}l^e l^{e+1}}[l^{e+1}, -l^{e+1}, -l^{e-1}, l^{e-1}] \begin{Bmatrix} w_{i-1} \\ w_i \\ w_{i+1} \\ w_{i+2} \end{Bmatrix} = \mathbf{B}_p \mathbf{w}_p \tag{2.21}$$

where the domain curvature matrix $\mathbf{B}_p$ is

$$\mathbf{B}_p = \frac{1}{2l^{e-1}l^e l^{e+1}}[l^{e+1}, -l^{e+1}, -l^{e-1}, l^{e-1}] \tag{2.22}$$

The vector $\mathbf{w}_p$ containing the nodal deflections of the element patch contributing to the p-th domain is

$$\mathbf{w}_p = [w_{i-1}, w_i, w_{i+1}, w_{i+2}]^T \tag{2.23}$$

Substituting equation (2.22) into (2.16) gives the domain stiffness matrix. It should be noted that the control domain coincides with an element in this case. Therefore, $\mathbf{K}_p = \mathbf{K}^{(e)}$.

Equation (2.16) can be expanded as

$$\mathbf{K}_p = \mathbf{K}^{(e)} = \frac{EI}{4l^e(l^{e+1}l^{e-1})^2}$$

$$\begin{bmatrix} (l^{e+1})^2 & (-l^{e+1})^2 & (-l^{e+1})(l^{e-1}) & (l^{e+1})(l^{e-1}) \\ (-l^{e+1})^2 & (l^{e+1})^2 & (-l^{e+1})(-l^{e-1}) & (-l^{e+1})(l^{e-1}) \\ (-l^{e+1})(l^{e-1}) & (-l^{e+1})(-l^{e-1}) & (l^{e-1})^2 & (-l^{e-1})^2 \\ (l^{e+1})(l^{e-1}) & (-l^{e+1})(l^{e-1}) & (-l^{e-1})^2 & (l^{e-1})^2 \end{bmatrix} \tag{2.25}$$

2.4.1a Imposition of the boundary conditions

Special care has to be taken when considering a control domain with boundary nodes. In this case, the discrete curvature approximation must be constructed in accordance with the particular boundary conditions.

2.4.1.2 Free or simply supported edge on the left end

The control domain contains an element with a free or simply supported node on the left end, as presented in Figure 2.4.

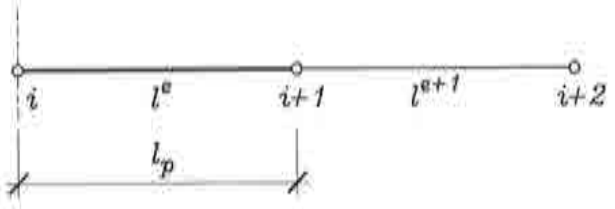

Figure 2.4 Control domain with free or simply supported node on the left end.

By the same theoretical consideration as for the general case, the constant curvature over the domain is

$$\chi_p = \frac{1}{l^e}\left[(\frac{\partial w}{\partial x})_{i+1} - (\frac{\partial w}{\partial x})_i\right] \tag{2.26}$$

where the slopes $(\frac{\partial w}{\partial x})_{i+1}$ and $(\frac{\partial w}{\partial x})_i$ are, respectively

$$(\frac{\partial w}{\partial x})_{i+1} = \frac{1}{2}\left[(\frac{\partial w}{\partial x})^e_{i+1} + (\frac{\partial w}{\partial x})^{e+1}_{i+1}\right] = \frac{1}{2}\left[\frac{w_{i+1} - w_i}{l^e} + \frac{w_{i+2} - w_{i+1}}{l^{e+1}}\right] \tag{2.27}$$

$$(\frac{\partial w}{\partial x})_i = \frac{w_{i+1} - w_i}{l^e} \tag{2.28}$$

Replacing equations (2.27) and (2.28) into equation (2.26), the domain curvature χ_p is obtained as

$$\chi_p = \frac{1}{2(l^e)^2 l^{e+1}}[0, l^{e+1}, -(l^e + l^{e+1}), l^e] \begin{Bmatrix} w_{i-1} \\ w_i \\ w_{i+1} \\ w_{i+2} \end{Bmatrix} = \mathbf{B}_p \mathbf{w}_p \tag{2.29}$$

where the domain curvature matrix $\mathbf{B}_p$ is

$$\mathbf{B}_p = \frac{1}{2(l^e)^2 l^{e+1}}[0, l^{e+1}, -(l^e + l^{e+1}), l^e] \tag{2.30}$$

Finally, the domain stiffness matrix $\mathbf{K}_p$ is

$$\mathbf{K}_p = \mathbf{K}^{(e)} = \frac{EI}{4(l^e)^3 (l^{e+1})^2}$$

$$\begin{bmatrix} 0 & 0 & 0 & 0 \\ 0 & (l^{e+1})^2 & (-l^{e+1})(l^e + l^{e+1}) & l^e(l^{e+1}) \\ 0 & (-l^{e+1})(l^e + l^{e+1}) & (l^e + l^{e+1})^2 & -l^e(l^e + l^{e+1}) \\ 0 & l^e(l^{e+1}) & -l^e(l^e + l^{e+1}) & (l^e)^2 \end{bmatrix} \tag{2.31}$$

2.4.1.3 Free or simply supported edge on the right end

The control domain contains an element with a free or simply supported node on the right end, as shown in Figure 2.5.

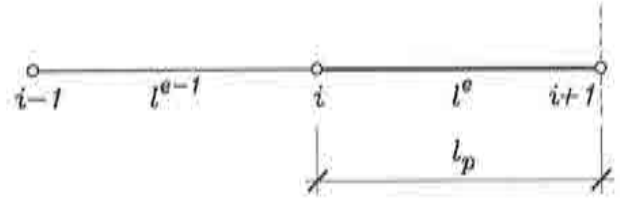

Figure 2.5 Control domain with free or simply supported node on the right end.

The domain curvature for this case is given as

$$\chi_p = \frac{1}{l^e}\Big[(\frac{\partial w}{\partial x})_{i+1} - (\frac{\partial w}{\partial x})_i\Big] \tag{2.32}$$

where the values $(\frac{\partial w}{\partial x})_{i+1}$ and $(\frac{\partial w}{\partial x})_i$ are computed by

$$(\frac{\partial w}{\partial x})_{i+1} = \frac{w_{i+1} - w_i}{l^e} \tag{2.33}$$

$$(\frac{\partial w}{\partial x})_i = \frac{1}{2}\Big[(\frac{\partial w}{\partial x})_i^e + (\frac{\partial w}{\partial x})_i^{e-1}\Big] = \frac{1}{2}\Big[\frac{w_{i+1} - w_i}{l^e} + \frac{w_i - w_{i-1}}{l^{e-1}}\Big] \tag{2.34}$$

Replacing equations (2.33) and (2.34) into (2.32), the domain curvature χ_p is given as

$$\chi_p = \frac{1}{2(l^e)^2 l^{e-1}}[l^e, -(l^e + l^{e-1}), l^{e-1}, 0]\begin{Bmatrix} w_{i-1} \\ w_i \\ w_{i+1} \\ w_{i+2} \end{Bmatrix} = \mathbf{B}_p \mathbf{w}_p \tag{2.35}$$

where the domain curvature matrix $\mathbf{B}_p$ is

$$\mathbf{B}_p = \frac{1}{2(l^e)^2 l^{e-1}}[l^e, -(l^e + l^{e-1}), l^{e-1}, 0] \tag{2.36}$$

Finally, the domain stiffness matrix $\mathbf{K}_p$ is given as

$$\mathbf{K}_p = \mathbf{K}^{(e)} = \frac{EI}{4(l^e)^3(l^{e-1})^2}$$

$$\begin{bmatrix} (l^e)^2 & -l^e(l^e + l^{e-1}) & l^e(l^{e-1}) & 0 \\ -l^e(l^e + l^{e-1}) & (l^e + l^{e-1})^2 & (-l^{e-1})(l^e + l^{e-1}) & 0 \\ l^e(l^{e-1}) & (-l^{e-1})(l^e + l^{e-1}) & (l^{e-1})^2 & 0 \\ 0 & 0 & 0 & 0 \end{bmatrix} \tag{2.37}$$

2.4.1.4 Clamped edge on the left end

The control domain includes an element with a clamped node on the left end, as shown in Figure 2.6.

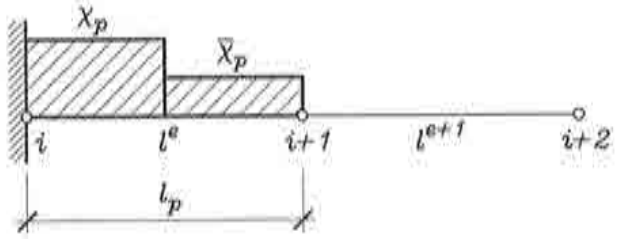

Figure 2.6 Control domain with clamped node on the left end.

The curvature of the control domain is divided into two parts, each of them calculated separately. The domain curvature χ_p is obtained as

$$\chi_p = \frac{1}{\frac{l^p}{2}}\left[\frac{w_{i+1} - w_i}{l^e}\right] = \frac{2}{l^{e2}}[-1, 1]\begin{Bmatrix} w_i \\ w_{i+1} \end{Bmatrix} = \mathbf{B}_p \mathbf{w}_p \tag{2.38}$$

where the curvature matrix $\mathbf{B}_p$ is

$$\mathbf{B}_p = \frac{2}{l^{e2}}[-1, 1] \tag{2.39}$$

and the stiffness matrix $\mathbf{K}_p^1$ is

$$\mathbf{K}_p^1 = \mathbf{B}_p^T \mathbf{D} \mathbf{B}_p \frac{l^e}{2} = \frac{4EI}{2(l^e)^3}\begin{bmatrix} 0 & 0 & 0 & 0 \\ 0 & 1 & -1 & 0 \\ 0 & -1 & 1 & 0 \\ 0 & 0 & 0 & 0 \end{bmatrix} \tag{2.40}$$

The curvature $\bar{\chi}_p$ is computed as

$$\bar{\chi}_p = \frac{1}{\frac{l^e}{2}}\left[\frac{1}{2}\left[\frac{w_{i+1} - w_i}{l^e} + \frac{w_{i+2} - w_{i+1}}{l^{e+1}}\right] - \frac{w_{i+1} - w_i}{l^e}\right] =$$

$$= \frac{1}{l^{e2} l^{e+1}}[0, l^{e+1}, (-l^{e+1} - l^e), l^e]\begin{Bmatrix} w_{i-1} \\ w_i \\ w_{i+1} \\ w_{i+2} \end{Bmatrix} = \bar{\mathbf{B}}_p \mathbf{w}_p \tag{2.41}$$

where the curvature matrix $\bar{\mathbf{B}}_p$ is

$$\bar{\mathbf{B}}_p = \frac{1}{l^{e2}l^{e+1}}[0, l^{e+1}, (-l^{e+1} - l^e), l^e] \tag{2.42}$$

and the stiffness matrix $\mathbf{K}_p^2$ is

$$\mathbf{K}_p^2 = \bar{\mathbf{B}}_p^T \mathbf{D} \bar{\mathbf{B}}_p \frac{l^e}{2} = \frac{EI}{2(l^e)^3(l^{e+1})^2}$$

$$\begin{bmatrix} 0 & 0 & 0 & 0 \\ 0 & (l^{e+1})^2 & (l^{e+1})(-l^{e+1} - l^e) & l^e(l^{e+1}) \\ 0 & (l^{e+1})(-l^{e+1} - l^e) & (-l^{e+1} - l^e)^2 & l^e(-l^{e+1} - l^e) \\ 0 & l^e(l^{e+1}) & l^e(-l^{e+1} - l^e) & (l^e)^2 \end{bmatrix} \tag{2.43}$$

The total stiffness matrix for the control domain is computed as

$$\mathbf{K}_p = \mathbf{K}^{(e)} = \mathbf{K}_p^1 + \mathbf{K}_p^2 \tag{2.44}$$

2.4.1.5 Clamped edge on the right end

The control domain includes an element with a clamped node on the right end, as shown in Figure 2.7.

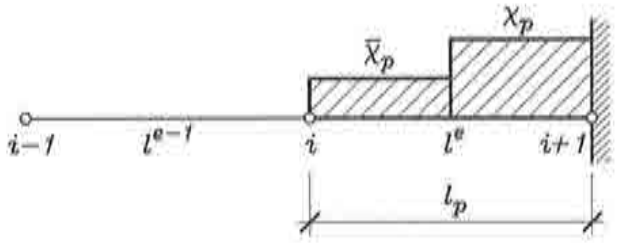

Figure 2.7 Control domain with clamped node on the right end.

The curvature of the control domain is divided into two parts, each of them calculated separately as follows.

The curvature χ_p is

$$\chi_p = \frac{1}{\frac{l^e}{2}}\left[\frac{w_{i+1} - w_i}{l^e}\right] = \frac{2}{l^{e2}}[-1, 1]\begin{Bmatrix} w_i \\ w_{i+1} \end{Bmatrix} = \mathbf{B}_p \mathbf{w}_p \tag{2.45}$$

where the curvature matrix $\mathbf{B}_p$ is

$$\mathbf{B}_p = \frac{2}{l^{e2}}[-1, 1] \tag{2.46}$$

and the stiffness matrix $\mathbf{K}_p^1$ is

$$\mathbf{K}_p^1 = \mathbf{B}_p^T \mathbf{D} \mathbf{B}_p \frac{l^e}{2} = \frac{4EI}{2(l^e)^3} \begin{bmatrix} 0 & 0 & 0 & 0 \\ 0 & 1 & -1 & 0 \\ 0 & -1 & 1 & 0 \\ 0 & 0 & 0 & 0 \end{bmatrix} \tag{2.47}$$

The curvature $\bar{\chi}_p$ is

$$\bar{\chi}_p = \frac{1}{\frac{l^e}{2}} \left[\frac{1}{2} \left[\frac{w_{i+1} - w_i}{l^e} + \frac{w_i - w_{i-1}}{l^{e-1}} \right] - \frac{w_{i+1} - w_i}{l^e} \right] =$$

$$\frac{1}{l^{e2} l^{e-1}} [-l^e, (l^{e-1} + l^e), -l^{e-1}, 0] \begin{Bmatrix} w_{i-1} \\ w_i \\ w_{i+1} \\ w_{i+2} \end{Bmatrix} = \bar{\mathbf{B}}_p \mathbf{w}_p \tag{2.48}$$

where the curvature matrix $\bar{\mathbf{B}}_p$ is

$$\bar{\mathbf{B}}_p = \frac{1}{l^{e2} l^{e-1}} [-l^e, (l^{e-1} + l^e), -l^{e-1}, 0] \tag{2.49}$$

and the stiffness matrix $\mathbf{K}_p^2$ is

$$\mathbf{K}_p^2 = \bar{\mathbf{B}}_p^T \mathbf{D} \bar{\mathbf{B}}_p \frac{l^e}{2} \frac{EI}{2(l^e)^3 (l^{e-1})^2}$$

$$\begin{bmatrix} (l^e)^2 & -l^e(l^{e-1} + l^e) & l^e(l^{e-1}) & 0 \\ -l^e(l^{e-1} + l^e) & (l^{e-1} + l^e)^2 & -l^{e-1}(l^{e-1} + l^e) & 0 \\ l^e(l^{e-1}) & -l^{e-1}(l^{e-1} + l^e) & (l^{e-1})^2 & 0 \\ 0 & 0 & 0 & 0 \end{bmatrix} \tag{2.50}$$

Again, the total stiffness matrix $\mathbf{K}_p$ for the control domain is computed as the sum of $\mathbf{K}_p^1$ and $\mathbf{K}_p^2$.

2.4.2 Cell Vertex scheme - CVB element

The deflection gradient in the Cell Vertex scheme is continuous across the control domain ends. It should be noted that a control domain is formed now by the two elements sharing a node. The interpolation functions for displacement field are shown in Figure 2.8.

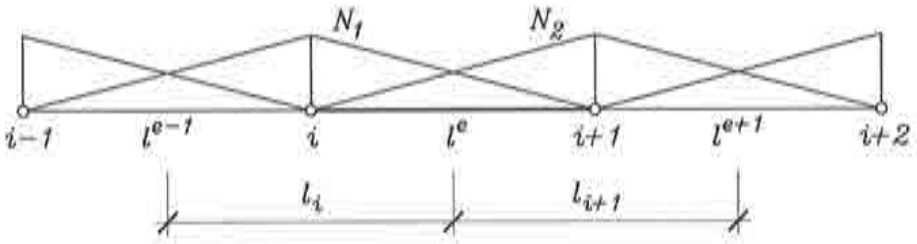

Figure 2.8 Interpolation functions for displacement field over Cell Vertex domain.

The curvature and bending moment are assumed to be constant over the control domain, as shown in Figure 2.9.

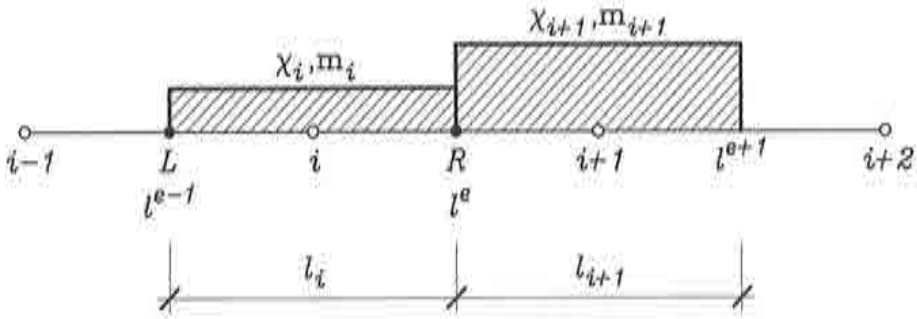

Figure 2.9 Interpolation functions for curvature and bending moment field over Cell Vertex domain.

The curvature associated to the control domain is obtained from equation (2.10) as

$$\chi_p = \frac{1}{l_p}\left[\left[\frac{\partial w}{\partial x}\right]_R - \left[\frac{\partial w}{\partial x}\right]_L\right] \tag{2.51}$$

2.4.2.1 General case

A general control domain is presented in Figure 2.10.

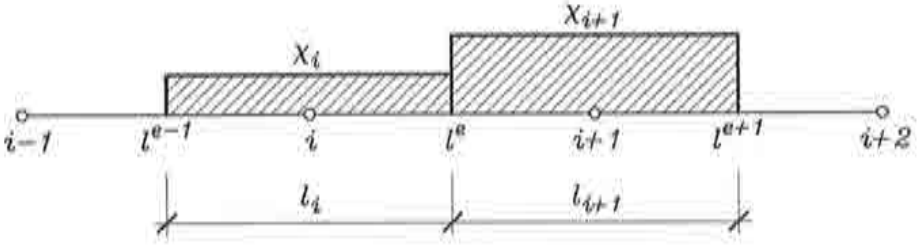

Figure 2.10 General control domain for the Cell Vertex scheme.

The constant curvature χ_i assigned to the control domain linked to node i is given as

$$\chi_i = \frac{2}{l^{e-1}+l^e}\left[\frac{w_{i+1}-w_i}{l^e} - \frac{w_i - w_{i-1}}{l^{e-1}}\right] \tag{2.52}$$

which can be rewritten in the following form

$$\chi_i = \frac{2}{l^e l^{e-1}(l^{e-1}+l^e)}[l^e, -(l^e+l^{e-1}), l^{e-1}, 0]\begin{Bmatrix} w_{i-1} \\ w_i \\ w_{i+1} \\ w_{i+2} \end{Bmatrix} = \mathbf{B}_i \mathbf{w}_i \tag{2.53}$$

where the domain curvature matrix $\mathbf{B}_i$ is

$$\mathbf{B}_i = \frac{2}{l^e l^{e-1}(l^{e-1}+l^e)}[l^e, -(l^e+l^{e-1}), l^{e-1}, 0] \tag{2.54}$$

It should be noted that as in the Cell Centered case, vector $\mathbf{w}_i$ contains contributions from the nodes linked to the i-th control domain. The curvature χ_{i+1} linked to node $i+1$ is

$$\chi_{i+1} = \frac{2}{l^e + l^{e+1}}\left[\frac{w_{i+2}-w_{i+1}}{l^{e+1}} - \frac{w_{i+1}-w_i}{l^e}\right] \tag{2.55}$$

From equation (2.55)

$$\chi_{i+1} = \frac{2}{l^e l^{e+1}(l^e + l^{e+1})}[0, l^{e+1}, -(l^e + l^{e+1}), l^e] \begin{Bmatrix} w_{i-1} \\ w_i \\ w_{i+1} \\ w_{i+2} \end{Bmatrix} = \mathbf{B}_{i+1}\mathbf{w}_i \quad (2.56)$$

where the domain curvature matrix $\mathbf{B}_{i+1}$ is

$$\mathbf{B}_{i+1} = \frac{2}{l^e l^{e+1}(l^e + l^{e+1})}[0, l^{e+1}, -(l^e + l^{e+1}), l^e] \quad (2.57)$$

The internal virtual work over an element can be obtained by summing the contributions from the two control domains involved, i.e.

$$\delta u^{(e)} = \int_{l_{\frac{i}{2}}} \delta\chi_i EI\chi_i dx + \int_{l_{\frac{i+1}{2}}} \delta\chi_{i+1} EI\chi_{i+1} dx \quad (2.58)$$

Substituting equations (2.53) and (2.56) into equation (2.58) gives the element stiffness matrix

$$\mathbf{K}^{(e)} = \mathbf{K}_p^1 + \mathbf{K}_p^2 \quad (2.59)$$

where

$$\mathbf{K}_p^1 = \frac{2EI}{l^e(l^{e-1})^2(l^e + l^{e-1})^2}$$

$$\begin{bmatrix} (l^e)^2 & -l^e(l^e + l^{e-1}) & l^e(l^{e-1}) & 0 \\ -l^e(l^e + l^{e-1}) & (l^e + l^{e-1})^2 & -l^{e-1}(l^e + l^{e-1}) & 0 \\ l^e(l^{e-1}) & -l^{e-1}(l^e + l^{e-1}) & (l^{e-1})^2 & 0 \\ 0 & 0 & 0 & 0 \end{bmatrix} \quad (2.60)$$

and

$$\mathbf{K}_p^2 = \frac{2EI}{l^e(l^{e+1})^2(l^e + l^{e+1})^2}$$

$$\begin{bmatrix} 0 & 0 & 0 & 0 \\ 0 & (l^{e+1})^2 & -l^{e+1}(l^e + l^{e+1}) & l^e(l^{e+1}) \\ 0 & -l^{e+1}(l^e + l^{e+1}) & (l^e + l^{e+1})^2 & -l^e(l^e + l^{e+1}) \\ 0 & l^e(l^{e+1}) & -l^e(l^e + l^{e+1}) & (l^e)^2 \end{bmatrix} \quad (2.61)$$

The stiffness matrix for the beam is obtained by assembling the contributions from the element stiffness matrices $\mathbf{K}^{(e)}$ in the standard manner. It is important to point out again that in the Cell Centered scheme the control domains coincide with elements, i.e. $\mathbf{K}_p = \mathbf{K}^{(e)}$. However, this is not the case in the Cell Vertex scheme. The approach shown above is based on the computation of the element stiffness matrix. A similar procedure could be followed to obtain the domain stiffness matrix in the Cell Vertex scheme. In both cases the global stiffness matrix is obviously the same. The element formulation described above allows to perform easily the element stiffness matrices in any finite element program.

2.4.2a Imposition of the boundary conditions

The imposition of the boundary conditions are simpler than the ones for the CCB element. Vanishing edge bending moments at free and simply supported edges are imposed 'a priori' by making zero of the corresponding terms of the constitutive matrix at the boundary nodes where the bending moments are constrained.

2.4.2.2 Free or simply supported edge on the left end

The control domain contains an element with a free or simply supported node on the left end, as shown in Figure 2.11.

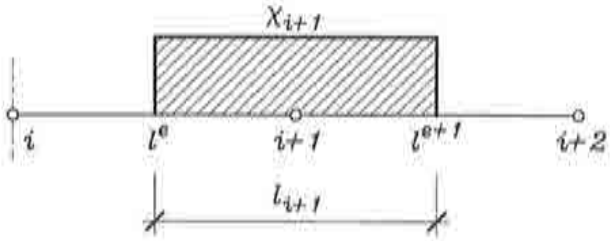

Figure 2.11 Control domain with free or simply supported node on the left end.

The curvature field at the node i is zero because of the end boundary condition and thus the stiffness matrix of element e has only the contribution from $\mathbf{K}_p^2$. In other words

$$\mathbf{K}^{(e)} = \mathbf{K}_p^2 \tag{2.62}$$

where $\mathbf{K}_p^2$ is expressed by equation (2.61).

2.4.2.3 Free or simply supported edge on the right end

The control domain contains an element with a free or simply supported node on the right end, as shown in Figure 2.12.

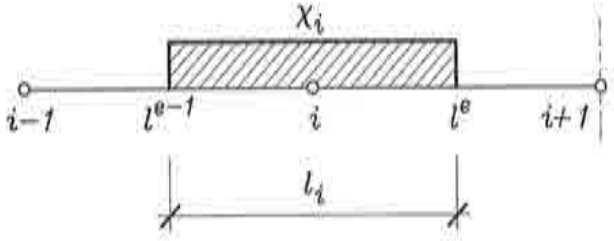

Figure 2.12 Control domain with free or simply supported node on the right end.

The curvature field for the node $i+1$ is zero because of the end boundary condition on the right hand end. Thus the stiffness matrix of the boundary element e has only the contribution from $\mathbf{K}_p^1$, i.e.

$$\mathbf{K}^{(e)} = \mathbf{K}_p^1 \tag{2.63}$$

where $\mathbf{K}_p^1$ is expressed by equation (2.60).

2.4.2.4 Clamped edge on the left end

The control domain includes an element with a clamped node on the left end, as shown in Figure 2.13.

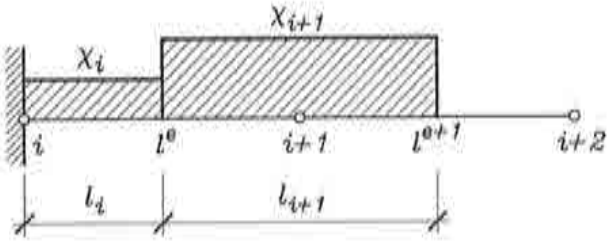

Figure 2.13 Control domain with clamped node on the left end.

Addopting the theory developed for the general case and applying the clamped boundary condition, the curvature assigned to node i can be written as

$$\chi_i = \frac{2}{l^e}\frac{w_{i+1} - w_i}{l^e} = \frac{2}{l^{e2}}[0, -1, 1, 0]\begin{Bmatrix} w_{i-1} \\ w_i \\ w_{i+1} \\ w_{i+2} \end{Bmatrix} = \mathbf{B}_i \mathbf{w}_i \tag{2.64}$$

where the domain curvature matrix $\mathbf{B}_i$ is

$$\mathbf{B}_i = \frac{2}{l^{e2}}[0, -1, 1, 0] \tag{2.65}$$

and the stiffness matrix $\mathbf{K}_p^1$ expressed by equation (2.60) is modified as

$$\mathbf{K}_p^1 = \frac{2EI}{l^{e3}}\begin{bmatrix} 0 & 0 & 0 & 0 \\ 0 & 1 & -1 & 0 \\ 0 & -1 & 1 & 0 \\ 0 & 0 & 0 & 0 \end{bmatrix} \tag{2.66}$$

Finally, the stiffness matrix of element e is given as

$$\mathbf{K}^{(e)} = \mathbf{K}_p^1 + \mathbf{K}_p^2 \tag{2.67}$$

where $\mathbf{K}_p^2$ is expressed by equation (2.61).

2.4.2.5 Clamped edge on the right end

The control domain includes an element with a clamped node on the right end, as shown in Figure 2.14.

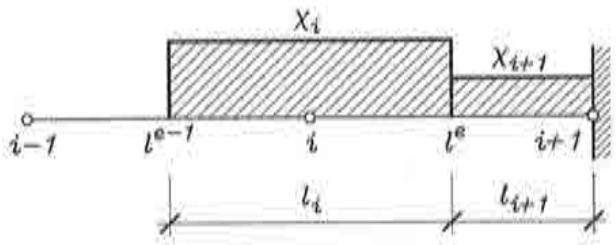

Figure 2.14 Control domain with clamped node on the right end.

Applying the same procedure and taking into account the clamped boundary condition, the curvature of the domain $i + 1$ is

$$\chi_{i+1} = \frac{2}{l^e}\frac{w_{i+1} - w_i}{l^e} = \frac{2}{l^{e2}}[0, -1, 1, 0]\begin{Bmatrix} w_{i-1} \\ w_i \\ w_{i+1} \\ w_{i+2} \end{Bmatrix} = \mathbf{B}_{i+1}\mathbf{w}_{i+1} \tag{2.68}$$

where the domain curvature matrix $\mathbf{B}_{i+1}$ is

$$\mathbf{B}_{i+1} = \frac{2}{l^{e2}}[0, -1, 1, 0] \tag{2.69}$$

and the stiffness matrix $\mathbf{K}_p^2$ expressed by equation (2.61) is modified as

$$\mathbf{K}_p^2 = \frac{2EI}{l^{e3}}\begin{bmatrix} 0 & 0 & 0 & 0 \\ 0 & 1 & -1 & 0 \\ 0 & -1 & 1 & 0 \\ 0 & 0 & 0 & 0 \end{bmatrix} \tag{2.70}$$

Finally, the stiffness matrix of element e is given as

$$\mathbf{K}^{(e)} = \mathbf{K}_p^1 + \mathbf{K}_p^2 \tag{2.71}$$

where $\mathbf{K}_p^1$ is expressed by equation (2.60).

2.5 EQUIVALENCE WITH A FINITE DIFFERENCE SCHEME

The coupled Finite Element - Finite Volume approach presented in the previous sections can be formed to be equivalent to a standard central Finite Difference scheme applied to the fourth order governing differential equations. This analogy is not surprising as it is well known that Galerkin finite elements yield the same equation system as the central finite differences for one dimensional problems. This analogy does not hold exactly for axisymmetric shell problem and indeed for the arbitrary shell case. The combined FE/FV method proposed in the thesis can be therefore viewed as a more general procedure for deriving rotation-free bending elements for a wide range of problems.

It is however instructing to present in some detail the analogy between the combined FE/FV method previously presented and the central FD scheme for the simple bending case considered in this chapter. The analogy is shown for the Cell Vertex FV scheme. A similar analogy can be found for the Cell Centered scheme.

Substituting the kinematic equation (2.1) into (2.4), the fourth order governing equation of a beam is obtained

$$EI\frac{d^4w}{dx^4} \pm q = 0 \tag{2.72}$$

The central Finite Difference scheme is applied to the irregular grid of five nodes shown in Figure 2.15.

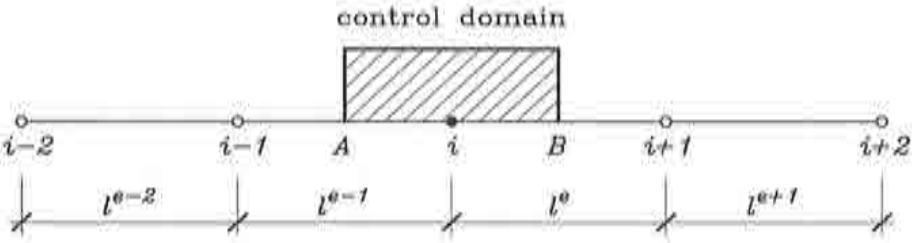

Figure 2.15 Five nodes grid for application of central finite difference scheme.

Satisfaction of the governing equation at node i implies

$$[EI\frac{d^4w}{dx^4}]_i \pm q_i = 0 \tag{2.73}$$

where $(\cdot)_i$ denote values at node i. In the following the geometrical and material properties will be assumed to be constant over the grid. This allows to rewrite equation (2.73) as

$$EI(\frac{d^4w}{dx^4})_i \pm q_i = 0 \tag{2.74}$$

The value of q_i can be simply estimated (assuming q to be constant) as

$$q_i = \frac{q}{2}[l^{e-1} + l^e] \tag{2.75}$$

The fourth derivative of the deflection is approximated using the central Finite Difference scheme as follows.

$$(\frac{d^4w}{dx^4})_i = \frac{(\frac{d^3w}{dx^3})_B - (\frac{d^3w}{dx^3})_A}{l^p}, \qquad l^p = \frac{l^{e-1}}{2} + \frac{l^e}{2} \tag{2.76}$$

where

$$(\frac{d^3w}{dx^3})_B = \frac{(\frac{d^2w}{dx^2})_{i+1} - (\frac{d^2w}{dx^2})_i}{l^e} \tag{2.77a}$$

$$(\frac{d^3w}{dx^3})_A = \frac{(\frac{d^2w}{dx^2})_i - (\frac{d^2w}{dx^2})_{i-1}}{l^{e-1}} \tag{2.77b}$$

and

$$(\frac{d^2w}{dx^2})_{i+1} = \frac{w_i - 2w_{i+1} + w_{i+2}}{l^{p2}}, \qquad l^p = \frac{l^{e+1}}{2} + \frac{l^e}{2} \tag{2.78a}$$

$$(\frac{d^2w}{dx^2})_i = \frac{w_{i-1} - 2w_i + w_{i+1}}{l^{p2}}, \qquad l^p = \frac{l^e}{2} + \frac{l^{e-1}}{2} \tag{2.78b}$$

$$(\frac{d^2w}{dx^2})_{i-1} = \frac{w_{i-2} - 2w_{i-1} + w_i}{l^{p2}}, \qquad l^p = \frac{l^{e-1}}{2} + \frac{l^{e-2}}{2} \tag{2.78c}$$

The final discretized equation at node i, can be written as follows

$$(\frac{d^4w}{dx^4})_i = \frac{1}{l^{p4}}(w_{i-2} - 4w_{i-1} + 6w_i - 4w_{i+1} + w_{i+2}) \tag{2.79}$$

and equation (2.74) in rewritten form is

$$\boxed{EI\frac{1}{l^{p4}}(w_{i-2} - 4w_{i-1} + 6w_i - 4w_{i+1} + w_{i+2}) \pm q_i = 0} \tag{2.80}$$

Equation (2.80) coincides precisely with the assumed equilibrium equation for node i obtained using the Cell Vertex FE/FV method presented in Section 2.4.2. The analogy between this procedure and the central Difference Scheme is therefore proved.

2.6 NUMERICAL EXAMPLES

Several numerical examples of simple beam problems [O-1],[Z-4] are presented in order to demonstrate the accuracy of the CVB and CCB elements. The rate of convergence for the deflections as well as for the bending moments, with the uniform and nonuniform meshes of 8,16,32 and 64 elements are presented. The uniform and nonuniform meshes for simply supported and clamped boundary conditions are presented in Figures 2.16 and 2.17, respectively. The uniform and nonuniform meshes for cantilever boundary condition are presented in Figures 2.18 and 2.19, respectively.

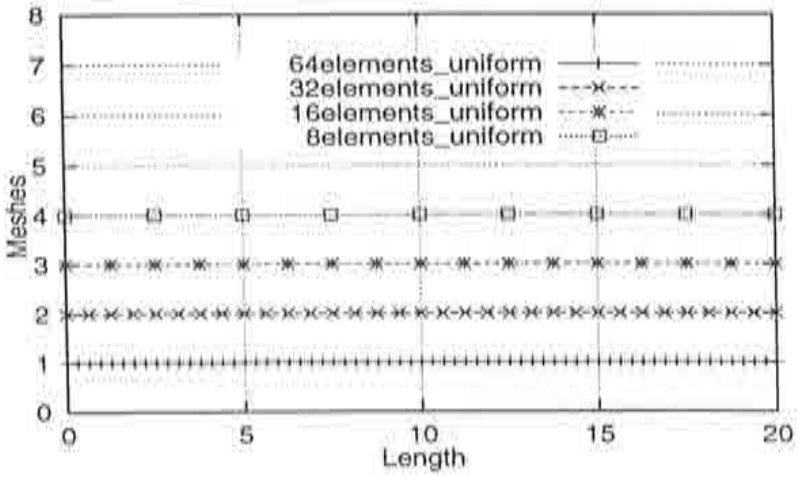

Figure 2.16 Simply supported and clamped end. Uniform meshes of 8,16,32 and 64 elements.

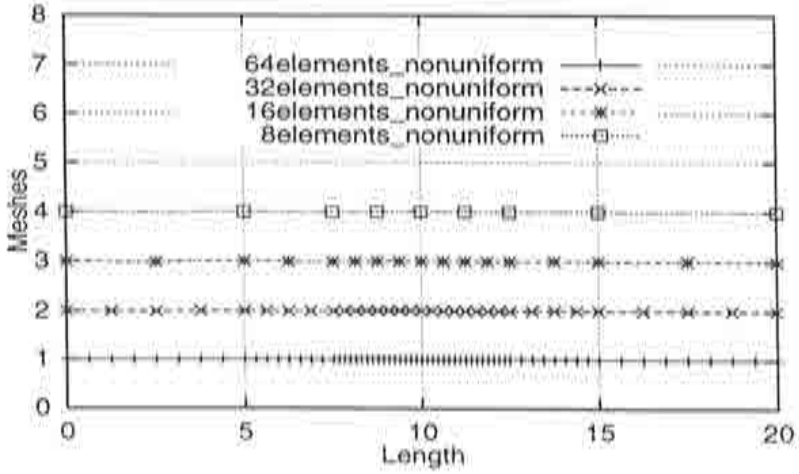

Figure 2.17 Simply supported and clamped end. Nonuniform meshes of 8,16,32 and 64 elements.

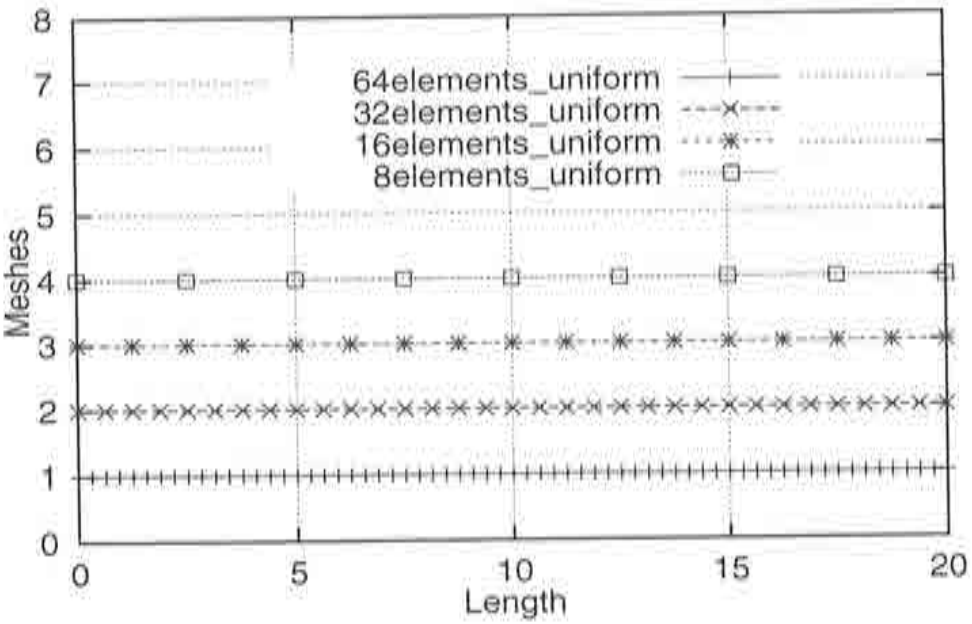

Figure 2.18 Cantilever beam. Uniform meshes of 8,16,32 and 64 elements.

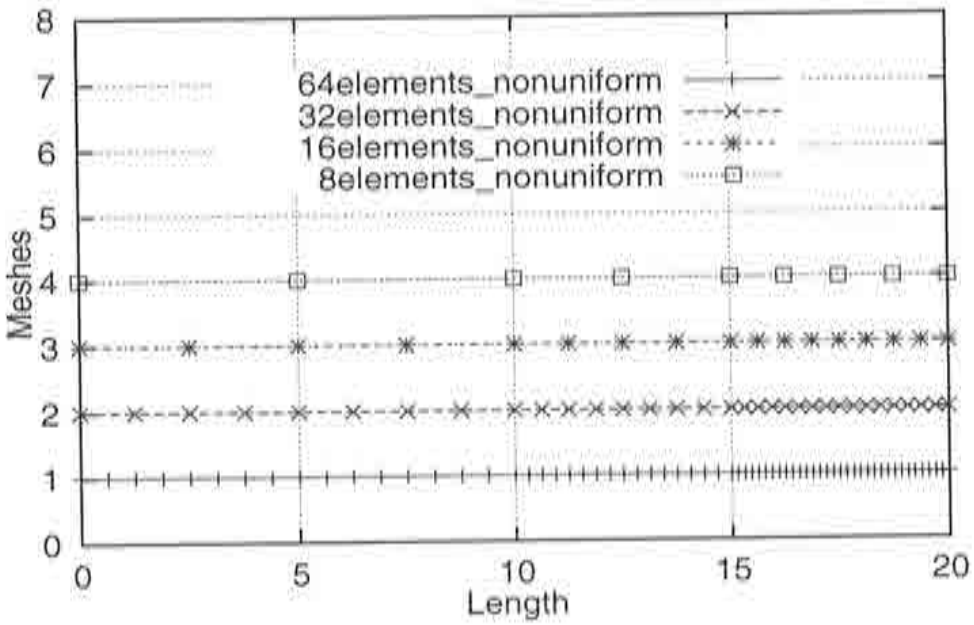

Figure 2.19 Cantilever beam. Nonuniform meshes of 8,16,32 and 64 elements.

2.6.1 Simply supported beam under point load

The beam is simply supported and subjected to a point load P acting at the center, as shown in Figure 2.20. The uniform and nonuniform meshes used in the analyses are presented in Figures 2.16 and 2.17. The geometrical and material properties are $l = 20m$ and $EI = 100000$.

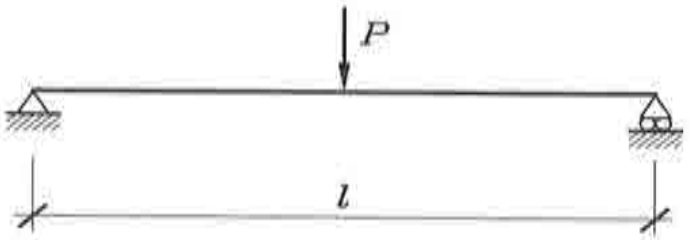

Figure 2.20 Simply supported beam under point load.

The numerical solution obtained for different number of elements is compared with the exact analytic solution for the deflection w_{ex} at the center point. The comparison is performed for the uniform as well as for the nonuniform meshes. The results are shown in Table 2.1 and Table 2.2, respectively.

The exact expression for the deflection is

$$w(x) = \frac{Pl^3}{12EI}\left\{\frac{x}{l}\left[\frac{3}{4} - \left(\frac{x}{l}\right)^2\right] + \frac{1}{4}\left(\frac{2x}{l} - 1\right)^3\right\} \tag{2.81}$$

and the exact deflection at the center point is

$$w_{ex} = \frac{Pl^3}{48EI} \tag{2.82}$$

MESH	CCB Central deflection error	CVB Central deflection error
8 elements	12.5000	3.1250
16 elements	3.1250	0.7814
32 elements	0.7814	0.1952
64 elements	0.1952	0.0488

Table 2.1 Simply supported beam under point load. Exact and numerical solution for the central deflection - uniform meshes.

MESH	CCB Central deflection error	CVB Central deflection error
8 elements	5.4686	7.22660
16 elements	7.2266	1.8068
32 elements	1.8068	0.4514
64 elements	0.4466	0.1130

Table 2.2 Simply supported beam under point load. Exact and numerical solution for the central deflection - nonuniform meshes.

The rate of the convergence for the central deflection for the CCB and CVB elements for the uniform and nonuniform meshes of 8,16,32 and 64 elements is presented in Figures 2.21 and 2.22, respectively. The CVB element presents a superior performance versus the CCB element for the uniform meshes. The results are less conclusive for the nonuniform meshes.

The rate of the convergence for the moment for both elements for the uniform as well as for the nonuniform meshes is presented in Figures 2.23, 2.24, 2.25 and 2.26, respectively. It should be noted that both, the CCB and CVB elements give the exact solution independently of the number of elements.

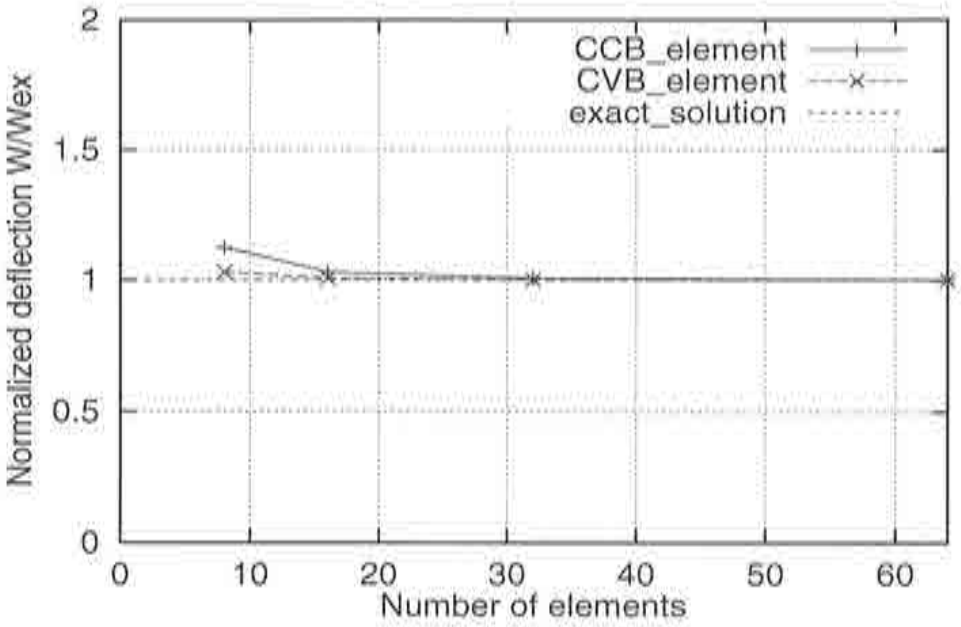

Figure 2.21 Rate of convergence for central deflection - uniform meshes.

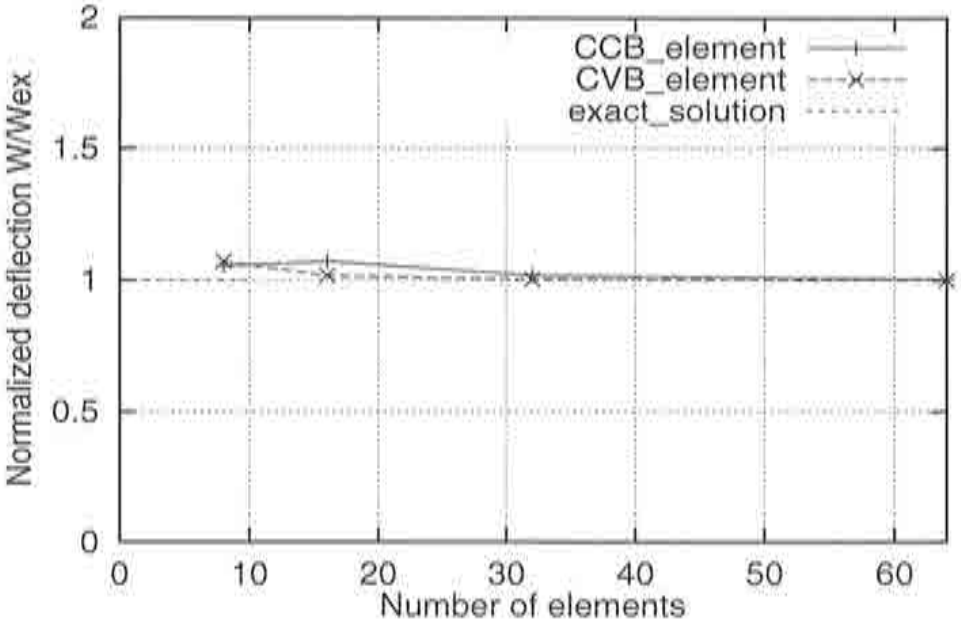

Figure 2.22 Rate of convergence for central deflection - nonuniform meshes.

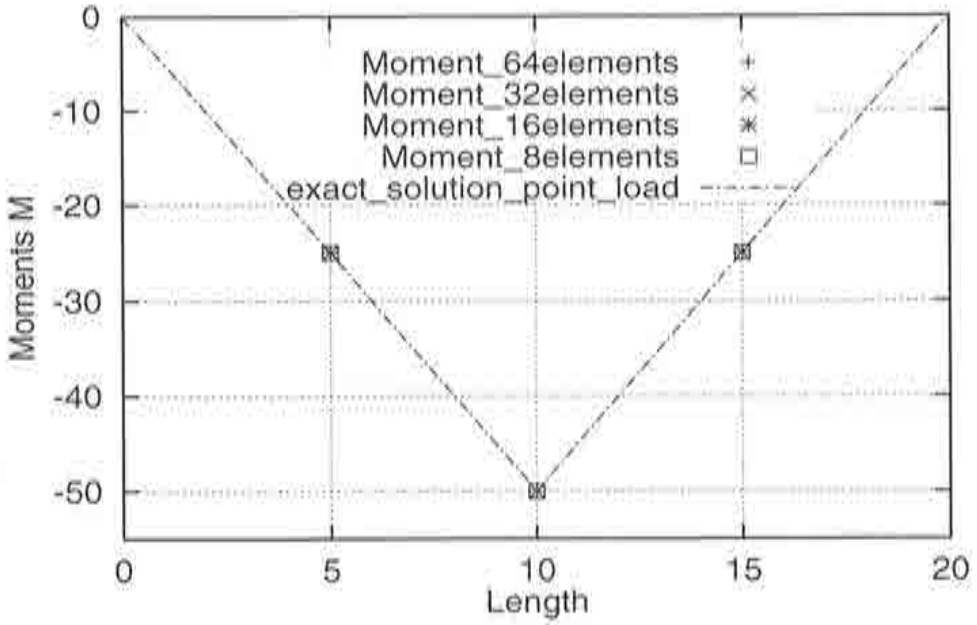

Figure 2.23 Rate of convergence of moment distribution for uniform meshes - CCB element.

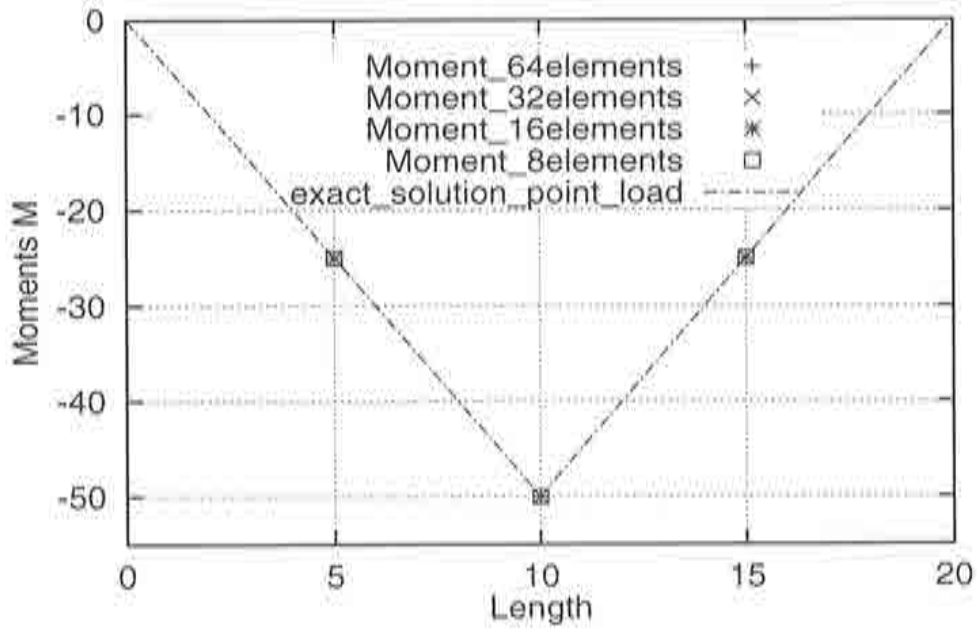

Figure 2.24 Rate of convergence of moment distribution for nonuniform meshes - CCB element.

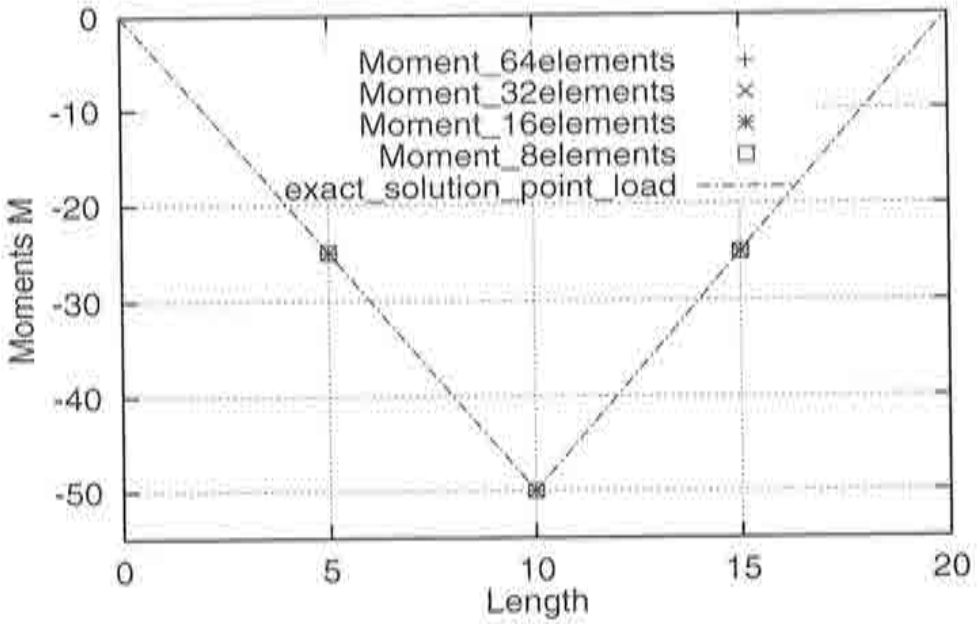

Figure 2.25 Rate of convergence of moment distribution for uniform meshes - CVB element.

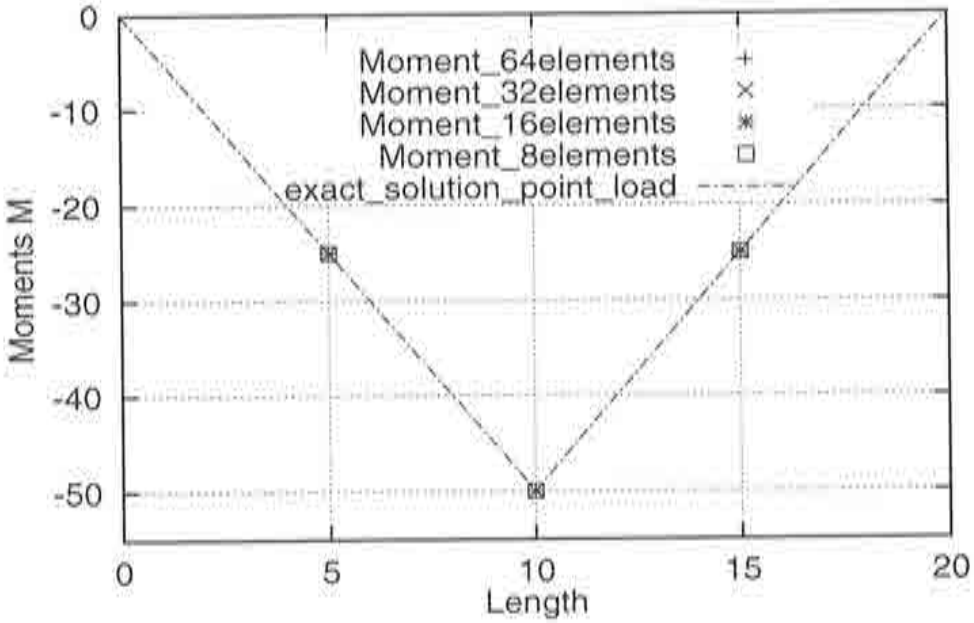

Figure 2.26 Rate of convergence of moment distribution for nonuniform meshes - CVB element.

2.6.2 Simply supported beam under distributed load

The selected test problem of the beam simply supported and subjected to a uniformly distributed load q, is shown in Figure 2.27. The uniform and nonuniform meshes used in the analyses are presented in Figures 2.16 and 2.17. The geometrical and material properties are $l = 20m$ and $EI = 100000$.

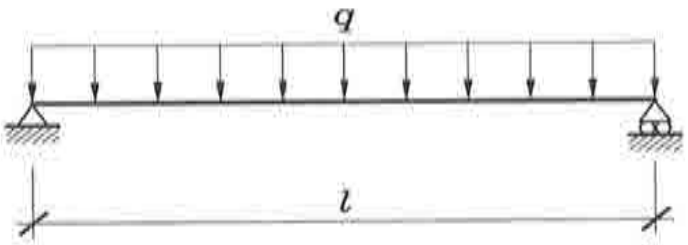

Figure 2.27 Simply supported beam under distributed load.

The numerical solution obtained for different number of elements, is compared with the exact analytic solution for the deflection w_{ex} at the center point. The comparison is performed for the uniform as well as for the nonuniform meshes. The results are shown in Table 2.3 and Table 2.4, respectively.

The exact expression for the deflection is

$$w(x) = \frac{ql^4}{24EI}\left[\frac{x}{l} - 2\frac{x^3}{l} + \frac{x^4}{l}\right] \tag{2.83}$$

and the exact deflection at the center point is

$$w_{ex} = \frac{8ql^4}{384EI} \tag{2.84}$$

MESH	CCB Central deflection error	CVB Central deflection error
8 elements	5.0000	1.2502
16 elements	1.2498	0.3123
32 elements	0.3123	0.0781
64 elements	0.0781	0.0195

Table 2.3 Simply supported beam under distributed load. Exact and numerical solution for the central deflection - uniform meshes.

MESH	CCB Central deflection error	CVB Central deflection error
8 elements	1.4845	6.2302
16 elements	5.3513	1.5574
32 elements	1.3381	0.3896
64 elements	0.3310	0.0973

Table 2.4 Simply supported beam under distributed load. Exact and numerical solution for the central deflection - nonuniform meshes.

The rate of the convergence for the central deflection for CCB and CVB elements for uniform and nonuniform meshes of 8,16,32 and 64 elements is presented in Figures 2.28 and 2.29, respectively. The CVB element presents a superior performance versus the CCB element specially for uniform meshes.

The rate of the convergence for the moment for both elements for the uniform as well as for the nonuniform meshes is presented in Figures 2.30, 2.31, 2.32 and 2.33, respectively. The CCB element gives the exact solution independently of the number of elements for the uniform and nonuniform meshes. The exact solution using the CVB element is achieved by mesh refinement, particularly notable for the nonuniform meshes.

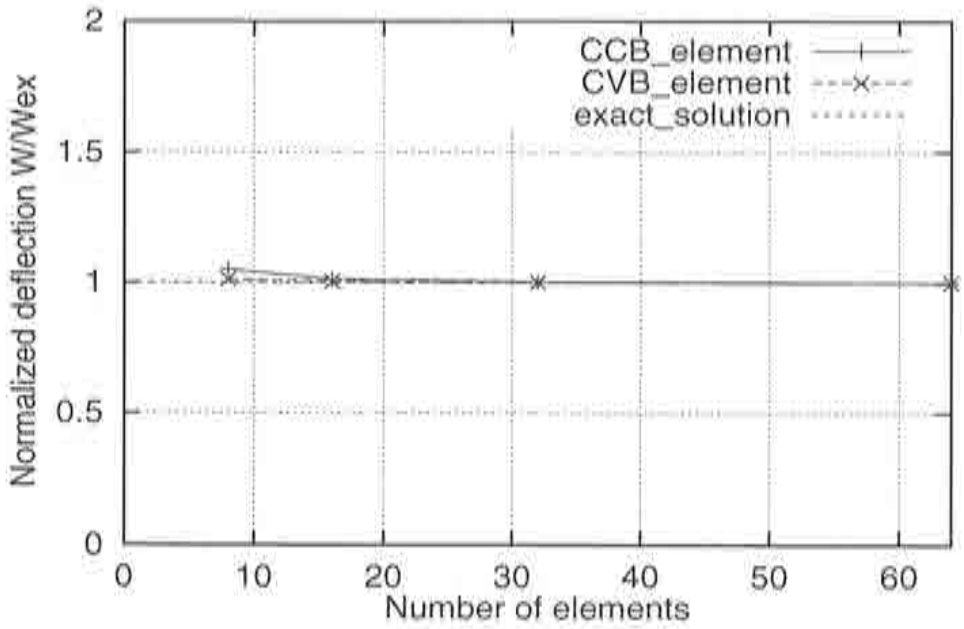

Figure 2.28 Rate of convergence for central deflection - uniform meshes.

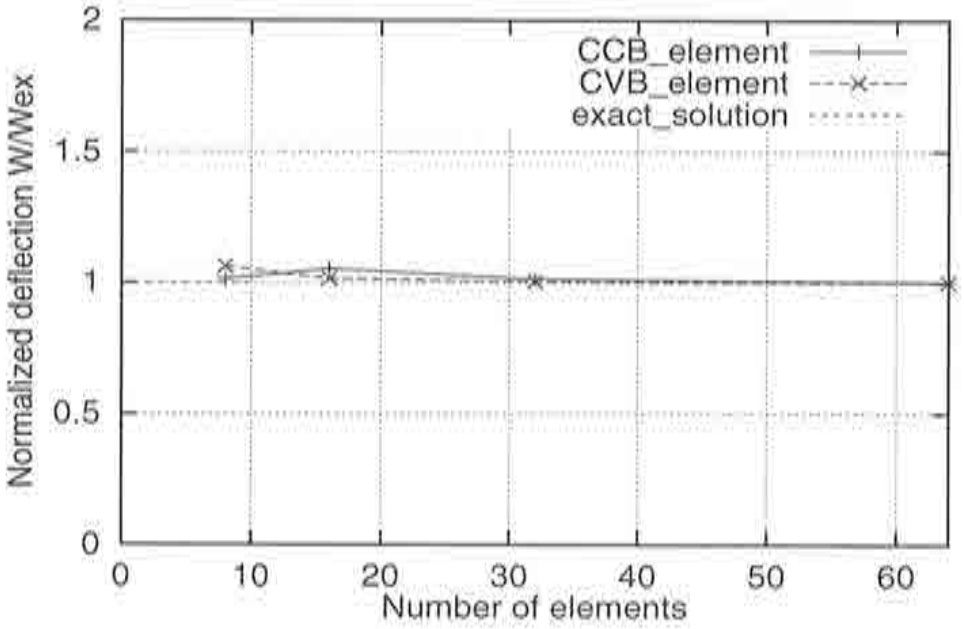

Figure 2.29 Rate of convergence for central deflection - nonuniform meshes.

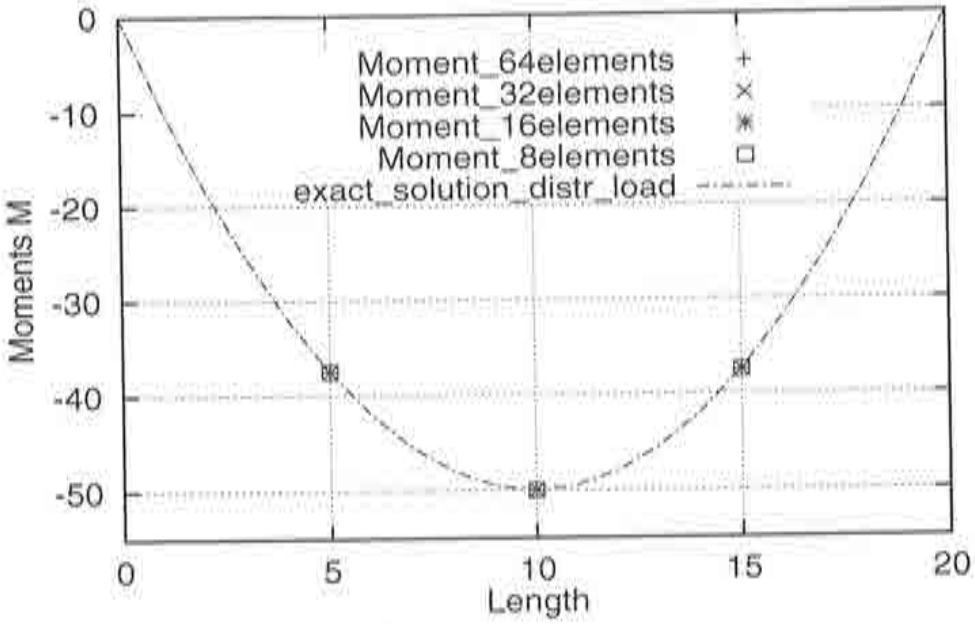

Figure 2.30 Rate of convergence of moment distribution for uniform meshes - CCB element.

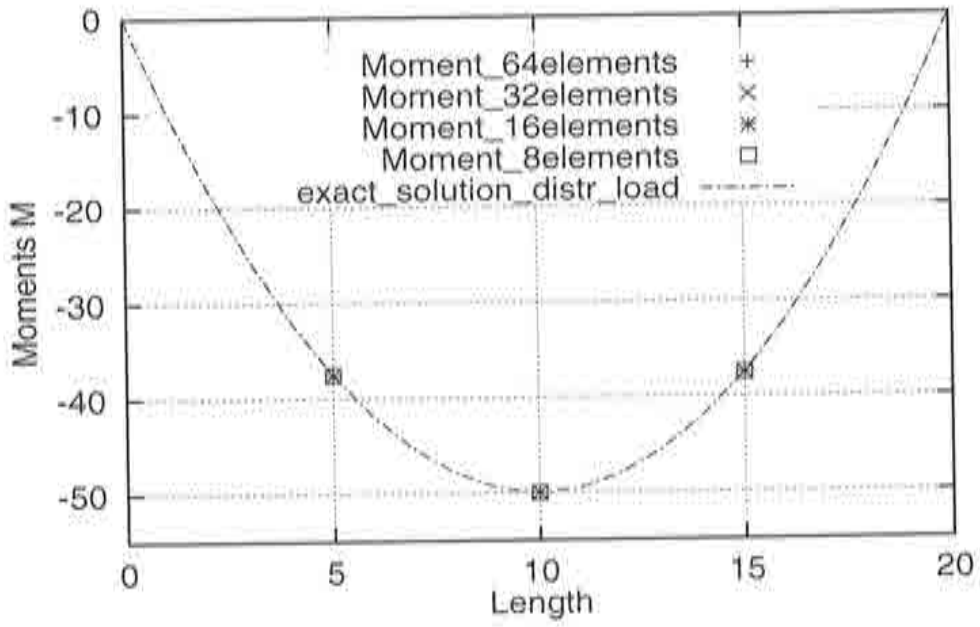

Figure 2.31 Rate of convergence of moment distribution for nonuniform meshes - CCB element.

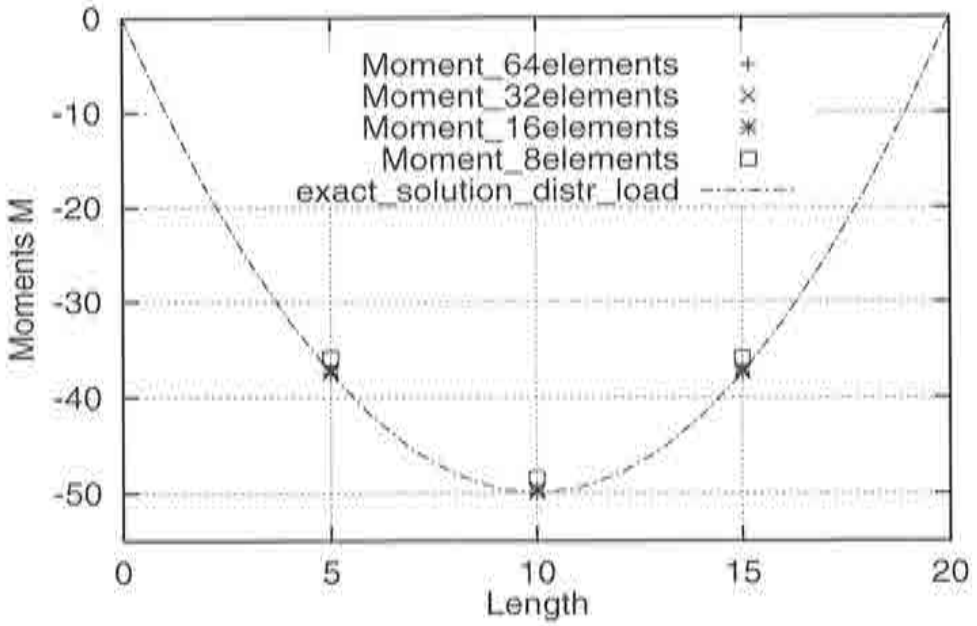

Figure 2.32 Rate of convergence of moment distribution for uniform meshes - CVB element.

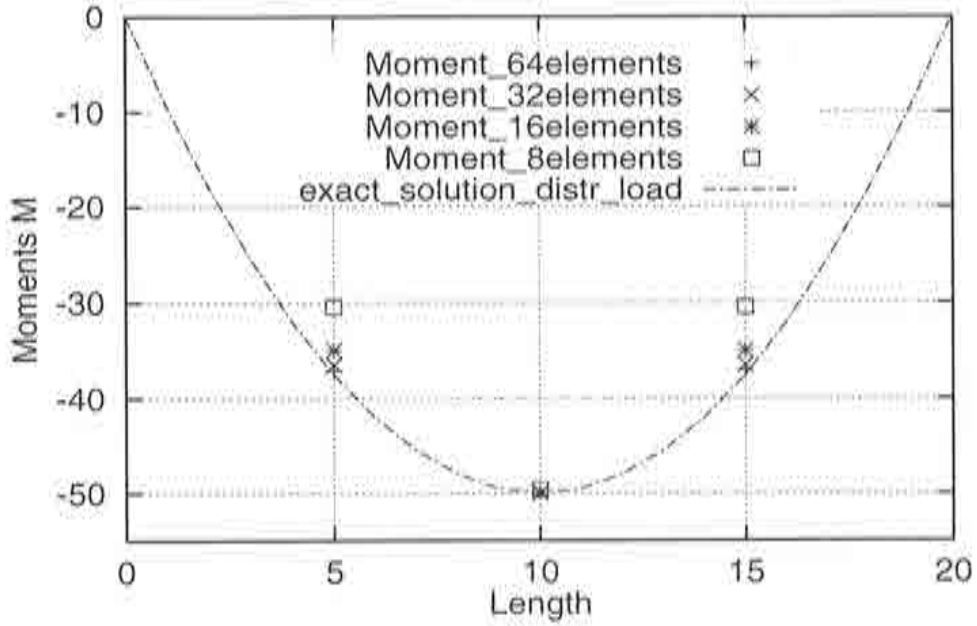

Figure 2.33 Rate of convergence of moment distribution for nonuniform meshes - CVB element.

2.6.3 Simply supported beam under distributed triangular load

The beam is simply supported and subjected to a distributed triangular load, as shown in Figure 2.34. The uniform and nonuniform meshes used in the analyses are presented in Figures 2.16 and 2.17. The geometrical and material properties are $l = 20m$ and $EI = 100000$.

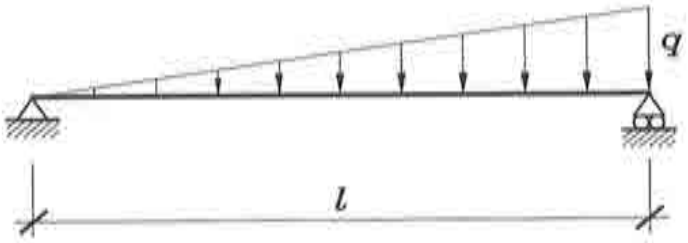

Figure 2.34 Simply supported beam under distributed triangular load.

The exact analytic solution for the deflection w_{ex} at the corresponding po int is compared with the numerical solution obtained for different number of elements. The results of the comparison performed for the uniform as well as for the nonuniform meshes are given in Table 2.5 and Table 2.6, respectively.

The exact expression for the deflection is

$$w(x) = \frac{q_o l^4}{350EI}\left[7(\frac{x}{l}) - 10(\frac{x}{l})^3 + 3(\frac{x}{l})^5\right] \tag{2.85}$$

and the exact deflection at the center point is

$$w_{ex} = 0.01304\frac{q_o l^4}{2EI} \tag{2.86}$$

MESH	CCB Central deflection error	CVB Central deflection error
8 elements	23.2563	18.5755
16 elements	10.5914	9.7718
32 elements	3.8918	3.6349
64 elements	2.1482	2.0868

Table 2.5 Simply supported beam under triangular distributed load. Exact and numerical solution for the central deflection - uniform meshes.

MESH	CCB Central deflection error	CVB Central deflection error
8 elements	28.2409	33.5151
16 elements	20.8263	16.1743
32 elements	11.4858	10.4198
64 elements	5.5636	5.3154

Table 2.6 Simply supported beam under triangular distributed load. Exact and numerical solution for the central deflection - uniform meshes.

The rate of the convergence for the deflection for CCB and CVB elements for uniform and nonuniform meshes of 8,16,32 and 64 elements is presented in Figures 2.35 and 2.36, respectively. The CVB element presents the slightly superior performance versus the CCB element, for the uniform meshes. In the nonuniform meshes the results are less conclusive.

The rate of the convergence for the moment for both elements for the uniform as well for the nonuniform meshes is presented in Figures 2.37, 2.38, 2.39 and 2.40, respectively. Both, the CCB and CVB elements show some discrepancy of the exact solution for the uniform as well as for the nonuniform meshes, advancing to the exact solution with the mesh refinement.

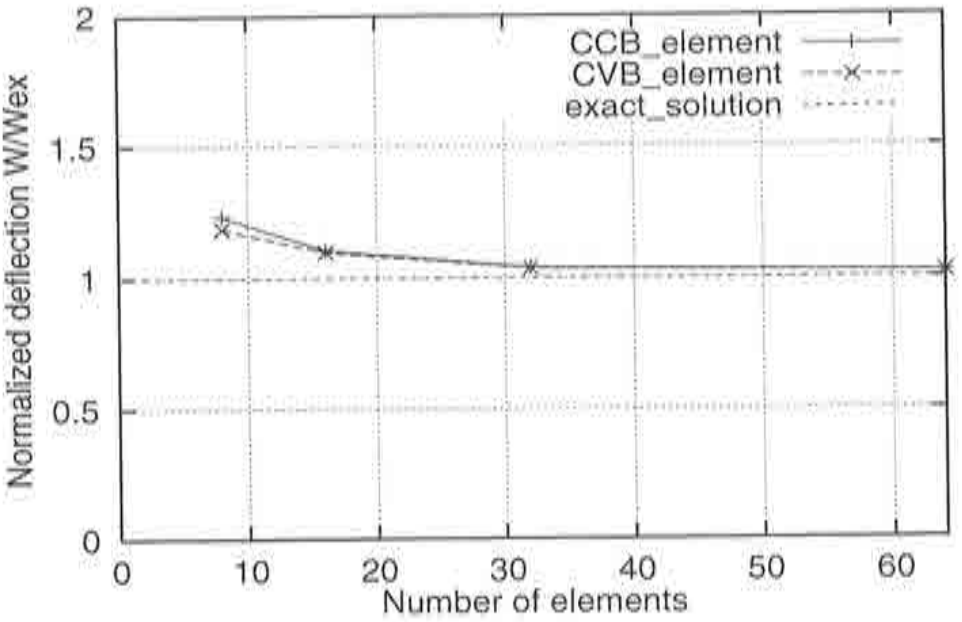

Figure 2.35 Rate of convergence for central deflection - uniform meshes.

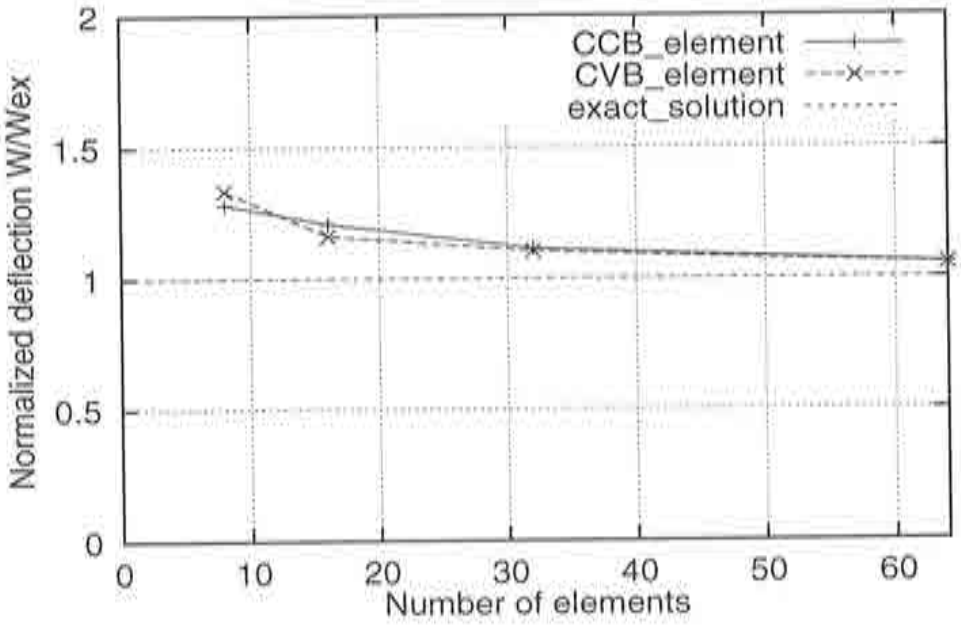

Figure 2.36 Rate of convergence for central deflection - nonuniform meshes.

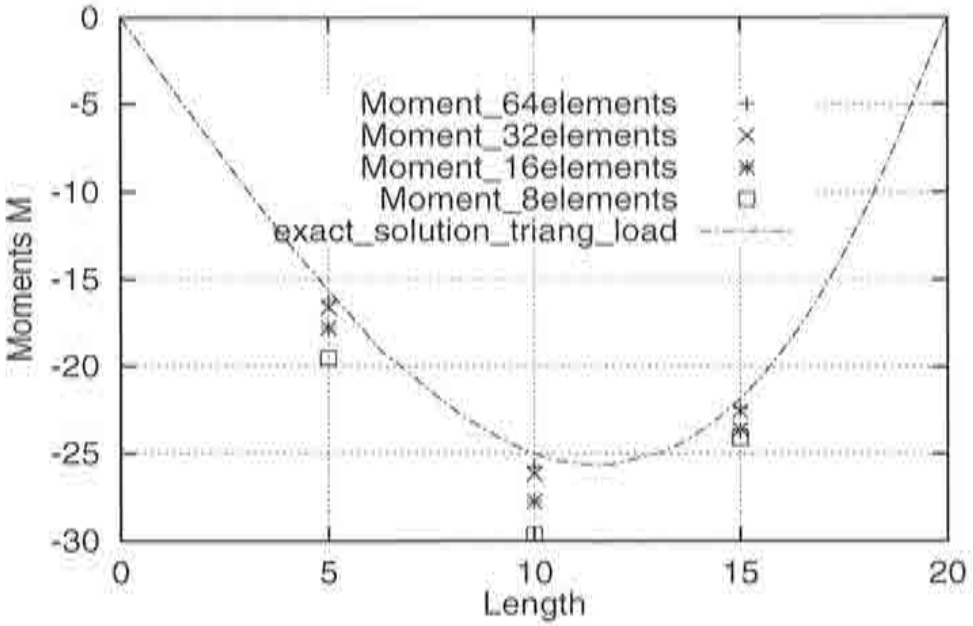

Figure 2.37 Rate of convergence of moment distribution for uniform meshes - CCB element.

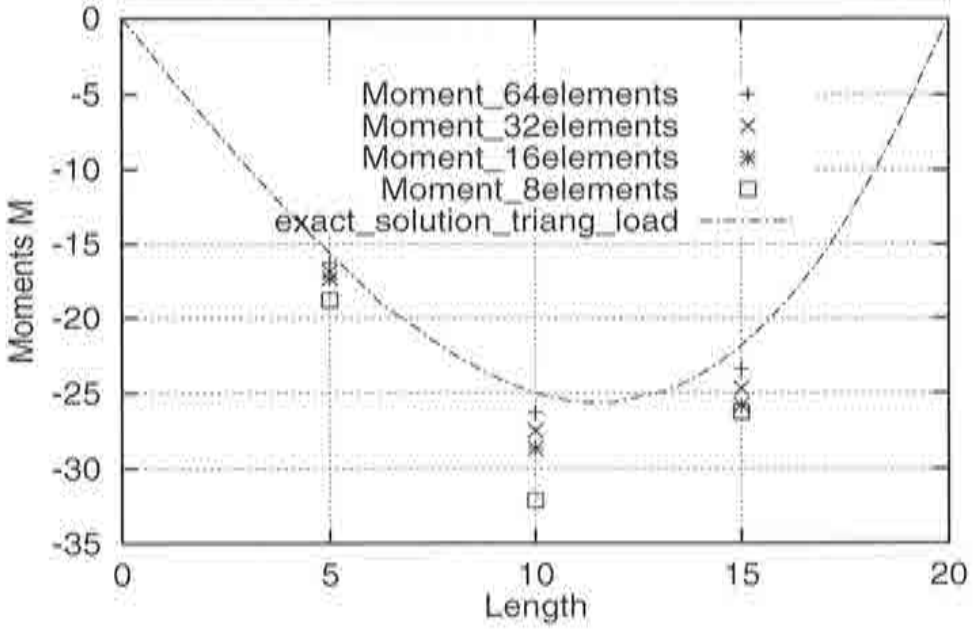

Figure 2.38 Rate of convergence of moment distribution for nonuniform meshes - CCB element.

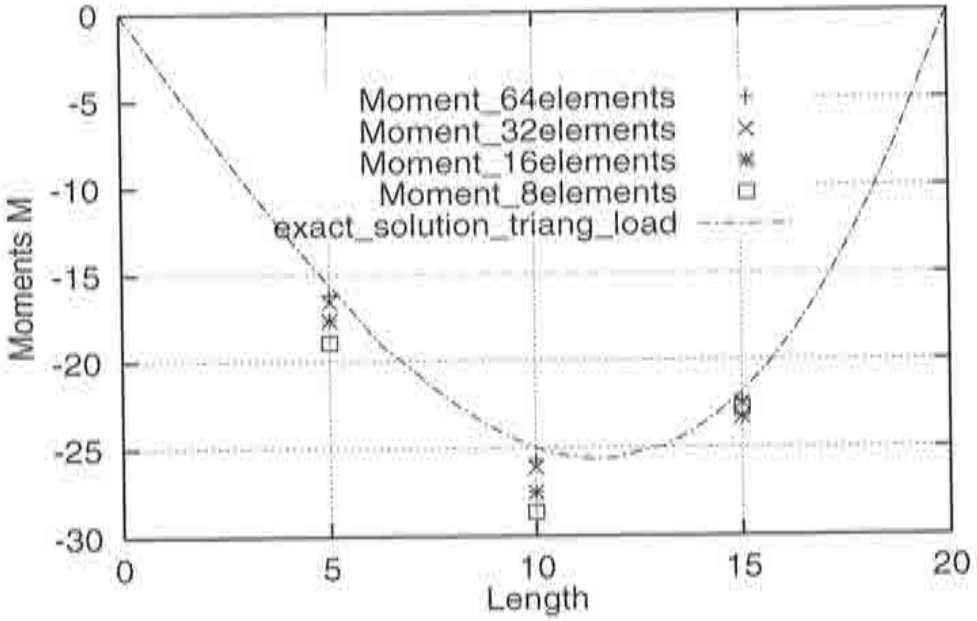

Figure 2.39 Rate of convergence of moment distribution for uniform meshes - CVB element.

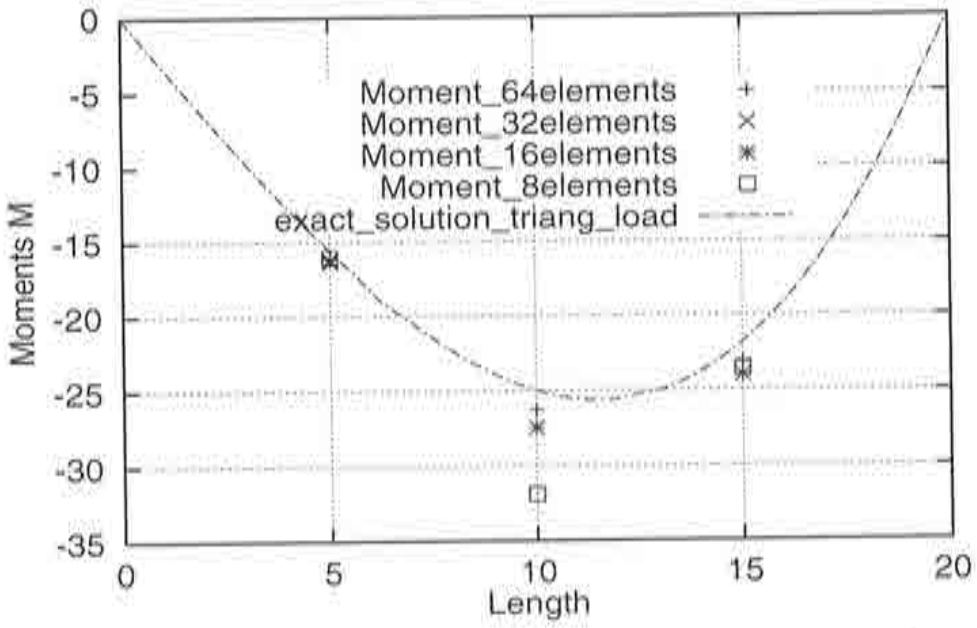

Figure 2.40 Rate of convergence of moment distribution for nonuniform meshes - CVB element.

2.6.4 Clamped beam under point load

The beam is clamped and subjected to a point load P at the center, as shown in Figure 2.41. The uniform and nonuniform meshes used in the analyses are presented in Figures 2.16 and 2.17. The geometrical and material properties are the same as in the previous examples.

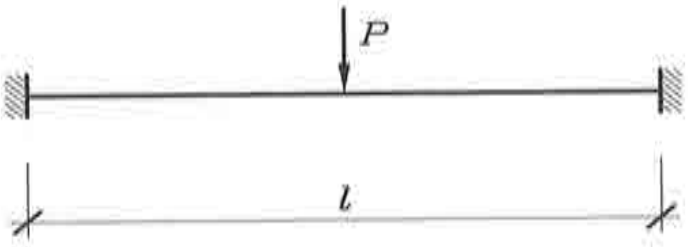

Figure 2.41 Clamped beam under point load.

The exact analytic solution for the deflection w_{ex} at the corresponding point is compared with the numerical solution obtained for different number of elements. The results of the comparison performed for the uniform as well as for the nonuniform meshes are given in Table 2.7 and Table 2.8, respectively.

The exact expression for the deflection is

$$w(x) = \frac{P}{12EIl}\left(\frac{x^2}{2} - \frac{l^2}{4}\right)^2 \tag{2.87}$$

and the exact deflection at the center point is

$$w_{ex} = \frac{Pl^3}{768EI} \tag{2.88}$$

MESH	CCB Central deflection error	CVB Central deflection error
8 elements	50.0000	12.5000
16 elements	12.5000	3.1251
32 elements	3.1249	0.7813
64 elements	0.7813	0.1952

Table 2.7 Clamped beam under point load. Exact and numerical solution for the central deflection - uniform meshes.

MESH	CCB Central deflection error	CVB Central deflection error
8 elements	58.2032	28.9062
16 elements	28.9062	7.2265
32 elements	7.2265	1.8066
64 elements	1.7950	0.4518

Table 2.8 Clamped beam under point load. Exact and numerical solution for the central deflection - nonuniform meshes.

The rate of the convergence for the deflection for CCB and CVB elements for uniform and nonuniform meshes of 8,16,32 and 64 elements is presented in Figures 2.42 and 2.43 respectively. The CVB element presents a superior performance versus the CCB element, for both uniform and nonuniform meshes. The more pronounced difference is the convergence rate of CVB element due to the better approximation of the clamped boundary condition.

The rate of the convergence for the moment for both elements for the uniform as well as for the nonuniform meshes is presented in Figures 2.44, 2.45, 2.46 and 2.47, respectively. The CVB element gives the exact solution independently of the number of elements for both, uniform and nonuniform meshes while the CCB element gives some discrepancy of the exact solution for the nonuniform meshes.

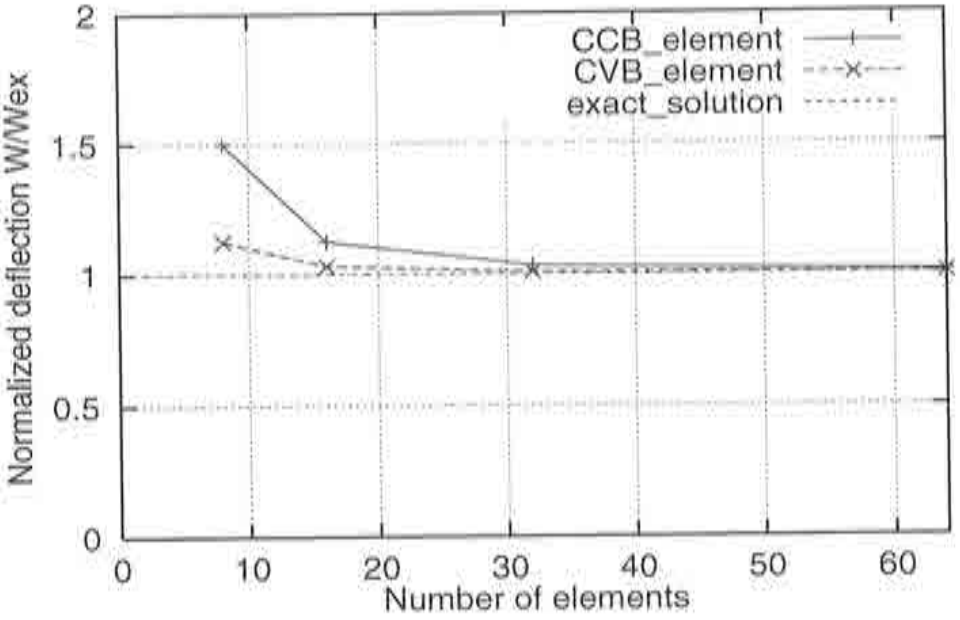

Figure 2.42 Rate of convergence for central deflection - uniform meshes.

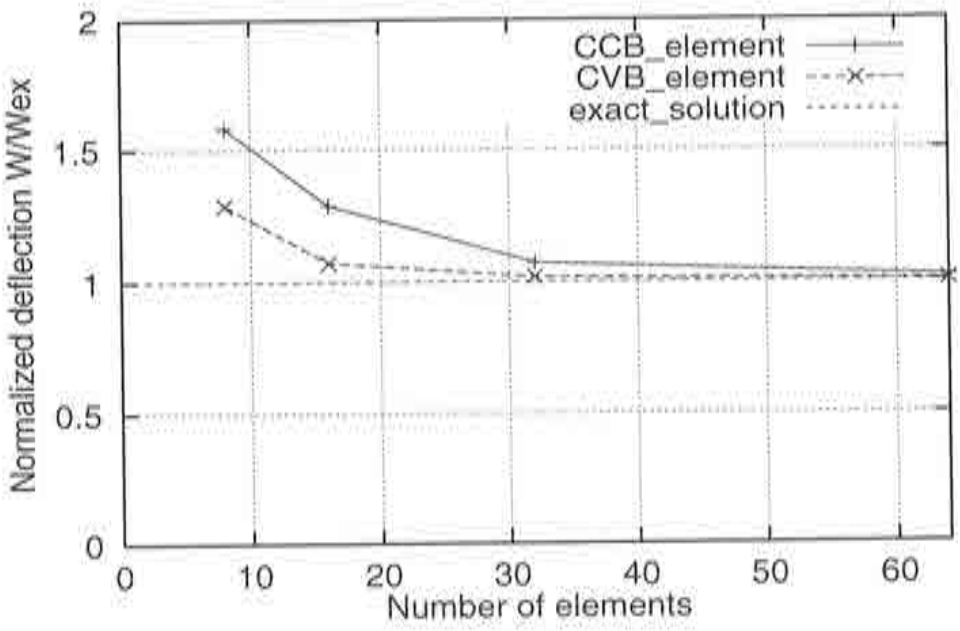

Figure 2.43 Rate of convergence for central deflection - nonuniform meshes.

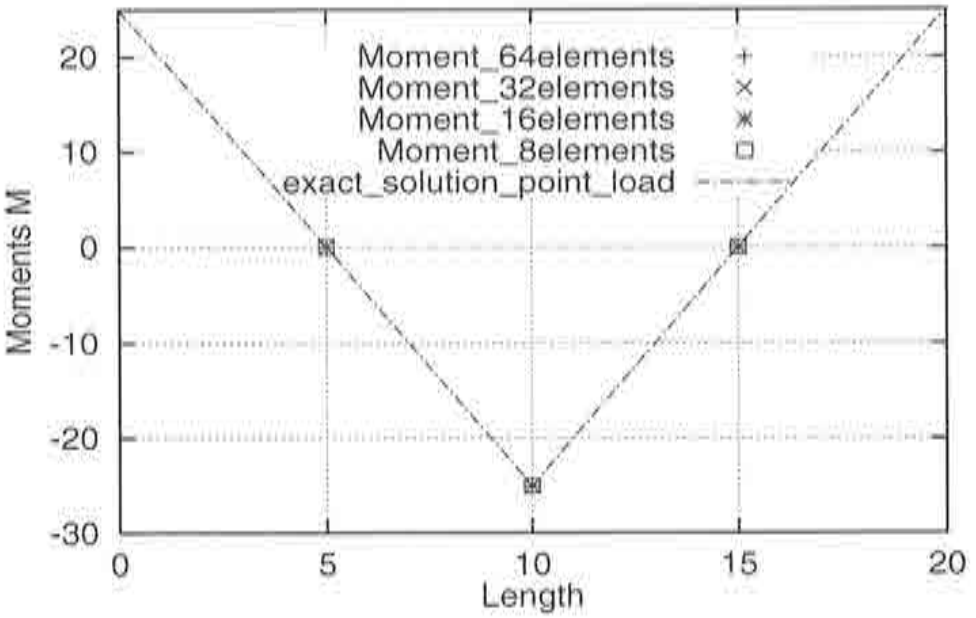

Figure 2.44 Rate of convergence of moment distribution for uniform meshes - CCB element.

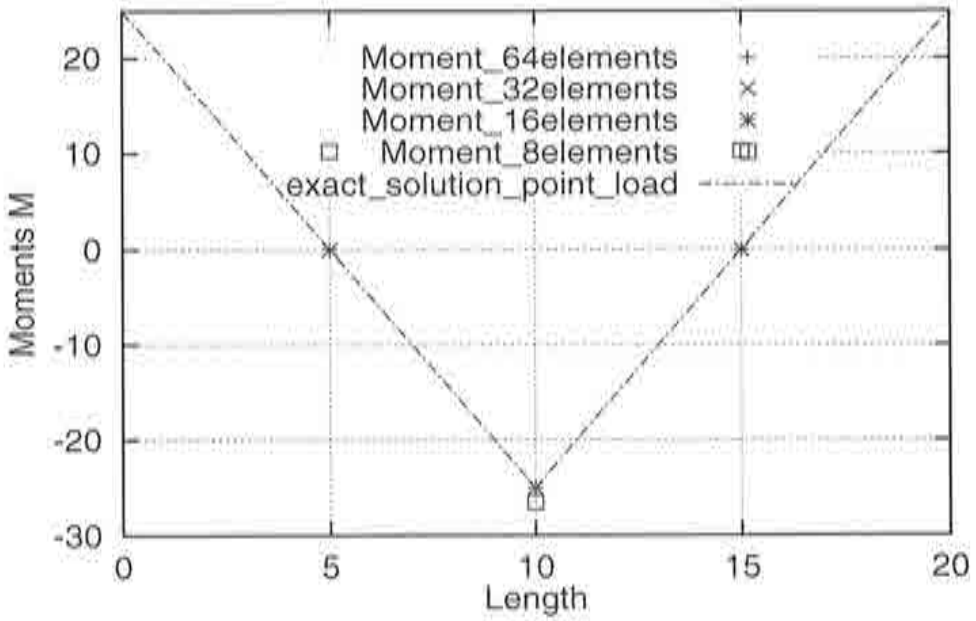

Figure 2.45 Rate of convergence of moment distribution for nonuniform meshes - CCB element.

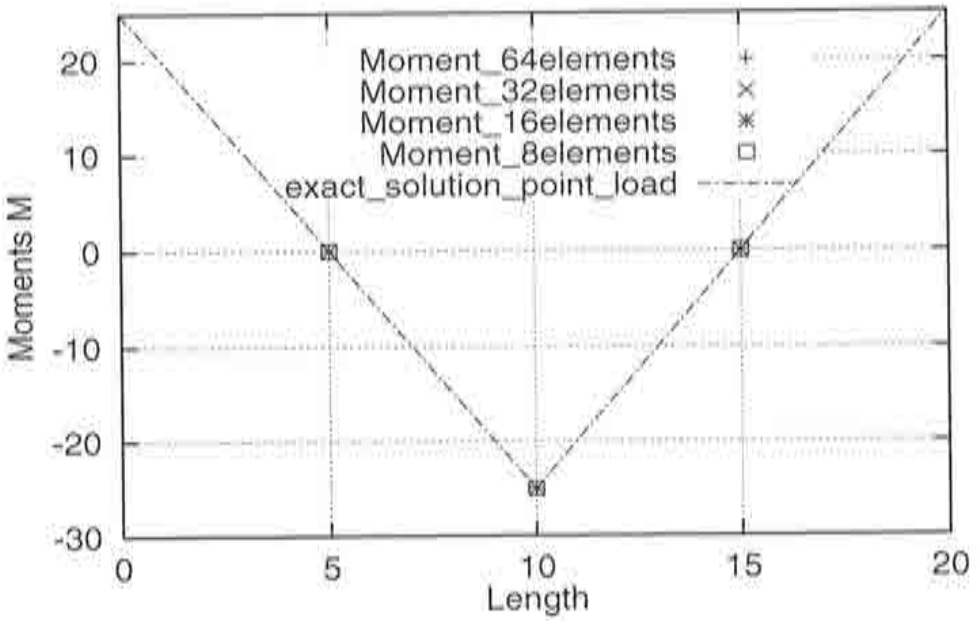

Figure 2.46 Rate of convergence of moment distribution for uniform meshes - CVB element.

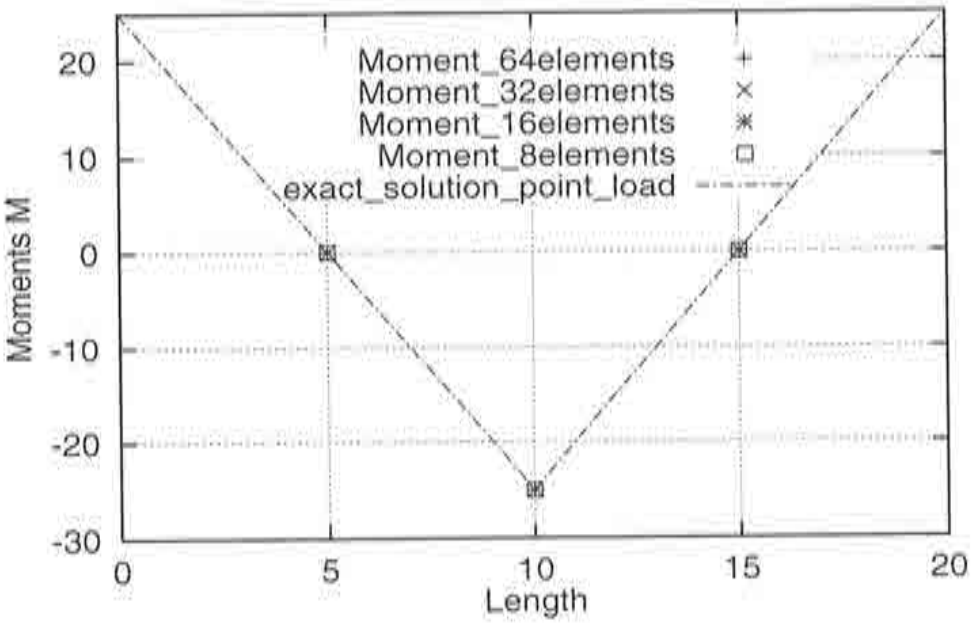

Figure 2.47 Rate of convergence of moment distribution for nonuniform meshes - CVB element.

2.6.5 Clamped beam under distributed load

The beam is clamped and subjected to a uniformly distributed load q, as shown in Figure 2.48. The uniform and nonuniform meshes used in the analyses are presented in Figures 2.16 and 2.17. The geometrical and material properties are the same as in the previous examples.

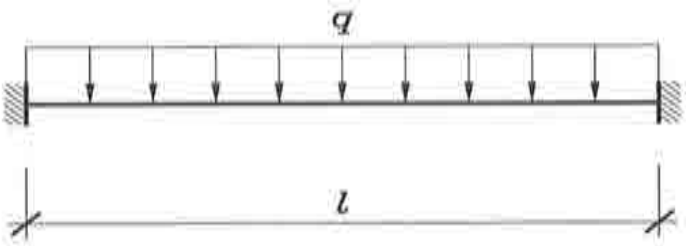

Figure 2.48 Clamped beam under distributed load.

The numerical solution obtained for different number of elements is compared with the exact analytic solution for the deflection w_{ex} at the center point. The comparison is performed for the uniform as well for the nonuniform meshes. The results are given in Table 2.9 And Table 2.10, respectively.

The exact expression for deflection is

$$w(x) = \frac{1}{EI}(-\frac{ql^2}{24}x^2 + \frac{ql}{12}x^3 - \frac{q}{24}x^4) \tag{2.89}$$

and the exact deflection at the center point is

$$w_{ex} = \frac{ql^4}{384EI} \tag{2.90}$$

MESH	CCB Center deflection error	CVB Center deflection error
8 elements	31.2500	12.5000
16 elements	7.8126	3.1251
32 elements	1.9532	0.7813
64 elements	0.4882	0.1952

Table 2.9 Clamped beam under distributed load. Exact and numerical solution for the central deflection - uniform meshes.

MESH	CCB Central deflection error	CVB Central deflection error
8 elements	58.0566	45.6054
16 elements	32.4219	11.4013
32 elements	8.1054	2.8503
64 elements	2.0177	0.7126

Table 2.10 Clamped beam under distributed load. Exact and numerical solution for the central deflection - nonuniform meshes.

The rate of the convergence for the deflection for CCB and CVB elements for uniform and nonuniform meshes of 8,16,32 and 64 elements is presented in Figures 2.49 and 2.50, respectively. The CVB element presents again a superior performance versus the CCB element for the uniform meshes. The same can be found for the nonuniform meshes only when the mesh is refined.

The rate of the convergence for the moment for both elements for the uniform as well as for the nonuniform meshes is presented in Figures 2.51, 2.52, 2.53 and 2.54, respectively. Both, the CCB and CVB elements show a good performance for the uniform meshes, while the CVB element shows a better performance versus the CCB element for the nonuniform meshes due to the better approximation of the clamped boundary conditions.

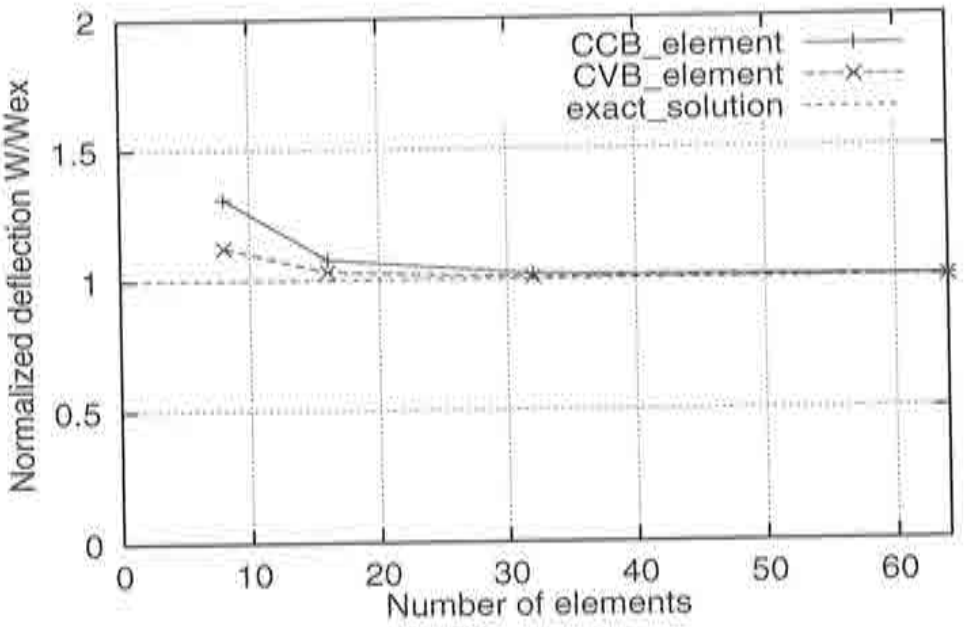

Figure 2.49 Rate of convergence for central deflection - uniform meshes.

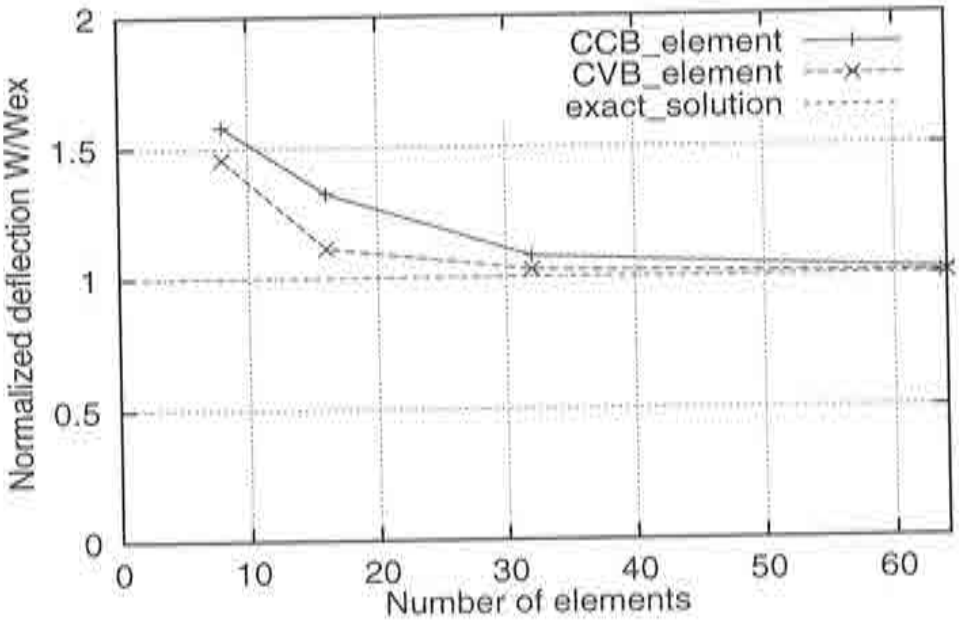

Figure 2.50 Rate of convergence for central deflection - nonuniform meshes.

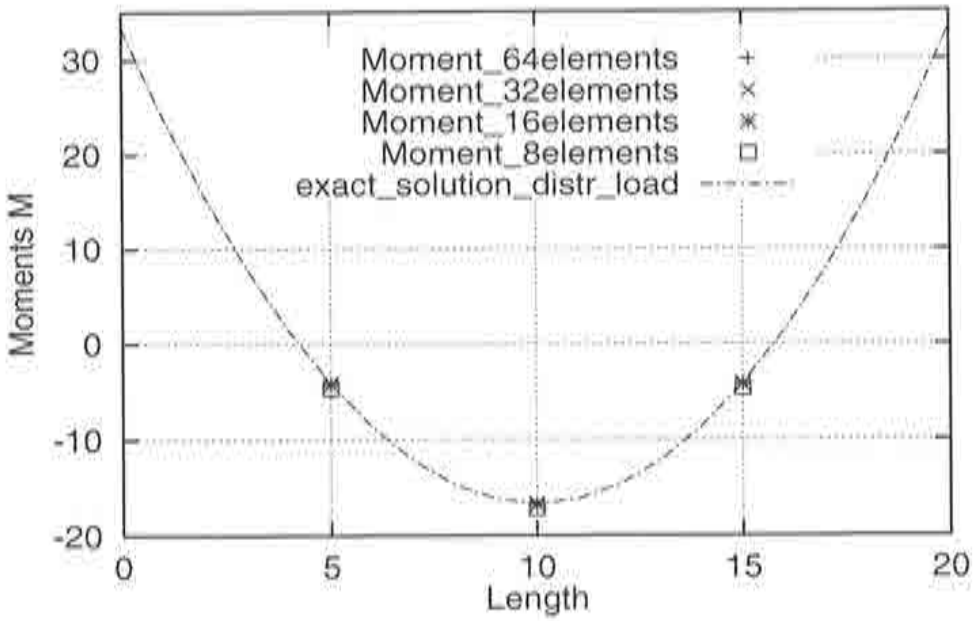

Figure 2.51 Rate of convergence of moment distribution for uniform meshes - CCB element.

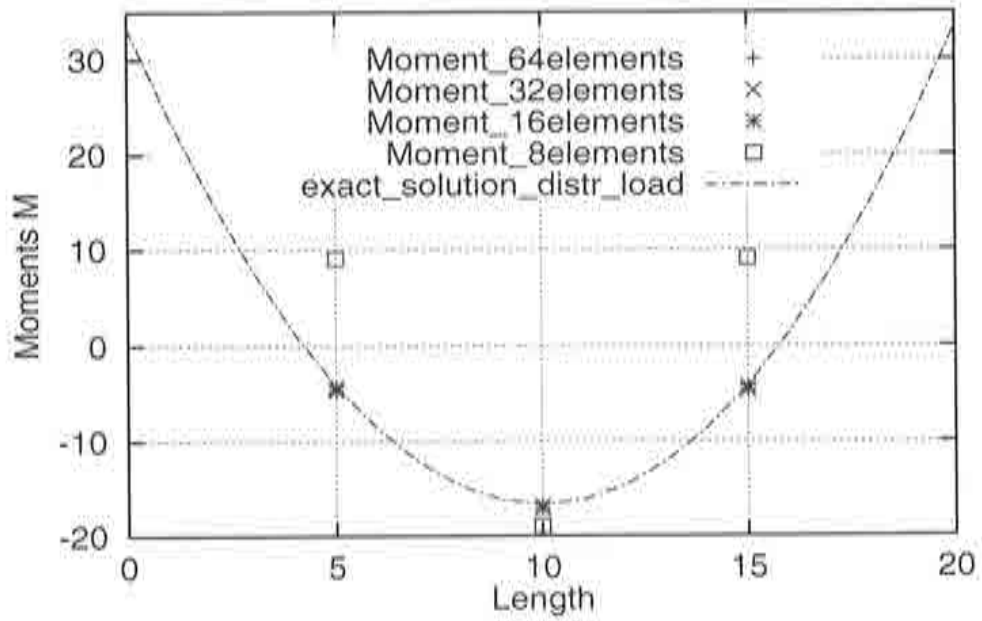

Figure 2.52 Rate of convergence of moment distribution for nonuniform meshes - CCB element.

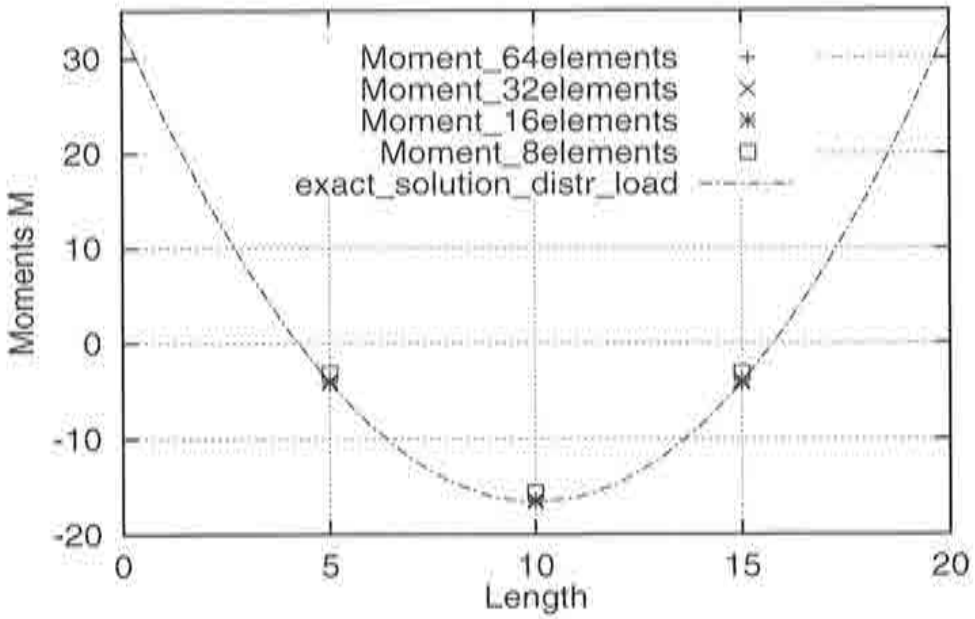

Figure 2.53 Rate of convergence of moment distribution for uniform meshes - CVB element.

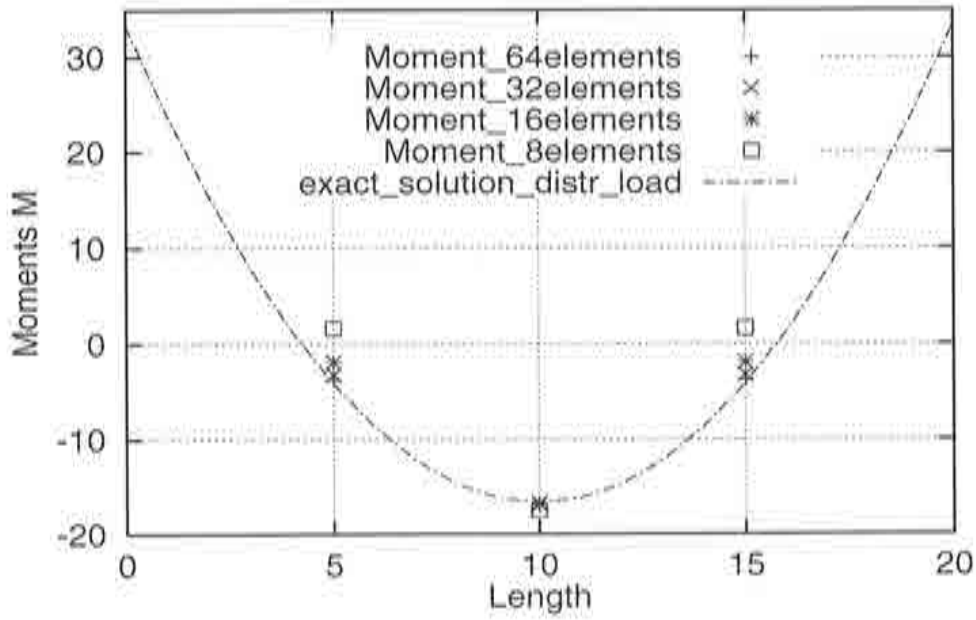

Figure 2.54 Rate of convergence of moment distribution for nonuniform meshes - CVB element.

2.6.6 Cantilever beam under point load

The beam is clamped at the left side and subjected to a point load P acting at the right end, as shown in Figure 2.55. The uniform and nonuniform meshes used in the analyses are presented in Figures 2.18 and 2.19. The geometrical and material properties are the same as in the previous examples.

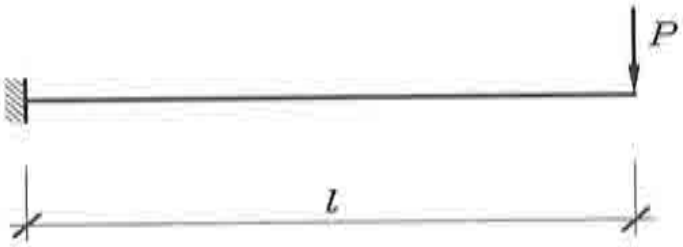

Figure 2.55 Cantilever beam under point load.

The numerical solution obtained for different number of elements is compared with the exact analytic solution for the deflection w_{ex} at the end point. The computation is performed for the uniform as well as for the nonuniform meshes. The results are given in Table 2.11 and Table 2.12, respectively.

The exact expression for deflection is

$$w(x) = \frac{Pl^3}{6EI}(\frac{x}{l})^2(3 - \frac{x}{l}) \tag{2.91}$$

and the exact deflection at the end point is

$$w_{ex} = \frac{Pl^3}{3EI} \tag{2.92}$$

MESH	CCB End deflection error	CVB End deflection error
8 elements	1.7859	0.7812
16 elements	0.4689	0.1955
32 elements	0.1198	0.0489
64 elements	0.0301	0.0121

Table 2.11 Cantilever beam under point load. Exact and numerical solution for the central deflection - uniform meshes.

MESH	CCB End deflection error	CVB End deflection error
8 elements	6.4453	1.8065
16 elements	1.6280	0.4516
32 elements	0.4089	0.1130
64 elements	0.1025	0.0283

Table 2.12 Cantilever beam under point load. Exact and numerical solution for the central deflection - nonuniform meshes.

The rate of the convergence for the deflection for CCB and CVB elements for uniform and nonuniform meshes of 8,16,32 and 64 elements is presented in Figures 2.56 and 2.57, respectively. The CVB element presents a superior performance versus the CCB element, for both uniform and nonuniform meshes.

The rate of the convergence for the moment for both elements for the uniform as well as for the nonuniform meshes is presented in Figures 2.58, 2.59, 2.60 and 2.61, respectively. The CCB and CVB elements give the exact solution independently of the number of elements.

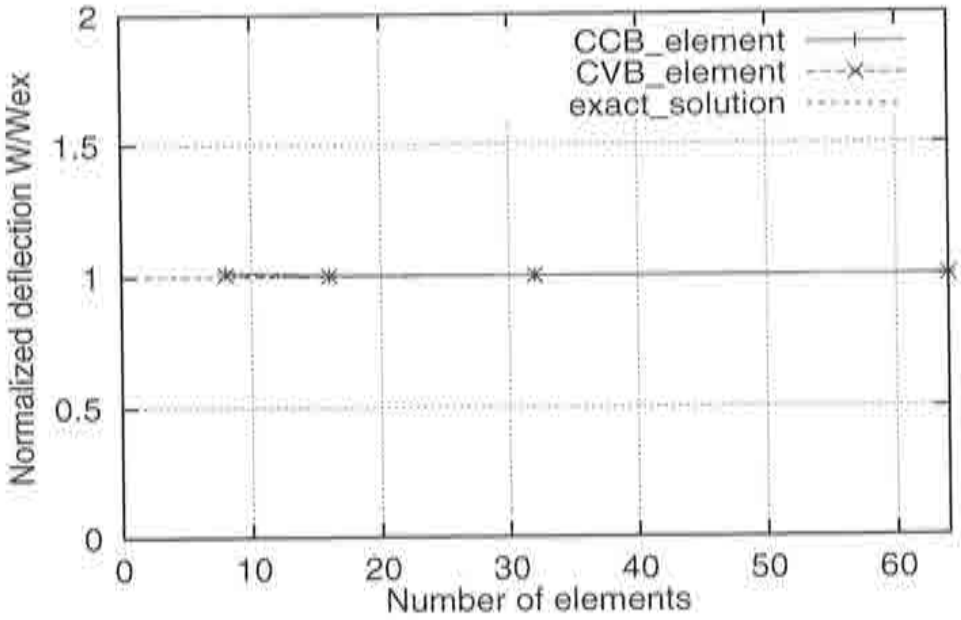

Figure 2.56 Rate of convergence of end deflection - uniform meshes.

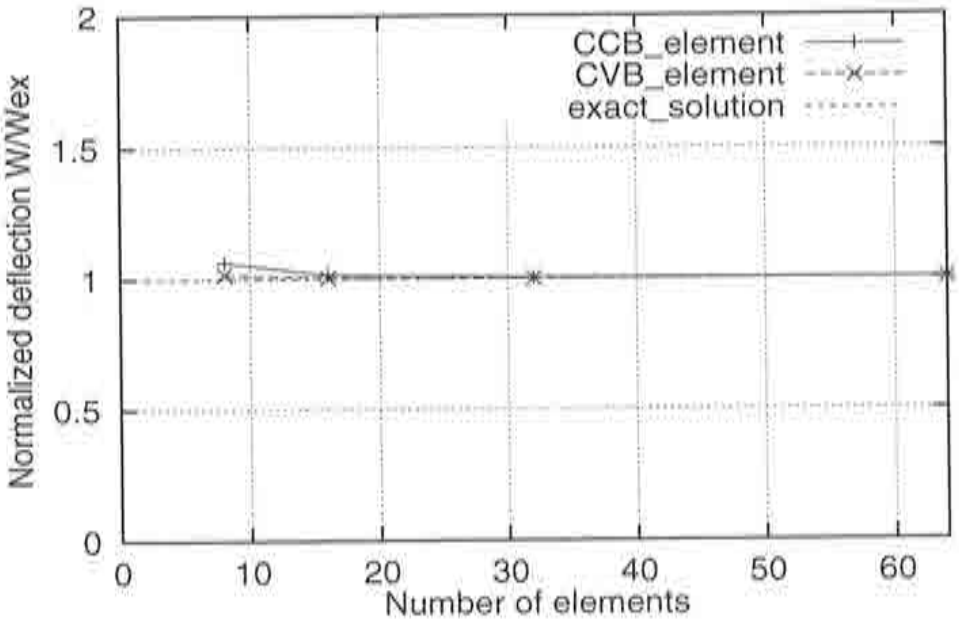

Figure 2.57 Rate of convergence of end deflection - nonuniform meshes.

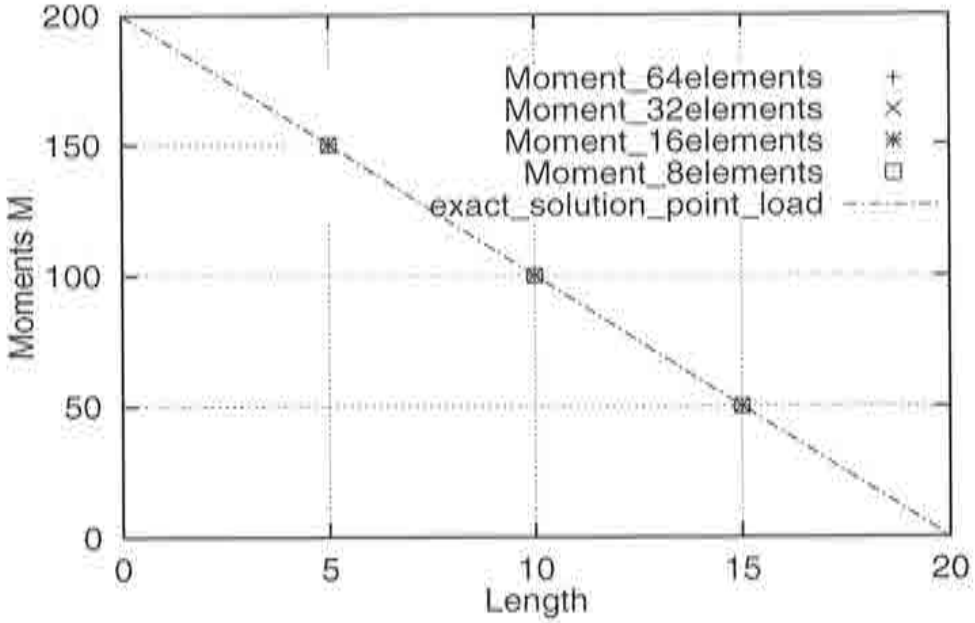

Figure 2.58 Rate of convergence of moment distribution for uniform meshes - CCB element.

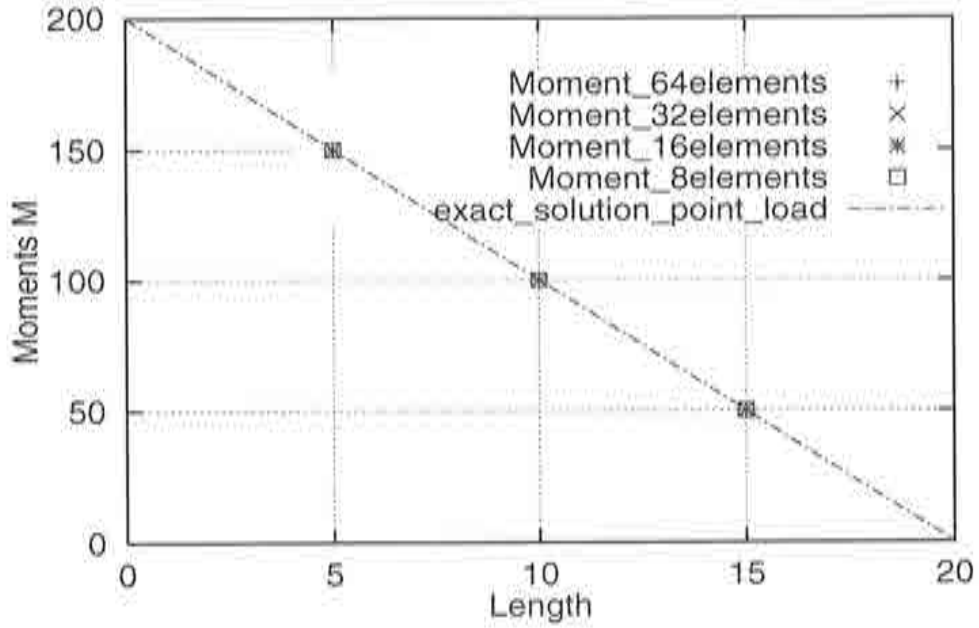

Figure 2.59 Rate of convergence of moment distribution for nonuniform meshes - CCB element.

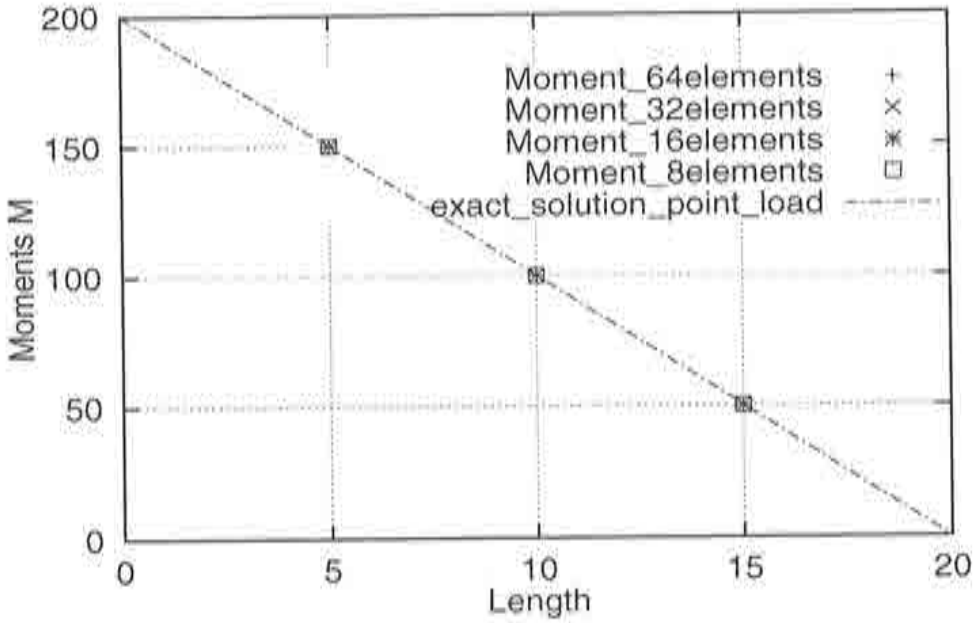

Figure 2.60 Rate of convergence of moment distribution for uniform meshes - CVB element.

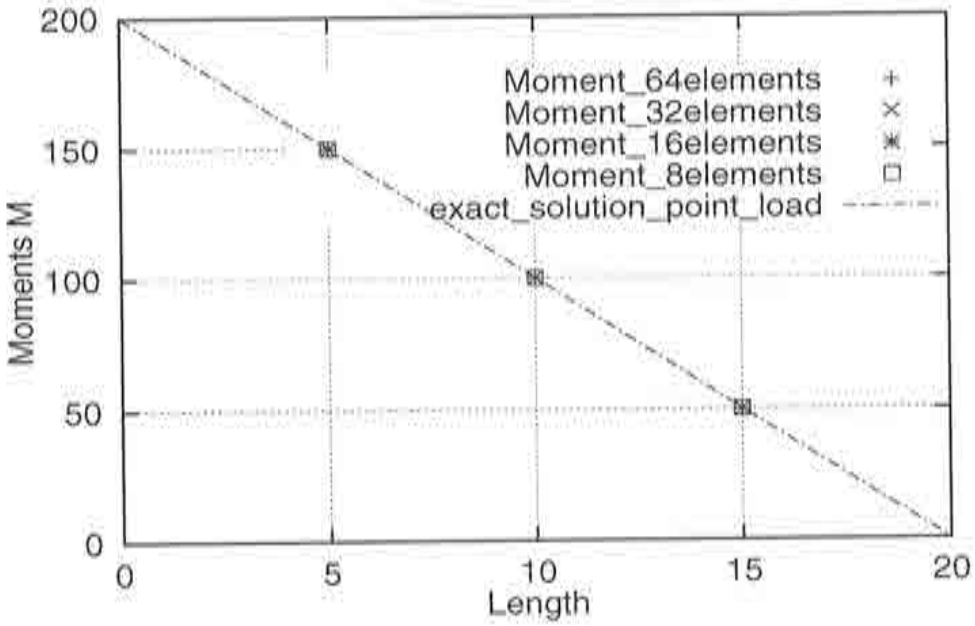

Figure 2.61 Rate of convergence of moment distribution for nonuniform meshes - CVB element.

2.6.7 Cantilever beam under distributed load

The beam is clamped at the left side and subjected to distributed load q, as shown in Figure 2.62. The uniform and nonuniform meshes used in the analyses are presented in Figures 2.18 and 2.19. The material and geometrical properties are the same as in the previous examples.

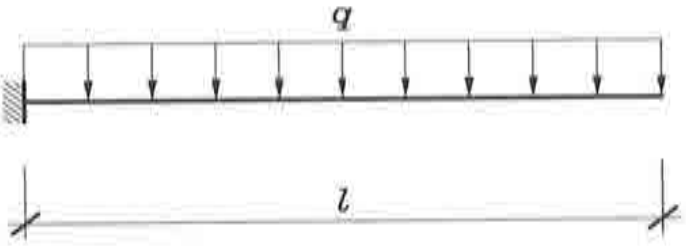

Figure 2.62 Cantilever beam under distributed load.

The exact analytic solution for the deflection w_{ex} at the corresponding po int is compared with the numerical solution obtained for different number of elements. The results of the comparison performed for the uniform as well as for the nonuniform meshes are given in Table 2.13 and Table 2.14, respectively.

The exact expression for deflection is

$$w(x) = \frac{ql^4}{24EI}\left(\frac{x}{l}\right)^2\left[6 - 4\left(\frac{x}{l}\right) + \left(\frac{x}{l}\right)^2\right] \tag{2.93}$$

and the exact deflection at the end point is

$$w_{ex} = \frac{ql^4}{8EI} \tag{2.94}$$

MESH	CCB End deflection error	CVB End deflection error
8 elements	2.9020	1.5625
16 elements	0.7550	0.3905
32 elements	0.1920	0.0975
64 elements	0.0485	0.0245

Table 2.13 Cantilever beam under distributed load. Exact and numerical solution for the central deflection - uniform meshes.

MESH	CCB End deflection error	CVB End deflection error
8 elements	11.6535	5.0050
16 elements	2.9900	1.2510
32 elements	0.7560	0.3130
64 elements	0.1900	0.0780

Table 2.14 Cantilever beam under distributed load. Exact and numerical solution for the central deflection - nonuniform meshes.

The rate of the convergence for the deflection for CCB and CVB elements for uniform and nonuniform meshes of 8,16,32 and 64 elements is presented in Figures 2.63 and 2.64, respectively. The CVB element presents a superior performance versus the CCB element, for both uniform and nonuniform meshes.

The rate of the convergence for the moment for both elements for the uniform as well as for the nonuniform meshes is presented in Figures 2.65, 2.66, 2.67 and 2.68, respectively. The CCB element gives the exact solution independently of the number of elements for both, uniform and nonuniform meshes. The CVB element gives the exact solution for the uniform meshes, while the same can be found for the nonuniform meshes only when the mesh is refined.

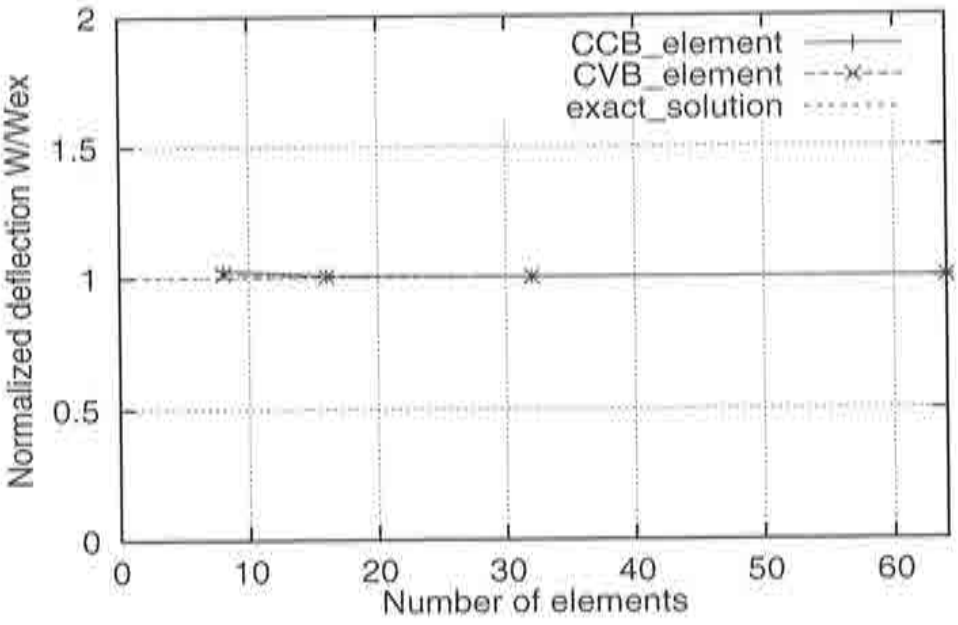

Figure 2.63 Rate of convergence of end deflection - uniform meshes.

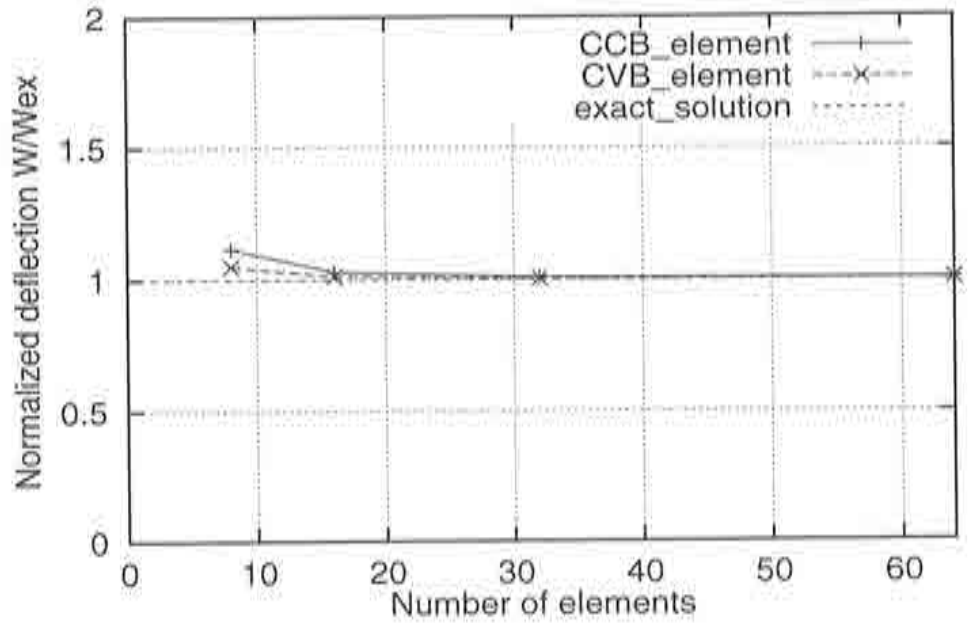

Figure 2.64 Rate of convergence of end deflection - nonuniform meshes.

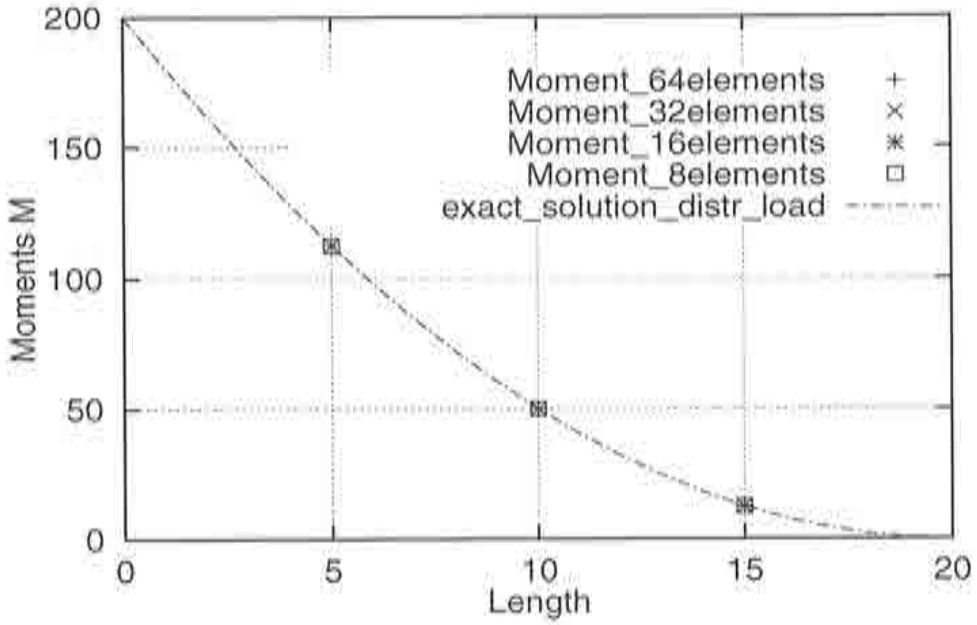

Figure 2.65 Rate of convergence of moment distribution for uniform meshes - CCB element.

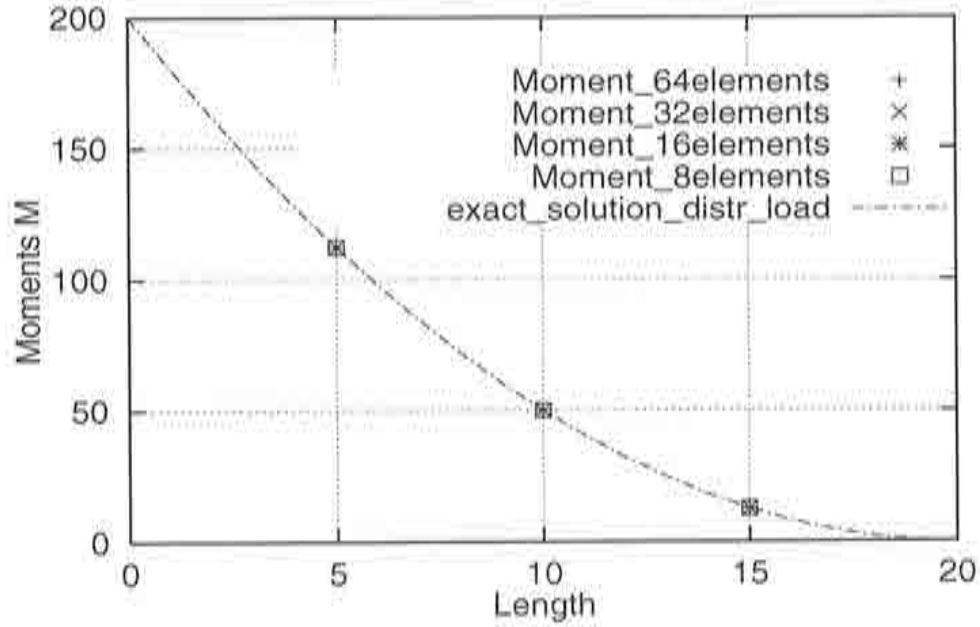

Figure 2.66 Rate of convergence of moment distribution for nonuniform meshes - CCB element.

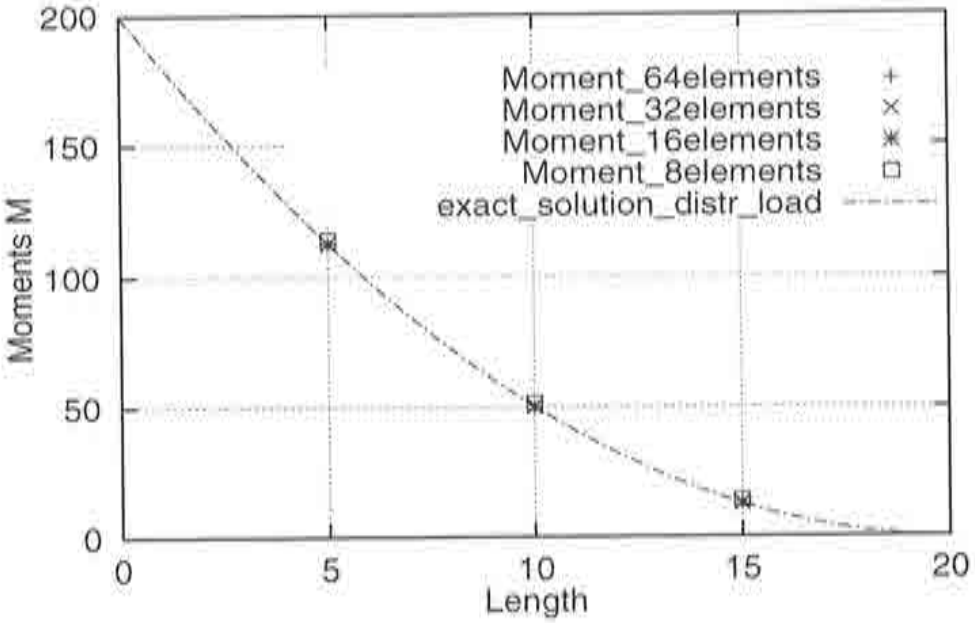

Figure 2.67 Rate of convergence of moment distribution for uniform meshes - CVB element.

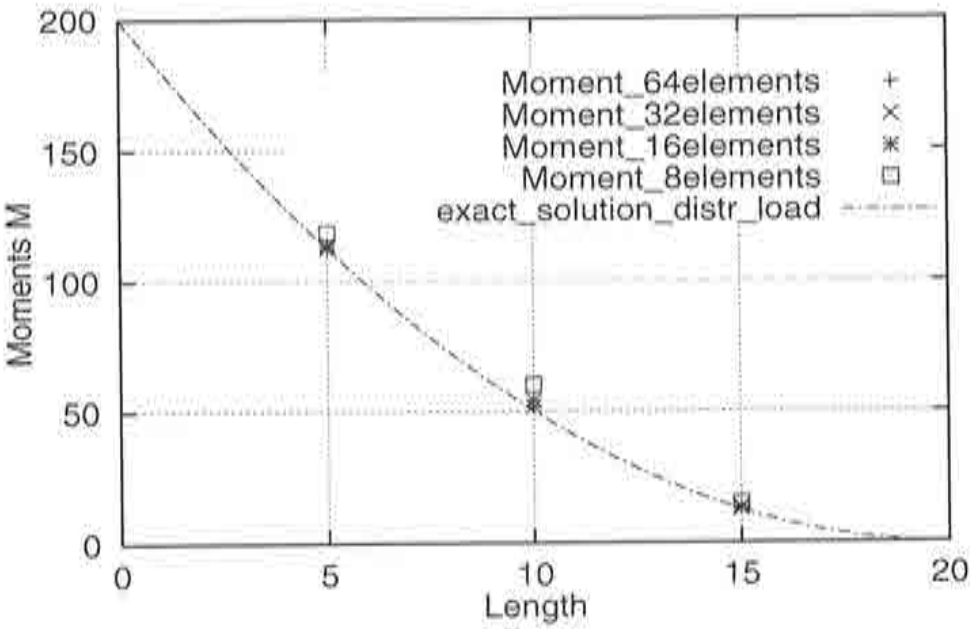

Figure 2.68 Rate of convergence of moment distribution for nonuniform meshes - CVB element.

2.6.8 Cantilever beam under distributed triangular load

The beam is clamped at the left side and subjected to triangular distributed load q, as shown in Figure 2.69. The uniform and nonuniform meshes used in the analyses are presented in Figures 2.18 and 2.19. The geometrical and material properties are the same as in the previous examples.

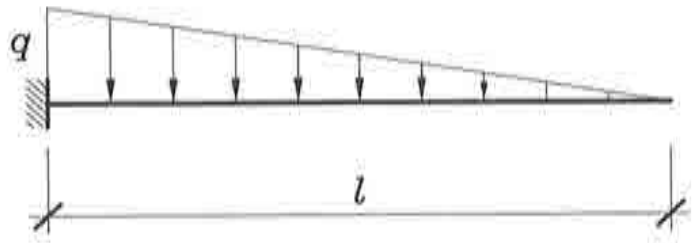

Figure 2.69 Cantilever beam under distributed triangular load.

The exact analytic solution for the deflection w_{ex} at the corresponding point is compared with the numerical solution obtained for different number of elements. The results of the comparison performed for the uniform as well as for the nonuniform meshes are given in Table 2.15 and Table 2.16, respectively.

The exact expression for deflection is

$$w(x) = \frac{F_q l^3}{60EI}\left(\frac{x}{l}\right)^2\left[10\left(1-\frac{x}{l}\right)+5\left(\frac{x}{l}\right)^2-\left(\frac{x}{l}\right)^3\right] \tag{2.95}$$

and the exact deflection at the center point is

$$w_{ex} = \frac{F_q l^3}{15EI} \tag{2.96}$$

MESH	CCB Central deflection error	CVB Central deflection error
8 elements	-0.6337	-0.6237
16 elements	-0.7937	-0.7901
32 elements	-0.8583	-0.8477
64 elements	-0.9432	-0.9430

Table 2.15 Cantilever beam under distributed triangular load. Exact and numerical solution for the central deflection - uniform meshes.

MESH	CCB Central deflection error	CVB Central deflection error
8 elements	-0.5798	-0.5435
16 elements	-0.7341	-0.7191
32 elements	-0.8484	-0.8437
64 elements	-0.9182	-0.9169

Table 2.16 Cantilever beam under distributed triangular load. Exact and numerical solution for the central deflection - nonuniform meshes.

The rate of the convergence for the deflection for CCB and CVB elements for uniform and nonuniform meshes of 8,16,32 and 64 elements is presented in Figures 2.70 and 2.71, respectively. The CVB element presents a superior performance versus the CCB element.

The rate of the convergence for the moment for both elements for the uniform as well as for the nonuniform meshes is presented in Figures 2.72, 2.73, 2.74 and 2.75, respectively. Both, the CCB and CVB elements give some discrepancy of the exact solution, which can be achieved by the mesh refinement.

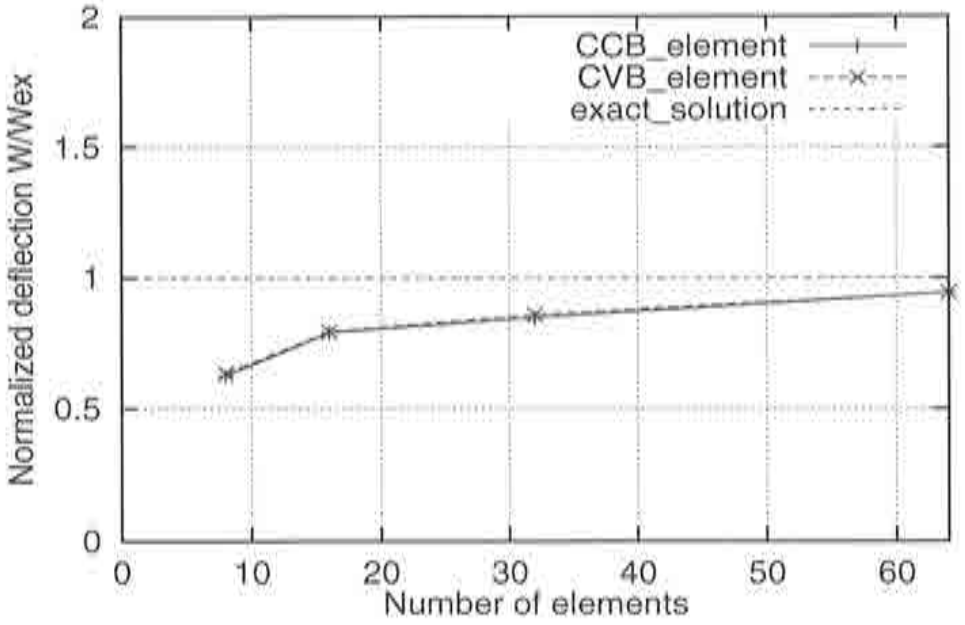

Figure 2.70 Rate of convergence of central deflection - uniform meshes.

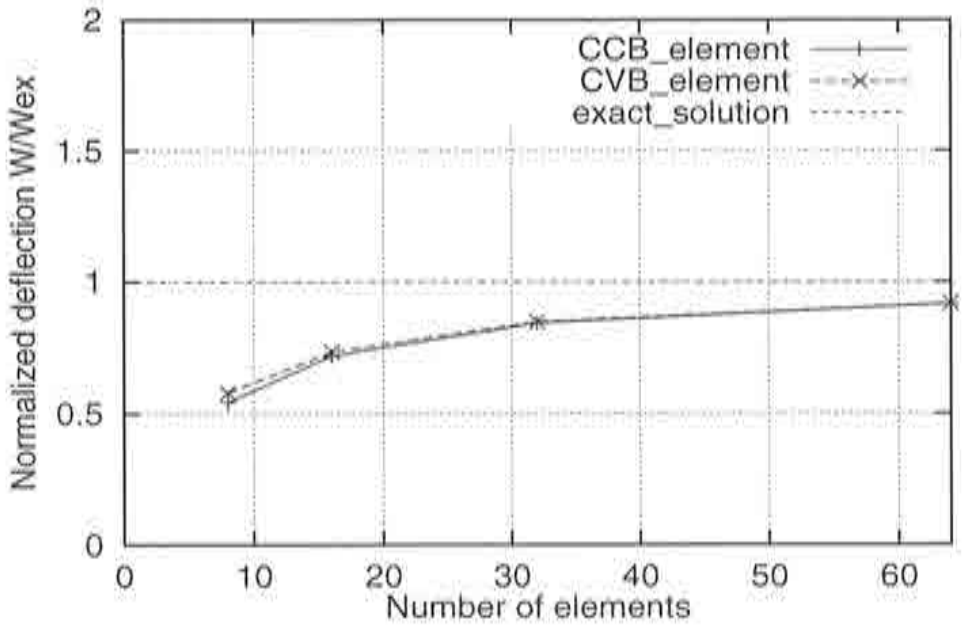

Figure 2.71 Rate of convergence of central deflection - nonuniform meshes.

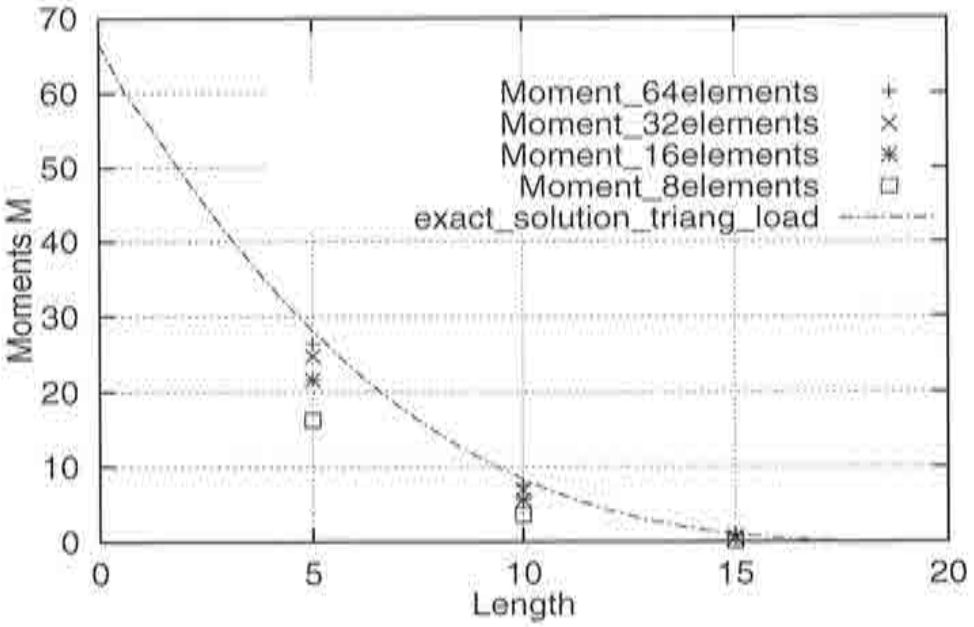

Figure 2.72 Rate of convergence of moment distribution for uniform meshes - CCB element.

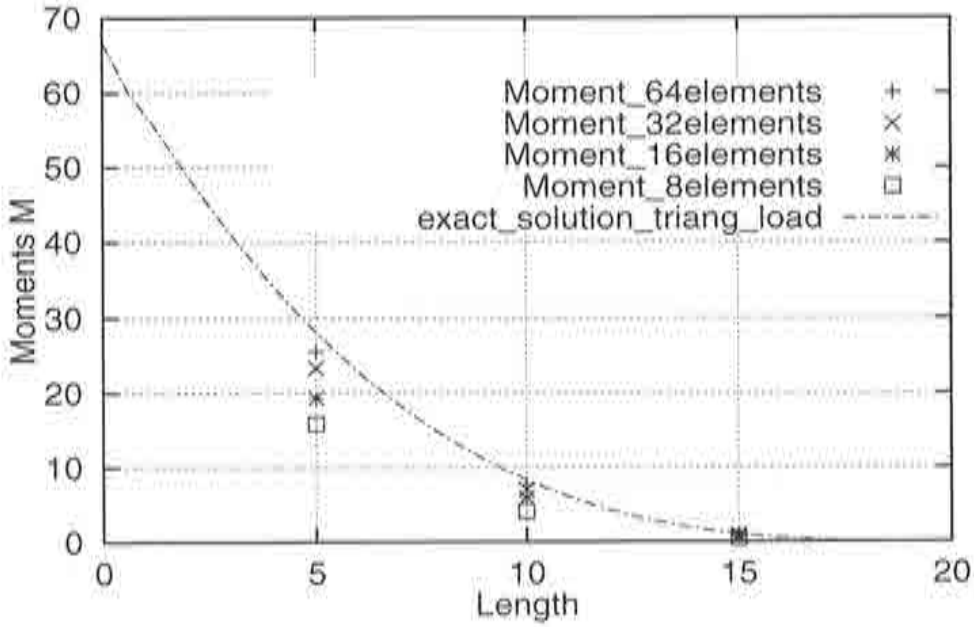

Figure 2.73 Rate of convergence of moment distribution for nonuniform meshes - CCB element.

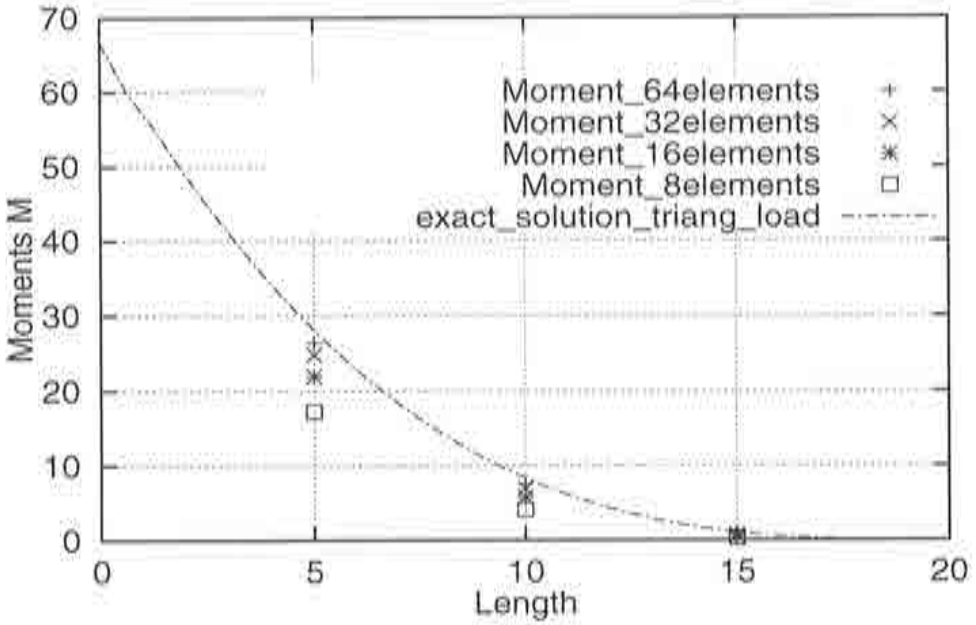

Figure 2.74 Rate of convergence of moment distribution for uniform meshes - CVB element.

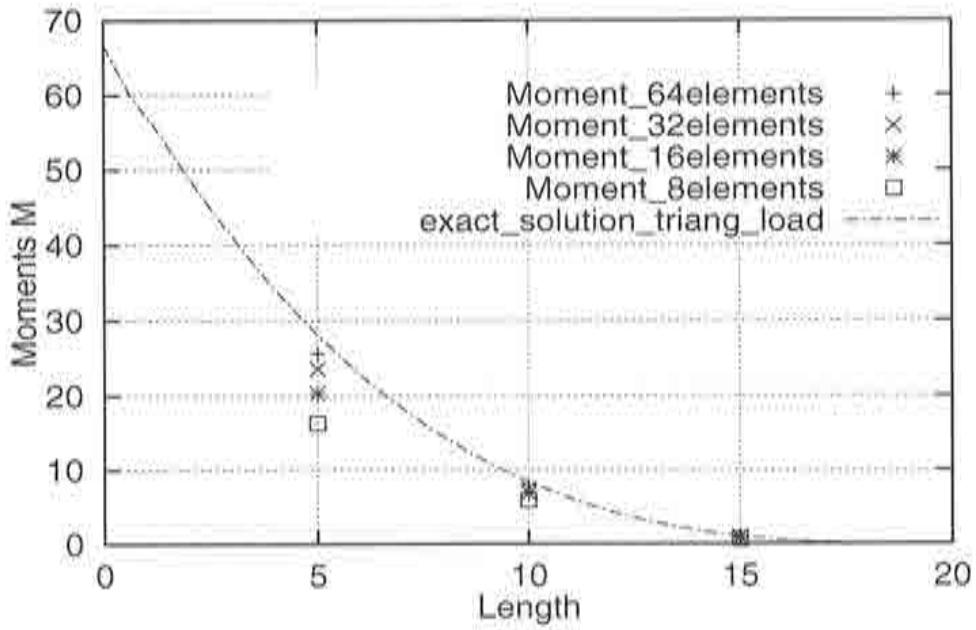

Figure 2.75 Rate of convergence of moment distribution for nonuniform meshes - CVB element.

CHAPTER 3

AXISYMMETRIC SHELLS

3.1 INTRODUCTION

A problem which is still 1D in nature but is more complicated than Euler-Bernoulli beam is the aisymmetric thin shell case where the Euler-Bernoulli orthogonality kinematic assumption is retained. This assumption is based on the principle that the normals to the shell middle surface remain normal to the given surface during the deformation. The main difference from the Euler-Bernoulli beam, which has to be treated with care, is the demand to account for circumferential direction and the use of polar coordinates.

In the analyses of thin shells it is of interest to reduce the number of degrees of freedom per node thus achieving reduction on the computational effort. This is accomplished by making explicit use of the Kirchhoff-Love hypothesis of shell fibres remaining straight and perpendicular to the midsurface of the shell.

The potential energy functional contains second derivatives of the lateral deflection. This is characteristic of a large class of physical problems associated with the fourth order differential equations, so C_1 continuity of the corresponding shape function is necessary [Z-4]. The difficulty to impose C_1 continuity on the shape functions results in searching for some alternative approach. The framework of the mixed Hu-Washizu formulation, using the concepts based on the coupled FE/FV technique is used in this thesis to develop two robust rotation-free axisymmetric shell elements for linear analysis, denoted ACC and ACV elements, respectively.

The outline of the chapter is as follows. First, the basic theory for axisymmetric shell is reviewed. Then, the set of the governing equations is developed in integral form from the standard Hu-Washizu functional. This set of equations represents the basis for the subsequent FE/FV discretization, which is discussed in detail in this chapter. Several numerical examples are presented in order to show the accuracy of the two rotation-free axisymmetric shell elements developed in this study.

3.2 BASIC THEORY

Taking into consideration that the axisymmetric thin shell problem, presented in Figure 3.1, is mathematically one-dimensional, that Euler-Bernoulli kinematic hypothesis is retained and introducing a polar coordinate system, the strong form of the basic governing equations can be written as follows.

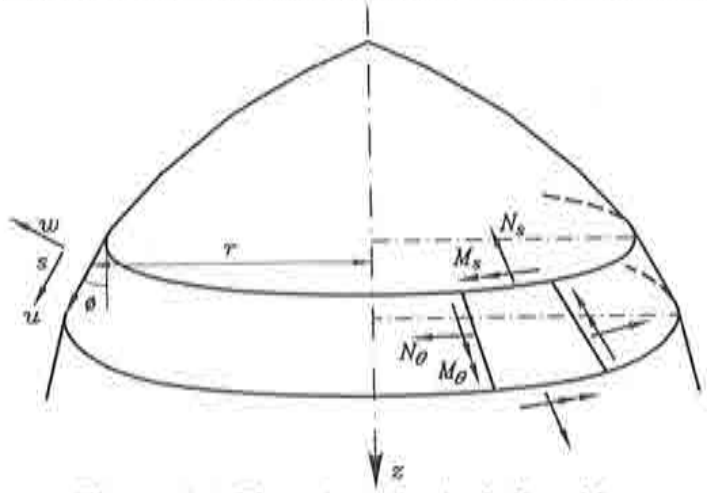

Figure 3.1 The axisymmetric shell problem.

The kinematic equation relating generalized strains and displacements is

$$\boldsymbol{\varepsilon} = \mathbf{L}\mathbf{u} \tag{3.1}$$

where $\mathbf{u} = [u, w]^T$, with u and w being the radial and vertical displacements of a shell point, respectively. The four generalized strain components are given by the following expression

$$\hat{\boldsymbol{\varepsilon}}' = \begin{Bmatrix} \hat{\varepsilon}'_m \\ \cdots \\ \hat{\varepsilon}'_f \end{Bmatrix} = \begin{Bmatrix} \lambda_s \\ \lambda_\theta \\ \cdots \\ \chi_s \\ \chi_\theta \end{Bmatrix} = \begin{Bmatrix} \frac{\partial u'}{\partial s} \\ \frac{u}{r} \\ \cdots \\ -\frac{\partial^2 w'}{\partial s^2} \\ -\frac{cos\phi}{r}\frac{\partial w'}{\partial s} \end{Bmatrix} = \begin{bmatrix} \frac{\partial}{\partial s} & 0 \\ \frac{1}{r} & 0 \\ \cdots & \cdots \\ 0 & -\frac{\partial^2}{\partial s^2} \\ 0 & -\frac{cos\phi}{r}\frac{\partial}{\partial s} \end{bmatrix} \begin{Bmatrix} u' \\ w' \end{Bmatrix} =$$

$$= \begin{Bmatrix} \mathbf{L}_m \\ \mathbf{L}_b \end{Bmatrix} \begin{Bmatrix} u' \\ w' \end{Bmatrix} \tag{3.2}$$

where λ_s and λ_θ are the axial and circumferential elongations and χ_s and χ_θ are the radial and circumferential curvatures, respectively. In the above equation

u' and w' are the local displacement components in the tangential and normal directions, respectively.

The matrix $\mathbf{L}$ is divided into membrane $\mathbf{L}_m$ and bending $\mathbf{L}_b$ parts, where

$$\mathbf{L}_m = \begin{bmatrix} \frac{\partial}{\partial s} & 0 \\ \frac{1}{r} & 0 \end{bmatrix} \quad \mathbf{L}_b = \begin{bmatrix} 0 & -\frac{\partial^2}{\partial s^2} \\ 0 & -\frac{cos\phi}{r}\frac{\partial}{\partial s} \end{bmatrix} \tag{3.3}$$

The constitutive equations relating generalized strains and resulting stresses can be written as

$$\hat{\boldsymbol{\sigma}}' = \begin{Bmatrix} \mathbf{a} \\ \mathbf{m} \end{Bmatrix} = \mathbf{D}\hat{\boldsymbol{\varepsilon}}' \tag{3.4}$$

where $\mathbf{a} = [N_s, N_\theta]^T$ and $\mathbf{m} = [M_s, M_\theta]^T$, with N_s and N_θ being the axial and circumferential forces and M_s and M_θ being the radial and circumferential moments, respectively.

The elasticity matrix $\mathbf{D}$ is defined as

$$\mathbf{D} = \begin{bmatrix} \mathbf{D}_m & 0 \\ 0 & \mathbf{D}_b \end{bmatrix} \tag{3.5}$$

where the appropriate matrices $\mathbf{D}_m$ and $\mathbf{D}_b$ are, respectively

$$\mathbf{D}_m = \frac{Et}{1-\nu^2}\begin{bmatrix} 1 & \nu \\ \nu & 1 \end{bmatrix} \quad \mathbf{D}_b = \frac{Et^3}{12(1-\nu^2)}\begin{bmatrix} 1 & \nu \\ \nu & 1 \end{bmatrix} \tag{3.6}$$

In further expressions $s \equiv x'$ will be taken, as the element is straight.

The set of the governing equations can be obtained in integral form, starting from the standard Hu-Washizu functional given by

$$\boldsymbol{\Pi} = \frac{1}{2}\int\int_A \hat{\boldsymbol{\varepsilon}}'^T \mathbf{D}\hat{\boldsymbol{\varepsilon}}' dA + \int\int_A \hat{\boldsymbol{\sigma}}'^T [\mathbf{L}\mathbf{u}' - \hat{\boldsymbol{\varepsilon}}']dA - \int\int_A \delta\mathbf{u}^T q dA \tag{3.7}$$

or in expanded form

$$\boldsymbol{\Pi} = \frac{1}{2}\int\int_A [\boldsymbol{\chi}^T \mathbf{D}_b \boldsymbol{\chi} + \boldsymbol{\lambda}^T \mathbf{D}_m \boldsymbol{\lambda}]dA +$$

$$+ \int\int_A [\mathbf{m}^T(\mathbf{L}_b w' - \boldsymbol{\chi}) + \mathbf{a}^T(\mathbf{L}_m u' - \boldsymbol{\lambda})]dA -$$

$$-\int\int_A [\delta w' q' + \delta u' t'] dA \tag{3.8}$$

where the elongations and curvatures are respectively

$$\boldsymbol{\lambda} = [\lambda_s, \lambda_\theta]^T \quad \text{and} \quad \boldsymbol{\chi} = [\chi_s, \chi_\theta]^T \tag{3.9}$$

with A being the area of the shell and q being the distributed loading.

Variation of $\boldsymbol{\Pi}$ expressed by equation (3.8) gives the integral form of the set of equilibrium, kinematic and constitutive equations. Thus

$$\delta\boldsymbol{\Pi} \Rightarrow 0 \tag{3.11}$$

leads to the set of equilibrium equations, where the bending and membrane contributions are

$$\int\int_A (\mathbf{L}_b \delta w')^T \mathbf{m}^T dA - \int\int_A \delta w' q' dA = 0 \tag{3.12a}$$

$$\int\int_A (\mathbf{L}_m \delta u')^T \mathbf{a}^T dA - \int\int_A \delta u' t' dA = 0 \tag{3.12b}$$

The set of kinematic equations for the curvature and elongation parts are respectively

$$\int\int_A \delta \mathbf{m}^T (\mathbf{L}_b w' - \boldsymbol{\chi}) dA = 0 \tag{3.13a}$$

$$\int\int_A \delta \mathbf{a}^T (\mathbf{L}_m u' - \boldsymbol{\lambda}) dA = 0 \tag{3.13b}$$

The set of constitutive equations, moment-curvature and elongation-axial force relationships are respectively

$$\int\int_A \delta \boldsymbol{\chi}^T (\mathbf{D}_b \boldsymbol{\chi} - \mathbf{m}) dA = 0 \tag{3.14a}$$

$$\int\int_A \delta \boldsymbol{\lambda}^T (\mathbf{D}_m \boldsymbol{\lambda} - \mathbf{a}) dA = 0 \tag{3.14b}$$

Equations (3.12), (3.13) and (3.14) are the basis for the coupled FE/FV discretization, presented in more detail in the next section.

3.3 FINITE ELEMENT - FINITE VOLUME DISCRETIZATION

A discretization of the shell into standard linear troncoconical elements is considered. The curvature and the bending moments, as well as the elongations and normal forces are assumed to be constant within each control domain, i.e.

$$\delta\mathbf{m}, \mathbf{m} = \delta\mathbf{m_p}, \mathbf{m_p} \qquad \delta\mathbf{a}, \mathbf{a} = \delta\mathbf{a_p}, \mathbf{a_p} \tag{3.15a}$$

$$\delta\boldsymbol{\chi}, \boldsymbol{\chi} = \delta\boldsymbol{\chi}_p, \boldsymbol{\chi}_p \qquad \delta\boldsymbol{\lambda}, \boldsymbol{\lambda} = \delta\boldsymbol{\lambda}_p, \boldsymbol{\lambda}_p \tag{3.15b}$$

where $(.)_p$ denotes constant values over the control domain p. Using these assumptions, the equilibrium, kinematic and constitutive equations are expressed as follows.

The set of equilibrium equations, respecting the assumptions given by equation (3.15) is

$$\sum_p \int_{2\pi} \int_{l_p} [\frac{\partial^2(\delta w')}{\partial x'^2} M_s + \frac{cos\phi}{r} \frac{\partial(\delta w')}{\partial x'} M_\theta] dA - \sum_p \int_{2\pi} \int_{l_p} \delta w' q' dA = 0 \tag{3.16a}$$

$$\sum_p \int_{2\pi} \int_{l_p} [\frac{\partial(\delta u')}{\partial x'} N_s + \frac{u}{r} N_\theta] dA - \sum_p \int_{2\pi} \int_{l_p} \delta u' t' dA = 0 \tag{3.16b}$$

Integrating the terms involving the deflection derivatives give

$$\int_{2\pi} \int_{l_p} \frac{\partial^2(\delta w')}{\partial x'^2} dA = 2\pi [r \frac{\partial(\delta w')}{\partial x'}]_{x_p^-}^{x_p^+} \tag{3.17}$$

Thus, equations (3.16a) and (3.16b) can be rewritten as

$$2\pi \sum_p [[r \frac{\partial(\delta w')}{\partial x'}]_{x_p^-}^{x_p^+} M_s + cos\phi \frac{\partial w'}{\partial x'} M_\theta l_p] - 2\pi \sum_p \int_{l_p} \delta w' q' r dx' = 0 \tag{3.18a}$$

$$2\pi \sum_p [\frac{\partial(\delta u')}{\partial x'} N_s r l_p + u N_\theta l_p] - 2\pi \sum_p \int_{l_p} \delta u' t' r dx' = 0 \tag{3.18b}$$

where r is the radial distance of the mid point of the p-th control domain and l_p is the length of the control domain.

The set of kinematic equations, respecting the assumptions given by equation (3.15) and taking into account that the virtual magnitudes are arbitrary, can be expressed for each control domain as

$$\int_{2\pi}\int_{l_p} -\frac{\partial^2 w'}{\partial x'^2}dA - \int_{2\pi}\int_{l_p} \chi_s dA = 0 \tag{3.20a}$$

$$\int_{2\pi}\int_{l_p} -\frac{cos\phi}{r}\frac{\partial w'}{\partial x'}dA - \int_{2\pi}\int_{l_p} \chi_\theta dA = 0 \tag{3.20b}$$

$$\int_{2\pi}\int_{l_p} \frac{\partial u'}{\partial x'}dA - 2\pi\lambda_s r l_p = 0 \tag{3.20c}$$

$$\int_{2\pi}\int_{l_p} \frac{u}{r}dA - 2\pi\lambda_\theta r l_p = 0 \tag{3.20d}$$

In order to express the radial curvature χ_s in terms of nodal deflections only some additional operations have to be done as follows. The expanded form of equation (3.20a) is

$$-\int_{l_p} 2\pi r\frac{\partial^2 w'}{\partial x'^2}dx' = 2\pi r l_p \chi_s \tag{3.21}$$

Integrating by parts the first integral in (3.21) gives

$$\int_{l_p} r\frac{\partial^2 w'}{\partial x'^2}dx' = -\int_{l_p}\frac{\partial r}{\partial x'}\frac{\partial w'}{\partial x'}dx' + [r\frac{\partial w'}{\partial x'}]_{x_p^-}^{x_p^+} \tag{3.22}$$

Replacing equation (3.22) into (3.21) the following expression is obtained

$$-[r\frac{\partial w'}{\partial x'}]_{x_p^-}^{x_p^+} + \int_{l_p}\frac{\partial r}{\partial x'}\frac{\partial w'}{\partial x'}dx' = r l_p \chi_s \tag{3.23}$$

The previous equation (3.23) yields

$$-r_{x_p^+}(\frac{\partial w'}{\partial x'})_{x_p^+} + r_{x_p^-}(\frac{\partial w'}{\partial x'})_{x_p^-} + \int_{x_p^-}^{i}\frac{\partial r}{\partial x'}\frac{\partial w'}{\partial x'}dx + \int_{i}^{x_p^+}\frac{\partial r}{\partial x'}\frac{\partial w'}{\partial x'}dx' = r l_p \chi_s \tag{3.24}$$

where

$$\int_{x_p^-}^{i} \frac{\partial r}{\partial x'}\frac{\partial w'}{\partial x'}dx' = \frac{r_i - r_{x_p^-}}{\frac{l_p}{2}}\frac{l_p}{2}(\frac{\partial w'}{\partial x'})_{x_p^-} \tag{3.25a}$$

$$\int_{i}^{x_p^+} \frac{\partial r}{\partial x'}\frac{\partial w'}{\partial x'}dx' = \frac{r_{x_p^+} - r_i}{\frac{l_p}{2}}\frac{l_p}{2}(\frac{\partial w'}{\partial x'})_{x_p^+} \tag{3.25b}$$

Introducing equations (3.25) into (3.24) gives

$$-r_{x_p^+}(\frac{\partial w'}{\partial x'})_{x_p^+} + r_{x_p^-}(\frac{\partial w'}{\partial x'})_{x_p^-} + \frac{r_i - r_{x_p^-}}{\frac{l_p}{2}}\frac{l_p}{2}(\frac{\partial w'}{\partial x'})_{x_p^-} + \frac{r_{x_p^+} - r_i}{\frac{l_p}{2}}\frac{l_p}{2}(\frac{\partial w'}{\partial xi'})_{x_p^+} = rl_p\chi \tag{3.26}$$

what finally gives

$$-r[\frac{\partial w'}{\partial x'}]_{x_p^-}^{x_p^+} = rl_p\chi_s \tag{3.27}$$

and the radial curvature χ_s is expressed as

$$-\chi_s = \frac{1}{l_p}[\frac{\partial w'}{\partial x'}]_{x_p^-}^{x_p^+} \tag{3.28}$$

The corresponding values for the x_p^+ and x_p^- are different for the Cell Centered and Cell Vertex schemes, as shown in Figure 3.2.

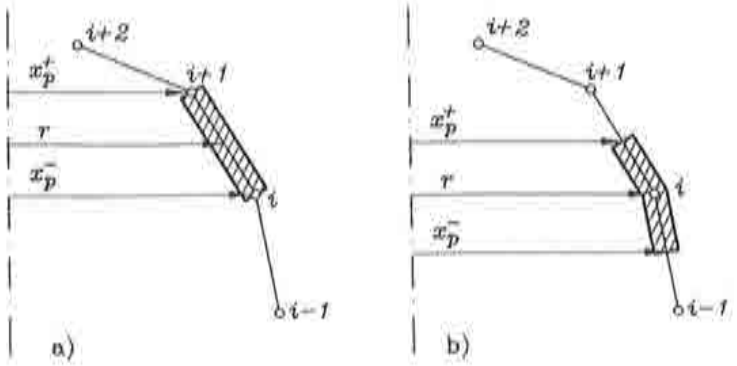

Figure 3.2 (a) Cell Centered and (b) Cell Vertex schemes.

From equation (3.20b) the circumferential curvature is expressed as

$$\chi_\theta = -\frac{cos\phi}{r}\frac{\partial w'}{\partial x'} \tag{3.29}$$

From equations (3.20c) and (3.20d) the axial and circumferential elongations are expressed respectively as

$$\lambda_s = \frac{\partial u'}{\partial x'} \tag{3.30}$$

$$\lambda_\theta = \frac{u}{r} \tag{3.31}$$

Replacing equations (3.28), (3.29), (3.30) and (3.31) into (3.2) gives

$$\bar{\varepsilon}' = \begin{Bmatrix} \bar{\varepsilon}'_m \\ \cdots \\ \bar{\varepsilon}'_f \end{Bmatrix} = \begin{Bmatrix} \lambda_s \\ \lambda_\theta \\ \cdots \\ \chi_s \\ \chi_\theta \end{Bmatrix} = \begin{Bmatrix} \frac{\partial u'}{\partial x'} \\ \frac{u}{r} \\ \cdots \\ -\frac{1}{l'_p}\left[\frac{\partial w'}{\partial x'}\right]_{x'_p}^{x'_p} \\ -\frac{cos\phi}{r}\frac{\partial w'}{\partial x'} \end{Bmatrix} = \mathbf{B'}_p\mathbf{u'} \tag{3.32}$$

where the matrix $\mathbf{B'}_p$ is

$$\mathbf{B'}_p = [\mathbf{B'}_{\lambda_s}, \mathbf{B'}_{\lambda_\theta}, \mathbf{B'}_{\chi_s}, \mathbf{B'}_{\chi_\theta}]^T \tag{3.33}$$

and

$$\bar{\varepsilon}' = \mathbf{B'}_p\mathbf{L}_p\mathbf{u} = \mathbf{B'}_p\mathbf{u} \tag{3.34}$$

with $\mathbf{u'} = \mathbf{L}_p\mathbf{u}$.

The discretization of the deflection field is done as follows. The simplest option is to interpolate linearly the deflection within each troncoconical element in terms of the nodal deflections in the standard finite element manner [Z-4] as

$$w' = \sum_{i=1}^{2} N_i w_i = \mathbf{N}^{(e)}\mathbf{w}^{(e)} \tag{3.35}$$

where $\mathbf{N}^{(e)} = [\mathbf{N}_1, \mathbf{N}_2]$ and $\mathbf{w}^{(e)} = [w_1, w_2]^T$ with N_i being the standard linear shape functions and w_i being the nodal deflection values.

As it is shown, the use of assumptions (3.15) is essential to express kinematic and constitutive equations for each patch. Thus, substituting equations (3.15) and (3.35) into governing set of equilibrium (3.12), kinematic (3.13) and constitutive equations (3.14) after some algebra gives the final system of algebraic equations

$$\mathbf{K}\mathbf{w} = \mathbf{f} \tag{3.36}$$

where the vector $\mathbf{w}$ contains the nodal deflections. The stiffness matrix $\mathbf{K}$ is obtained by assembling the contributions from the different control volumes

$$\mathbf{K} = \mathop{\mathbf{A}}_{p} \mathbf{K}_p \tag{3.37}$$

where

$$\mathbf{K}_p = 2\pi \mathbf{B}_p^T \mathbf{D}_p \mathbf{B}_p r l_p \tag{3.38}$$

The matrix $\mathbf{B}_p$ is different for the Cell Centered and Cell Vertex schemes and it is defined in the next section.

The nodal force vector $\mathbf{f}$ is obtained also by assembling the contributions from the different patches

$$\mathbf{f} = \mathop{\mathbf{A}}_{p} \mathbf{f}_p \tag{3.39}$$

where f_i for a constant distributed force is calculated as

$$f_i = \frac{l}{2} \begin{Bmatrix} q \\ t \end{Bmatrix} \tag{3.40}$$

3.4 COMPUTATION OF THE B_p MATRIX

The matrix $\mathbf{B}_p$ is the curvature matrix relating the constant curvature field within a control domain and the nodal deflections associated to the patch. The computation of the matrix $\mathbf{B}_p$ is different for the Cell Centered and Cell Vertex schemes. The practical application of the axisymmetric shell element requires the consideration of the various types of boundary conditions: free edges, simply supported edges and clamped edges. The corresponding $\mathbf{B}_p$ matrices can be then easily evaluated for each condition separately. In these situations, the adjacent element is missing one in the corresponding patch. Details are given below.

3.4.1 Cell Centered scheme - ACC axisymmetric shell element

The integrals in equations (3.12), (3.13) and (3.14) are expressed as the sum of contributions over the different patches by equations (3.16), (3.18) and (3.20), respectively. The radial and circumferential curvatures χ_s and χ_θ and the axial and circumferential elongations λ_s and λ_θ expressed by equations (3.28), (3.29), (3.30) and (3.31) respectively, within each element patch are expressed in terms of the local deflection gradients at the patch edges and in terms of the values at the adjacent elements sharing each side. A transformation of the local matrices $\mathbf{B'}_p$ with the corresponding matrices of transformation $\mathbf{T}$ is then performed for assembly.

3.4.1.1 General case

The left and right side adjacent elements with respect to the element under the consideration l^e are connected together forming one patch presented in Figure 3.3. The boundary conditions are not applied. Each of the patch elements has two local corresponding displacements u' and w'.

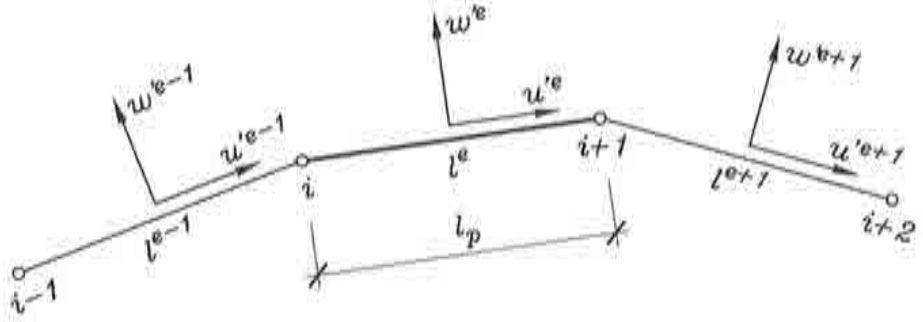

Figure 3.3 General patch for the Cell Centered scheme.

The local displacements u' and w' are transformed to global displacements u and w by the corresponding matrices of transformations. The local and global systems are presented in Figure 3.4.

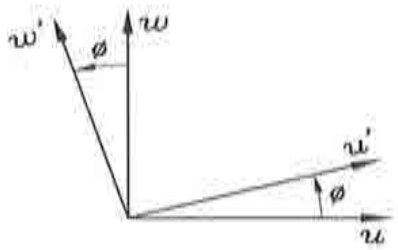

Figure 3.4 The local and global system.

The radial curvature is expressed as the difference of the first derivative displacements of the element nodes $(\frac{\partial w'}{\partial x'})_{i+1}$ and $(\frac{\partial w'}{\partial x'})_i$

$$\chi_s^p l_e = (\frac{\partial w'}{\partial x'})_{i+1} - (\frac{\partial w'}{\partial x'})_i \tag{3.41}$$

Using the theory of distributions, the values $(\frac{\partial w'}{\partial x'})_{i+1}$ and $(\frac{\partial w'}{\partial x'})_i$ across the boundary should be given as an average value as follows

$$(\frac{\partial w'}{\partial x'})_{i+1} = \frac{1}{2}\Big[\frac{\partial w'}{\partial x'}\Big|_{i+1}^{i} + \frac{\partial w'}{\partial x'}\Big|_{i+1}^{i+2}\Big] = \frac{1}{2}\Big[\frac{w'^e_{i+1} - w'^e_i}{l^e} + \frac{w'^{e+1}_{i+2} - w'^{e+1}_{i+1}}{l^{e+1}}\Big] \tag{3.42}$$

$$(\frac{\partial w'}{\partial x'})_i = \frac{1}{2}\Big[\frac{\partial w'}{\partial x'}\Big|_{i}^{i-1} + \frac{\partial w'}{\partial x'}\Big|_{i}^{i}\Big] = \frac{1}{2}\Big[\frac{w'^{e-1}_i - w'^{e-1}_{i-1}}{l^{e-1}} + \frac{w'^e_{i+1} - w'^e_i}{l^e}\Big] \tag{3.43}$$

Substituting the last two equations into (3.41), yields

$$\chi_s^p = \frac{1}{2l^{e-1}l^e l^{e+1}}[l^{e+1}, -l^{e+1}, -l^{e-1}, l^{e-1}] \begin{Bmatrix} w'^{e-1}_{i-1} \\ w'^{e-1}_{i} \\ w'^{e+1}_{i+1} \\ w'^{e+1}_{i+2} \end{Bmatrix} = \mathbf{B'}_{\chi s}\mathbf{w'} \tag{3.44}$$

where the curvature matrix $\mathbf{B'}_{\chi s}$ is

$$\mathbf{B'}_{\chi s} = \frac{1}{2l^{e-1}l^e l^{e+1}}[l^{e+1}, -l^{e+1}, -l^{e-1}, l^{e-1}] \tag{3.45}$$

The global curvature matrix $\mathbf{B}_{\chi s}$ is expressed as

$$\mathbf{B}_{\chi s} = \mathbf{B'}_{\chi s}\mathbf{T}_{\chi s} \tag{3.46}$$

where the matrix $\mathbf{T}_{\chi s}$ is the transformation matrix.

For clarity, in order to evaluate the transformation matrices the following expressions are given

$$w'^{e-1}_{i-1} = -u_{i-1}sin\phi_{e-1} + w_{i-1}cos\phi_{e-1} \tag{3.47a}$$

$$w'^{e-1}_{i} = -u_{i}sin\phi_{e-1} + w_{i}cos\phi_{e-1} \tag{3.47b}$$

$$w'^{e}_{i} = -u_{i}sin\phi_{e} + w_{i}cos\phi_{e} \tag{3.48a}$$

$$w'^{e}_{i+1} = -u_{i+1}sin\phi_{e} + w_{i+1}cos\phi_{e} \tag{3.48b}$$

$$w'^{e+1}_{i+1} = -u_{i+1}sin\phi_{e+1} + w_{i+1}cos\phi_{e+1} \tag{3.49a}$$

$$w'^{e+1}_{i+2} = -u_{i+2}sin\phi_{e+1} + w_{i+2}cos\phi_{e+1} \tag{3.49b}$$

where

$$\mathbf{n}^{e-1} = \begin{Bmatrix} -sin\phi_{e-1} \\ cos\phi_{e-1} \end{Bmatrix} \quad \mathbf{n}^{e} = \begin{Bmatrix} -sin\phi_{e} \\ cos\phi_{e} \end{Bmatrix} \quad \mathbf{n}^{e+1} = \begin{Bmatrix} -sin\phi_{e+1} \\ cos\phi_{e+1} \end{Bmatrix} \tag{3.50}$$

Thus, the transformation matrix $\mathbf{T}_{\chi s}$ is

$$\mathbf{T}_{\chi s} = \begin{bmatrix} [\mathbf{n}^{e-1}]^T & \mathbf{0} & \mathbf{0} & \mathbf{0} \\ \mathbf{0} & [\mathbf{n}^{e-1}]^T & \mathbf{0} & \mathbf{0} \\ \mathbf{0} & \mathbf{0} & [\mathbf{n}^{e+1}]^T & \mathbf{0} \\ \mathbf{0} & \mathbf{0} & \mathbf{0} & [\mathbf{n}^{e+1}]^T \end{bmatrix} \tag{3.51}$$

The circumferential curvature χ_θ is expressed as

$$\chi_\theta = \frac{-cos\phi}{r}\frac{\partial w'}{\partial x'} \tag{3.52}$$

where $\frac{\partial w'}{\partial x'}$ can be evaluated as

$$\frac{\partial w'}{\partial x'}\Big|_{i+1}^{i} = \frac{w'^{e}_{i+1} - w'^{e}_{i}}{l^e} = \frac{1}{l^e}[-1, 1]\begin{Bmatrix} w'^{e}_{i} \\ w'^{e}_{i+1} \end{Bmatrix} \tag{3.53}$$

Substituting equation (3.53) into (3.52), yields

$$\chi_\theta = \frac{-cos\phi}{r}\frac{1}{l^e}[-1, 1]\begin{Bmatrix} w'^{e}_{i} \\ w'^{e}_{i+1} \end{Bmatrix} \tag{3.54}$$

and the curvature matrix $\mathbf{B}'_{\chi\theta}$ is expressed as

$$\mathbf{B}'_{\chi\theta} = \frac{-cos\phi}{r}\frac{1}{l^e}[-1, 1] \tag{3.55}$$

The global curvature matrix $\mathbf{B}_{\chi\theta}$ is expressed as

$$\mathbf{B}_{\chi\theta} = \mathbf{B}'_{\chi\theta}\mathbf{T}_{\chi\theta} \tag{3.56}$$

where the corresponding transformation matrix $T_{\chi\theta}$ is

$$\mathbf{T}_{\chi\theta} = \begin{bmatrix} \mathbf{0} & [\mathbf{n}^e]^T & \mathbf{0} & \mathbf{0} \\ \mathbf{0} & \mathbf{0} & [\mathbf{n}^e]^T & \mathbf{0} \end{bmatrix} \tag{3.57}$$

The membrane strain λ_s is expressed as

$$\lambda_s = \frac{\partial u'}{\partial x'} \tag{3.58}$$

where $\frac{\partial u'}{\partial x'}$ can be evaluated as

$$\frac{\partial u'}{\partial x'} = \frac{u'^{e}_{i+1} - u'^{e}_{i}}{l^e} = \frac{1}{l^e}[-1, 1]\begin{Bmatrix} u'^{e}_{i} \\ u'^{e}_{i+1} \end{Bmatrix} \tag{3.59}$$

where the curvature matrix $\mathbf{B}'_{\lambda s}$ is

$$\mathbf{B}'_{\lambda s} = \frac{1}{l^e}[-1, 1] \tag{3.60}$$

The global curvature matrix $\mathbf{B}'_{\lambda s}$ is expressed as

$$\mathbf{B}_{\lambda s} = \mathbf{B}'_{\lambda s}\mathbf{T}_{\lambda s} \tag{3.61}$$

The global matrix $\mathbf{T}_{\lambda s}$ is evaluated in the same manner, considering that

$$u'^{e}_{i} = u_i cos\phi_e + w_i sin\phi_e \tag{3.62a}$$

$$u'^{e}_{i+1} = u_{i+1} cos\phi_e + w_{i+1} sin\phi_e \tag{3.62b}$$

where

$$\mathbf{t}^e = \begin{Bmatrix} cos\phi_e \\ sin\phi_e \end{Bmatrix} \tag{3.63}$$

Thus, the transformation matrix $\mathbf{T}_{\lambda s}$ is expressed as

$$\mathbf{T}_{\lambda s} = \begin{bmatrix} \mathbf{0} & [\mathbf{t}^e]^T & \mathbf{0} & \mathbf{0} \\ \mathbf{0} & \mathbf{0} & [\mathbf{t}^e]^T & \mathbf{0} \end{bmatrix} \tag{3.64}$$

The membrane strain λ_θ is expressed as

$$\lambda_\theta = \frac{u}{r} = \left[\frac{u_{i+1} + u_i}{r_c}\right] \tag{3.65}$$

where $r_c = \frac{r_i + r_{i+1}}{2}$ without necessity for transformation, where

$$\mathbf{B}_{\lambda\theta} = \frac{1}{2r_c}[0, 0, 1, 0, 1, 0, 0, 0] \tag{3.66}$$

3.4.1a Imposition of the boundary conditions

The various types of boundary conditions are considered: free and simply supported edges as well as clamped edges, taking into account the side of the imposed boundary condition. The only change, for each case is the curvature matrix $\mathbf{B'}_{\chi s}$, being developed from the curvature corresponding to each case separately.

3.4.1.2 Free or simply supported edge on the left end

The control domain contains an element with a free or simply supported node on the left end, as presented in Figure 3.5.

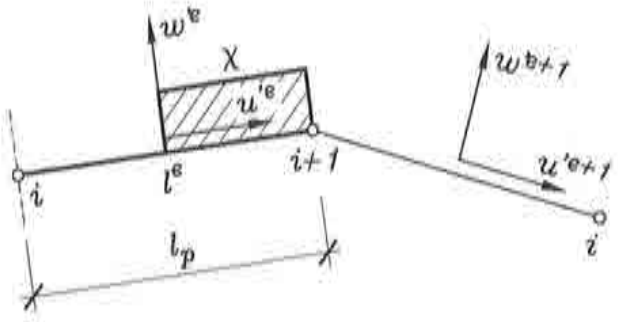

Figure 3.5 Control domain with free or simply supported node on the left end.

The radial curvature is expressed as the difference of the first derivative displacements of the element nodes $(\frac{\partial w'}{\partial x'})_{i+1}$ and $(\frac{\partial w'}{\partial x'})_i$

$$\chi_s^p \frac{l^e}{2} = (\frac{\partial w'}{\partial x'})_{i+1} - (\frac{\partial w'}{\partial x'})_i \tag{3.67}$$

Using the theory of distributions, the values $(\frac{\partial w'}{\partial x'})_{i+1}$ and $(\frac{\partial w'}{\partial x'})_i$ across the boundary should be given as an average value as follows

$$(\frac{\partial w'}{\partial x'})_{i+1} = \frac{1}{2}\Big[\frac{\partial w'}{\partial x'}\Big|_{i+1}^{i} + \frac{\partial w'}{\partial x'}\Big|_{i+1}^{i+2}\Big] = \frac{1}{2}\Big[\frac{w'^e_{i+1} - w'^e_i}{l^e} + \frac{w'^{e+1}_{i+2} - w'^{e+1}_{i+1}}{l^{e+1}}\Big] \tag{3.68}$$

$$(\frac{\partial w'}{\partial x'})_i = \frac{1}{2}\Big[\frac{\partial w'}{\partial x'}\Big|_{i}^{i-1} + \frac{\partial w'}{\partial x'}\Big|_{i}^{i}\Big] = \frac{1}{2}\Big[\frac{w'^e_{i+1} - w'^e_i}{l^e} 2\Big] \tag{3.69}$$

Substituting the last two equations into (3.67), yields

$$\chi_s^p = \frac{1}{l^{e2} l^{e+1}}[l^{e+1}, -l^{e+1}, -l^e, l^e] \begin{Bmatrix} w'^e_i \\ w'^e_{i+1} \\ w'^{e+1}_{i+1} \\ w'^{e+1}_{i+2} \end{Bmatrix} = \mathbf{B'}_{\chi s} \mathbf{w'} \tag{3.70}$$

where the curvature matrix $\mathbf{B'}_{\chi s}$ is

$$\mathbf{B'}_{\chi s} = \frac{1}{l^{e2} l^{e+1}}[l^{e+1}, -l^{e+1}, -l^e, l^e] \tag{3.71}$$

The global curvature matrix $\mathbf{B}_{\chi s}$ is expressed as

$$\mathbf{B}_{\chi s} = \mathbf{B'}_{\chi s}\mathbf{T}_{\chi s} \tag{3.72}$$

where the transformation matrix $\mathbf{T}_{\chi s}$ is

$$\mathbf{T}_{\chi s} = \begin{bmatrix} \mathbf{0} & [\mathbf{n}^e]^T & \mathbf{0} & \mathbf{0} \\ \mathbf{0} & \mathbf{0} & [\mathbf{n}^e]^T & \mathbf{0} \\ \mathbf{0} & \mathbf{0} & [\mathbf{n}^{e+1}]^T & \mathbf{0} \\ \mathbf{0} & \mathbf{0} & \mathbf{0} & [\mathbf{n}^{e+1}]^T \end{bmatrix} \tag{3.73}$$

The corresponding expressions for the matrices $\mathbf{B}_{\chi\theta}, \mathbf{B}_{\lambda_s}$ and $\mathbf{B}_{\lambda_\theta}$ are the same as for the general case, expressed by equations (3.56), (3.61) and (3.66), respectively.

3.4.1.3 Free or simply supported edge on the right end

The control domain contains an element with a free or simply supported node on the right end, as presented in Figure 3.6.

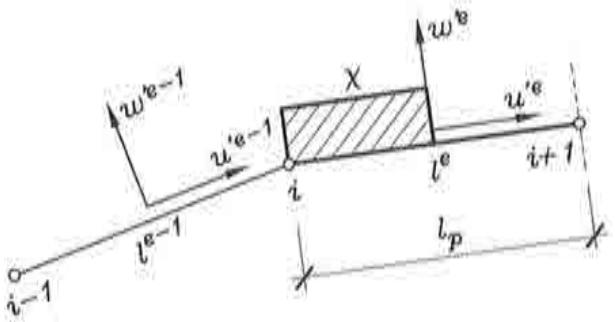

Figure 3.6 Control domain for with or simply supported node on the right end.

The radial curvature is expressed as the difference of the first derivative displacements of the element nodes $(\frac{\partial w'}{\partial x'})_{i+1}$ and $(\frac{\partial w'}{\partial x'})_i$

$$\chi_s^p \frac{l^e}{2} = (\frac{\partial w'}{\partial x'})_{i+1} - (\frac{\partial w'}{\partial x'})_i \tag{3.74}$$

Using the theory of distributions, the values $(\frac{\partial w'}{\partial x'})_{i+1}$ and $(\frac{\partial w'}{\partial x'})_i$ across the boundary should be given as an average value as follows

$$(\frac{\partial w'}{\partial x'})_{i+1} = \frac{1}{2}\Big[\frac{\partial w'}{\partial x'}\Big|_{i+1}^{i} + \frac{\partial w'}{\partial x'}\Big|_{i+1}^{i+2}\Big] = \frac{1}{2}\Big[2\frac{w'^{e}_{i+1} - w'^{e}_{i}}{l^{e}}\Big] \tag{3.75}$$

$$(\frac{\partial w'}{\partial x'})_{i} = \frac{1}{2}\Big[\frac{\partial w'}{\partial x'}\Big|_{i}^{i-1} + \frac{\partial w'}{\partial x'}\Big|_{i}^{i}\Big] = \frac{1}{2}\Big[\frac{w'^{e-1}_{i} - w'^{e-1}_{i-1}}{l^{e-1}} + \frac{w'^{e}_{i+1} - w'^{e}_{i}}{l^{e}}\Big] \tag{3.76}$$

Substituting the last two equations into (3.74), yields

$$\chi_s^p = \frac{1}{l^{e2}l^{e-1}}[l^e, -l^e, -l^{e-1}, l^{e-1}] \begin{Bmatrix} w'^{e-1}_{i-1} \\ w'^{e-1}_{i} \\ w'^{e}_{i} \\ w'^{e}_{i+1} \end{Bmatrix} = \mathbf{B'}_{\chi s}\mathbf{w'} \tag{3.77}$$

where the curvature matrix $\mathbf{B'}_{\chi s}$ is

$$\mathbf{B'}_{\chi s} = \frac{1}{l^{e2}l^{e-1}}[l^e, -l^e, -l^{e-1}, l^{e-1}] \tag{3.78}$$

The global curvature matrix $\mathbf{B}_{\chi s}$ is expressed as

$$\mathbf{B}_{\chi s} = \mathbf{B'}_{\chi s}\mathbf{T}_{\chi s} \tag{3.79}$$

where the transformation matrix $\mathbf{T}_{\chi s}$ is

$$\mathbf{T}_{\chi s} = \begin{bmatrix} [\mathbf{n}^{e-1}]^T & \mathbf{0} & \mathbf{0} & \mathbf{0} \\ \mathbf{0} & [\mathbf{n}^{e-1}]^T & \mathbf{0} & \mathbf{0} \\ \mathbf{0} & [\mathbf{n}^{e}]^T & \mathbf{0} & \mathbf{0} \\ \mathbf{0} & \mathbf{0} & [\mathbf{n}^{e}]^T & \mathbf{0} \end{bmatrix} \tag{3.80}$$

The corresponding expressions for the matrices $\mathbf{B}_{\chi\theta}, \mathbf{B}_{\lambda_s}$ and $\mathbf{B}_{\lambda_\theta}$ are the same as for the general case, expressed by equations (3.56), (3.61) and (3.66), respectively.

3.4.1.4 Clamped edge on the left end

The control domain includes an element with a clamped node on the left end, as presented in Figure 3.7.

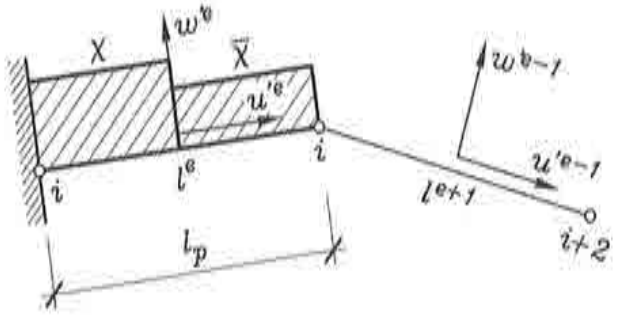

Figure 3.7 Control domain with clamped node on the left end.

The radial curvature χ_s^p is expressed as follows

$$\chi_s^p = \frac{1}{\frac{l^e}{2}}\left[\frac{w'^e_{i+1} - w'^e_i}{l^e}\right] = \frac{2}{l^{p2}}[-1,1]\begin{Bmatrix} w'^e_i \\ w'^e_{i+1} \end{Bmatrix} = \mathbf{B'}_{\chi s}\mathbf{w'} \tag{3.81}$$

where the curvature matrix $\mathbf{B'}_{\chi s}$ is

$$\mathbf{B'}_{\chi s} = \frac{2}{l^{p2}}[-1,1] \tag{3.82}$$

The global curvature matrix $\mathbf{B}_{\chi s}$ is expressed as

$$\mathbf{B}_{\chi s} = \mathbf{B'}_{\chi s}\mathbf{T}_{\chi s} \tag{3.83}$$

where the transformation matrix $\mathbf{T}_{\chi s}$ is

$$\mathbf{T}_{\chi s} = \begin{bmatrix} \mathbf{0} & [\mathbf{n}^e]^T & \mathbf{0} & \mathbf{0} \\ \mathbf{0} & \mathbf{0} & [\mathbf{n}^e]^T & \mathbf{0} \end{bmatrix} \tag{3.84}$$

The radial curvature $\bar{\chi}_s^p$ is expressed as

$$\bar{\chi}_s^p = \frac{1}{\frac{l^e}{2}}\left[\frac{1}{2}\left[\frac{w'^e_{i+1} - w'^e_i}{l^e} + \frac{w'^{e+1}_{i+2} - w'^{e+1}_{i+1}}{l^{e+1}}\right] - \frac{w'^e_{i+1} - w'^e_i}{l^e}\right] =$$

$$= \frac{1}{l^{e2}l^{e+1}}[l^{e+1}, -l^{e+1}, -l^e, l^e] \begin{Bmatrix} w'^e_i \\ w'^e_{i+1} \\ w'^{e+1}_{i+1} \\ w'^{e+1}_{i+2} \end{Bmatrix} = \bar{\mathbf{B}}'_{\chi s}\mathbf{w}' \tag{3.85}$$

where the curvature matrix $\bar{\mathbf{B}}'_{\chi s}$ is

$$\bar{\mathbf{B}}'_{\chi s} = \frac{1}{l^{e2}l^{e+1}}[l^{e+1}, -l^{e+1}, -l^e, l^e] \tag{3.86}$$

The global curvature matrix $\bar{\mathbf{B}}_{\chi s}$ is expressed as

$$\bar{\mathbf{B}}_{\chi s} = \bar{\mathbf{B}}'_{\chi s}\bar{\mathbf{T}}_{\chi s} \tag{3.87}$$

where the transformation matrix $\bar{\mathbf{T}}_{\chi s}$ is

$$\bar{\mathbf{T}}_{\chi s} = \begin{bmatrix} \mathbf{0} & [\mathbf{n}^e]^T & \mathbf{0} & \mathbf{0} \\ \mathbf{0} & \mathbf{0} & [\mathbf{n}^e]^T & \mathbf{0} \\ \mathbf{0} & \mathbf{0} & [\mathbf{n}^{e+1}]^T & \mathbf{0} \\ \mathbf{0} & \mathbf{0} & \mathbf{0} & [\mathbf{n}^{e+1}]^T \end{bmatrix} \tag{3.88}$$

The corresponding expressions for the matrices $\mathbf{B}_{\chi\theta}, \mathbf{B}_{\lambda_s}$ and $\mathbf{B}_{\lambda\theta}$ are the same as for the general case, expressed by equations (3.56), (3.61) and (3.66), respectively.

3.4.1.5 Clamped edge on the right end

The control domain includes an element with a clamped node on the right end, as presented in Figure 3.8.

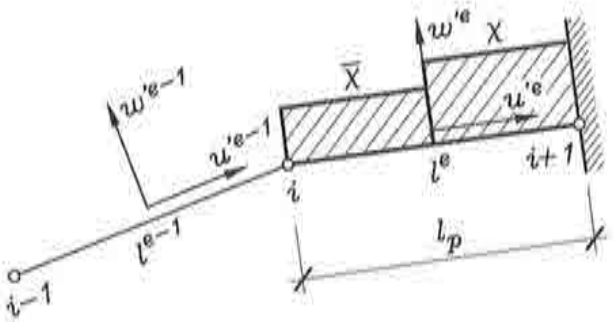

Figure 3.8 Control domain with clamped node on the right end.

The radial curvature χ_s^p is expressed as

$$\chi_s^p = -\frac{1}{\frac{l^e}{2}}\left[\frac{w'^e_{i+1} - w'^e_i}{l^e}\right] = -\frac{2}{l^{e2}}[-1, 1]\left\{\begin{array}{c} w'^e_i \\ w'^e_{i+1} \end{array}\right\} = \mathbf{B'}_{\chi s}\mathbf{w'} \tag{3.89}$$

where the curvature matrix $\mathbf{B'}_{\chi s}$ is

$$\mathbf{B'}_{\chi s} = \frac{2}{l^{e2}}[-1, 1] \tag{3.90}$$

The global curvature matrix $\mathbf{B}_{\chi s}$ is expressed as

$$\mathbf{B}_{\chi s} = \mathbf{B'}_{\chi s}\mathbf{T}_{\chi s} \tag{3.91}$$

where the transformation matrix $\mathbf{T}_{\chi s}$ is

$$\mathbf{T}_{\chi s} = \begin{bmatrix} \mathbf{0} & [\mathbf{n}^e]^T & \mathbf{0} & \mathbf{0} \\ \mathbf{0} & \mathbf{0} & [\mathbf{n}^e]^T & \mathbf{0} \end{bmatrix} \tag{3.92}$$

The radial curvature $\bar{\chi}_s^p$ is expressed as

$$\bar{\chi}_s^p = \frac{1}{\frac{l^e}{2}}\left[\frac{1}{2}\left[\frac{w'^e_{i+1} - w'^e_i}{l^e} + \frac{w'^{e-1}_i - w'^{e-1}_{i-1}}{l^{e-1}}\right] - \frac{w'^e_{i+1} - w'^e_i}{l^e}\right] =$$

$$= \frac{1}{l^{e2}l^{e-1}}[l^e, -l^e, -l^{e-1}, l^{e-1}]\left\{\begin{array}{c} w'^{e-1}_{i-1} \\ w'^{e-1}_i \\ w'^e_i \\ w'^e_{i+1} \end{array}\right\} = \bar{\mathbf{B}}'_{\chi s}\mathbf{w'} \tag{3.93}$$

where the curvature matrix $\bar{\mathbf{B}}'_{\chi s}$ is

$$\bar{\mathbf{B}}'_{\chi s} = \frac{1}{l^{e2}l^{e-1}}[l^e, -l^e, -l^{e-1}, l^{e-1}] \tag{3.94}$$

The global curvature matrix $\bar{\mathbf{B}}_{\chi s}$ is expressed as

$$\bar{\mathbf{B}}_{\chi s} = \bar{\mathbf{B}}'_{\chi s}\bar{\mathbf{T}}_{\chi s} \tag{3.95}$$

where the transformation matrix $\bar{\mathbf{T}}_{\chi s}$ is

$$\bar{\mathbf{T}}_{\chi s} = \begin{bmatrix} [\mathbf{n}^{e-1}]^T & \mathbf{0} & \mathbf{0} & \mathbf{0} \\ \mathbf{0} & [\mathbf{n}^{e-1}]^T & \mathbf{0} & \mathbf{0} \\ \mathbf{0} & [\mathbf{n}^{e}]^T & \mathbf{0} & \mathbf{0} \\ \mathbf{0} & \mathbf{0} & [\mathbf{n}^{e}]^T & \mathbf{0} \end{bmatrix} \tag{3.96}$$

The corresponding expressions for the matrices $\mathbf{B}_{\chi\theta}, \mathbf{B}_{\lambda_s}$ and $\mathbf{B}_{\lambda_\theta}$ are the same as for the general case, expressed by equations (3.56), (3.61) and (3.66), respectively.

3.4.2 Cell Vertex scheme - ACV axisymmetric shell element

The corresponding matrices $\mathbf{B}'_p$ for radial and circumferential curvatures as well as for the axial and circumferential elongations are defined in the local nodal axes. A transformation from the nodal to global axes is performed with the corresponding matrices of transformation $\mathbf{T}$ for assembly.

3.4.2.1 General case

The control domain for the ACV element is presented in Figure 3.9. The boundary conditions are not applied. Each of the patch elements has two local corresponding displacements u' and w'.

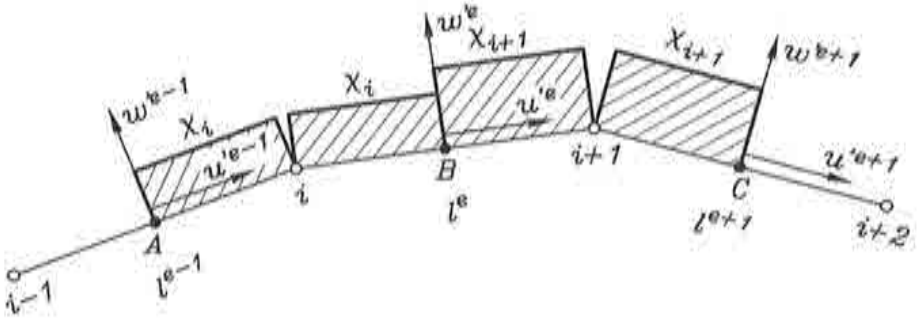

Figure 3.9 The patch for general case.

The curvature is expressed in each element node, thus the stiffness matrix $\mathbf{K}_p$ is expressed as

$$\mathbf{K}_p = 2\pi \frac{l_p^e}{2} [\mathbf{B}_{1p}^T \mathbf{D}_p \mathbf{B}_{1p} r_1 + \mathbf{B}_{2p}^T \mathbf{D}_p \mathbf{B}_{2p} r_2] \tag{3.97}$$

The radial curvature of the node i is

$$\chi_i = \frac{2}{l^{e-1}+l^e}\Big[\frac{\partial w'}{\partial x'}\Big|_B - \frac{\partial w'}{\partial x'}\Big|_A\Big] \tag{3.98}$$

or in rewritten form is

$$\chi_i = \frac{2}{l^{e-1}+l^e}\Big[\frac{w'^e_{i+1}-w'^e_i}{l^e} - \frac{w'^{e-1}_i - w'^{e-1}_{i-1}}{l^{e-1}}\Big] =$$

$$= \frac{2}{l^e l^{e-1}(l^{e-1}+l^e)}\Big[l^e, -l^e, -l^{e-1}, l^{e-1}\Big]\begin{Bmatrix} w'^{e-1}_{i-1} \\ w'^{e-1}_i \\ w'^e_i \\ w'^e_{i+1}\end{Bmatrix} = \mathbf{B'}_{\chi s1}\mathbf{w'} \tag{3.99}$$

where the curvature matrix $\mathbf{B'}_{\chi s1}$ is

$$\mathbf{B'}_{\chi s1} = \frac{2}{l^e l^{e-1}(l^{e-1}+l^e)}\Big[l^e, -l^e, -l^{e-1}, l^{e-1}\Big] \tag{3.100}$$

The global curvature matrix $\mathbf{B}_{\chi s1}$ is expressed as

$$\mathbf{B}_{\chi s1} = \mathbf{B'}_{\chi s1}\mathbf{T}_{\chi s1} \tag{3.101}$$

where the transformation matrix $\mathbf{T}_{\chi s1}$ is

$$\mathbf{T}_{\chi s1} = \begin{bmatrix} [\mathbf{n}^{e-1}]^T & \mathbf{0} & \mathbf{0} & \mathbf{0} \\ \mathbf{0} & [\mathbf{n}^{e-1}]^T & \mathbf{0} & \mathbf{0} \\ \mathbf{0} & [\mathbf{n}^e]^T & \mathbf{0} & \mathbf{0} \\ \mathbf{0} & \mathbf{0} & [\mathbf{n}^e]^T & \mathbf{0} \end{bmatrix} \tag{3.102}$$

The radial curvature of the node $i+1$ is

$$\chi_{i+1} = \frac{2}{l^e+l^{e+1}}\Big[\frac{\partial w'}{\partial x'}\Big|_C - \frac{\partial w'}{\partial x'}\Big|_B\Big] \tag{3.103}$$

or in rewritten form is

$$\chi_{i+1} = \frac{2}{l^e+l^{e+1}}\Big[\frac{w'^{e+1}_{i+2}-w'^{e+1}_{i+1}}{l^{e+1}} - \frac{w'^e_{i+1}-w'^e_i}{l^e}\Big] =$$

$$= \frac{2}{l^e l^{e+1}(l^e + l^{e+1})}\left[l^{e+1}, -l^{e+1}, -l^e, l^e\right]\begin{Bmatrix} w'^e_i \\ w'^e_{i+1} \\ w'^{e+1}_{i+1} \\ w'^{e+1}_{i+2} \end{Bmatrix} = \mathbf{B'}_{\chi s2}\mathbf{w'} \tag{3.104}$$

where the curvature matrix $\mathbf{B'}_{\chi s2}$ is

$$\mathbf{B'}_{\chi s2} = \frac{2}{l^e l^{e+1}(l^e + l^{e+1})}\left[l^{e+1}, -l^{e+1}, -l^e, l^e\right] \tag{3.105}$$

The global curvature matrix $\mathbf{B}_{\chi s2}$ is expressed as

$$\mathbf{B}_{\chi s2} = \mathbf{B'}_{\chi s2}\mathbf{T}_{\chi s2} \tag{3.106}$$

where the transformation matrix $\mathbf{T}_{\chi s2}$ is

$$\mathbf{T}_{\chi s2} = \begin{bmatrix} \mathbf{0} & [\mathbf{n}^e]^T & \mathbf{0} & \mathbf{0} \\ \mathbf{0} & \mathbf{0} & [\mathbf{n}^e]^T & \mathbf{0} \\ \mathbf{0} & \mathbf{0} & [\mathbf{n}^{e+1}]^T & \mathbf{0} \\ \mathbf{0} & \mathbf{0} & \mathbf{0} & [\mathbf{n}^{e+1}]^T \end{bmatrix} \tag{3.107}$$

The circumferential curvature χ_θ is expressed as

$$\chi_\theta = \frac{-cos\phi}{r}\frac{\partial w'}{\partial x'} \tag{3.108}$$

where $\frac{\partial w'}{\partial x'}$ can be evaluated as

$$\frac{\partial w'}{\partial x'}\Big|^i_{i+1} = \frac{w'^e_{i+1} - w'^e_i}{l^e} = \frac{1}{l^e}[-1, 1]\begin{Bmatrix} w'^e_i \\ w'^e_{i+1} \end{Bmatrix} \tag{3.109}$$

Substituting equation (3.109) into (3.108), yields

$$\chi_{\theta 1} = \frac{-cos\phi}{r_1}\frac{1}{l^e}[-1, 1]\begin{Bmatrix} w'^e_i \\ w'^e_{i+1} \end{Bmatrix} \tag{3.110}$$

where the curvature $\mathbf{B'}_{\chi\theta 1}$ is expressed as

$$\mathbf{B'}_{\chi\theta 1} = \frac{1}{r_1 l^e}[-1, 1] \tag{3.111}$$

The global curvature matrix $\mathbf{B}_{\chi\theta 1}$ is expressed as

$$\mathbf{B}_{\chi\theta 1} = \mathbf{B'}_{\chi\theta 1}\mathbf{T}_{\chi\theta 1} \tag{3.112}$$

where the corresponding transformation matrix $T_{\theta 1}$ is

$$\mathbf{T}_{\chi\theta 1} = \begin{bmatrix} \mathbf{0} & [\mathbf{n}^e]^T & \mathbf{0} & \mathbf{0} \\ \mathbf{0} & \mathbf{0} & [\mathbf{n}^e]^T & \mathbf{0} \end{bmatrix} \tag{3.113}$$

and

$$\chi_{\theta 2} = \frac{-cos\phi}{r_2}\frac{1}{l^e}[-1, 1]\begin{Bmatrix} w'^e \\ w'^e_{i+1} \end{Bmatrix} \tag{3.114}$$

where the curvature matrix $\mathbf{B'}_{\chi\theta 2}$ is expressed as

$$\mathbf{B'}_{\chi\theta 2} = \frac{1}{r_2 l^e}[-1, 1] \tag{3.115}$$

The global curvature matrix $\mathbf{B}_{\chi\theta 2}$ is expressed as

$$\mathbf{B}_{\chi\theta 2} = \mathbf{B'}_{\chi\theta 2}\mathbf{T}_{\chi\theta 2} \tag{3.116}$$

where the corresponding transformation matrix $\mathbf{T}_{\theta 2}$ is

$$\mathbf{T}_{\chi\theta 2} = \begin{bmatrix} \mathbf{0} & [\mathbf{n}^e]^T & \mathbf{0} & \mathbf{0} \\ \mathbf{0} & \mathbf{0} & [\mathbf{n}^e]^T & \mathbf{0} \end{bmatrix} \tag{3.117}$$

The membrane strain λ_s is expressed as

$$\lambda_s = \frac{\partial u'}{\partial x'} \tag{3.118}$$

where $\frac{\partial u'}{\partial x'}$ can be evaluated as

$$\frac{\partial u'}{\partial x'} = \frac{1}{l^e}\left[\frac{u'^e_{i+1} - u'^e_i}{l^e}\right] = \frac{1}{l^e}[-1, 1]\begin{Bmatrix} u'^e_i \\ u'^e_{i+1} \end{Bmatrix} \tag{3.119}$$

where the curvature matrix $\mathbf{B'}_{\lambda s}$ is

$$\mathbf{B'}_{\lambda s} = \mathbf{B'}_{\lambda s1} = \mathbf{B'}_{\lambda s2} = \frac{1}{l^e}[-1, 1] \tag{3.120}$$

Thus, the transformation matrix $\mathbf{T}_{\lambda s}$ is expressed as

$$\mathbf{T}_{\lambda s} = \mathbf{T}_{\lambda s1} = \mathbf{T}_{\lambda s2} = \begin{bmatrix} \mathbf{0} & [\mathrm{t}^e]^T & \mathbf{0} & \mathbf{0} \\ \mathbf{0} & \mathbf{0} & [\mathrm{t}^e]^T & \mathbf{0} \end{bmatrix} \tag{3.121}$$

The global matrix $\mathbf{B'}_{\lambda s1}$ and $\mathbf{B'}_{\lambda s2}$ are expressed as

$$\mathbf{B}_{\lambda s1} = \mathbf{B'}_{\lambda s1}\mathbf{T}_{\lambda s1} \tag{1.122}$$

$$\mathbf{B}_{\lambda s2} = \mathbf{B'}_{\lambda s2}\mathbf{T}_{\lambda s2} \tag{1.123}$$

The membrane strain λ_θ is expressed as

$$\lambda_{\theta 1} = \frac{u_1}{r_1} \tag{3.124}$$

$$\lambda_{\theta 2} = \frac{u_2}{r_2} \tag{3.125}$$

where

$$u_1 = \frac{3}{4}u_i + \frac{1}{4}u_{i+1} \tag{3.126}$$

$$u_2 = \frac{1}{4}u_i + \frac{3}{4}u_{i+1} \tag{3.127}$$

thus the corresponding matrices $\mathbf{B}_{\lambda\theta 1}$ and $\mathbf{B}_{\lambda\theta 2}$ are

$$\mathbf{B}_{\lambda\theta 1} = [0, 0, \frac{3}{4r_1}, 0, \frac{1}{4r_1}, 0, 0, 0] \tag{3.128}$$

$$\mathbf{B}_{\lambda\theta 2} = [0, 0, \frac{1}{4r_2}, 0, \frac{3}{4r_2}, 0, 0, 0] \tag{3.129}$$

3.4.2a Imposition of the boundary conditions

The same types of boundary conditions are considered: free and simply supported edges as well as clamped edges, taking into account the side of the imposed boundary conditions.

3.4.2.2 Free or simply supported edge on the left end

The control domain contains an element with a free or simply supported node on the left end, as presented in Figure 3.10.

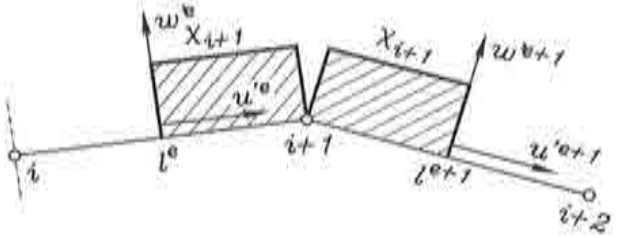

Figure 3.10 Control domain with free or simply supported node on the left end.

Because of the boundary conditions, the radial curvature for the node i is zero. Therefore the stiffness matrix expressed by equation (3.100) has only the second part, i.e.

$$\mathbf{K}_p = 2\pi \mathbf{B}_{2p}^T \mathbf{D}_p \mathbf{B}_{2p} r_2 \tag{3.130}$$

The corresponding expressions for the matrices $\mathbf{B}_{\chi s2}$, $\mathbf{B}_{\chi\theta 2}$, $\mathbf{B}_{\lambda s1}$, $\mathbf{B}_{\lambda s2}$, $\mathbf{B}_{\lambda\theta 1}$ and $\mathbf{B}_{\lambda\theta 2}$ are the same as for the general case expressed by equations (3.106), (3.116), (3.122), (3.123), (3.128) and (3.129), respectively.

3.4.2.3 Free or simply supported edge on the right end

The control domain contains an element with a free or simply supported node on the right end, as presented in Figure 3.11.

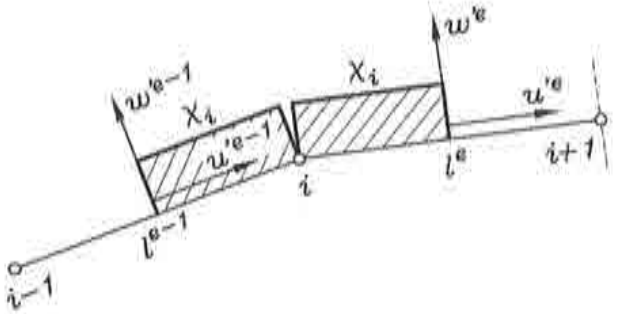

Figure 3.11 Control domain with free or simply supported node on the right end.

Because of the boundary conditions, the radial curvature for the node $i+1$ is zero. Therefore the stiffness matrix expressed by equation (3.97) has only the first part, i.e.

$$\mathbf{K}_p = 2\pi \mathbf{B}_{1p}^T \mathbf{D}_p \mathbf{B}_{1p} r_1 \tag{3.131}$$

The corresponding expressions for the matrices $\mathbf{B}_{\chi s1}$, $\mathbf{B}_{\chi\theta 1}$, $\mathbf{B}_{\lambda s1}$, $\mathbf{B}_{\lambda s2}$, $\mathbf{B}_{\lambda\theta 1}$ and $\mathbf{B}_{\lambda\theta 2}$ are the same as for the general case expressed by equations (3.101), (3.112), (3.122), (3.123), (3.128) and (3.129), respectively.

3.4.2.4 Clamped edge on the left end

The control domain includes an element with clamped node on the left end, as presented in Figure 3.12.

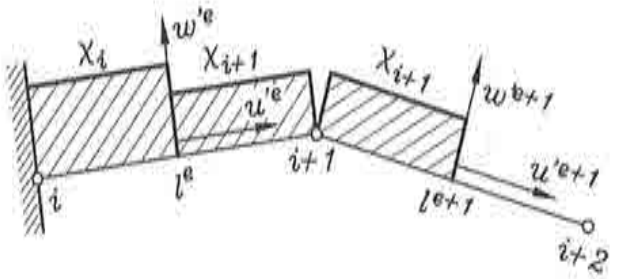

Figure 3.12 Control domain for clamped node on the left end.

The radial curvature of the node i is

$$\chi_i = \frac{2}{l^e}\left[\frac{w'^e_{i+1} - w'^e_i}{l^e}\right] = \frac{2}{l^{e2}}\left[0,-1,1,0\right]\left\{\begin{array}{c} w'^{e-1}_{i-1} \\ w'^{e-1}_{i} \\ w'^{e}_{i} \\ w'^{e}_{i+1} \end{array}\right\} = \mathbf{B'}_{\chi s1}\mathbf{w'} \tag{3.132}$$

where the curvature matrix $\mathbf{B'}_{\chi s1}$ is

$$\mathbf{B'}_{\chi s1} = \frac{2}{l^{e2}}\left[0,-1,1,0\right] \tag{3.133}$$

The global curvature matrix $\mathbf{B}_{\chi s1}$ is expressed as

$$\mathbf{B}_{\chi s1} = \mathbf{B'}_{\chi s1}\mathbf{T}_{\chi s1} \tag{3.134}$$

where the transformation matrix $\mathbf{T}_{\chi s1}$ is

$$\mathbf{T}_{\chi s1} = \begin{bmatrix} \mathbf{0} & \mathbf{0} & \mathbf{0} & \mathbf{0} \\ \mathbf{0} & [\mathbf{n}^e]^T & \mathbf{0} & \mathbf{0} \\ \mathbf{0} & \mathbf{0} & [\mathbf{n}^e]^T & \mathbf{0} \\ \mathbf{0} & \mathbf{0} & \mathbf{0} & \mathbf{0} \end{bmatrix} \tag{3.135}$$

The radial curvature of the node $i+1$ is

$$\chi_{i+1} = \frac{2}{l^e + l^{e+1}} \left[\frac{w'^{e+1}_{i+2} - w'^{e+1}_{i+1}}{l^{e+1}} - \frac{w'^{e}_{i+1} - w'^{e}_{i}}{l^e} \right] =$$

$$= \frac{2}{l^e l^{e+1}(l^e + l^{e+1})} \left[l^{e+1}, -l^{e+1}, -l^e, l^e \right] \begin{Bmatrix} w'^{e}_{i} \\ w'^{e}_{i+1} \\ w'^{e+1}_{i+1} \\ w'^{e+1}_{i+2} \end{Bmatrix} = \mathbf{B'}_{\chi s2} \mathbf{w'} \tag{3.136}$$

where the curvature matrix $\mathbf{B'}_{\chi s2}$ is

$$\mathbf{B'}_{\chi s2} = \frac{2}{l^e l^{e+1}(l^e + l^{e+1})} \left[l^{e+1}, -l^{e+1}, -l^e, l^e \right] \tag{3.137}$$

The global curvature matrix $\mathbf{B}_{\chi s2}$ is expressed as

$$\mathbf{B}_{\chi s2} = \mathbf{B'}_{\chi s2} \mathbf{T}_{\chi s2} \tag{3.138}$$

where the transformation matrix $\mathbf{T}_{\chi s2}$ is

$$\mathbf{T}_{\chi s2} = \begin{bmatrix} \mathbf{0} & [\mathbf{n}^e]^T & \mathbf{0} & \mathbf{0} \\ \mathbf{0} & \mathbf{0} & [\mathbf{n}^e]^T & \mathbf{0} \\ \mathbf{0} & \mathbf{0} & [\mathbf{n}^{e+1}]^T & \mathbf{0} \\ \mathbf{0} & \mathbf{0} & \mathbf{0} & [\mathbf{n}^{e+1}]^T \end{bmatrix} \tag{3.139}$$

The corresponding expressions for the $\mathbf{B}_{\chi\theta 1}$, $\mathbf{B}_{\chi\theta 2}$, $\mathbf{B}_{\lambda s1}$, $\mathbf{B}_{\lambda s2}$, $\mathbf{B}_{\lambda\theta 1}$ and $\mathbf{B}_{\lambda\theta 2}$ are the same as for the general case expressed by equations (3.112),(3.116), (3.122), (3.123), (3.128) and (3.129), respectively.

3.4.2.5 Clamped edge on the right end

The control domain includes an element with a clamped node on the right end, as presented in Figure 3.13.

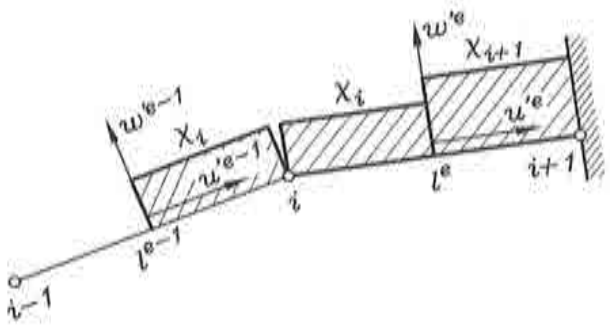

Figure 3.13 Control domain for clamped edge on the right end.

The radial curvature of the node i is

$$\chi_i = \frac{2}{l^{e-1}+l^e}\left[\frac{w'^e_{i+1}-w'^e_i}{l^e} - \frac{w'^{e-1}_i - w'^{e-1}_{i-1}}{l^{e-1}}\right] =$$

$$= \frac{2}{l^e l^{e-1}(l^{e-1}+l^e)}\left[l^e, -l^e, -l^{e-1}, l^{e-1}\right]\begin{Bmatrix} w'^{e-1}_{i-1} \\ w'^{e-1}_i \\ w'^e_i \\ w'^e_{i+1}\end{Bmatrix} = \mathbf{B}'_{\chi s1}\mathbf{w}' \qquad (3.140)$$

where the curvature matrix $\mathbf{B}'_{\chi s1}$ is

$$\mathbf{B}'_{\chi s1} = \frac{2}{l^e l^{e-1}(l^{e-1}+l^e)}\left[l^e, -l^e, -l^{e-1}, l^{e-1}\right] \qquad (3.141)$$

The global curvature matrix $\mathbf{B}_{\chi s1}$ is expressed as

$$\mathbf{B}_{\chi s1} = \mathbf{B}'_{\chi s1}\mathbf{T}_{\chi s1} \qquad (3.142)$$

where the transformation matrix $\mathbf{T}_{\chi s1}$ is

$$\mathbf{T}_{\chi s1} = \begin{bmatrix} [\mathbf{n}^{e-1}]^T & \mathbf{0} & \mathbf{0} & \mathbf{0} \\ \mathbf{0} & [\mathbf{n}^{e-1}]^T & \mathbf{0} & \mathbf{0} \\ \mathbf{0} & [\mathbf{n}^e]^T & \mathbf{0} & \mathbf{0} \\ \mathbf{0} & \mathbf{0} & [\mathbf{n}^e]^T & \mathbf{0} \end{bmatrix} \qquad (3.143)$$

The radial curvature of the node $i+1$ is

$$\chi_{i+1} = \frac{2}{l^e}\Big[\frac{w'^e_{i+1} - w'^e_i}{l^e}\Big] = \frac{2}{l^{2e}}\Big[0,-1,1,0\Big]\left\{\begin{array}{c} w'^e_i \\ w'^e_{i+1} \\ w'^{e+1}_{i+1} \\ w'^{e+1}_{i+2} \end{array}\right\} = \mathbf{B'}_{\chi s2}\mathbf{w'} \tag{3.144}$$

where the curvature matrix $\mathbf{B'}_{\chi s2}$ is

$$\mathbf{B'}_{\chi s2} = \frac{2}{l^{e2}}\Big[0,-1,1,0\Big] \tag{3.145}$$

The global curvature matrix $\mathbf{B}_{\chi s2}$ is expressed as

$$\mathbf{B}_{\chi s2} = \mathbf{B'}_{\chi s2}\mathbf{T}_{\chi s2} \tag{3.146}$$

where the transformation matrix $\mathbf{T}_{\chi s2}$ is

$$\mathbf{T}_{\chi s2} = \begin{bmatrix} \mathbf{0} & \mathbf{0} & \mathbf{0} & \mathbf{0} \\ \mathbf{0} & [\mathbf{n}^e]^T & \mathbf{0} & \mathbf{0} \\ \mathbf{0} & \mathbf{0} & [\mathbf{n}^e]^T & \mathbf{0} \\ \mathbf{0} & \mathbf{0} & \mathbf{0} & \mathbf{0} \end{bmatrix} \tag{3.147}$$

The corresponding expressions for the $\mathbf{B}_{\chi\theta 1}$, $\mathbf{B}_{\chi\theta 2}$, $\mathbf{B}_{\lambda s1}$, $\mathbf{B}_{\lambda s2}$, $\mathbf{B}_{\lambda\theta 1}$ and $\mathbf{B}_{\lambda\theta 2}$ are the same as for the general case expressed by equations (3.112),(3.116), (3.122), (3.123), (3.128) and (3.129), respectively.

3.5. NUMERICAL EXAMPLES

Several numerical examples are presented dealing with the linear analysis of axisymmetric shells.

3.5.1 Bending of circular plate under uniform load

The first test is a circular clamped plate under uniform load $p = lb/in^2$, shown in Figure 3.14. The material model is linear elastic, with the Young modulus $E = 1.0 \times 10^7 lb/in^2$ and the Poisson's ratio $\nu = 0.3$. The analysis is performed using the different uniform meshes of 10, 20 and 40 elements. The obtained results are compared with theoretical results [Z-4], for the vertical displacements and radial bending moments.

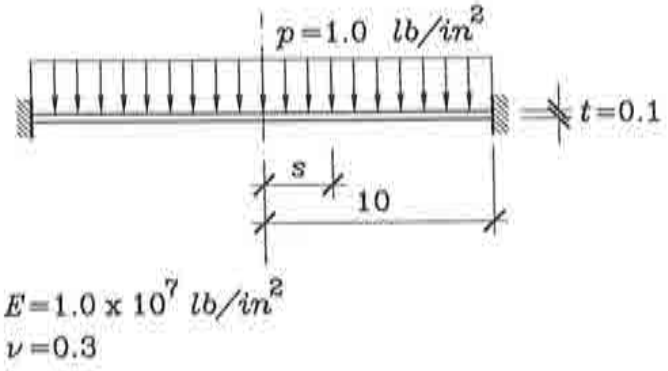

Figure 3.14 Circular plate under uniform load.

The numerical results for the center displacement obtained with the ACC and ACV elements are presented in Figures 3.15 and 3.16, respectively. The Cell Vertex scheme based element ACV demonstrates somewhat faster convergence rate.

The same kind of observation, concerning the advantageous convergence rate, can also be observed in Figures 3.17 and 3.18, where the bending moment M_x is presented.

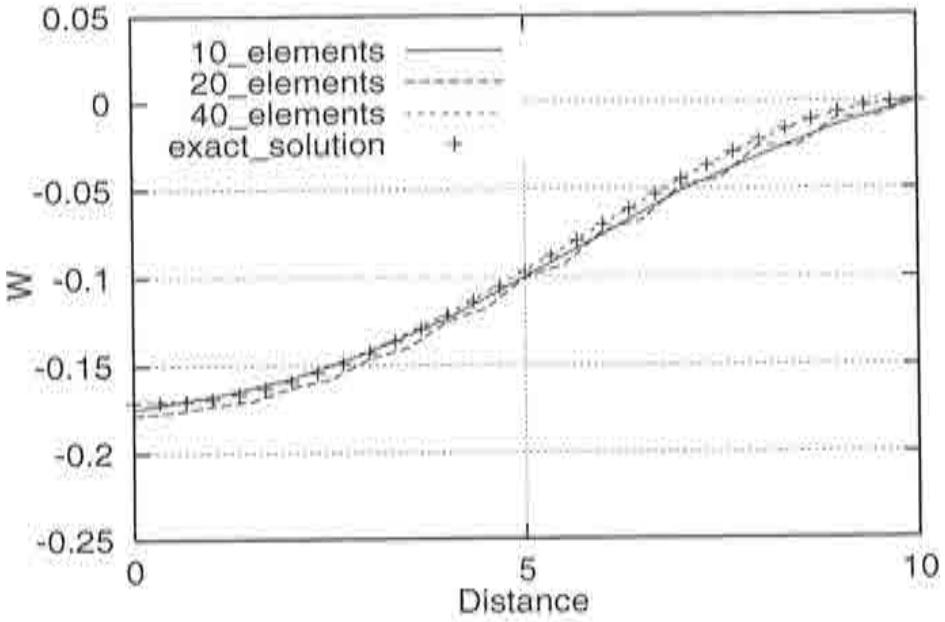

Figure 3.15 Displacement diagram for different meshes - ACC element.

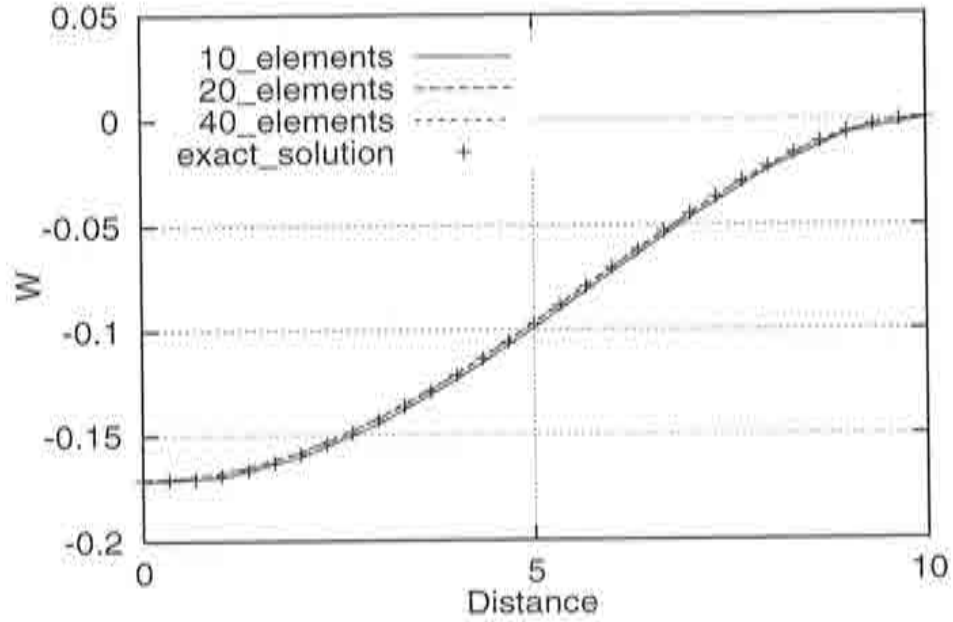

Figure 3.16 Displacement diagram for different meshes - ACV element.

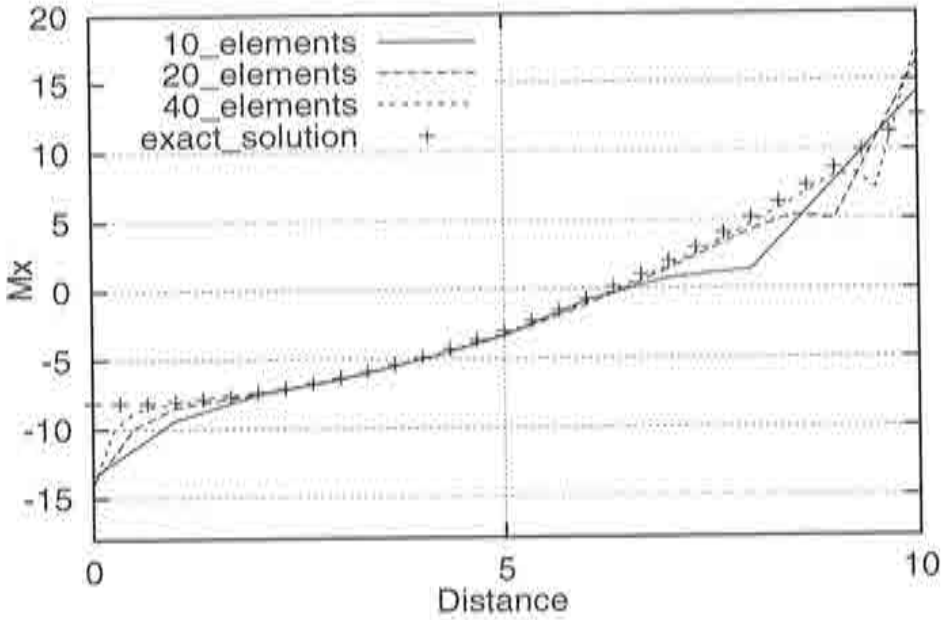

Figure 3.17 Radial moment diagram for different meshes - ACC element.

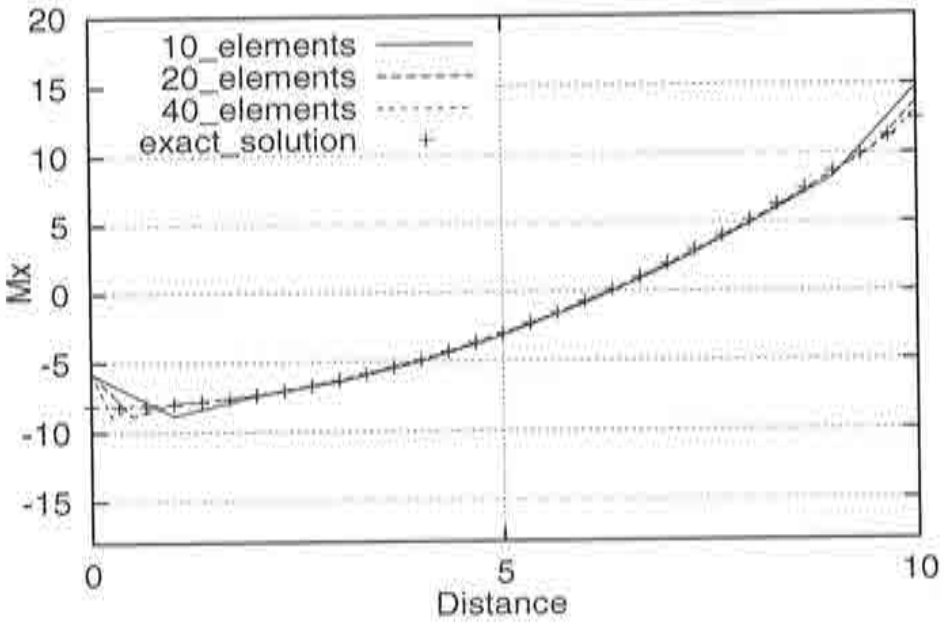

Figure 3.18 Radial moment diagram for different meshes - ACV element.

3.5.2 Spherical dome under uniform pressure

Figure 3.19 shows a spherical dome with clamped edges, under the uniform pressure of $p = 1lb/in^2$. The dome radius is $r = 90ins$ and the thickness is $t = 3ins$. The Young modulus is $E = 2 \times 10^6 lb/in^2$ and the Poisson's ratio is $\nu = \frac{1}{6}$. The analysis is carried out with the uniform meshes of 10, 20 and 40 elements. The obtained results are compared with theoretical Timoshenko results [Z-4], for the radial moments and circumferential normal forces.

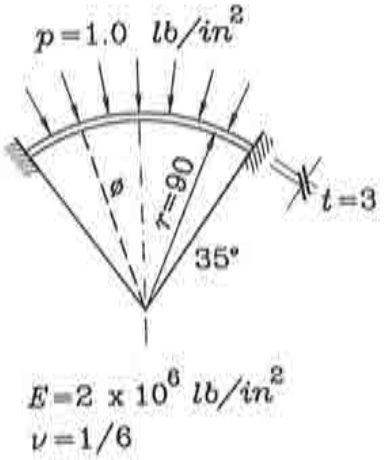

Figure 3.19 Spherical dome under uniform pressure.

The circumferential normal force diagrams obtained by the ACC and ACV elements are presented in Figures 3.20 and 3.21, respectively. It is clear that the ACV element leads to the superior result, yielding a much better representation of the analytic solution. The same accuracy is obtained with the ACC element only when the mesh is refined.

The same kind of observation can be made for the accuracy of bending moments M_x, where the significant better results are obtained with the ACV element, as shown in Figures 3.22 and 3.23, respectively.

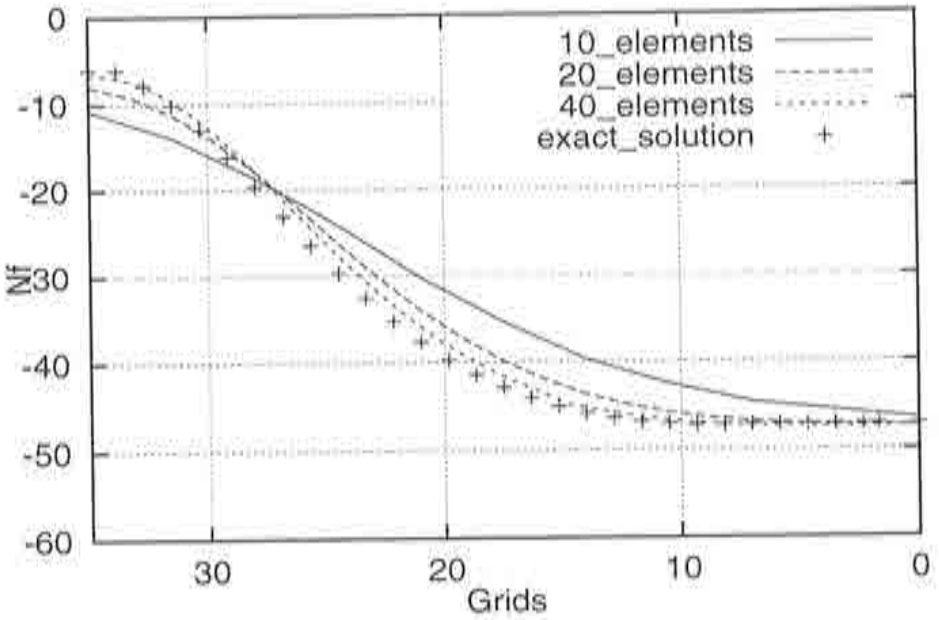

Figure 3.20 Circumferential normal forces diagram for different meshes - ACC element.

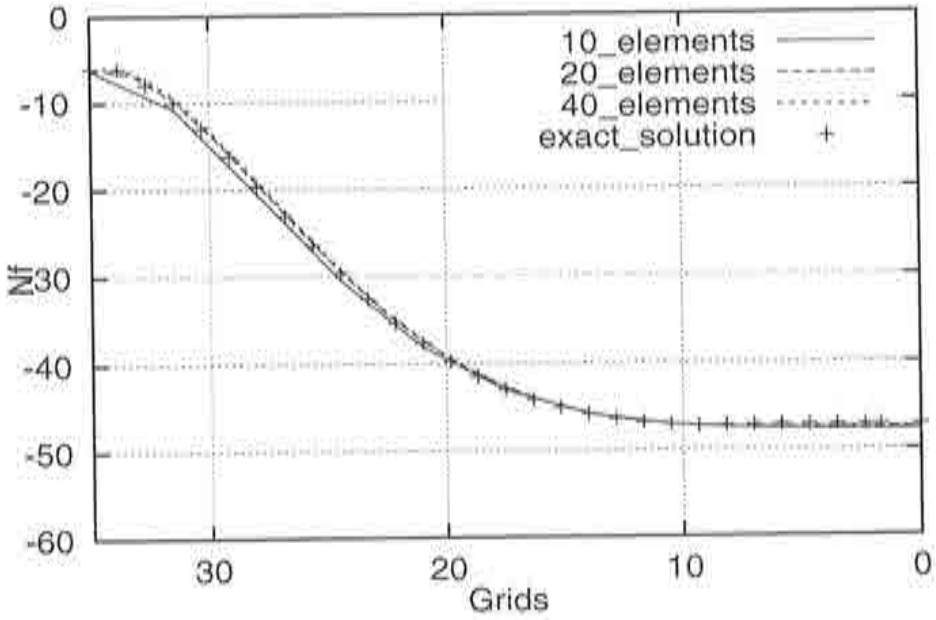

Figure 3.21 Circumferential normal forces diagram for different meshes - ACV element.

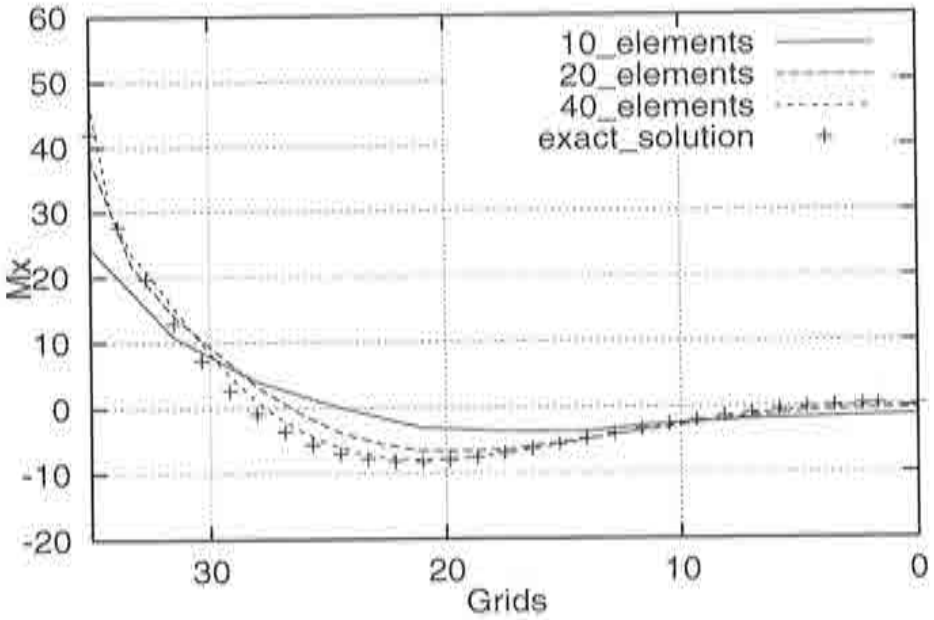

Figure 3.22 Radial moment diagram for different meshes - ACC element.

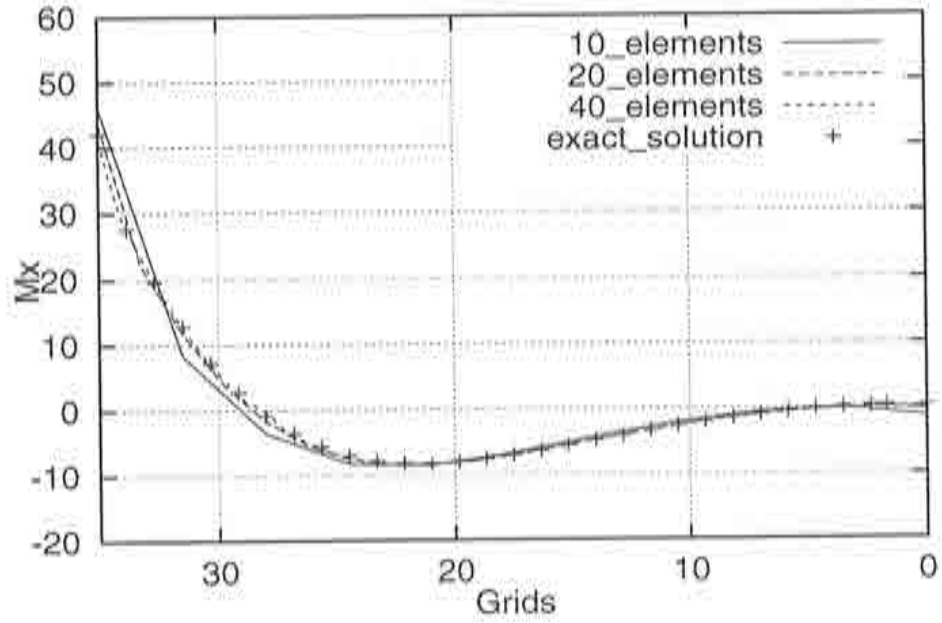

Figure 3.23 Radial moment diagram for different meshes - ACV element.

3.5.3 Toroidal shell under internal pressure

Figure 3.24 presents a toroidal shell under internal pressure of $p = 1.0 lb/in^2$. The radius has the value $r = 10 ins$ and the thickness $t = 0.5 ins$. The Young modulus is $E = 1.0^7 lb/in^2$ and the Poisson's ratio is $\nu = 0.3$. The analysis is performed with the meshes of 10, 20 and 40 elements and the obtained results for the radial displacements, axial and circumferential forces are compared with the theoretical results.

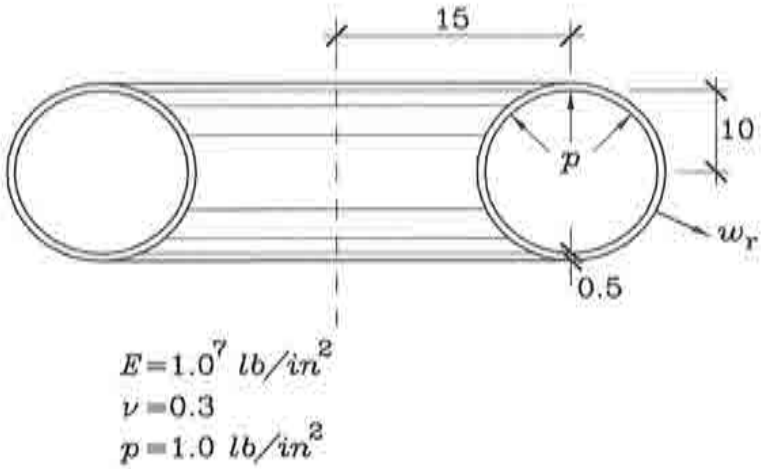

Figure 3.24 Toroidal shell under internal pressure.

The diagrams of the vertical displacement, shown in Figures 3.25 and 3.26, demonstrate that the ACV element leads to the excellent result accuracy, whereas the ACC element is significantly less accurate.

The same tendency is demonstrated in Figures 3.27, 3.28, 3.29 and 3.30, where the normal axial and circumferential forces component diagrams are presented. The coarse mesh leads to the oscillatory result at $\theta = 90^o$, with dissapearing of the mesh refinement.

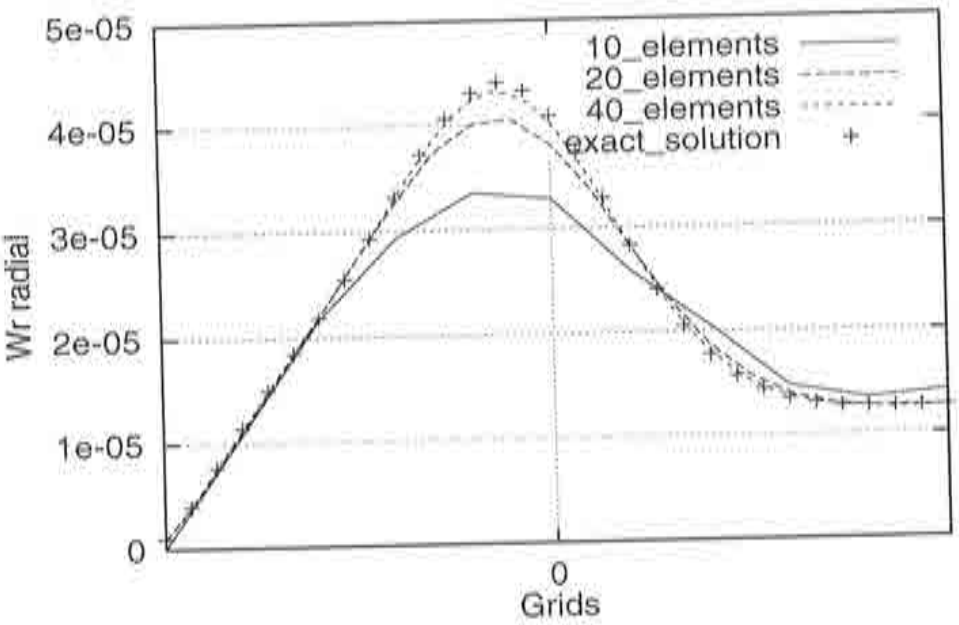

Figure 3.25 Radial displacement diagram for different meshes - ACC element.

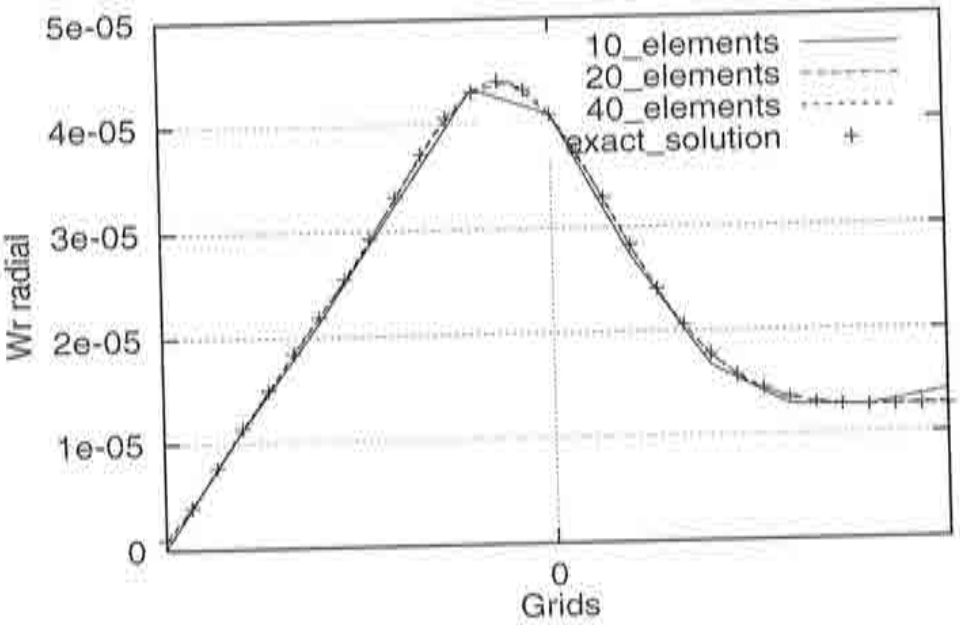

Figure 3.26 Radial displacement diagram for different meshes - ACV element.

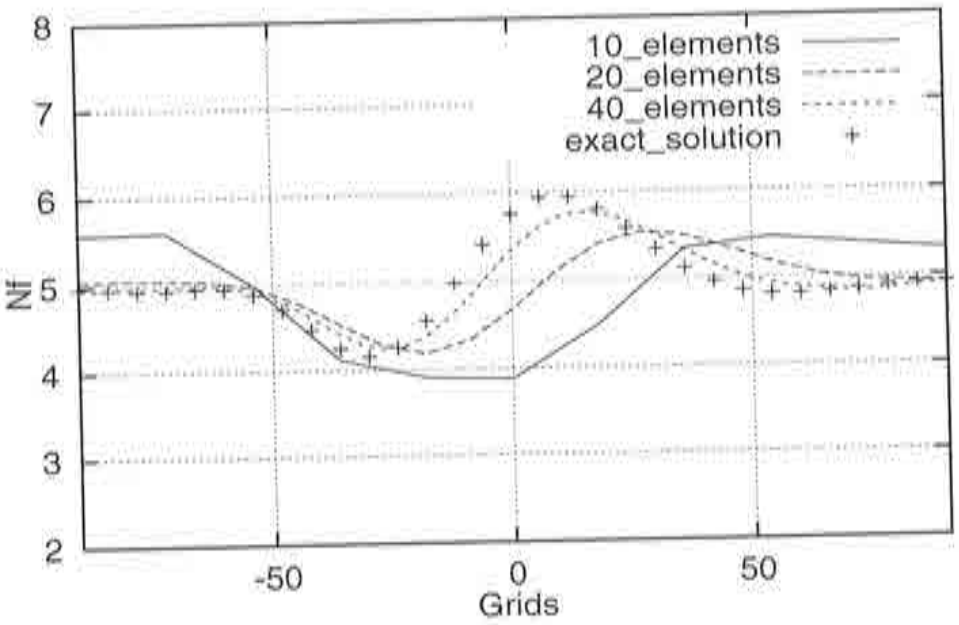

Figure 3.27 Circumferential normal forces diagram for different meshes - ACC element.

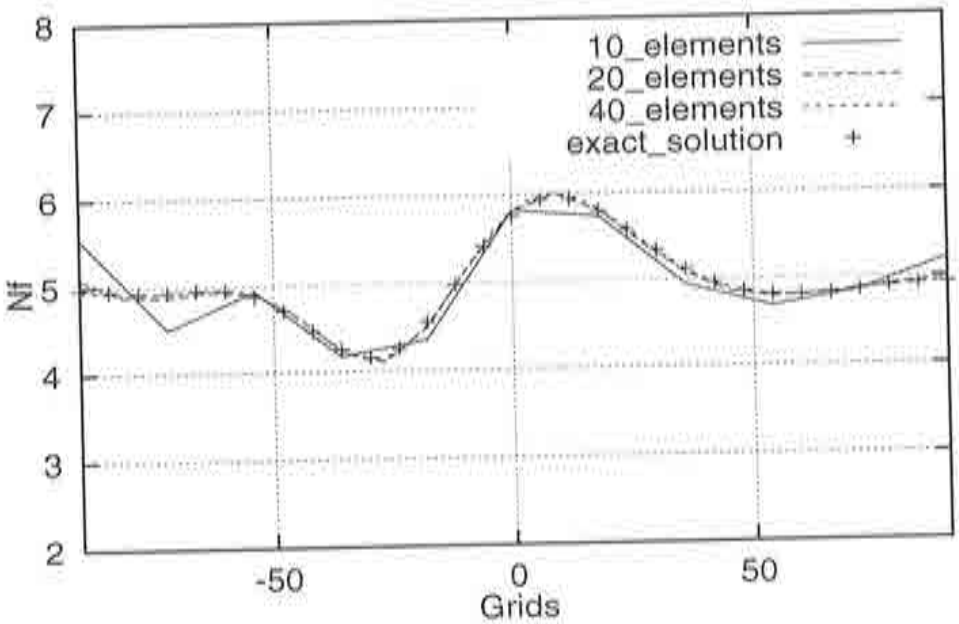

Figure 3.28 Circumferential normal forces diagram for different meshes - ACV element.

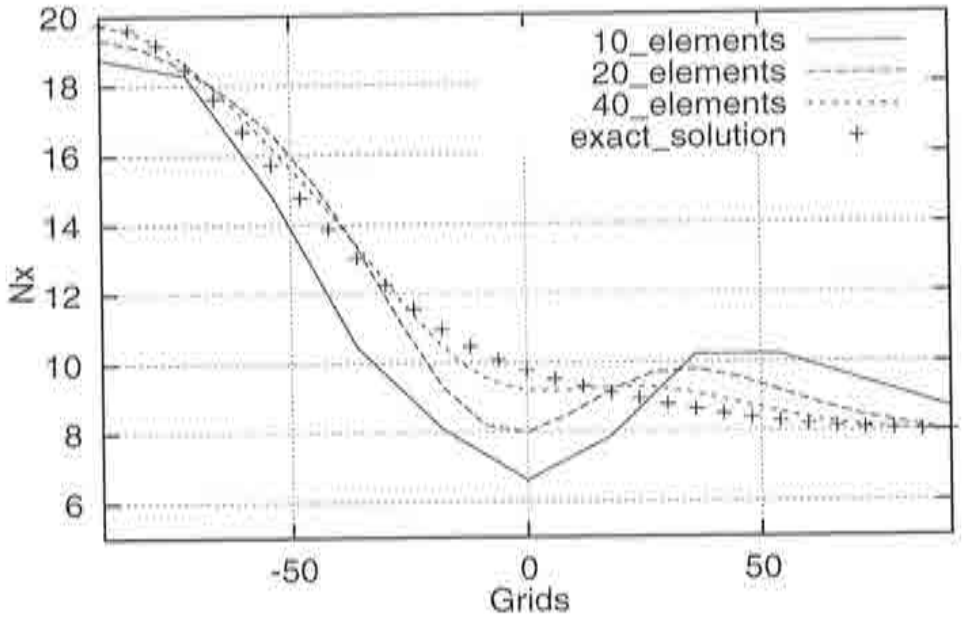

Figure 3.29 Axial normal forces diagram for different meshes - ACC element.

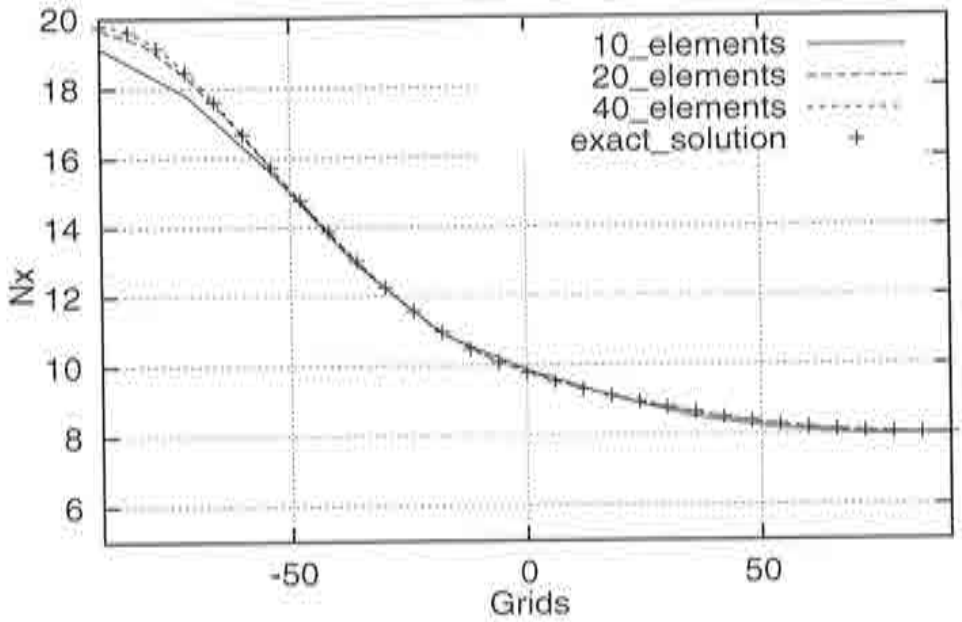

Figure 3.30 Axial normal forces diagram for different meshes - ACV element.

3.5.4 Hemispherical shell

Figure 3.31 presents a hemispherical shell with the unit moment at the free end $M = 1 inlb/in^2$. The radius has the value $r = 100 ins$, the Young modulus is $E = 1.0 \times 10^7 lb/in^2$ and the Poisson's coefficient is $\nu = 0.33$. The analysis is performed with the uniform meshes of 10, 20 and 40 elements and the obtained results for the horizontal displacements and the radial moment are compared with the reference solution obtained with two node linear axisymmetric shell element based on Reissner-Mindlin theory with reduced integration.

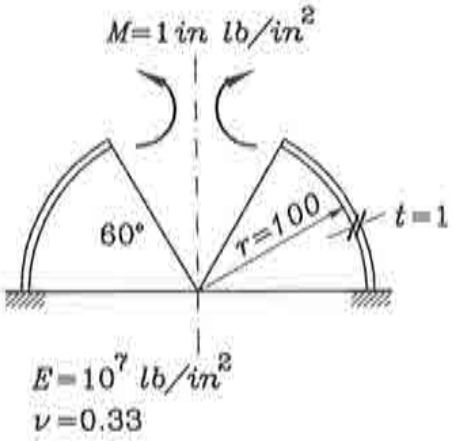

Figure 3.31 Hemispherical shell.

The diagrams of vertical displacements, shown in Figures 3.32 and 3.33, demonstrate again that the ACV element leads to the excellent result accuracy, whereas the ACC element is significantly less accurate.

The same tendency is demonstrated in Figures 3.34 and 3.35, where the bending moment M_x component diagram is presented for both elements. The coarse mesh leads to some discrepancy of the exact solution for the ACC element specially at the free end, while the ACV element shows the excellent result accuracy.

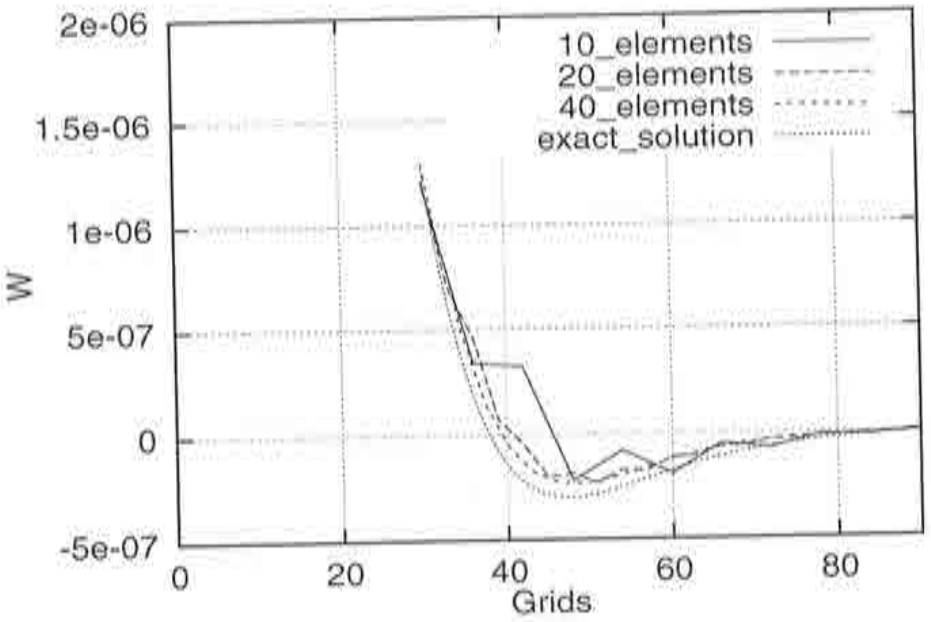

Figure 3.32 Horizontal displacements diagram - ACC element.

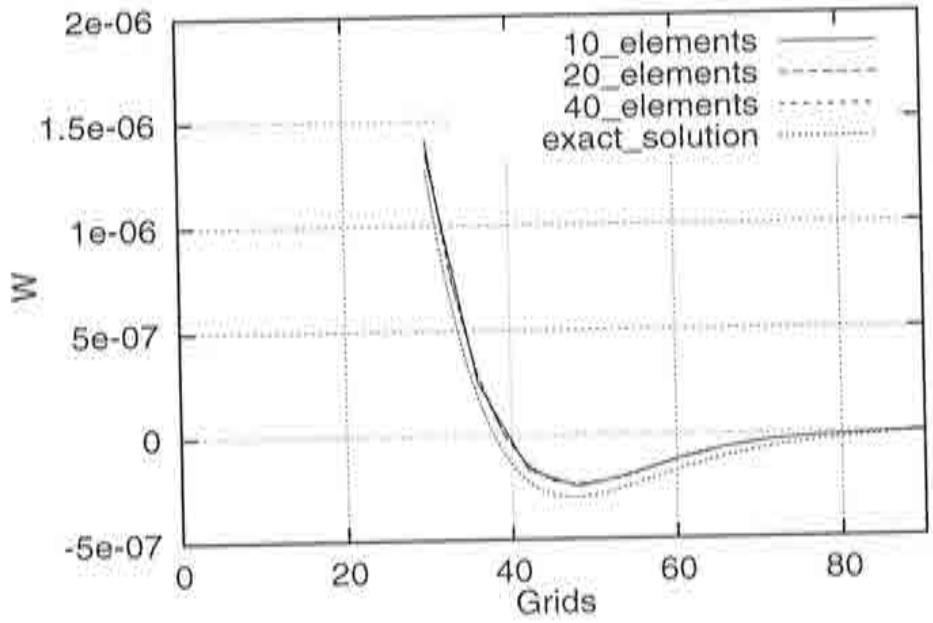

Figure 3.33 Horizontal displacements diagram - ACV element.

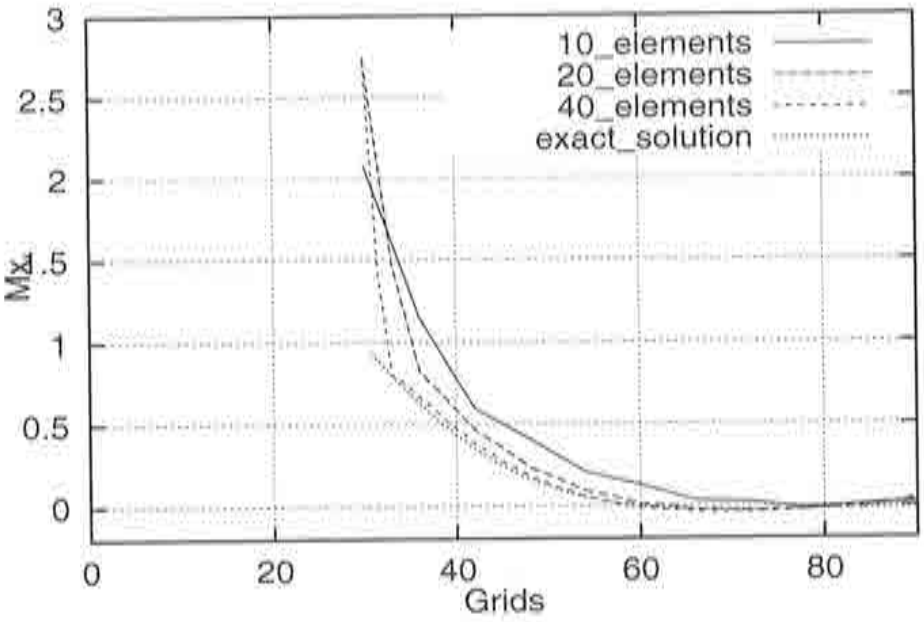

Figure 3.34 Radial moment diagram for different meshes - ACC element.

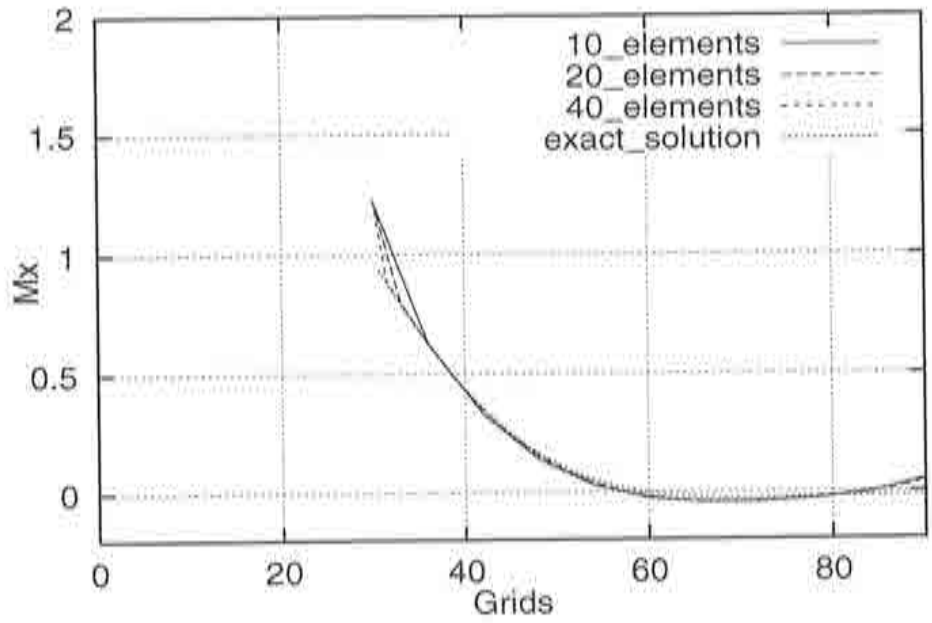

Figure 3.35 Radial moment diagram for different meshes - ACV element.

CHAPTER 4

NON-LINEAR AXISYMMETRIC SHELL

4.1 INTRODUCTION

In an actual engineering analysis, it is a good practice that a nonlinear analysis of a problem is always preceded by a linear analysis, in other words, the nonlinear analysis is considered as an extention of the complete analysis process based on the assumptions of linear analysis.

The nonlinear extension of the axisymmetric shell element is presented in this chapter. This has been accomplished only for the ASV axisymmetric shell element based on Cell Vertex scheme, since it was proved that it is superior to the ASC Cell Centered scheme based element.

The establishment of an appropriate finite element model for the nonlinear analysis is based on the sufficient understanding of the problem under consideration as quite a few solution variables have to be judiciously selected - nonlinear kinematic formulation, material model and iterative solution strategy. By the basic hypothesis of the Updated Lagrangian formulation and explicit dynamic formulation this element is extended to the domain of nonlinear analysis, both materially and geometrically and provide the very powerful method for the practical applications, most notably sheet metal forming analysis.

The outline of the chapter is as follows. First, the basic expressions of nonlinear solid mechanics theory are reviewed, supported by Appendix 4.1. Then, the particularization of nonlinear theory for the axisymmetric shell element ASV is presented with the basic assumptions of the shell model adopted. The explicit dynamic formulation is described with the dynamic equilibrium equations written in terms of the principle of virtual work using the Updated Lagrangian formulation. A short overview on the time integration of the equations of motion and the stability of explicit time integration is also given. Some remarks about the treatment of frictional contact and a short view on sheet metal forming analysis for better understanding of examples are given.

Finally, the ASV element has been implemented in a nonlinear explicit dynamic code available at CIMNE. The extensive set of numerical simulations has been carried out in order to corroborate a very satisfying performance of the developed ASV shell element.

4.2 BASIC EXPRESSIONS OF NON-LINEAR SOLID MECHANICS THEORY

This section gives a brief introduction of expressions of nonlinear solid mechanics theory, what is presented more extensively in the Appendix 4.1 dealing with the details of nonlinear solid mechanics theory. The review of the expressions important for description and deformation of a solid body as well as the main stress measures are given. The equations of motion are presented in the spatial and material configurations and the weak form of equation of motion is described.

4.2.1 Description of motion and deformation of a solid body with the main stress measures

Two different descriptions of motion of a continuum medium are used in mechanics [B-1], [C-2], [H-4], namely Eulerian and Lagrangian descriptions.

- In the Lagrangian or material description the behaviour is described in terms of material coordinates $\mathbf{X}$

$$\mathbf{x} = \mathbf{x}(\mathbf{X}, t) \tag{4.1}$$

- In the Eulerian or spatial description the behaviour is described in terms of the spatial coordinates $\mathbf{x}$

$$\mathbf{X} = \mathbf{X}(\mathbf{x}, t) \tag{4.2}$$

- The deformation gradient tensor $\mathbf{F}$ is defined as the derivative of the spatial coordinates with respect to the material coordinates

$$\mathbf{F} = \frac{\partial \mathbf{x}}{\partial \mathbf{X}} \tag{4.3}$$

- Using the expression for the squared length in the deformed configuration rewritten in terms of the vector $d\mathbf{X}$ in the reference configuration the right and left Cauchy-Green tensors are defined as

$$\mathbf{C} = \mathbf{F}^T \cdot \mathbf{F}, \quad \mathbf{b} = \mathbf{F} \cdot \mathbf{F}^T \tag{4.4}$$

- Using the expression for the squared length in the reference configuration written in terms of the vector $d\mathbf{x}$ in the deformed configuration, the Cauchy's deformation tensor or Finger deformation tensor is

$$\mathbf{c} = (\mathbf{F}^{-1})^T \cdot \mathbf{F}^{-1} = \mathbf{b}^{-1} \tag{4.5}$$

- The difference between the squared lengths for the two neighbouring particles (used as a measure of deformation) expressed in terms of the vector $d\mathbf{X}$ in the reference configuration leads to the Green-Lagrange strain tensor

$$\mathbf{E} = \frac{1}{2}(\mathbf{C} - \mathbf{I}) \tag{4.6}$$

- The difference between the squared lengths for the two neighbouring particles expressed in terms of the vector $d\mathbf{x}$ in the deformed configuration leads to the Almansi strain tensor

$$\mathbf{e} = \frac{1}{2}(\mathbf{I} - \mathbf{c}) \tag{4.7}$$

- The relation between the Green-Lagrange strain tensor and the Almansi strain tensor is

$$\mathbf{E} = \mathbf{F}^T \cdot \mathbf{e} \cdot \mathbf{F} \tag{4.8}$$

- The spatial velocity gradient $\mathbf{L}$ with the respect to deformed position is expressed as

$$\mathbf{L} = \frac{\partial \dot{\mathbf{u}}}{\partial \mathbf{x}} = \mathbf{d} + \boldsymbol{\omega} \tag{4.9}$$

where the rate of the deformation tensor $\mathbf{d}$ is

$$\mathbf{d} = \frac{1}{2}(\mathbf{L} + \mathbf{L}^T) \tag{4.10}$$

and the spin tensor $\boldsymbol{\omega}$ is

$$\boldsymbol{\omega} = \frac{1}{2}(\mathbf{L} - \mathbf{L}^T) \tag{4.11}$$

- The relation between the Green-Lagrange strain rate $\dot{\mathbf{E}}$ and the rate of the deformation $\mathbf{d}$ is

$$\dot{\mathbf{E}} = \mathbf{F}^T \cdot \mathbf{d} \cdot \mathbf{F}, \quad \mathbf{d} = \mathbf{F}^{-T} \cdot \dot{\mathbf{E}} \cdot \mathbf{F}^{-1} \tag{4.12}$$

- The force vector $d\mathbf{P}$ acts on the elemental surface $d\Gamma$ and it is expressed by

$$d\mathbf{P} = \mathbf{t}d\Gamma = \mathbf{n} \cdot \boldsymbol{\sigma} d\Gamma \tag{4.13}$$

where $\mathbf{t}$ is the surface traction, $\mathbf{n}$ is the unit normal vector and $\boldsymbol{\sigma}$ is the Cauchy stress tensor.

- The force $d\mathbf{P}$ expressed in terms of the initial undeformed area $d\Gamma_0$, gives the first Piola-Kirchhoff stress tensor $\mathbf{T}$

$$d\mathbf{P} = \mathbf{T} \cdot \mathbf{N} d\Gamma_0 \tag{4.14}$$

- The force $d\hat{\mathbf{P}}$ expressed by application of the transformation $\mathbf{F}^{-1}$ to the force vector $d\mathbf{P}$, gives the second Piola-Kirchhoff stress tensor $\mathbf{S}$

$$d\hat{\mathbf{P}} = \mathbf{F}^{-1} d\mathbf{P} = \mathbf{F}^{-1}\mathbf{T} \cdot \mathbf{N} d\Gamma_0 = \mathbf{N} \cdot \mathbf{S} d\Gamma_0 \tag{4.15}$$

- The relation between the first and second Piola-Kirchhoff stress tensors is

$$\mathbf{S} = \mathbf{T}(\mathbf{F}^{-1})^T, \quad \mathbf{T} = \mathbf{S}\mathbf{F}^T \tag{4.16}$$

- The relations between the 'true' Cauchy stress and the first and second Piola-Kirchhoff stresses are

$$\boldsymbol{\sigma} = \frac{1}{J}\mathbf{F} \cdot \mathbf{T}, \quad \mathbf{T} = J\mathbf{F}^{-1} \cdot \boldsymbol{\sigma} \tag{4.17a}$$

$$\boldsymbol{\sigma} = \frac{1}{J}\mathbf{F} \cdot \mathbf{S} \cdot \mathbf{F}^T, \quad \mathbf{S} = J\mathbf{F}^{-1} \cdot \boldsymbol{\sigma} \cdot \mathbf{F}^T \tag{4.17b}$$

4.2.2 Equations of motion

4.2.2.1 Equations of motion in the spatial configuration

The equations of motion in the spatial configuration are described in the strong form [M-2], by the following set of equations

- Cauchy equation of motion

$$\nabla_{\mathbf{x}}\boldsymbol{\sigma} + \rho\mathbf{b} = \rho\mathbf{a} \qquad \mathbf{x} \in \Omega^t, \quad t \in [0,T] \tag{4.18}$$

- boundary conditions

  traction:

$$\mathbf{n}\cdot\boldsymbol{\sigma} = \mathbf{t} \qquad \mathbf{x} \in F_\sigma^t, \quad t \in [0,T] \tag{4.19}$$

  displacement:

$$\mathbf{u} = \hat{\mathbf{u}} \qquad \mathbf{x} \in \Gamma_u^t, \quad t \in [0,T] \tag{4.20}$$

  initial:

$$\mathbf{u} = \mathbf{u}_0 \qquad \mathbf{x} \in \Omega^t, \quad t = 0 \tag{4.21a}$$

$$\mathbf{v} = \mathbf{v}_0 \qquad \mathbf{x} \in \Omega^t, \quad t = 0 \tag{4.21b}$$

  where $\mathbf{b}$ is the body force vector, Γ_u^t and Γ_σ^t are the parts of the boundary on which displacement and traction are specified.

4.2.2.2 Equations of motion in the material configuration

The equations of motion in the material configuration are described in the strong form [M-2], by the following set of equations

- Cauchy's equation of motion

$$\nabla_{\mathbf{X}}\mathbf{T} + \rho_0\mathbf{b}_0 = \rho\mathbf{A}, \quad \mathbf{X} \in \Omega^0, \quad t \in [0,T] \tag{4.22a}$$

$$\nabla_{\mathbf{X}}(\mathbf{S}\cdot\mathbf{F}^T) + \rho_0\mathbf{b}_0 = \rho\mathbf{A}, \quad \mathbf{X} \in \Omega^0, \quad t \in [0,T] \tag{4.22b}$$

- boundary conditions

  traction:

$$\mathbf{N}\cdot\mathbf{T} = \bar{\mathbf{T}} \quad \mathbf{X} \in \Gamma_\sigma^0, \quad t \in [0,T] \tag{4.23}$$

displacement:

$$\mathbf{u} = \bar{\mathbf{u}} \quad \mathbf{X} \in \Gamma_u^0, \quad t \in [0, T] \tag{4.24}$$

initial:

$$\mathbf{u} = \mathbf{u}_0, \quad \mathbf{X} \in \Omega^0, \quad t \in [0, T] \tag{4.25a}$$

$$\mathbf{v} = \mathbf{v}_0, \quad \mathbf{X} \in \Omega^0, \quad t \in [0, T] \tag{4.25b}$$

where $\mathbf{b}_0$ is the body force vector, $\mathbf{T}$ is the first Piola- Kirchhoff stress tensor and $\mathbf{S}$ is the second Piola-Kirchhoff stress tensor.

4.2.3 Weak form of equation of motion

By employing a standard variational procedure to the Cauchy's equations of motion in the spatial configuration [S-4], its weak form is

$$\int_{\Omega^t} \boldsymbol{\sigma} : \nabla_{\mathbf{x}}(\delta\mathbf{u}) d\Omega = \int_{\Omega^t} \rho(\mathbf{b} - \mathbf{a}) \cdot \delta\mathbf{u} d\Omega + \int_{\Gamma_\sigma^t} \mathbf{t} \cdot \delta\mathbf{u} d\Omega \tag{4.26}$$

where $\mathbf{u}$ is the arbitrary kinematically admissible displacement field and $\delta\mathbf{u}$ is the virtual displacement field. The above equation physically expresses the principle of virtual work that establishes the condition of a dynamic equilibrium equality of the internal and external virtual work.

In the same fashion, the variational procedure applied to the equations of motion in the material configuration in terms of the first Piola-Kirchhoff stress tensor and the second Piola-Kirchhoff stress tensor, leads to

$$\int_{\Omega^0} \mathbf{T} : \nabla_{\mathbf{X}}(\delta\mathbf{u}) d\Omega = \int_{\Omega^0} \rho_0(\mathbf{b}_0 - \mathbf{A}) \cdot \delta\mathbf{u} d\Omega + \int_{\Gamma_\sigma^0} \bar{\mathbf{T}} \cdot \delta\mathbf{u} d\Omega \tag{4.27}$$

$$\int_{\Omega^0} (\mathbf{S} \cdot \mathbf{F}^T) : \nabla_{\mathbf{X}}(\delta\mathbf{u}) d\Omega = \int_{\Omega^0} \rho_0(\mathbf{b}_0 - \mathbf{A}) \cdot \delta\mathbf{u} d\Omega + \int_{\Gamma_\sigma^0} \bar{\mathbf{T}} \cdot \delta\mathbf{u} d\Omega \tag{4.28}$$

The same set of equations in rewritten form by introducing the corresponding energy conjugate deformation measures is the base to formulate finite element equations

$$\int_{\Omega^t} \boldsymbol{\sigma} : \delta\boldsymbol{\varepsilon} d\Omega = \int_{\Omega^t} \rho(\mathbf{b} - \mathbf{a}) \cdot \delta\mathbf{u} d\Omega + \int_{\Gamma_\sigma^t} \mathbf{t} \cdot \delta\mathbf{u} d\Omega \tag{4.29}$$

$$\int_{\Omega^0} \mathbf{T} : \delta\mathbf{F} d\Omega = \int_{\Omega^0} \rho_0(\mathbf{b}_0 - \mathbf{A}) \cdot \delta\mathbf{u} d\Omega + \int_{\Gamma_\sigma^0} \bar{\mathbf{T}} \cdot \delta\mathbf{u} d\Omega \tag{4.30}$$

$$\int_{\Omega^0} \mathbf{S} : \delta\mathbf{E} d\Omega = \int_{\Omega^0} \rho_0(\mathbf{b}_0 - \mathbf{A}) \cdot \delta\mathbf{u} d\Omega + \int_{\Gamma_\sigma^0} \bar{\mathbf{T}} \cdot \delta\mathbf{u} d\Omega \tag{4.31}$$

4.3 PARTICULARIZATION OF NON-LINEAR THEORY FOR AXISYMMETRIC SHELLS

4.3.1 General expressions

In the development of a nonlinear finite element model for axisymmetric shells, the Updated Lagrangian formulation is used. The Updated Lagrangian formulation is derived from the Total Lagrangian formulation with the reference configuration updated as the body deforms instead of keeping it fixed as the original undeformed configuration [H-4].

The local updated Green-Lagrange strain vector at any point within the shell with respect to the reference configuration for axisymmetric shell element is given as

$$\mathbf{E} = \left\{ \begin{array}{c} E_{ss} \\ E_{\theta\theta} \end{array} \right\} = \left\{ \begin{array}{c} \frac{\partial u_1}{\partial s_o} + \frac{1}{2}\left(\frac{\partial u_1}{\partial s_o}\right)^2 + \frac{1}{2}\left(\frac{\partial u_3}{\partial s_o}\right)^2 \\ \frac{\bar{u}_1}{R_o} + \frac{1}{2}\left(\frac{\bar{u}_1}{R_o}\right)^2 \end{array} \right\} \tag{4.32}$$

where u_1 and u_3 are the local displacements from the current reference configuration (and not total displacements), as shown in Figure 4.1.

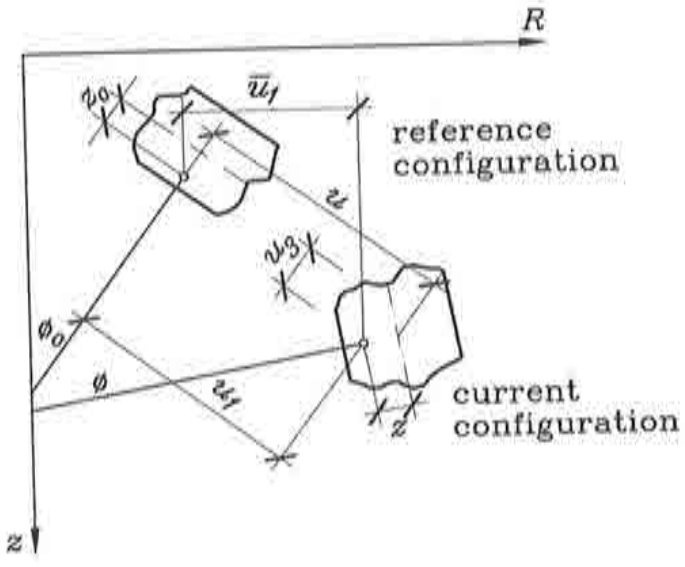

Figure 4.1 Updated Lagrangian formulation.

The global radial displacement from the reference configuration is given in terms of the local displacements as

$$\bar{u}_1 = u_1 cos\phi_o - u_3 sin\phi_o \tag{4.33}$$

where u_1 and u_3 are the local displacements from the current reference configuration and ϕ_o is the inclination in the reference configuration of the local coordinate system to the global coordinate system. The derivatives with respect to the local coordinate system s_o and z_o are performed with respect to the reference configuration and R_o is the radius in the reference configuration expressed as

$$R_o = R_{oNP} - z_o sin\phi_o \tag{4.34}$$

with R_{oNP} being the radius of the nodal plane in the reference configuration. The displacement through the thickness of the shell is given by

$$u_1 = u - zsin\phi \tag{4.35a}$$

$$u_3 = w - z_o + zcos\phi \tag{4.35b}$$

where u and w are the nodal plane displacements from the reference configuration. The distance from the nodal plane to the point considered in the current configuration is denoted by z and depends on the thickness strain which is not known a priori. Thus, the approximation has to be done, where

$$z = z_o \tag{4.36}$$

what substituting in equation (4.35a) and (4.35b) gives the local displacements at any point within the shell

$$u_1 = u - z_o sin\phi \tag{4.37a}$$

$$u_3 = w - z_o(1 - cos\phi) \tag{4.37b}$$

The Green-Lagrange strain vector can be expressed as a sum of linear and nonlinear parts

$$\mathbf{E} = \mathbf{E}_L + \mathbf{E}_{NL} \tag{4.38}$$

where

$$\mathbf{E}_L = \left\{ \begin{array}{c} \frac{\partial u_1}{\partial s_o} \\ \frac{u_1}{R_o} \end{array} \right\} \quad \mathbf{E}_{NL} = \left\{ \begin{array}{c} \frac{1}{2}\left(\frac{\partial u_1}{\partial s_o}\right)^2 + \frac{1}{2}\left(\frac{\partial u_3}{\partial s_o}\right)^2 \\ \frac{1}{2}\left(\frac{u_1}{R_o}\right)^2 \end{array} \right\} \tag{4.39}$$

The virtual work equation for the Updated Lagrangian formulation involves the virtual variation of the Green-Lagrange strain. Thus, the expression for the virtual variation of the Green-Lagrange strain is expressed as a sum of the linear $d\mathbf{E}_L$ and nonlinear $d\mathbf{E}_{NL}$ parts

$$d\mathbf{E} = d\mathbf{E}_L + d\mathbf{E}_{NL} \tag{4.40}$$

where the expressions for the linear and nonlinear parts are not presented in detail because of their lengths (it can be found in [H-4]) and as it will be shown later, the nonlinear part is not necessary in the Updated Lagrangian formulation.

The finite element discretization requires more amenable expressions, so the discretization of the variation of the Green-Lagrange strain vector is done. The discretized variation of the Green-Lagrange strain vector, presented in standard notation is

$$d\mathbf{E} = \sum_{i=1}^{2} \mathbf{B}_i d\mathbf{a}_i \tag{4.41}$$

where

$$\mathbf{B}_i = \mathbf{B}_{Li} + \mathbf{B}_{NLi} \tag{4.42}$$

If the reference configuration coincides with the position where the $\mathbf{B}$ matrix is calculated, $\mathbf{B}_{NL} = \mathbf{0}$, so the equation (4.42) is rewritten as

$$\mathbf{B}_i = \mathbf{B}_{Li} \tag{4.43}$$

and as it is evaluated with the current configuration as the reference configuration, it contains none of the large rotation terms that appear in the Total Lagrangian formulation.

Having updated the coordinates, the updated stresses with respect to the current configuration are required. The relevant stresses with respect to the current configuration are 'true' or Cauchy stresses. Thus, the previous second Piola-Kirchhoff stresses must be modified from the previous configuration into the Cauchy stresses.

4.3.2 Particularization for axisymmetric Cell Vertex ASV element

The element extended to the nonlinear analysis is the ASV axisymmetric shell element. It is an elasto-plastic two node axisymmetric shell element which allows for membrane and bending deformations. Each node has two degrees of freedom, namely radial and axial displacements. The axisymmetric shell model adopted is suitable for the analysis of axisymmetric shells allowing for large displacements, large rotations and small strains. The Updated Lagrangian formulation is used for the description of the nonlinear kinematics. The expression for the matrix $\mathbf{B}$ given by equation (4.43) from the previous section can be rewritten as

$$\mathbf{B}_i = \mathbf{B}_p \tag{4.44}$$

The matrix $\mathbf{B}_p$ for the ASV element, for the general case as well as for the imposed boundary conditions is developed in detail in the previous chapter.

The element is formulated using the layered approach where each layer is assumed to be in the state of the plane stress. This layering allows for the gradual spread of plasticity through the thickness, as shown in Figure 4.2.

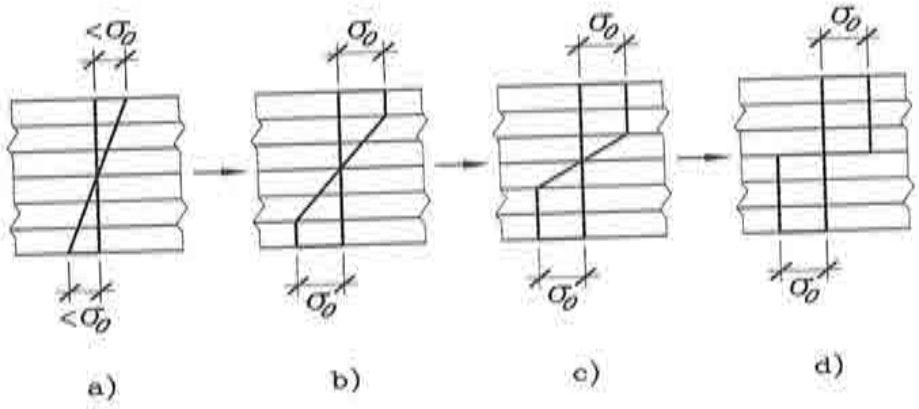

Figure 4.2 Yielding of layered element.

The stress through each layer thickness is assumed to be constant. The consequence of this assumption is that there are no moments acting on a single layer, while membrane stress exists. As the plastification advances, more layers become plastic, until eventually the whole cross section becomes plastic.

Material nonlinearities are considered by means of the hypoelastic model of elastoplasticity. To describe the elasto-plastic material behaviour, in addition to the elastic stress-strain relation, the following properties are necessary:

- a yield criterion which specifies the state of multiaxial stress corresponding to the start of plastic flow. For the given element, the von Mises yield criterion is adopted; details are given in Appendix 4.1.
- a flow rule which relates the plastic strain increments to the current stresses and the stress increments subsequent to yielding. The associated flow rule is adopted.
- a hardening rule which specifies how the yield condition is modified during plastic flow. The isotropic work hardening is adopted.

In order to develop plastic flow, the stress must remain on the yield surface. If the stress is outside the yield surface, it should be returned to the yield surface. The stress-strain matrix is dependent on the current conditions of the stresses, strains and other state variables plus their history. The aim is to update the old stresses, strains and equivalent plastic strains. Thus, to obtain an accurate response prediction, it is necessary to imply the constitutive equation in an integration process. There are some alternative procedures for such a process as the forward Euler scheme, use of subincrements and use of the chosen form of the backward Euler scheme.

4.3.2.1 Backward Euler return

For all procedures mentioned above, the first step is to use an elastic relationship to update the stresses. If the updated stresses are found to lie within the yield surface, the material is assumed to be elastic, so there is no need to integrate the rate equations. However, if the elastic stresses are outside the yield surface, integration procedure is necessary. The use of the backward scheme is performed and it has turned out to be efficient and particularly simple in form because of the von Mises yield criterion. The yield function in squared form is expressed as

$$f = \sigma_e^2 - \sigma_o^2 \tag{4.45}$$

The generalized algorithm has the form

$$\boldsymbol{\sigma}_C = \boldsymbol{\sigma}_A + \mathbf{C}(\Delta\boldsymbol{\varepsilon} - \Delta\boldsymbol{\varepsilon}_p) = \boldsymbol{\sigma}_B - \mathbf{C}\Delta\boldsymbol{\varepsilon}_p \tag{4.46}$$

$$\Delta\boldsymbol{\varepsilon}_p = \Delta\lambda[(1-\eta)\mathbf{a}_A + \eta\mathbf{a}_C] \tag{4.47}$$

If the coefficient $\eta = 1$, the backward Euler or closest point algorithm is implemented. The full backward Euler scheme involves the vector $\mathbf{a}_C$ that is normal to the yield surface at the final position C for which the stress satisfies (4.46). Hence, an iterative procedure must be used to solve the nonlinear

equations (4.46) and (4.47). Thus, the backward Euler return is based on the equation

$$\boldsymbol{\sigma}_C = \boldsymbol{\sigma}_B - \Delta\lambda \mathbf{C}\mathbf{a}_C \tag{4.48}$$

The general and backward Euler returns are presented in Figure 4.3.

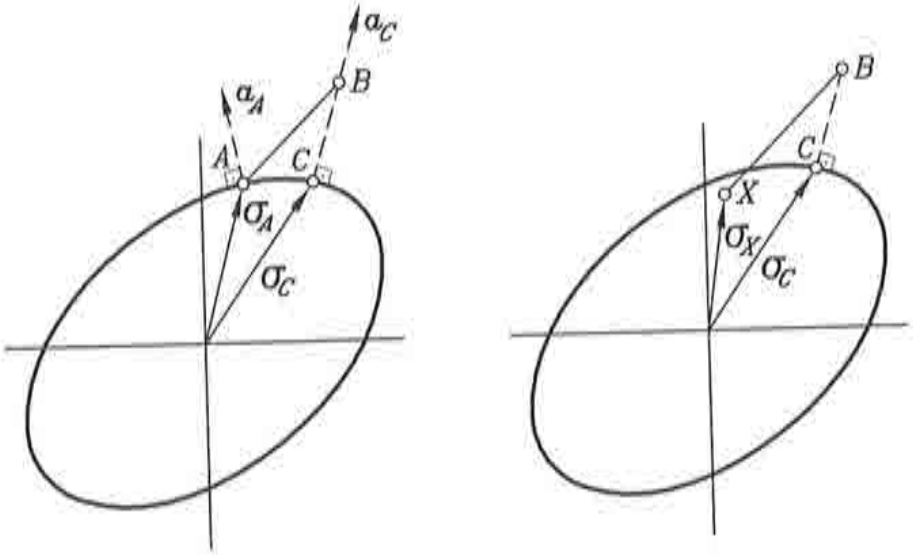

Figure 4.3 General and backward Euler returns. a)the flow vectors $\mathbf{a}_A$ and $\mathbf{a}_C$ b)backward Euler return form inside the yield surface.

After some algebra [C-2], the yield function expressed by the equation (4.45) can be rewritten as follows

$$f = \frac{1}{4}\Big(\frac{C_1}{(1+\Delta\lambda'\mu r)^2} + \frac{C_2}{(1+\Delta\lambda'\mu r)^2}\Big) - \boldsymbol{\sigma}_{oC}^2 = 0 \tag{4.49}$$

where

$$r = \frac{1+\nu}{1-\nu}, \quad C_1 = (\sigma_x + \sigma_y)_B^2, \quad C_2 = 3(\sigma_x + \sigma_y)_B^2 \tag{4.50}$$

The values C_1 and C_2 in the equation (4.49) are based on the stresses which are estimated at point B. The corrector for the first iteration is found by calculating the flow vector at point B, current hardening parameter, plastic multiplier increment and the current value of stresses at point C. Knowing all these values, it is possible to calculate the equation (4.49).

The nonlinear equation for the square form of the yield function is solved for $\Delta\lambda^{\prime}$. The value of the square form of the yield function is calculated and checked if the stress point lies on the plasticity surface. If the solution is not converged, the current value of the flow vector and the plastic multiplier are calculated and returned again to calculation of the square form of the yield function, repeating the process untill the convergence is achieved.

If converged, the actual corrected stresses and flow vector are calculated. Having the last plastic multiplier for the converged state of the stresses the plastic strains are calculated. The stresses are restored on the plasticity surface.

4.3.2.2 Thickness update

The thickness of each layer must be updated as well as the reference configuration from the last converged solution into the current solution [H-4]. The thickness strain for axisymmetric shells is expressed by elastic and plastic parts as follows

$$E_{33} = -\frac{\nu}{1-\nu}(E^{e}_{11} + E^{e}_{22}) - E^{p}_{11} - E^{p}_{22} \tag{4.51}$$

The elastic part is formed due to the Poisson's ratio effects and the plastic part is formed due to the fact that the plastic flow in metals occurs at the constant volume. The thickness update permits a substantial change of the thickness of the shell accompanied by large rotations provided that the incremental quantities are kept small at each update of the reference configuration.

4.3.2.3 Computation of stresses

In order to establish the reference configuration, the stresses at the current position, which are the updated second Piola-Kirchhoff stresses at the position of the last converged solution, must be transformed into the Cauchy stresses in the current configuration.

The stresses at the end of the increment using the small time increments (of the order of 10^{-6}), are obtained by

$$\boldsymbol{\sigma}^{\prime t+\Delta t} = \boldsymbol{\sigma}^{\prime t} + \mathbf{D}\boldsymbol{\varepsilon}^{\prime} \tag{4.52}$$

The stresses $\boldsymbol{\sigma}^{\prime t}$ must be transfered to the $t + \Delta t$ configuration before the sum (4.52) is performed. The resultant stresses are computed from the local stresses by

$$\hat{\boldsymbol{\sigma}}' = \left\{ \begin{array}{c} \hat{\boldsymbol{\sigma}}'_m \\ \hat{\boldsymbol{\sigma}}'_f \end{array} \right\} = \int_{-\frac{h}{2}}^{\frac{h}{2}} \left\{ \begin{array}{c} \boldsymbol{\sigma}' \\ z\boldsymbol{\sigma}' \end{array} \right\} dz' \tag{4.53}$$

where $\boldsymbol{\sigma}' = [\sigma'_x, \sigma'_y]^T$ and h is the shell thickness.

4.4 EXPLICIT DYNAMIC FORMULATION

The explicit dynamic formulation has recently become very popular as it does not require the solution of a system of equations. The idea is based on solving the dynamic equilibrium equations at time t using an explicit integration scheme with a diagonal matrix. The dynamic equilibrium equations are written in terms of the principle of virtual work using the Updated Lagrangian formulation. The Updated Lagrangian formulation includes all kinematic nonlinear effects due to the large displacements, large rotations and large strains [H-4].

The discretized form of equilibrium equations is expressed as [Z-4]

$$\mathbf{M}\ddot{\mathbf{a}} + \mathbf{p} = \mathbf{f} \tag{4.54}$$

where $\mathbf{M}$ is the mass matrix and $\mathbf{p}$ and $\mathbf{f}$ are the vectors of internal and external forces, respectively. These forces are calculated by assembling the element contributions

$$\mathbf{p}^e = \int\int_A \mathbf{B}^T \hat{\boldsymbol{\sigma}}' dA \tag{4.55}$$

$$\mathbf{f}^e = \int\int_A \mathbf{N}^T \mathbf{t} dA \tag{4.56}$$

where $\mathbf{t}$ is the vector of surface forces, i.e. contact forces acting on the element. The strain matrix $\mathbf{B}$ and stresses $\boldsymbol{\sigma}$ are divided into membrane and bending parts

$$\mathbf{B} = \begin{bmatrix} \mathbf{B}_m \\ \mathbf{B}_b \end{bmatrix} \quad \text{and} \quad \hat{\boldsymbol{\sigma}}' = \begin{bmatrix} \boldsymbol{\sigma}_m \\ \boldsymbol{\sigma}_b \end{bmatrix} \tag{4.57}$$

with

$$\boldsymbol{\sigma}_m = [N_s, N_\theta] \quad \boldsymbol{\sigma}_b = [M_s, M_\theta] \tag{4.58}$$

where N_s and N_θ are axial and circumferential forces and M_s and M_θ are the radial and circumferential moments, respectively. The equation (4.54) is integrated in time using the standard explicit dynamic scheme with a diagonal (lumped) mass matrix, presented in detail later. The flow chart of the explicit dynamic solution can be presented as follows:

EXPLICIT DYNAMIC SOLUTION

Discrete dynamic equilibrium equation

$$\mathbf{M}\ddot{\mathbf{a}} + \mathbf{p} = \mathbf{f}$$

Solution at time t_n

1.In order to compute kinematic variables, the following steps are undertaken:

accelerations:

$$\ddot{\mathbf{a}}^n = \mathbf{M}_D^{-1}[\mathbf{f}^n - \mathbf{p}^n] \quad \mathbf{M_D} = \mathrm{diag}\mathbf{M}$$

velocities:

$$\dot{\mathbf{a}}^{\frac{n+1}{2}} = \dot{\mathbf{a}}^{\frac{n-1}{2}} + \ddot{\mathbf{a}}^n \Delta t^{\frac{n+1}{2}}$$

displacements:

$$\mathbf{a}^{n+1} = \mathbf{a}^n + \dot{\mathbf{a}}^{\frac{n+1}{2}} \Delta t^{n+1}$$

where $\Delta t^{\frac{n+1}{2}} = \frac{1}{2}(\Delta t^n + \Delta t^{n+1})$.

2. Strains and stresses $\boldsymbol{\varepsilon}^{n+1}$, $\boldsymbol{\sigma}^{n+1}$ are computed.

3. Internal force vector $\mathbf{p}^{n+1}$ is computed.

4. Frictional contact conditions are checked.

5. External force vector $\mathbf{f}^{n+1}$ is computed.

6. The first step is performed again and the process for the next time step is repeated.

4.4.1 Lumping of a mass matrix

The mass matrix $\mathbf{m}_e$ is called the consistent mass matrix. The equations of the motion are coupled with the consistent mass matrix because the global mass matrix is not diagonal what leads to computationally costly solution. To overcome this problem, the use of diagonal mass matrices with zero off-diagonal terms are performed. It grounds the base of the efficiency of the explicit dynamic code.

A diagonal (lumped) mass matrix is obtained by applying a special lumping procedure to a consistent matrix. The lumped mass matrix can also be obtained by distributing the element mass equally to the nodes.

The diagonal terms for translational degrees of freedom are obtained as follows:

- the diagonal coefficients of the consistent mass matrix are computed
- the total mass of the element m is computed
- the number s by adding the diagonal coefficients m_{ii} associated with translation is computed
- the diagonal coefficients m_{ii} are scaled by multiplying with the ratio m/s.

4.4.2 Time integration of equation of motion

The solution of the dynamic problem is performed by integrating equation (4.54) with respect to time. The time integration is a step-by-step procedure in which the deformed configurations are found in the incremental way at the time instants $t_1, t_2, ...t_{n-1}...T$ where $t_1 = \Delta t_1$, $t_n = t_{n-1} + \Delta t_n$ and Δt_n represent the length of the time steps employed in the integration of equations of motion and n is the number of the integration step.

The equation whose solution is known at time t is used to calculate the solution at $t + \delta t$ time, for the explicit formulation. The solution at time $t + \delta t$ is obtained using the central difference scheme [B-1].

The finite element model has only the translational degrees of freedom. The deformed configuration at a certain time t_n is defined by the displacement vectors $\mathbf{u}_n$ of all nodal points. The incremental displacements are calculated at each time step and are used to update nodal cartesian coordinates.

The following steps are performed for the translational equations of a certain nodal point. First, the vector of the nodal translational accelerations is calculated

$$\ddot{\mathbf{u}}_n = \frac{1}{M}(\mathbf{F}_n^{ext} - \mathbf{F}_n^{int}) \tag{4.59}$$

The vector of the nodal translational velocities is calculated as

$$\dot{\mathbf{u}}^{\frac{n+1}{2}} = \dot{\mathbf{u}}^{\frac{n-1}{2}} + \frac{1}{2}\ddot{\mathbf{u}}_n(\Delta t_{n-1} + \Delta t_n) \tag{4.60}$$

Finally, the vector of the nodal translational displacements is

$$\mathbf{u}_{n+1} = \mathbf{u}_n + \dot{\mathbf{u}}^{\frac{n+1}{2}} \Delta t_n \tag{4.61}$$

where M is the mass assigned to the nodal point.

The time integration algorithm allows the use of a variable time step. The condition of stability of the explicit time integration requires a time step size which should not exceed a critical time step, and it is computed for each time step or at determined intervals.

4.4.3 Stability of explicit time integration

In explicit time integration, the selection of an appropriate time step is crucially important. The central difference sheme time of integration is conditionally stable. The time step length is limited by the expression

$$\Delta t \leq \Delta t_{cr} = \frac{2}{\omega_{max}} \tag{4.62}$$

where Δt_{cr} is the critical time step and ω_{max} is the highest circular frequency of the discrete system, so equation (4.62) holds for nonlinear problems.

4.5 TREATMENT OF FRICTIONAL CONTACT

Contact and friction appears as a consequence of the interaction between different bodies. Such interactions are typical for metal forming problems where the metal interacts with the tools, producing a source of complexity to the numerical simulation due to the nonlinear nature of the boundary conditions. The used contact algorithm is based on the penalty method with friction governed by the Coulomb law.

In 2D contact, the interface surfaces are discretized with 2 node straight line segments. One side of the contact surface is designated as the slave surface and the other one as the master surface with the nodes defining these surfaces called slave or master node, respectively. The contact conditions are considered nodally. Each slave node is checked for penetration through the master surface. If a penetration is detected, an interface force is applied between the slave node

and the appropriate master nodes. The magnitude of this force is proportional to the amount of the penetration and penalty coefficient.

The contact algorithm performs two tasks: contact search and calculation of contact forces.

4.5.1 Contact search procedure

The searching procedure should be employed at every time step to find the current contacting area. The contact search procedure [S-1], includes the following steps:

- For each slave node, the closest master node is found through checking the distance between the slave node and all the master nodes. The search procedure is started from the closest master node from the previous time step.
- The master segment candidate for contact with the given slave node is determined and a simple penetration check is performed. The segments connected to the closest master node are only checked.
- If the penetration is found, the exact location of the contact point on the master segment and the amount of the penetration is calculated.

4.5.2 Calculation of contact force

The searching procedure is to be employed at every time step to find the current contacting area. The penalty method is used to enforce the normal contact conditions and to compute normal contact forces. The normal contact force F^n, applied to the slave node is proportional to the amount of penetration ($g < 0$) and a penalty coefficient k^n

$$F^n = -k^n g \tag{4.63}$$

The tangential contact forces are calculated using the local regularized Coulomb friction law

$$F^t = \mu |F^n| \tag{4.64}$$

A contact interface is defined by the control parameters for the contact algorithm, as the penalty coefficient friction data and topological definition of contact surfaces. The topology of master and slave surfaces in each contact surface has to be given by the lists of nodes used in the segment definitions as well as the segment connectivities for the master and slave surfaces.

4.6 SHEET FORMING PROCESSES

This section gives a short overview of the problems encountered in the course of modelling sheet forming processes and provides some information on the data preparation for these problems. The data required contains all the physical parameters associated with the finite element model for the sheet forming process being considered: the discrete model of the material parts including discretized geometry, material properties, interaction between the sheet and tools, loading and time dependent parameters. The discretized geometry is given by the list of nodal points with their coordinates and the lists of finite elements used in the discretization.

The modelling of the material parts for the simulation of a sheet forming process consists of modelling a **sheet** and modelling the tools used, namely the **die, punch** and **blankholder**.

4.6.1 Sheet

The sheet can be discretized with either solid (continuum) or shell elements. Using solid elements requires two surface contact conditions to be introduced, but this allows the change in thickness to be treated more precisely. Through the thickness, stresses can therefore also be accounted for. Shell elements used in the discretization of the sheet yield the possibility to represent complex deformations properly. Problems can be either analyzed using three dimensional models or two dimensional models for plane stress, plane strain or axisymmetric cases.

4.6.2 Die and punch

Since the deformation of the die and punch is usually negligible small compared to the deformation of the sheet, they can be considered rigid. In the finite element model the rigid surfaces of the die and punch can be approximated with straight line segments in 2D models and with triangular and/or quadrilateral facets in 3D models. Discretized tool lines or surfaces are used in the contact analysis and the algorithms analyze the interaction between the tools and the sheet. For this reason the discretization of the contact surfaces should be compatible with the finite element discretization. Visualization of the rigid surfaces is obtained by means of an additional description with element type Dummy.

In the model, the die is usually completely restrained by fixing all the die nodes. The punch usually moves as a rigid body with a prescribed rigid body velocity.

4.6.3 Blankholder

The blankholder can be treated as rigid tool similarly to the die and punch or it can be modelled as deformable body. The mesh for a deformable blankholder is usually very coarse in order not to increase the size of the model excessively. In the rigid model of the blankholder one of the nodes is usually chosen as the master one and the other nodes are treated as slaves by means of kinematic constraints. The interaction between the blankholder and the sheet is considered in the analysis and the contact data must be input for the blankholder–sheet interface as for the other tools. The application of the blankholding force should be considered very carefully. In the dynamic analysis it is necessary to apply this force along with some damping to ensure the steady value of the pressure on the sheet.

4.7 NUMERICAL EXAMPLES

In order to corroborate a very satisfying performance of the developed ASV shell element, several numerical simulations have been carried out as follows:

- Stretching benchmark test proposed by the Ohio State University.
- Deep drawing benchmark test proposed by the Ohio State University.
- Deep drawing benchmark test proposed by the Department of Structural Mechanics of the Chalmers University of Technology.

The obtained numerical results with the solid element, Timoshenko shell element and new ASV element are compared with the given experimental results. The problem description, finite element model, analysis consideration, results and discussion as well as conclusions for each of the examples are presented further.

4.7.1 Ohio State University Benchmark - STRETCHING

4.7.1.1 Problem description

The analysis of the stretching process of a thin sheet by a hemispherical punch is carried out. To demonstrate the performance of developed ASC element, three different element types were used for this problem: QSOL4R quadrilateral axisymmetric solid element, AXIS2K axisymmetric shell element based on Timoshenko theory and ASC axisymmetric shell element. The final shape of the sheet is a hemisphere of radius 59.18mm and depth 40 mm.

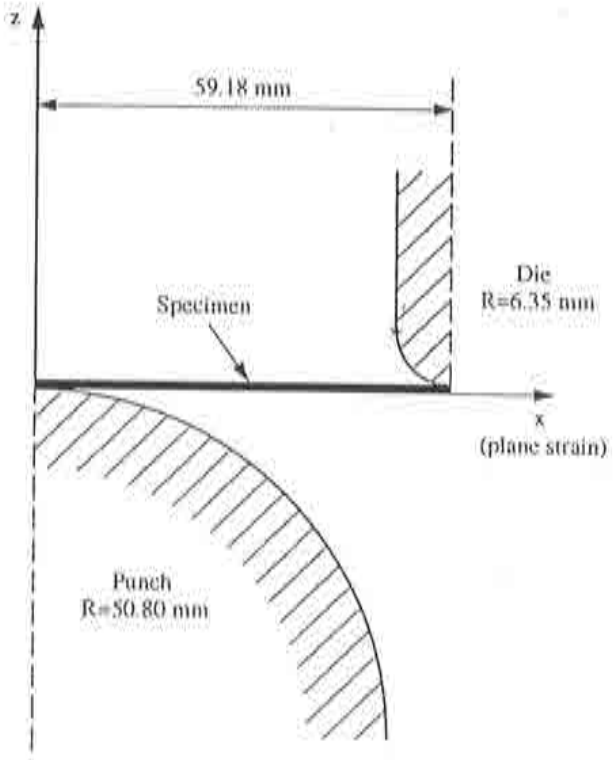

Figure 4.4 Geometry of the OSU Benchmark - Stretching.

4.7.1.2 Finite element model

Geometry

The geometry of the punch, die and sheet are shown in Figure 4.4. The punch radius is $R_p = 50.80mm$, the die corner radius is $R_D = 6.35mm$ and the sheet thickness is $t = 1.00mm$. The initial diameter of the sheet rim is $D_o = 59.18mm$ and the punch travel is $40.00mm$.

Mesh

The sheet was modelled using 29 QSOL4R quadrilateral axisymmetric solid elements (4 node), 29 AXIS2K axisymmetric shell elements (2 node) and 29 ASV axisymmetric shell elements (2 node). The punch and the die were modelled using 80 DUMQ rigid elements (4 node).

Materials

The sheet material was aluminium using a nonlinear isotropic hardening elasto-plastic model. The following properties were used:

Young's modulus: $= YOUNG = 69GPa$

Poisson's ratio: $= POISS = 0.3$

Mass density: $= MASSD = 2700kg/m^3$

Nonlinear hardening: $= CONSO = 589MPa$

$EFREF = 1.0 \times 10^{-4}$

$CONSN = 0.216$

Boundary Conditions

The die was held in place while the punch was moved vertically. Contact surfaces between all tools and the sheet (punch - sheet and die - sheet contact pairs) were modelled using a different friction coefficients of 0.0, 0.15 and 0.30; the penalty coefficient for both normal and tangential contact forces was 0.5.

Loading

The punch was moved vertically for $40mm$ by applying a sinusoidal velocity over the total analysis time period.

4.7.1.3 Analysis considerations

The total response time was obtained using automatic time stepping calculation and was terminated when the punch stroke was completed. Material non-linearities were considered to be rate independent and the Updated Lagrangian formulation was used to describe geometrical non-linearities.

4.7.1.4 Results and discussion

Figures 4.5 and 4.6 show the initial geometry layout as well as the final sheet geometry for the 2D solid axisymmetric mesh. The final shape agrees very well with the solution in [L-3]. The radial and circumferential strain distributions calculated in nodal points along the upper line for different values of frictional coefficient: 0.0, 0.15 and 0.30 are presented in Figures 4.7 and 4.8 respectively and a contour of the final sheet thickness is presented in Figure 4.9.

4.7.1.5 Conclusions

The radial strain distributions for the solid and shell elements agree reasonably well with the reference solution given in [L-3]. Similar results were obtained for the circumferential and thickness distributions for all elements.

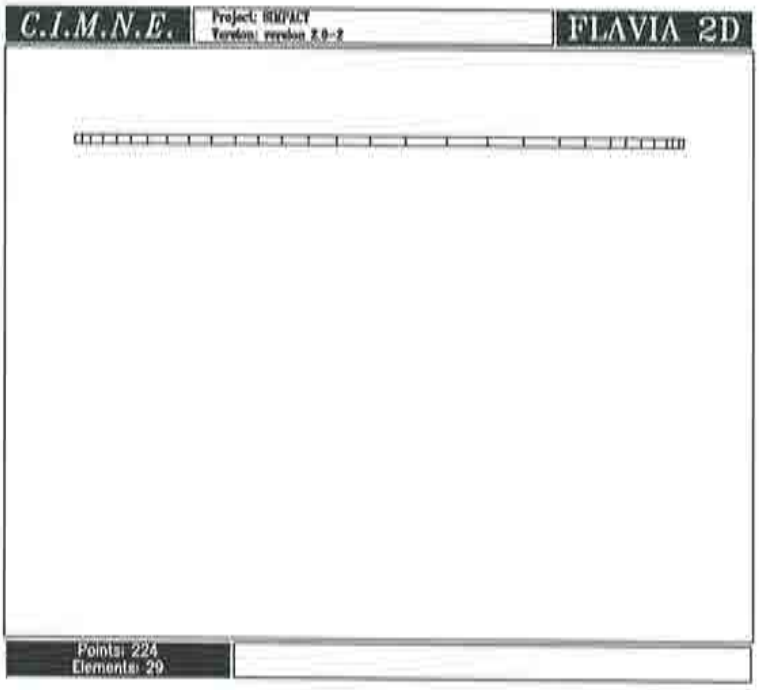

Figure 4.5 Initial geometry of sheet (2D solid elements).

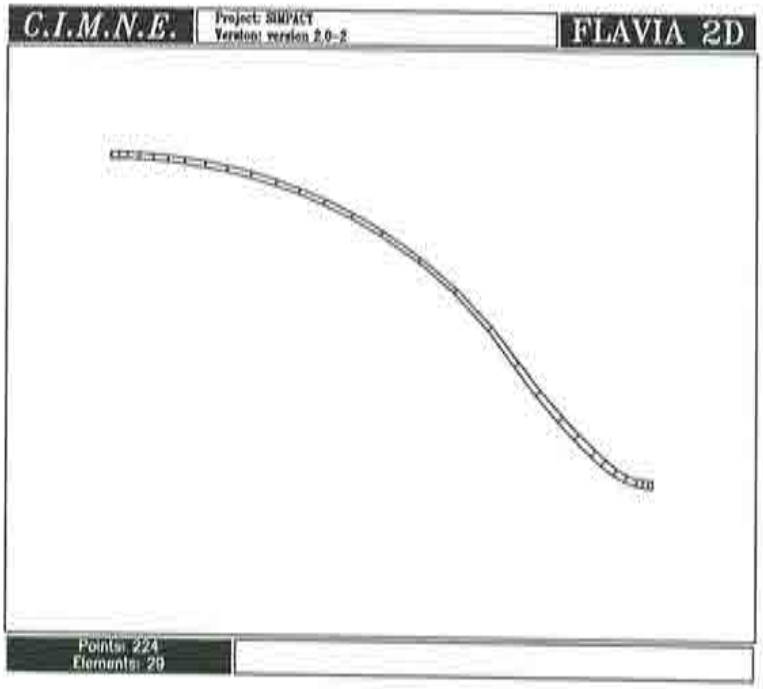

Figure 4.6 Sheet geometry after deformations were complete.

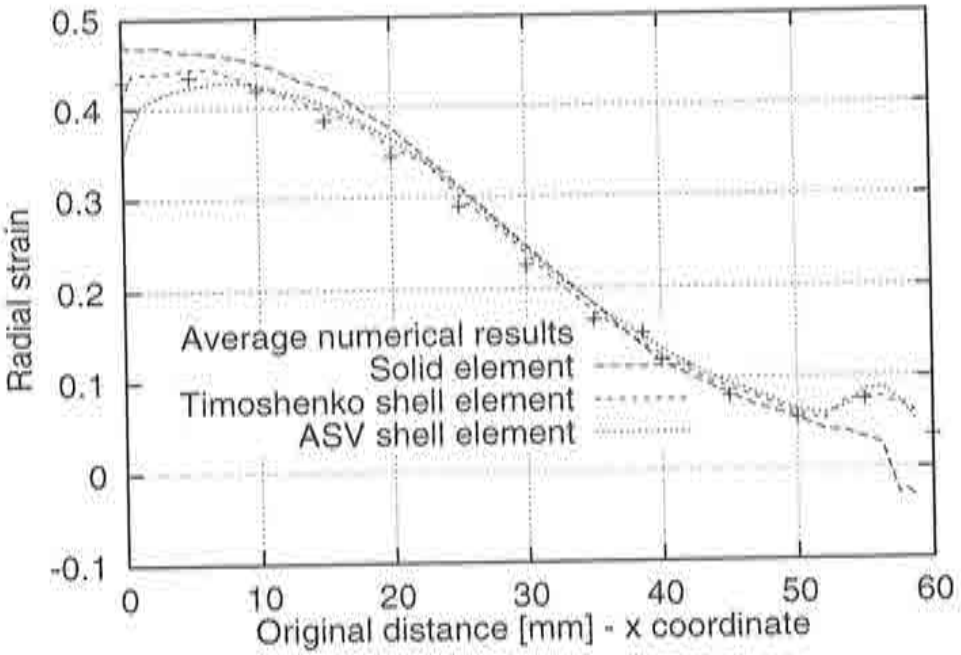

Figure 4.7a Radial strain distribution - f=0.0.

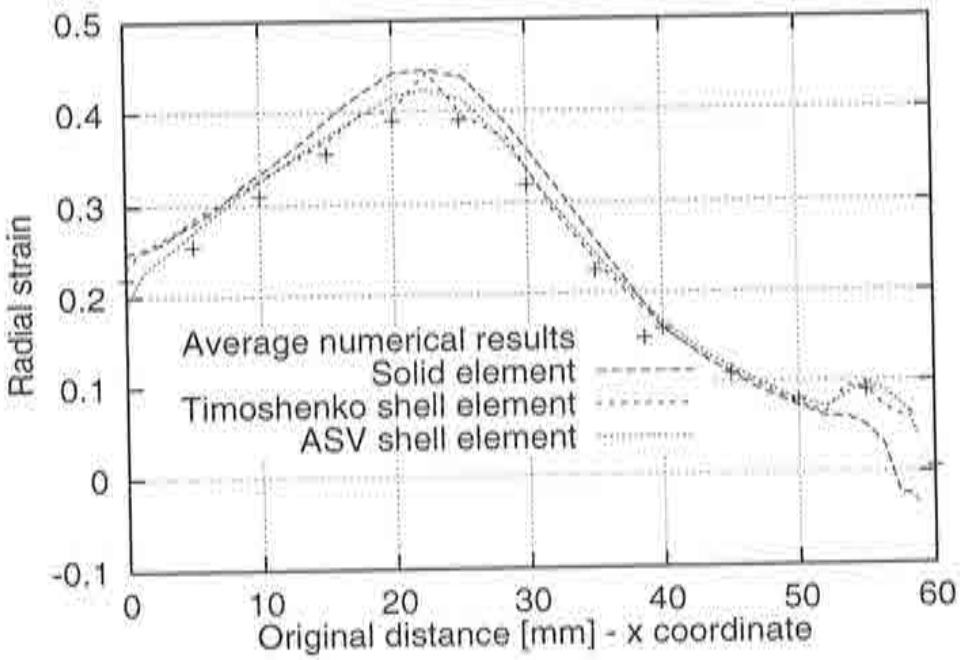

Figure 4.7b Radial strain distribution - f=0.15.

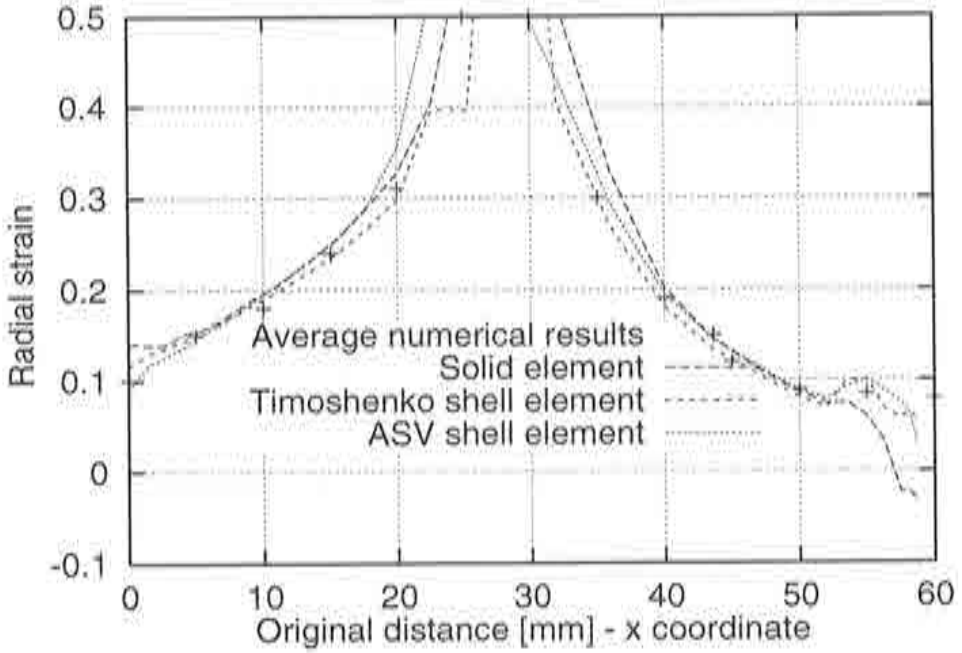

Figure 4.7c Radial strain distribution - f=0.30.

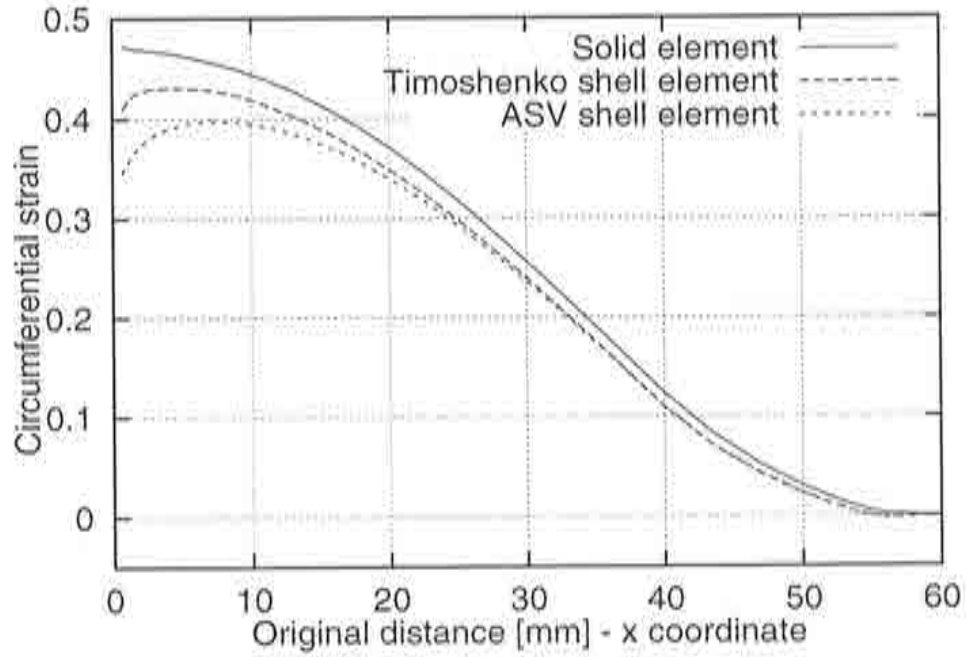

Figure 4.8a Circumferential strain distribution - f=0.0.

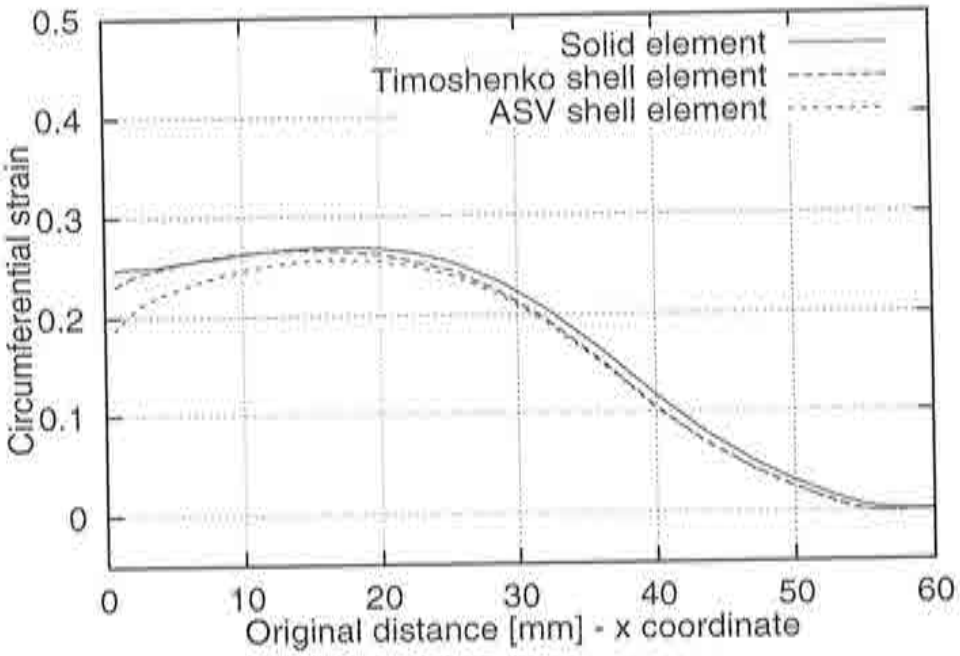

Figure 4.8b Circumferential strain distribution - f=0.15.

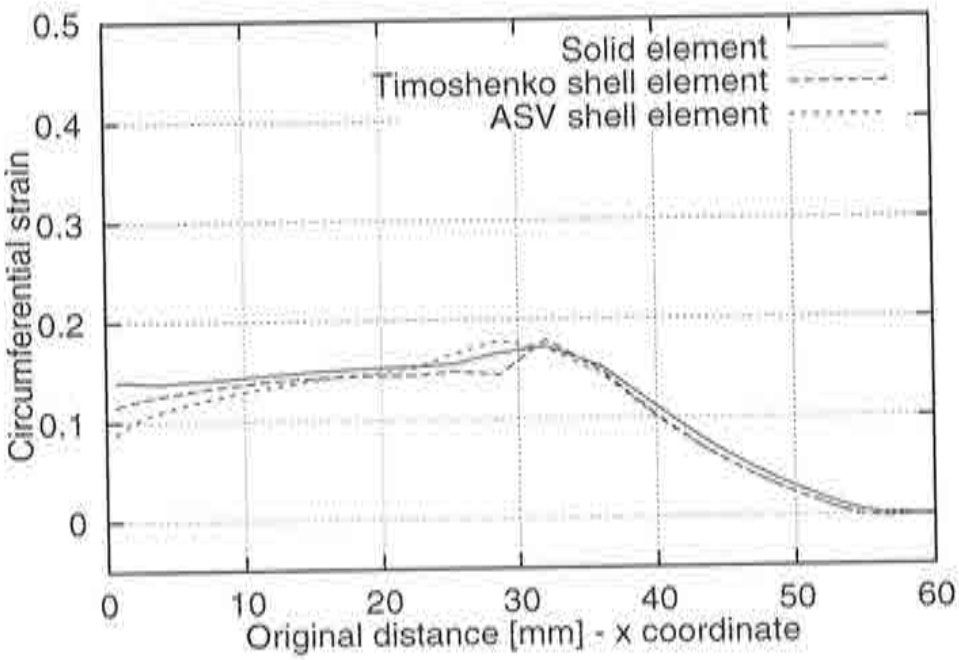

Figure 4.8c Circumferential strain distribution - f=0.30.

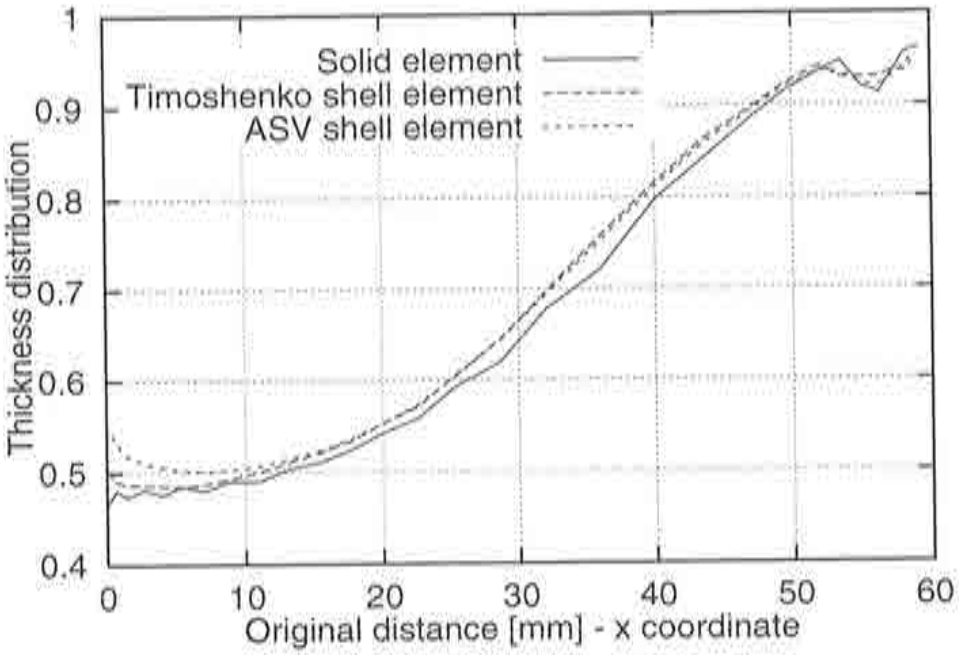

Figure 4.9a Thickness distribution - f=0.0.

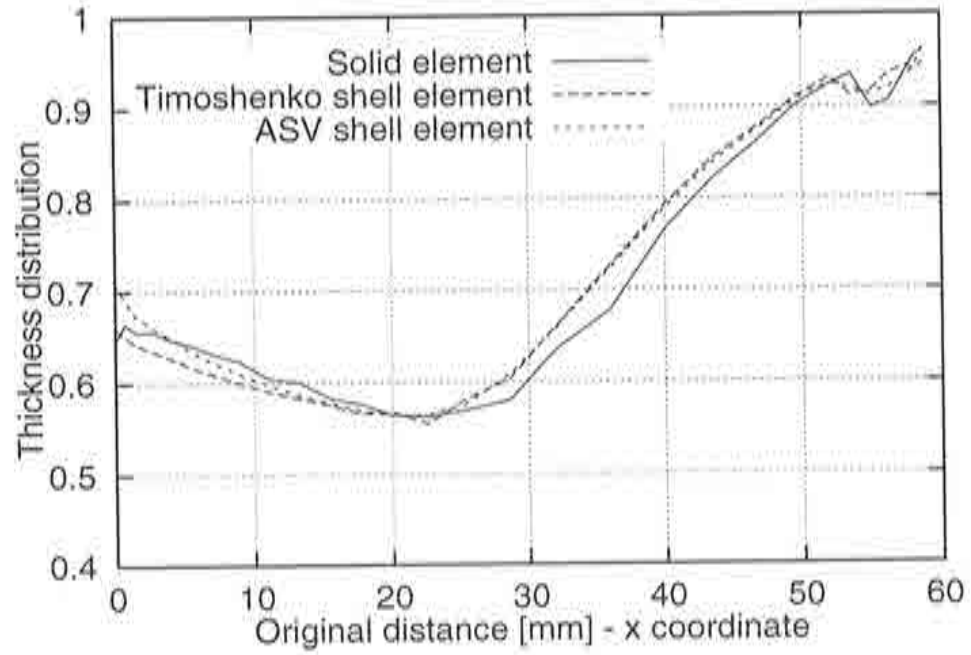

Figure 4.9b Thickness distribution - f=0.15.

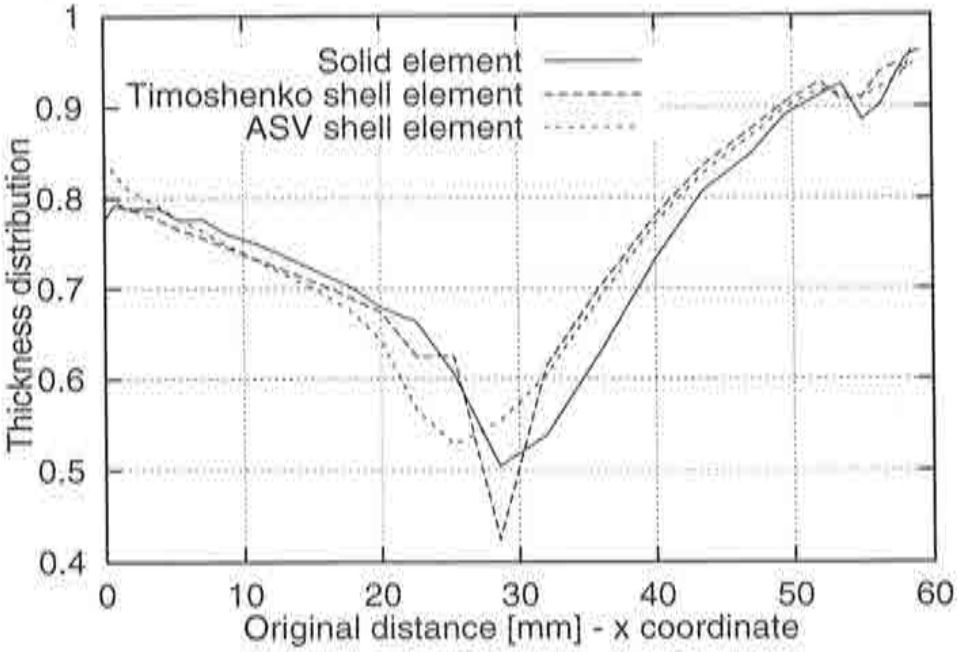

Figure 4.9c Thickness distribution - f=0.30.

4.7.2 Ohio State University Benchmark - DEEP DRAWING

4.7.2.1 Problem description

The analysis of the deep drawing process of a thin sheet by a hemispherical punch is carried out. To demonstrate the performance of evaluated ASC element, three different element types were used for this problem: QSOL4R axisymmetric quadrilateral solid element, AXIS2K axisymmetric shell element based on Timoshenko theory and ASC axisymmetric shell element. The final shape of the sheet is a hemisphere of radius $59.18mm$ and depth $40mm$.

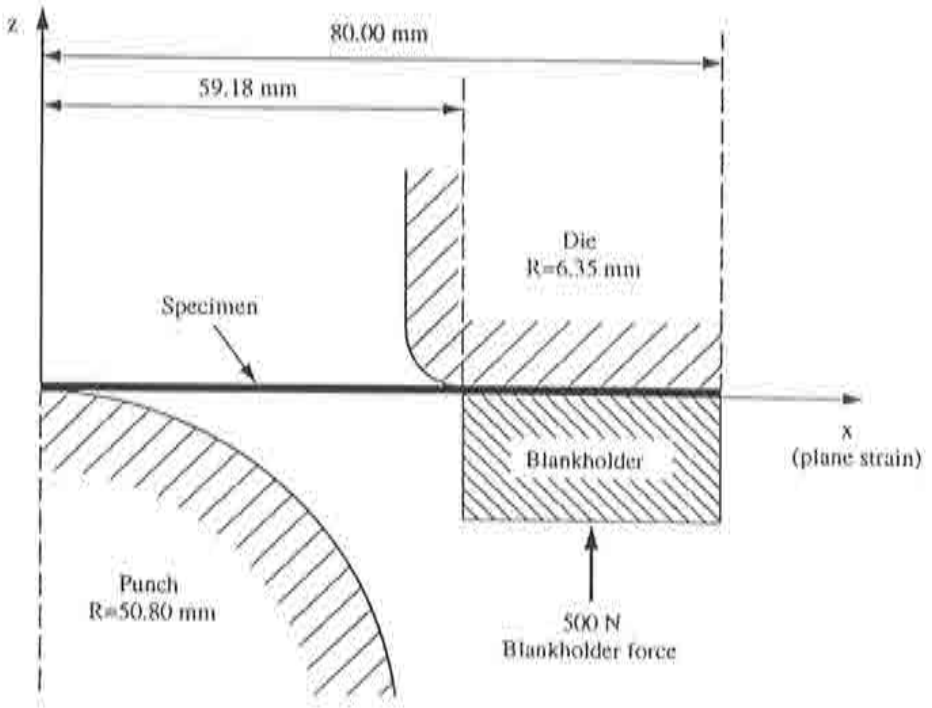

Figure 4.10 Geometry of the OSU Benchmark - Deep Drawing.

4.7.2.2 Finite element model

Geometry

The geometry of the punch, die, blankholder and sheet are shown in Figure 4.10. The punch radius is $R_P = 50.80mm$, the die corner radius is $R_D = 6.35mm$ and the sheet thickness is $t = 1.00mm$. The initial diameter of the sheet rim is $D_o = 80.00mm$ and the punch travel is $40.00mm$.

Mesh

The sheet was modelled using 49 QSOLR4R quadrilateral axisymmetric solid elements(4 node), 49 AXIS2K axisymmetric shell elements (2 node) and 49 ASV axisymmetric shell elements (2 node). The blankholder was modelled using 10 QSOL4R quadrilateral solid elements (4 node) to facilitate the application of the blankholder force. The punch and the die were modelled using 81 DUMQ rigid elements (4 node).

Materials

The sheet material was aluminium using a nonlinear isotropic hardening elasto-plastic model. The following properties were used:

Young's modulus: $= YOUNG = 69GPa$

Poisson's ratio: $= POISS = 0.3$

Mass density: $= MASSD = 2700kg/m^3$

Nonlinear hardening: $= CONSO = 589MPa$

$EFREF = 1.0 \times 10^{-4}$

$CONSN = 0.216$

The blankholder material was steel using a linear elastic model with the following properties:

Young's modulus: $= YOUNG = 210GPa$

Poisson's ratio: $= POISS = 0.3$

Mass density: $= MASSD = 7900kg/m^3$

Nonlinear hardening: $= CONSO =$ very high value to prevent yielding

$EFREF =$ value is unimportant

$CONSN =$ value is unimportant

Boundary Conditions

The die was held in place while the punch was moved vertically. Contact surfaces between all tools and the sheet (punch - sheet, die - sheet and blankholder - sheet contact pairs) were modelled using a different friction coefficient of 0.0, 0.15 and 0.30; the penalty coefficient for both normal and tangential contact forces was 0.01.

Loading

A constant blankholding force of 500N was applied to the surface of the blankholder as a surface load on those elements. The punch was moved vertically for $40mm$ by applying a sinusoidal velocity over the total analysis time period.

4.7.2.3 Analysis considerations

The total response time was obtained using an automatic time stepping calculation and was terminated when the punch stroke was completed. Material non-linearities were considered to be rate independent and the Updated Lagrangian formulation was used to describe geometrical non-linearities.

4.7.2.4 Results and discussion

Figures 4.11 and 4.12 show the initial geometry layout as well as the final sheet geometry for the 2D solid axisymmetric mesh. The final shape agrees very well with the solution in [L-3]. The radial and circumferential strain distributions calculated at nodal points along the upper surface for different values of frictional coefficient: 0.0, 0.15 and 0.30 are presented in Figures 4.13 and 4.14 respectively and a contour of the final sheet thickness is presented in Figure 4.15. Punch load - punch die curve is presented in Figure 4.16.

4.7.2.5 Conclusions

The radial strain distributions for the solid and shell elements agree reasonably well with the reference solution given in [L-3]. Similar results were obtained for the circumferential and thickness distributions as well as for punch load - punch force curves for all elements.

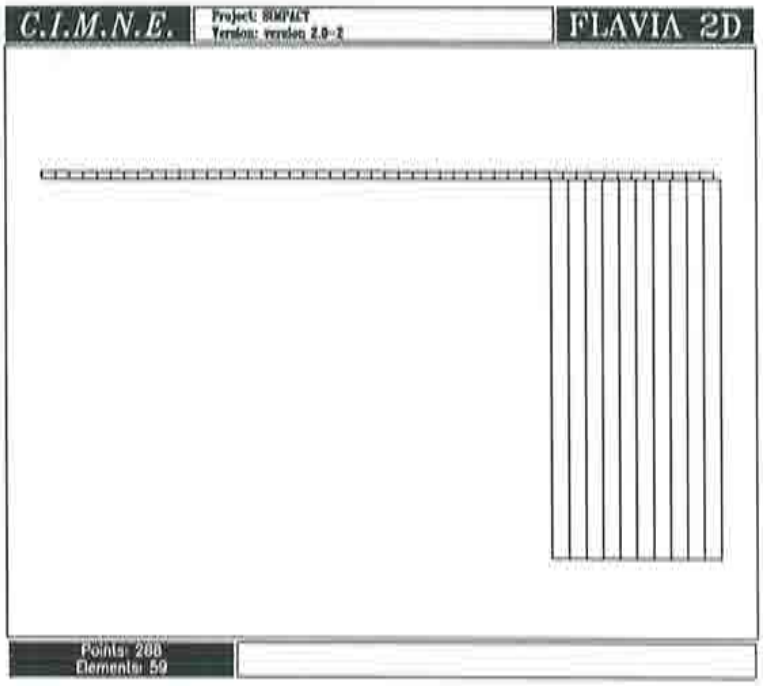

Figure 4.11 Initial geometry of sheet (2D solid elements).

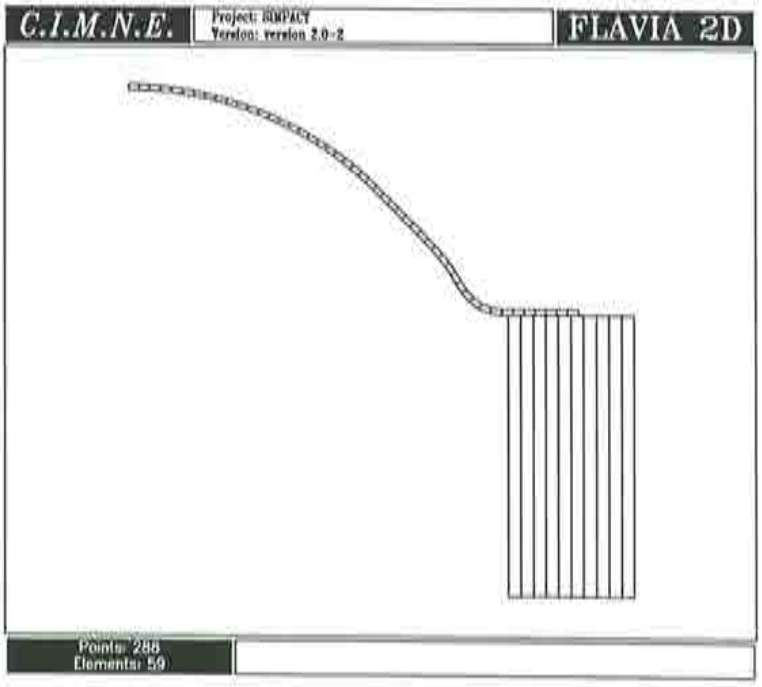

Figure 4.12 Sheet geometry after deformations were complete.

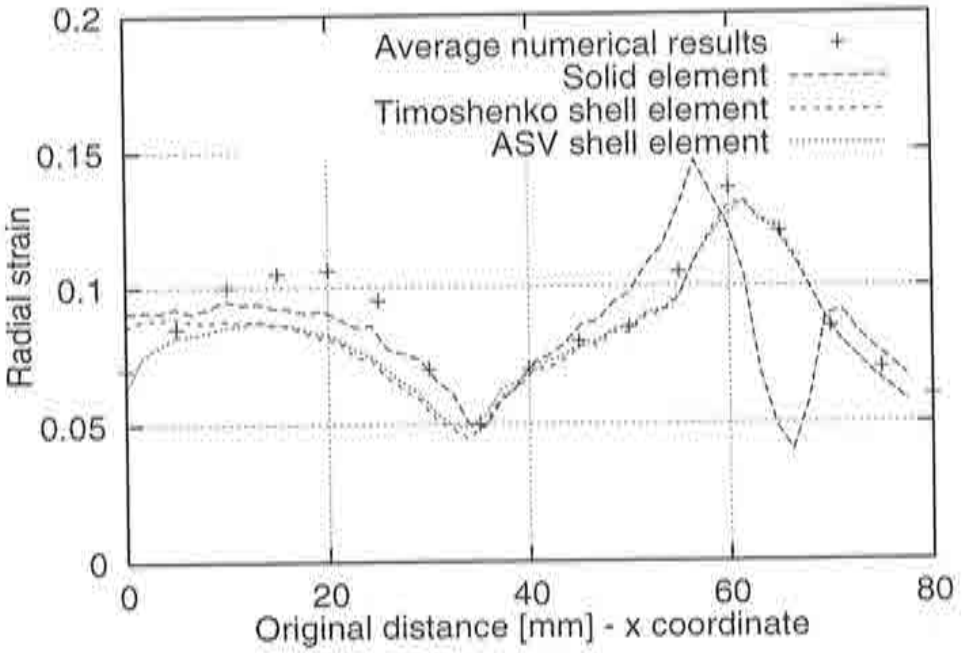

Figure 4.13a Radial strain distribution - f=0.0.

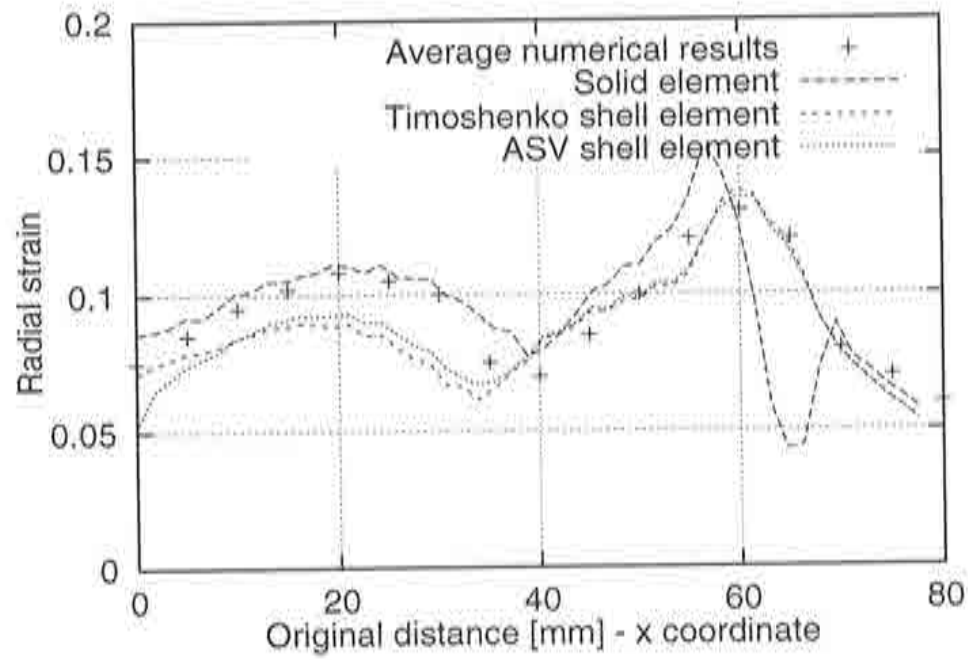

Figure 4.13b Radial strain distribution - f=0.15.

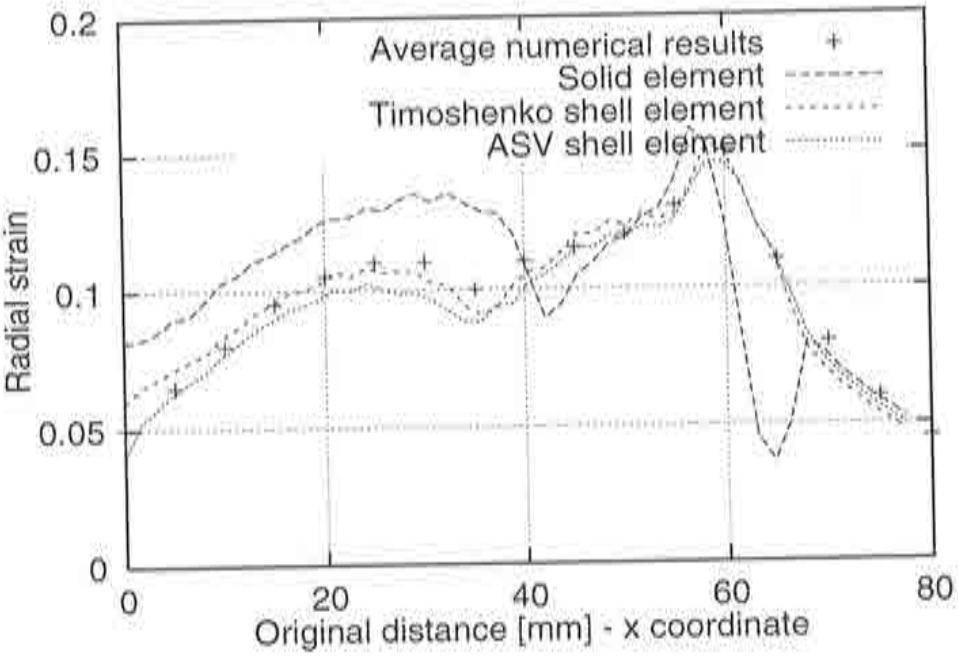

Figure 4.13c Radial strain distribution - f= 0.30.

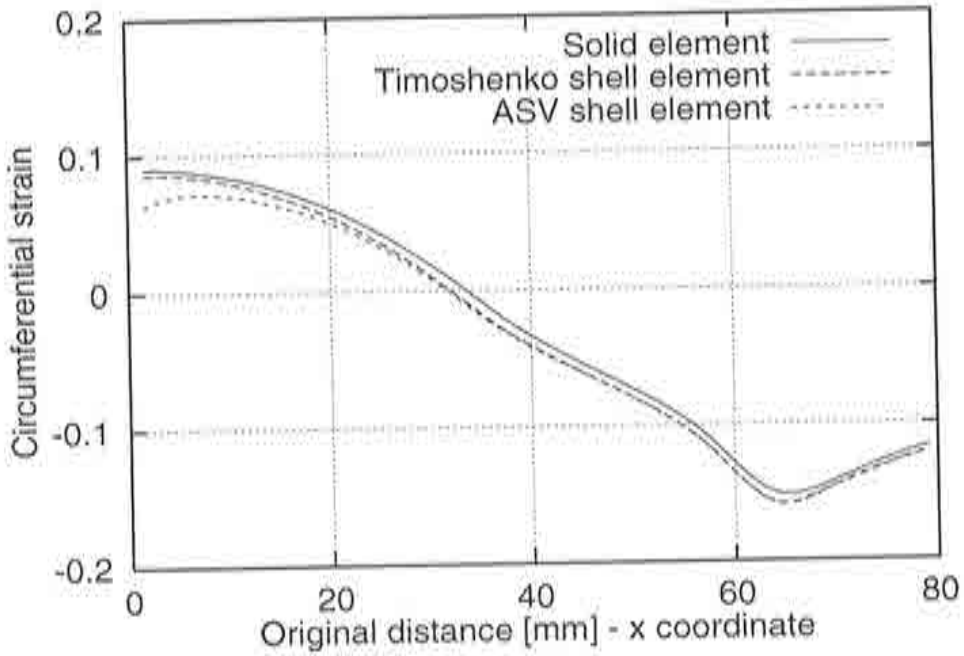

Figure 4.14a Circumferential strain distribution - f=0.0.

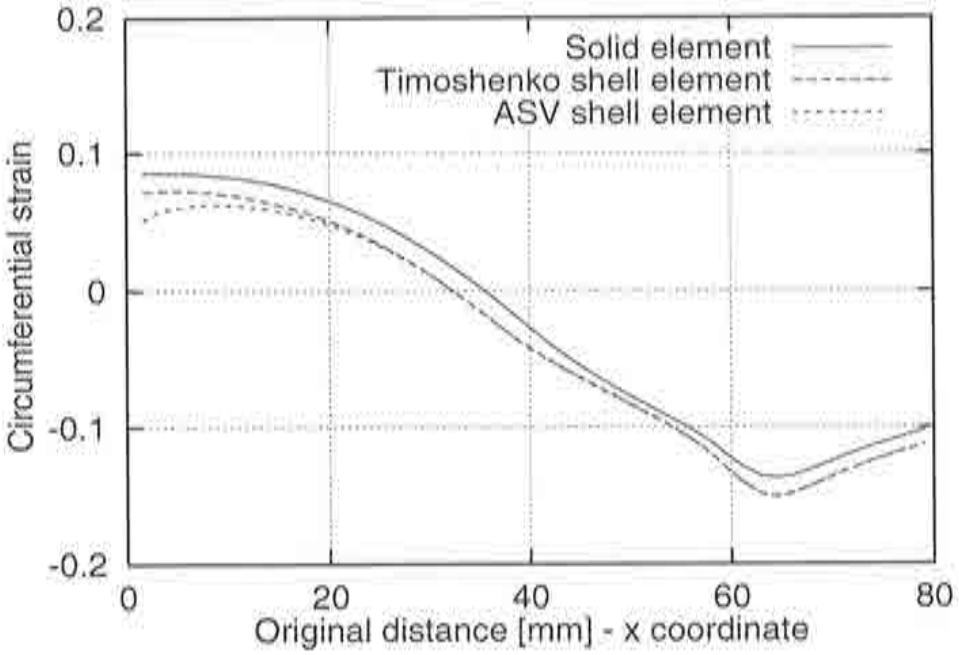

Figure 4.14b Circumferential strain distribution - f=0.15.

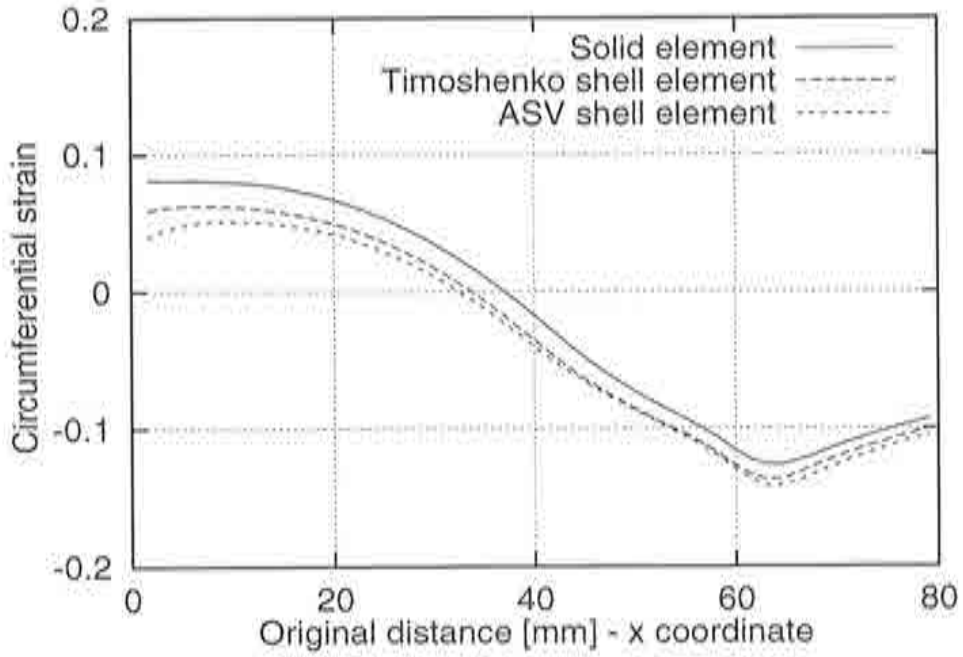

Figure 4.14c Circumferential strain distribution - f=0.30.

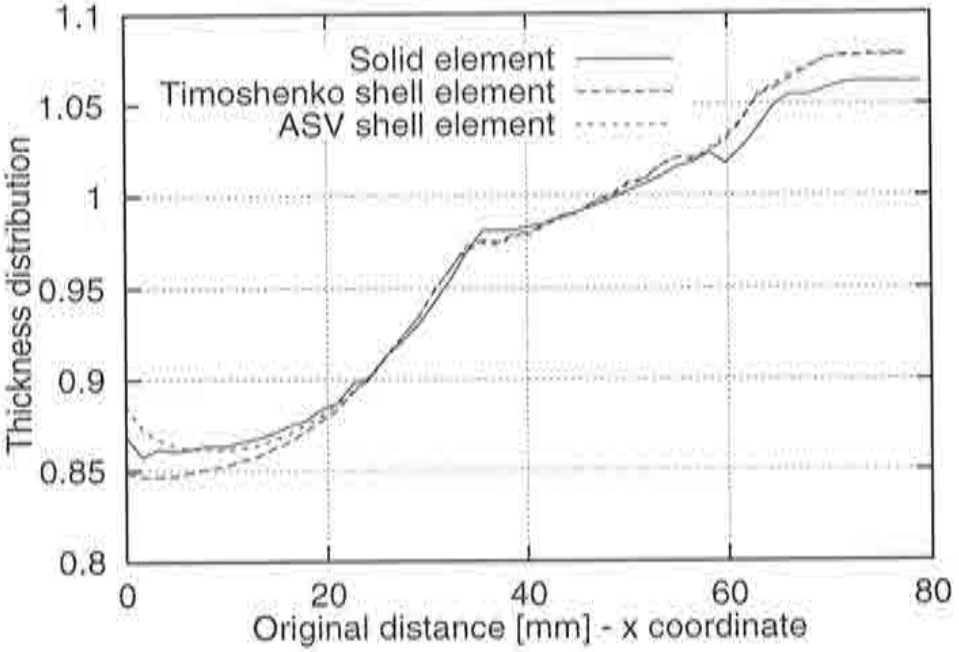

Figure 4.15a Thickness distribution - f=0.0.

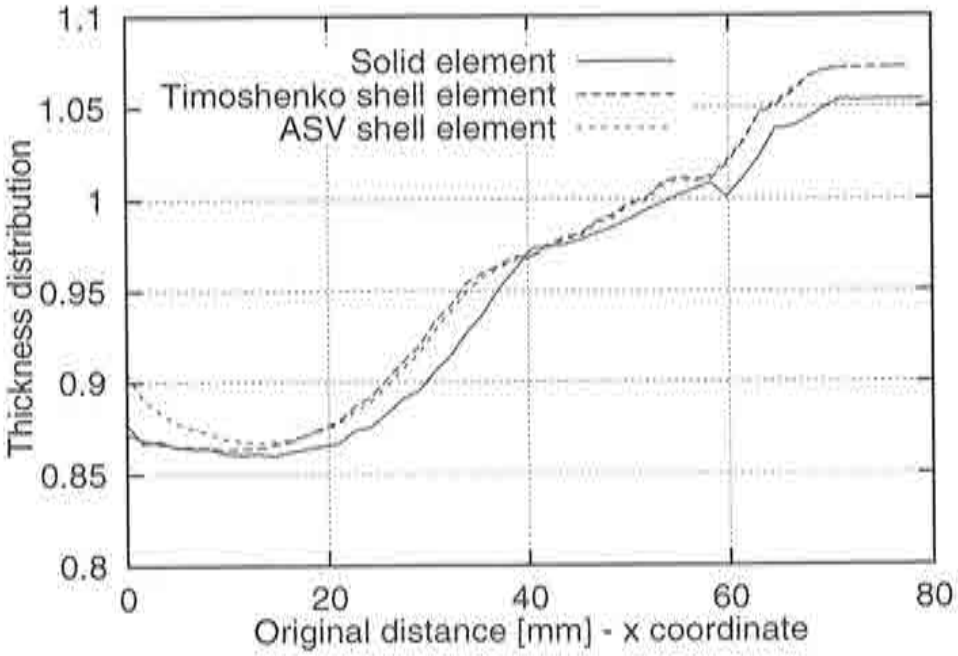

Figure 4.15b Thickness distribution - f=0.15.

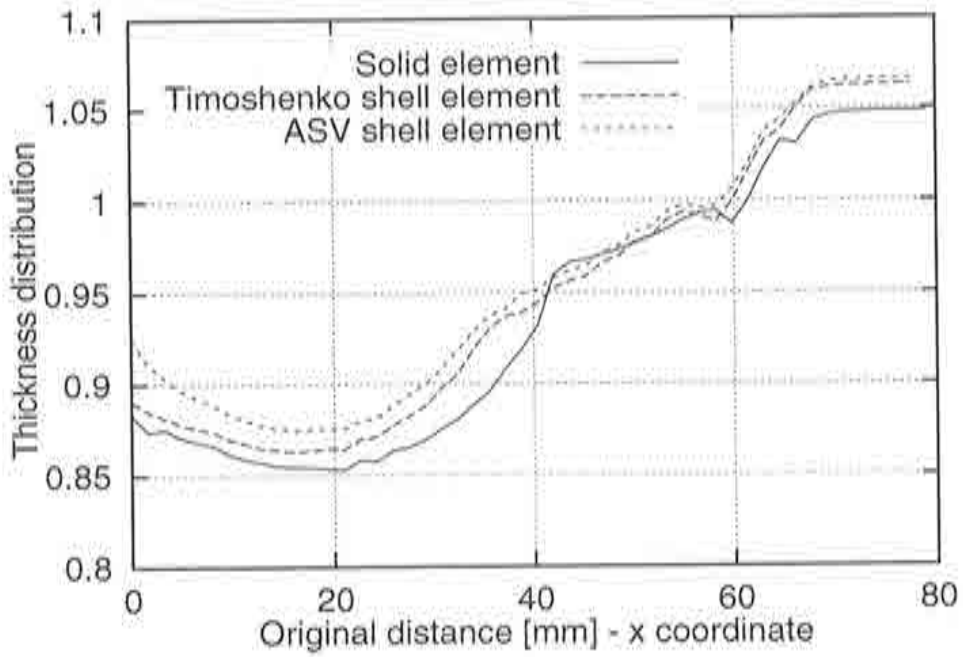

Figure 4.15c Thickness distribution - f=0.30.

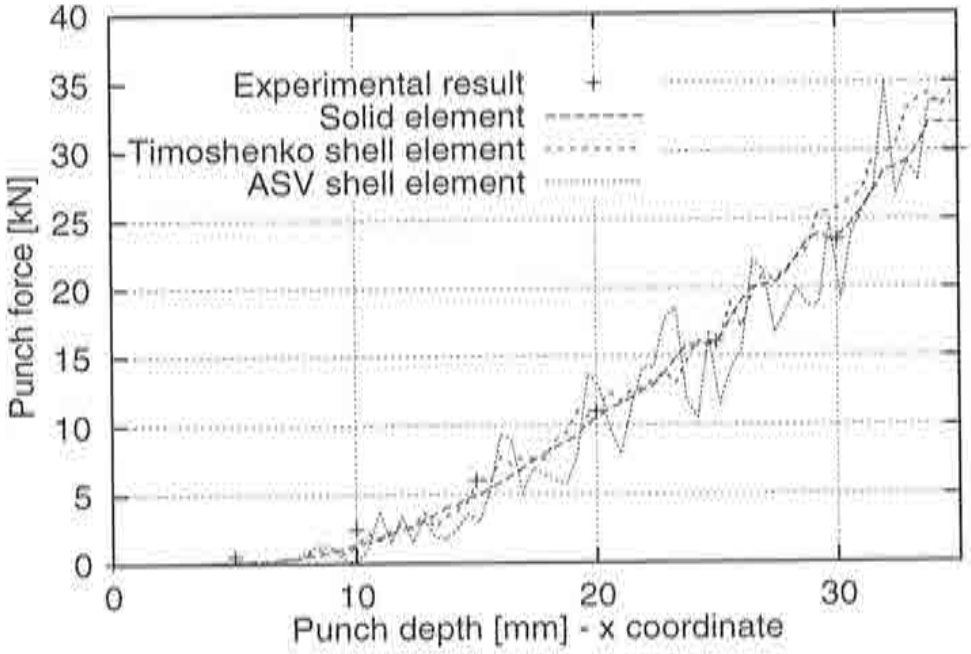

Figure 4.16a Curve punch load - punch travel - f=0.0.

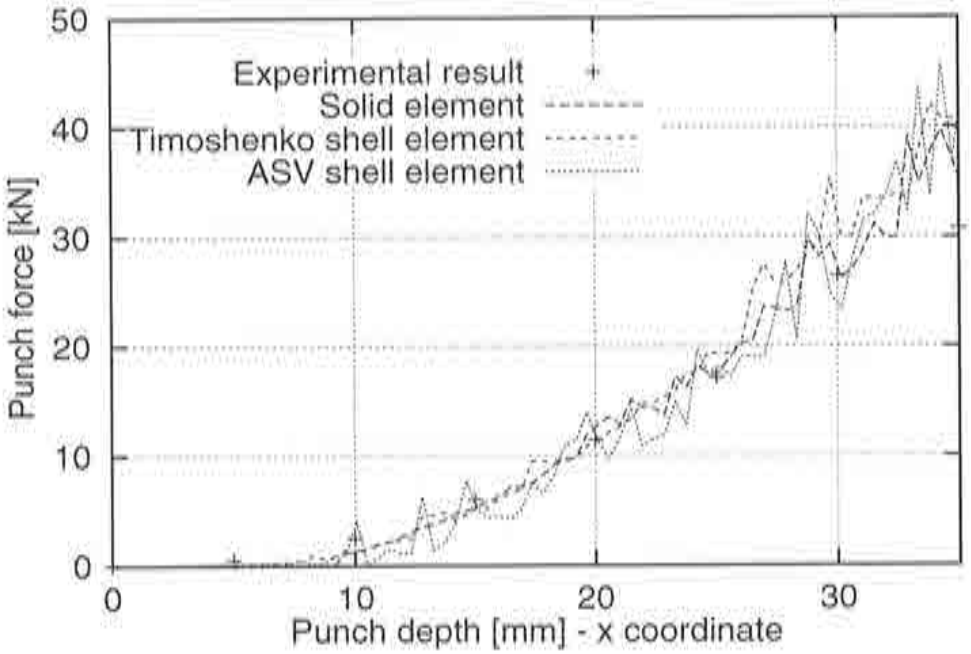

Figure 4.16b Curve punch load - punch travel - f=0.15.

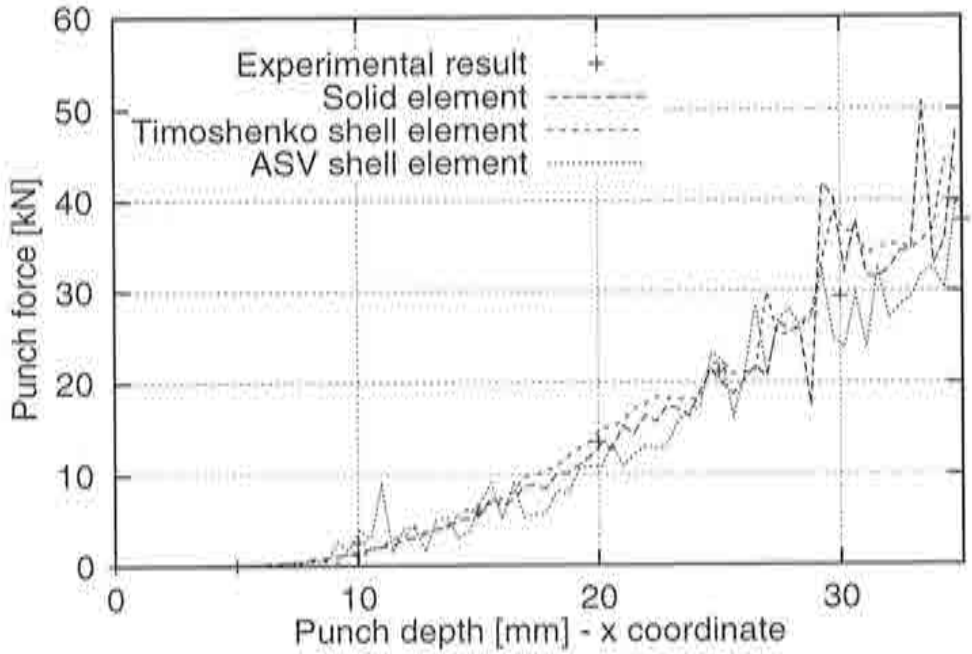

Figure 4.16c Curve punch load - punch travel - f=0.30.

4.7.3 Chalmers Test

4.7.3.1 Problem description

The analysis of the deep drawing process of a thin sheet by a cylindrical punch is carried out. The experimental data obtained by the Department of Structural Mechanics of the Chalmers University of Technology [S-2] is compared with the numerical result obtained by the code Stampack, with three different element types: QSOL4R axisymmetric quadrilateral solid element, AXIS2K axisymmetric shell element based on Timoshenko theory and ASC axisymmetric shell element.

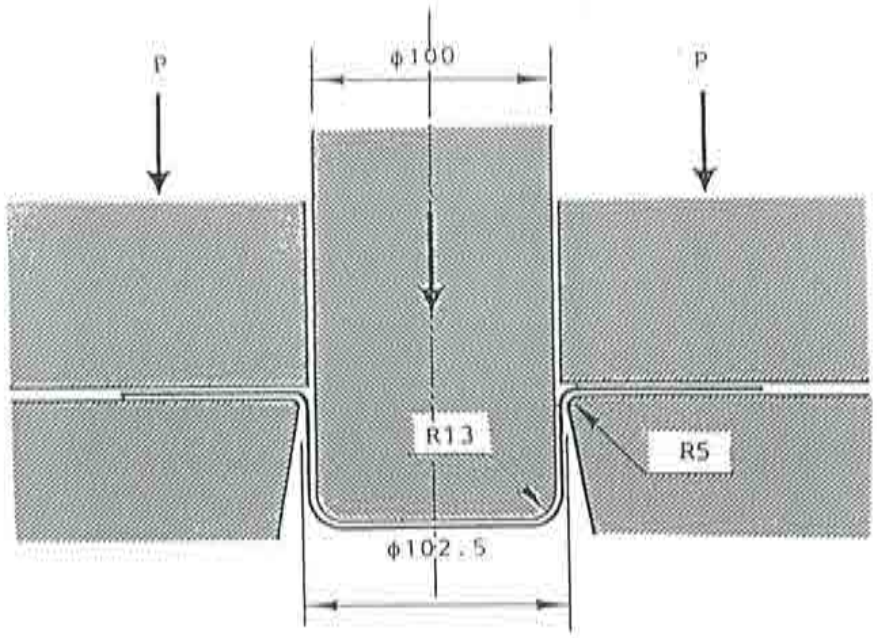

Figure 4.17 Geometry of the Chalmers University Test.

4.7.3.2 Finite element model

Geometry

The geometry of the punch, die and blankholder is shown in Figure 4.17. The punch corner radius is $R_p = 13.00mm$, the die corner radius is $R_D = 5.00mm$ and the sheet thickness is $t = 0.70mm$. The diameter of the punch rim is $D_o = 100.00mm$ and the punch travel is $31.50mm$.

Mesh

The sheet was modelled using 100 QSOL4R quadrilateral axisymmetric solid elements (4 node), 100 AXIS2K axisymmetric shell elements (2 node) and 100 ASV axisymmetric shell elements (2 node). The blankholder was modelled using 10 QSOL4R quadrilateral solid elements (4 node) to facilitate the application of the blankholder force. The punch and the die were modelled using 40 DUMQ rigid elements (2 node). The initial mesh is shown in Figure 4.18.

Materials

The sheet material was steel using a nonlinear isotropic hardening elasto-plastic model. The following properties were used:

Young's modulus: $= YOUNG = 210GPa$

Poisson's ratio: $= POISS = 0.3$

Mass density: $= MASSD = 7900kg/m^3$

Nonlinear hardening: $= CONSO = 547.0MPa$

$EFREF = 16.15 \times 10^{-16}$

$CONSN = 0.18$

The blankholder material was steel using a linear elastic model with the following properties:

Young's modulus: $= YOUNG = 210GPa$

Poisson's ratio: $= POISS = 0.3$

Mass density: $= MASSD = 7900kg/m^3$

Nonlinear hardening: $=$ very high value to prevent yielding

$EFREF =$ value is unimportant

$CONSN =$ value is unimportant

Boundary Conditions

The die and the blankholder were held in place while the punch was moved vertically. Contact surfaces between all tools and the sheet (punch - sheet, die - sheet and blankholder - sheet contact pairs) were modelled using a friction coefficient of 0.05 which corresponds to slightly lubricated tool surfaces; the penalty coefficient for both normal and tangential contact forces was 0.01.

Loading

A constant blankholding force of 80N was applied to the surface of the blankholder as a surface load on those elements. The punch was moved vertically for $31.50mm$ by applying a sinusoidal velocity over the total analysis time period.

4.7.3.3 Analysis considerations

The total response time was obtained using an automatic time stepping calculation and the analysis was terminated when the punch stroke was completed. Material non-linearities were considered to be rate independent and the Updated Lagrangian formulation was used to describe geometrical non-linearities.

4.7.3.4 Results and discussion

Figures 4.18 and 4.19 show the initial geometry layout as well as the final sheet geometry for the 2D solid axisymmetric mesh. The final shape agrees very well with the solution in [S-2]. The radial and circumferential strain distributions calculated at nodal points along the upper surface are presented in Figures 4.20 and 4.21 respectively and are compared with the obtained experimental results [S-2] and show a good correlation. The contour of the final sheet thickness is presented in Figure 4.22. The comparison between the experimental result [S-2] and numerical result for the curve punch load - punch travel is presented in Figure 4.23. This comparison is reasonably good with a maximum error of 40% when the punch has travelled $15mm$.

4.7.3.5 Conclusions

The numerical results obtained using the ASV element show good correlation with the experimental results obtained by Chalmers University [S-2].

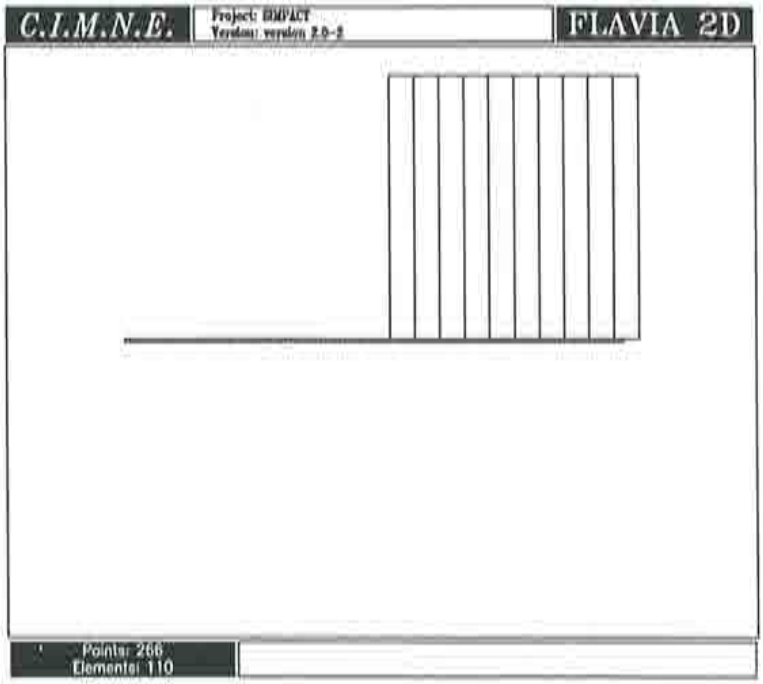

Figure 4.18 Initial geometry of sheet (2D solid elements).

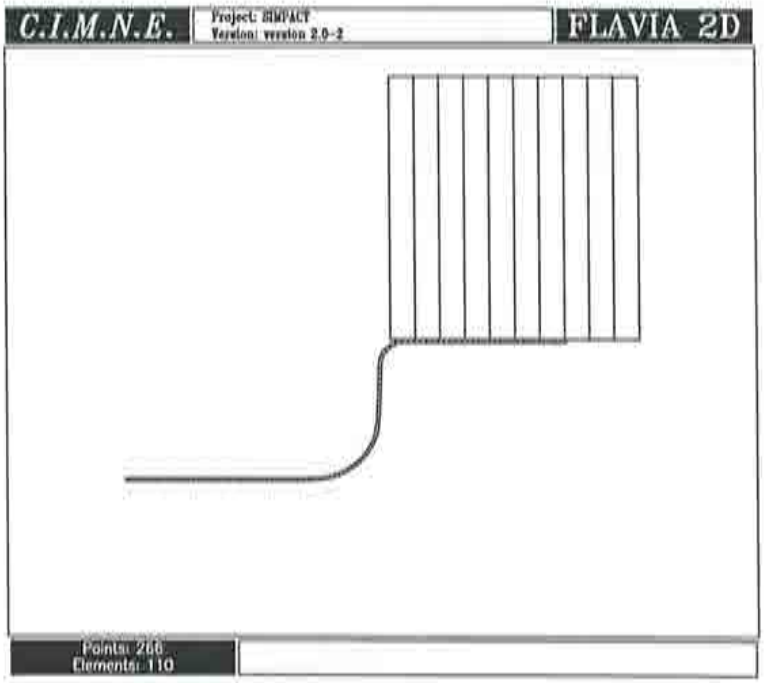

Figure 4.19 Sheet geometry after deformations were complete.

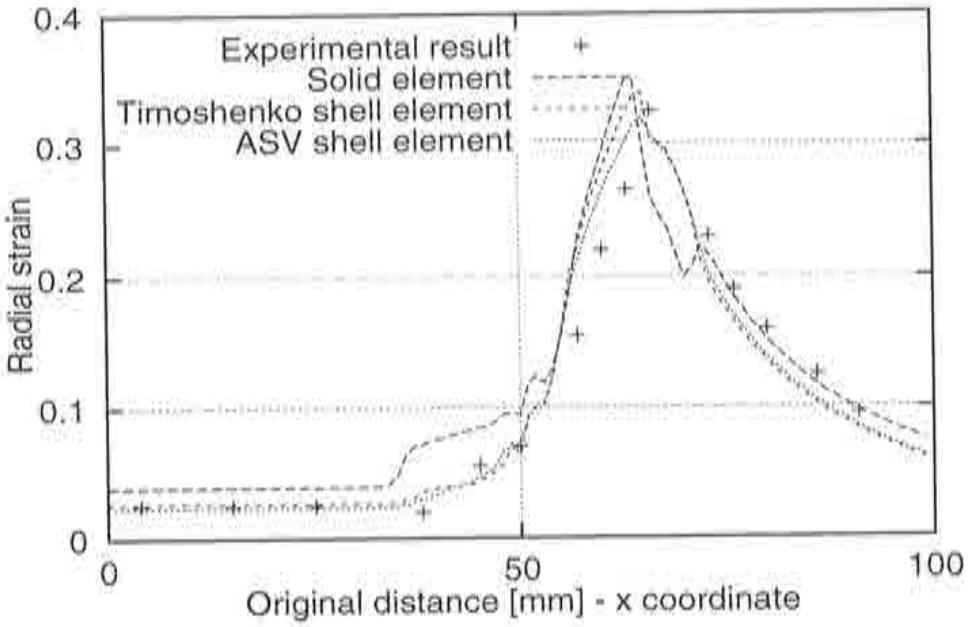

Figure 4.20 Radial strain distribution.

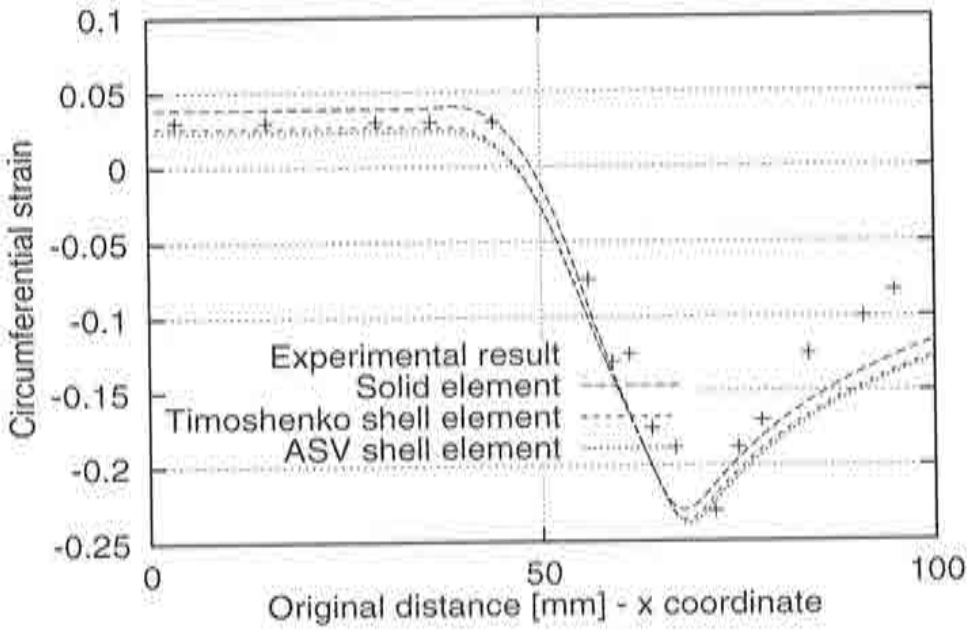

Figure 4.21 Circumferential strain distribution.

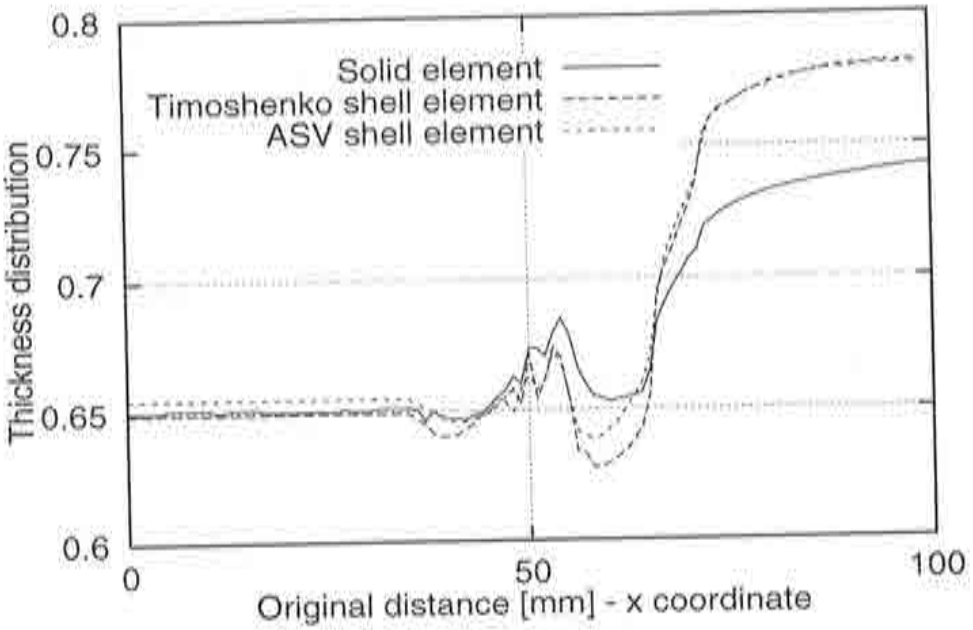

Figure 4.22 Thickness distribution.

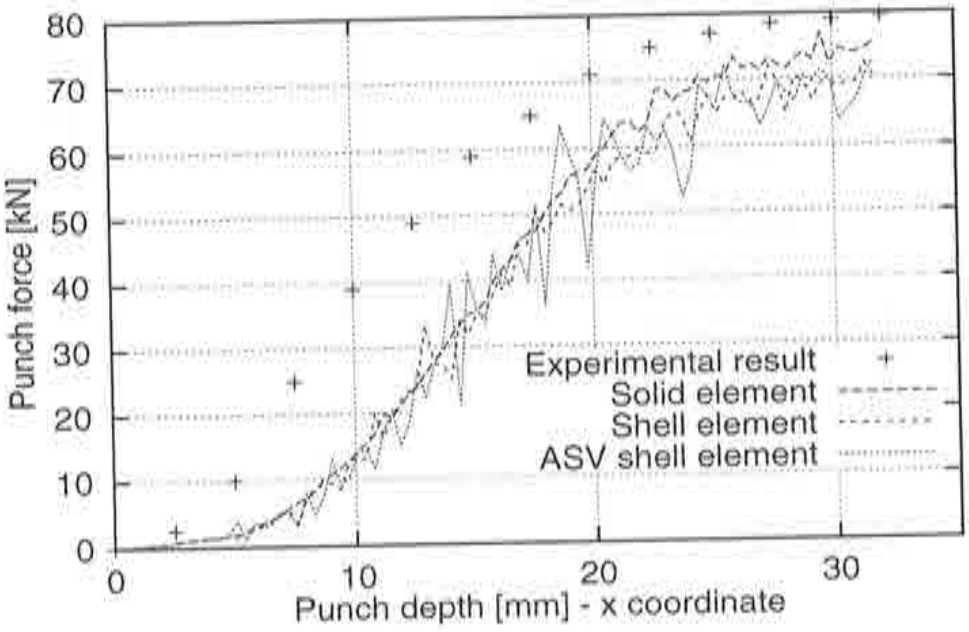

Figure 4.23 Curve punch load - punch travel.

APPENDIX 4.1

DETAILS OF NON-LINEAR SOLID MECHANICS THEORY

A4.1 BASIC THEORY

The present appendix is aimed to introduce sufficient continuum mechanics for the Chapter 4 and Chapter 5 which concentrate on particularization of non-linear theory for the axisymmetric ASV shell and thin BSN shell, respectively. There are reviewed descriptions of motion and deformation of a solid body as well as the most important stress and strain tensors and the stress and strain rate measures. The equations of motion are presented in the spatial and material configurations. The weak form of equations of motion is also given. Finally, the constitutive equations necessary for the definition of the motion problem of a deformable body as well as the yield conditions are presented.

A4.1.1 Description of motion

Two different descriptions of the motion of a continuum medium are used in mechanics, namely the Eulerian and Lagrangian descriptions. The Eulerian or spatial description concentrates on the behaviour at the fixed points in the space. The Lagrangian or material description concentrates on the behaviour of a set of material particles. The consequence of applying the concept of Lagrangian description to the spatial configuration as the reference one is the Updated Lagrangian formulation.

The motion of a body in the time interval 0 to T is presented in Figure 4A.1, where Ω^0 is the body configuration at time 0 called original or material, Ω^t is the body configuration at time T called deformed or spatial, Γ^0 is the boundary of the body in material configuration and Γ^t is the boundary of the body in spatial configuration.

The material coordinates $\mathbf{X} = \{X_1, X_2, X_3\}^T, (\mathbf{X} \in \Omega^0)$ and the spatial coordinates $\mathbf{x} = \{x_1, x_2, x_3\}^T, (\mathbf{x} \in \Omega^t)$ are expressed in the same cartesian coordinate system.

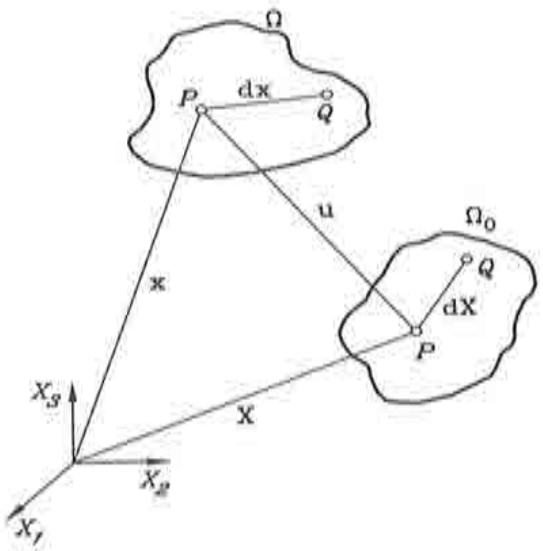

Figure 4A.1 Motion of a body.

The particle P in the reference configuration Ω^0 has the position vector $\mathbf{X}$ and occupies the location p in the current configuration Ω^t with the position vector $\mathbf{x}$. Mathematically, the motion is expressed as

$$\mathbf{x} = \mathbf{x}(\mathbf{X}, t) \tag{Ap4.1}$$

or

$$\mathbf{X} = \mathbf{X}(\mathbf{x}, t) \tag{Ap4.2}$$

In a similar fashion, the displacement field $\mathbf{u} = \{u_1, u_2, u_3\}^T$ can be defined on Ω^0 as material description

$$\mathbf{u}(\mathbf{X}, t) = \mathbf{x}(\mathbf{X}, t) - \mathbf{X} \tag{Ap4.3}$$

or on Ω^t as spatial description

$$\mathbf{u}(\mathbf{x}, t) = \mathbf{x} - \mathbf{X}(\mathbf{x}, t) \tag{Ap4.4}$$

The equations (*Ap*4.3) and (*Ap*4.4) have different physical meanings. The first one express the displacement of the particle with position vector $\mathbf{X}$ in the reference configuration at the current time t. The second, is the displacement of any particle which is currently at position $\mathbf{x}$.

A4.1.2 Deformation gradient

The deformation gradient tensor $\mathbf{F}$ is defined as the derivative of the spatial coordinates with respect to the material coordinates

$$\mathbf{F} = \frac{\partial \mathbf{x}}{\partial \mathbf{X}} \tag{Ap4.5}$$

This tensor relates the vectors $d\mathbf{x}$ and $d\mathbf{X}$ as

$$d\mathbf{x} = \mathbf{F} d\mathbf{X} \tag{Ap4.6}$$

The deformation gradient in terms of displacements is expressed substituting (*Ap*4.4) into (*Ap*4.5) as

$$\mathbf{F} = \mathbf{I} + \frac{\partial \mathbf{u}}{\partial \mathbf{X}} \tag{Ap4.7}$$

A4.1.3 Green-Lagrange and Almansi strain tensors

The squares of the lengths of the vectors $d\mathbf{X}$ and $d\mathbf{x}$ are respectively

$$d\mathbf{r}_0^2 = \mid d\mathbf{X} \mid^2 = d\mathbf{X}^T d\mathbf{X} \tag{Ap4.8a}$$

$$d\mathbf{r}^2 = \mid d\mathbf{x} \mid^2 = d\mathbf{x}^T d\mathbf{x} \tag{Ap4.8b}$$

The squared length in the deformed configuration can be rewritten in terms of the vector $d\mathbf{X}$ in the reference configuration

$$d\mathbf{r}^2 = d\mathbf{X}^T \mathbf{F}^T \mathbf{F} d\mathbf{X} = d\mathbf{X}^T \mathbf{C} d\mathbf{X} \tag{Ap4.9}$$

Using the equation (*Ap*4.9), the right and left Cauchy-Green tensors are defined respectively

$$\mathbf{C} = \mathbf{F}^T \cdot \mathbf{F}, \quad \mathbf{b} = \mathbf{F} \cdot \mathbf{F}^T \tag{Ap4.10}$$

Similarly, the squared length in the reference configuration can be written in terms of the vector $d\mathbf{x}$ in the deformed configuration as

$$d\mathbf{r}_0^2 = d\mathbf{x}^T (\mathbf{F}^{-1})^T \mathbf{F}^{-1} d\mathbf{x} = d\mathbf{x}^T \mathbf{c} d\mathbf{x} \tag{Ap4.11}$$

what gives the Cauchy's deformation tensor - Finger deformation tensor

$$\mathbf{c} = (\mathbf{F}^{-1})^T \cdot \mathbf{F}^{-1} = \mathbf{b}^{-1} \qquad (Ap4.12)$$

The difference between the squared lengths for two neighbouring particles in a continuum is used as a measure of deformation.

The difference expressed in terms of the vector $d\mathbf{X}$ in the reference configuration leads to the Lagrangian description

$$d\mathbf{r}^2 - d\mathbf{r}_0^2 = d\mathbf{x}^2 - d\mathbf{X}^2 = d\mathbf{X}^T(\mathbf{C} - \mathbf{I})d\mathbf{X} = 2d\mathbf{X}^T\mathbf{E}d\mathbf{X} \qquad (Ap4.13)$$

what gives the Green-Lagrange strain tensor

$$\mathbf{E} = \frac{1}{2}(\mathbf{C} - \mathbf{I}) = \frac{1}{2}[(\frac{\partial \mathbf{u}}{\partial \mathbf{X}}) + (\frac{\partial \mathbf{u}}{\partial \mathbf{X}})^T + (\frac{\partial \mathbf{u}}{\partial \mathbf{X}})^T \cdot (\frac{\partial \mathbf{u}}{\partial \mathbf{X}})] \qquad (Ap4.14)$$

The difference expressed in terms of the vector $d\mathbf{x}$ in the deformed configuration leads to the Eulerian description

$$d\mathbf{r}^2 - d\mathbf{r}_0^2 = d\mathbf{x}^2 - d\mathbf{X}^2 = d\mathbf{x}^T(\mathbf{I} - \mathbf{c})d\mathbf{x} = 2d\mathbf{x}^T\mathbf{e}d\mathbf{x} \qquad (Ap4.15)$$

what gives the Almansi strain tensor

$$\mathbf{e} = \frac{1}{2}(\mathbf{I} - \mathbf{c}) = \frac{1}{2}[(\frac{\partial \mathbf{u}}{\partial \mathbf{x}}) + (\frac{\partial \mathbf{u}}{\partial \mathbf{x}})^T - (\frac{\partial \mathbf{u}}{\partial \mathbf{x}})^T \cdot (\frac{\partial \mathbf{u}}{\partial \mathbf{x}})] \qquad (Ap4.16)$$

where $\mathbf{I}$ is the unit matrix. The Green Lagrange and Almansi strain tensors are symmetric and are derived from the difference between the square lengths $d\mathbf{r}^2 - d\mathbf{r}_0^2$ which is zero for rigid body motions.

The Green-Lagrange tensor and the Almansi tensor are related as follows

$$\mathbf{E} = \mathbf{F}^T \cdot \mathbf{e} \cdot \mathbf{F} \qquad (Ap4.17)$$

A4.1.4 Rate of deformation and spin

In the Lagrangian description of motion, the material velocity field $\mathbf{V}(\mathbf{X}, t)$ and the material acceleration field $\mathbf{A}(\mathbf{X}, t)$ are expressed as

$$\mathbf{V}(\mathbf{X}, t) = \frac{\partial \mathbf{u}(\mathbf{X}, t)}{\partial t} \tag{Ap4.18}$$

$$\mathbf{A}(\mathbf{X}, t) = \frac{\partial \mathbf{V}(\mathbf{X}, t)}{\partial t} = \frac{\partial^2 \mathbf{u}(\mathbf{X}, t)}{\partial t^2} \tag{Ap4.19}$$

In the Eulerian description of motion, the spatial velocity field $\mathbf{v}(\mathbf{x}, t)$ and spatial acceleration field $\mathbf{a}(\mathbf{x}, t)$ are expressed as

$$\mathbf{v}(\mathbf{x}, t) = \mathbf{V}(\mathbf{X}, t)\big|_{\mathbf{X}=\mathbf{x}-\mathbf{u}(\mathbf{x},t)} \tag{Ap4.20}$$

$$\mathbf{a}(\mathbf{x}, t) = \mathbf{A}(\mathbf{X}, t)\big|_{\mathbf{X}=\mathbf{x}-\mathbf{u}(\mathbf{x},t)} \tag{Ap4.21}$$

The spatial acceleration is the material time derivative of the spatial velocity

$$\mathbf{a}(\mathbf{x}, t) = \dot{\mathbf{v}}(\mathbf{x}, t) \tag{Ap4.22}$$

where $(\dot{-})$ denotes the material derivative, what can be rewritten as

$$\mathbf{a}(\mathbf{x}, t) = \frac{\partial \mathbf{v}(\mathbf{x}, t)}{\partial t} + \mathbf{L} \cdot \mathbf{v}(\mathbf{x}, t) \tag{Ap4.23}$$

where the tensor $\mathbf{L}$ is the spatial velocity gradient expressed as

$$\mathbf{L} = \frac{\partial \dot{\mathbf{u}}}{\partial \mathbf{x}} \tag{Ap4.24}$$

The spatial velocity gradient $\mathbf{L}$ with respect to deformed position, may be decomposed into symmetric and antisymmetric parts

$$\mathbf{L} = \mathbf{d} + \boldsymbol{\omega} \tag{Ap4.25}$$

where the rate of deformation tensor $\mathbf{d}$ is the symmetric part

$$\mathbf{d} = \frac{1}{2}(\mathbf{L} + \mathbf{L}^T) \tag{Ap4.26}$$

and the spin tensor $\boldsymbol{\omega}$ is the antisymmetric part

$$\boldsymbol{\omega} = \frac{1}{2}(\mathbf{L} - \mathbf{L}^T) \tag{Ap4.27}$$

The relation between the Green-Lagrange strain rate $\dot{\mathbf{E}}$ and the rate of deformation $\mathbf{d}$ is

$$\dot{\mathbf{E}} = \mathbf{F}^T \cdot \mathbf{d} \cdot \mathbf{F}, \quad \mathbf{d} = \mathbf{F}^{-T} \cdot \dot{\mathbf{E}} \cdot \mathbf{F}^{-1} \tag{Ap4.28}$$

If $\mathbf{d}$ is equal to zero at a certain point P, then the instantaneous motion in the neighbourhood of P is a rigid body motion.

Substituting the equation (*Ap*4.17) into (*Ap*4.28) leads to

$$\mathbf{d} = \mathbf{F}^{-T}\{\frac{\partial}{\partial t}[\mathbf{F}^T \cdot \mathbf{e} \cdot \mathbf{F}]\} \cdot \mathbf{F}^{-1} \tag{Ap4.29}$$

or in rewritten form as the Lie derivative of $\mathbf{e}$

$$\mathbf{d} = L_{\mathbf{v}}\mathbf{e} \tag{Ap4.30}$$

The Lie derivative $L_{\mathbf{v}}$ [M-4] of a spatial tensor $\mathbf{a}$ with respect to the velocity field $\mathbf{v}$ is

$$L_{\mathbf{v}}\mathbf{a} = \Phi_{\star}\frac{\partial}{\partial t}(\Phi^{\star}\mathbf{a}) \tag{Ap4.31}$$

where $\Phi_{\star}$ and Φ^{*} denote the pull-back and push-forward operators, respectively.

A4.1.5 Logarithmic strain

The logarithmic or natural strain is particularly useful in plasticity. The variation in strain in a fibre $d\boldsymbol{\varepsilon}$ is

$$d\boldsymbol{\varepsilon} = \frac{dl}{l} \tag{Ap4.32}$$

where dl is the variation in fibre length and l is the current fibre length. The total strain $\boldsymbol{\varepsilon}$ in a fibre of original length l_0, using the equation (*Ap*4.32) is expressed as

$$\varepsilon = \int_{l_0}^{l} \frac{dl}{l} = ln\frac{l}{l_0} \qquad (Ap4.33)$$

This strain measure is called the logarithmic strain.

The variation of logarithmic strain tensor is expressed as

$$d\varepsilon = \frac{1}{2}[(\frac{\partial d\mathbf{u}}{\partial \mathbf{x}}) + (\frac{\partial d\mathbf{u}}{\partial \mathbf{x}})^T] \qquad (Ap4.34)$$

where $d\mathbf{u}$ is the variation in displacement what physically means the infinitesimal change in position of one particle but not the difference in displacement between neighbouring particles [H-4].

The variation of logarithmic strain tensor is related to the rate of deformation $\mathbf{d}$ as

$$d\varepsilon = \mathbf{d}dt \qquad (Ap4.35)$$

where dt is an infinitesimal interval in time. The total logarithmic strain ϵ is then

$$\epsilon = \int_{t_0}^{t} d\varepsilon = \int_{t_0}^{t} \mathbf{d}dt \qquad (Ap4.36)$$

representing a material time integral (there is no physical significance to such an integration at a point in space) and is evaluated by following a particle during deformation.

A4.1.6 Relation between Green-Lagrange strain rate and rate of deformation

The relation between the Green Lagrange strain rate $\dot{\mathbf{E}}$ and the rate of deformation $\mathbf{d}$ is given by

$$\dot{\mathbf{E}} = \mathbf{F}^T \cdot \mathbf{d} \cdot \mathbf{F} \qquad (Ap4.37)$$

$$\mathbf{d} = \mathbf{F}^{-T} \cdot \dot{\mathbf{E}} \cdot \mathbf{F} \qquad (Ap4.38)$$

The establishment of these relations is important in order to transform equations from the Lagrangian description (where variables are refered to the reference configuration) to the Eulerian description (where variables are refered to the deformed configuration) and vice versa.

A4.1.7 Density ratio

For the same reasons, it is necessary to establish the relation between the ratio of the density in the reference configuration ρ_0 to that in the deformed configuration ρ as

$$J = \frac{\rho_0}{\rho} = det|\mathbf{F}| \qquad (Ap4.39)$$

A4.1.8 Stress measures

An element of a continuum in the initial Ω^0 and deformed Ω^T configuration is presented in Figure 4A.2.

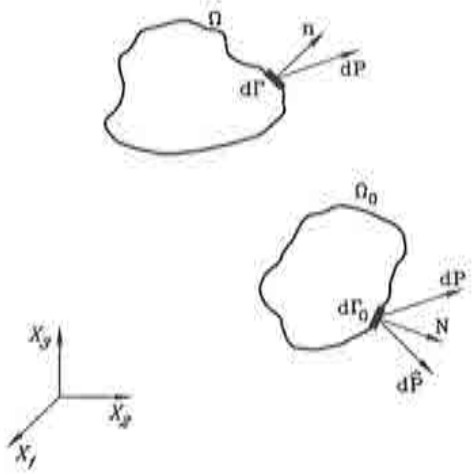

Figure 4A.2 Force vectors for stress tensor definitions.

The force vector $d\mathbf{P}$ acts on the elemental surface $d\Gamma$ and it is expressed by

$$d\mathbf{P} = \mathbf{t}d\Gamma = \mathbf{n} \cdot \boldsymbol{\sigma} d\Gamma \qquad (Ap4.40)$$

where $\mathbf{t}$ is the surface traction, $\mathbf{n}$ is the unit normal vector and $\boldsymbol{\sigma}$ is the Cauchy stress tensor. Multiplying the Cauchy stress tensor by the density ratio leads to the Kirchhoff stress tensor $\boldsymbol{\tau}$

$$\boldsymbol{\tau} = \frac{\rho_0}{\rho}\boldsymbol{\sigma} \qquad (Ap4.41)$$

The Cauchy and Kirchhoff stress tensors are refered to the spatial configuration.

The original configuration gives the possibility for deriving different stresses as follows. The correspondence rule is chosen such that $d\mathbf{P}$ is related to $d\hat{\mathbf{P}}$ in the same manner as the vector $d\mathbf{X}$ in the reference configuration is related to the vector $d\mathbf{x}$ in the deformed configuration. By expressing the force $d\mathbf{P}$ in terms of the initial undeformed area $d\Gamma_0$, the first Piola-Kirchhoff stress tensor $\mathbf{T}$ is defined [B-2], [H-4] as

$$d\mathbf{P} = \mathbf{T} \cdot \mathbf{N} d\Gamma_0 \qquad (Ap4.42)$$

where $\mathbf{N}$ is the unit normal vector in the undeformed configuration. The first Piola-Kirchhoff stress tensor is not symmetric. The force $d\hat{\mathbf{P}}$ is evaluated by application of the transformation $\mathbf{F}^{-1}$ to the force vector $d\mathbf{P}$ as

$$d\hat{\mathbf{P}} = \mathbf{F}^{-1} d\mathbf{P} \qquad (Ap4.43)$$

and introducing $(Ap4.42)$ into $(Ap4.43)$

$$d\hat{\mathbf{P}} = \mathbf{F}^{-1}\mathbf{T} \cdot \mathbf{N} d\Gamma_0 = \mathbf{N} \cdot \mathbf{S} d\Gamma_0 \qquad (Ap4.44)$$

where $\mathbf{S}$ is the second Piola-Kirchhoff stress tensor. The second Piola-Kirchhoff stress tensor is symmetric.

The relationships between the first and second Piola-Kirchhoff stress tensors are expressed [H-4] as

$$\mathbf{S} = \mathbf{T}(\mathbf{F}^{-1})^T, \quad \mathbf{T} = \mathbf{S}\mathbf{F}^T \qquad (Ap4.45)$$

Finally, the relationships between the true Cauchy stresses and the first and second Piola-Kirchhoff stresses are

$$\boldsymbol{\sigma} = \frac{1}{J}\mathbf{F} \cdot \mathbf{T}, \quad \mathbf{T} = J\mathbf{F}^{-1} \cdot \boldsymbol{\sigma} \qquad (Ap4.46a)$$

$$\boldsymbol{\sigma} = \frac{1}{J}\mathbf{F} \cdot \mathbf{S} \cdot \mathbf{F}^T, \quad \mathbf{S} = J\mathbf{F}^{-1} \cdot \boldsymbol{\sigma} \cdot (\mathbf{F}^{-1})^T \qquad (Ap4.46b)$$

A4.1.9 Stress rates

The constitutive equation relates stress rate to strain rate and must be objective, i.e. invariant under the change of frame reference. The requirement of objectivity means that the stress rate must vanish when the body is performing rigid body motions, what leads to difficulties in definition of a unique stress rate. The freedom of a choice of a stress rate that fulfils this requirement gives many definitions of stress rate.

The most commonly used objective stress rate is the Jauman-Zaremba rate, defined as the material time derivative of the stress tensor as it would appear to an observer in a frame of reference attached to the particle and rotating with it at an angular velocity of the rigid body rotation of the particle.

The material derivative of the Cauchy stress tensor $\dot{\boldsymbol{\sigma}}$ is not objective, therefore is inappropriate to use in formulating constitutive equations in plasticity theory. The most commonly used objective stress rate is the Jauman-Zaremba rate, related to the material derivative of the Cauchy stress tensor as

$$\boldsymbol{\sigma}^{\nabla} = \dot{\boldsymbol{\sigma}} - \boldsymbol{\omega} \cdot \boldsymbol{\sigma} + \boldsymbol{\sigma} \cdot \boldsymbol{\omega} \qquad (Ap4.47)$$

where $\boldsymbol{\sigma}, \boldsymbol{\omega}$ and $\dot{\boldsymbol{\sigma}}$ are the Cauchy stress tensor, spin tensor and the rate of Cauchy stress, respectively. It is coronational that it represents a rate relative to a rotating frame of reference with the rate of rotation given by the spin tensor $\boldsymbol{\omega}$. The Jauman-Zaremba stress rate thus reduces to the material time derivative for vanishing rigid body rotation.

A4.2 EQUATIONS OF MOTION

The equations of motion are expressed in the spatial and material configurations.

A4.2.1 Equations of motion in the spatial configuration

The motion of body can be described in the strong (differential) form by the following set of equations [M-2]:

- Cauchy equation of motion

$$\nabla_{\mathbf{x}} \boldsymbol{\sigma} + \rho \mathbf{b} = \rho \mathbf{a} \qquad \mathbf{x} \in \Omega^t, \quad t \in [0, T] \qquad (Ap4.48)$$

- traction boundary conditions

$$\mathbf{n} \cdot \boldsymbol{\sigma} = \mathbf{t} \qquad \mathbf{x} \in F_{\sigma}^t, \quad t \in [0, T] \qquad (Ap4.49)$$

- displacement boundary conditions

$$\mathbf{u} = \bar{\mathbf{u}} \qquad \mathbf{x} \in \Gamma_u^t, \quad t \in [0, T] \tag{Ap4.50}$$

- initial conditions

$$\mathbf{u} = \mathbf{u}_0 \qquad \mathbf{x} \in \Omega^t, \quad t = 0 \tag{Ap4.51a}$$

$$\mathbf{v} = \mathbf{v}_0 \qquad \mathbf{x} \in \Omega^t, \quad t = 0 \tag{Ap4.51b}$$

where $\mathbf{b}$ is the body force vector, Γ_u^t and Γ_σ^t are the parts of the boundary on which displacement and traction are specified, respectively as follows

$$\Gamma_\sigma^t \cap \Gamma_u^t = 0 \tag{Ap4.52a}$$

$$\Gamma_\sigma^t \cup \Gamma_u^t = \Gamma^t \tag{Ap4.52b}$$

The goal of the analysis is to find a displacement field $\mathbf{u} = \mathbf{u}(\mathbf{x}, t)$ which satisfy above set of equations. To complete the calculation, a corresponding constitutive equation has to be specified (relation between $\boldsymbol{\sigma}$ and $\mathbf{u}$). Constitutive models used for the present element in the program formulation is described later.

A4.2.2 Equations of motion in the material configuration

The equations of motion can be written in the material configuration by the following set of equations [M-2]:

- Cauchy's equation of motion

$$\nabla_{\mathbf{X}} \mathbf{T} + \rho_0 \mathbf{b}_0 = \rho \mathbf{A}, \quad \mathbf{X} \in \Omega^0, \quad t \in [0, T] \tag{Ap4.53a}$$

$$\nabla_{\mathbf{X}} (\mathbf{S} \cdot \mathbf{F}^T) + \rho_0 \mathbf{b}_0 = \rho \mathbf{A}, \quad \mathbf{X} \in \Omega^0, \quad t \in [0, T] \tag{Ap4.53b}$$

- traction boundary conditions

$$\mathbf{N} \cdot \mathbf{T} = \bar{\mathbf{T}} \quad \mathbf{X} \in \Gamma_\sigma^0, \quad t \in [0, T] \tag{Ap4.54}$$

- displacement boundary conditions

$$\mathbf{u} = \bar{\mathbf{u}} \quad \mathbf{X} \in \Gamma_u^0, \quad t \in [0, T] \tag{Ap4.55}$$

- initial conditions

$$\mathbf{u} = \mathbf{u}_0, \quad \mathbf{X} \in \Omega^0, \quad t \in [0, T] \tag{Ap4.56a}$$

$$\mathbf{v} = \mathbf{v}_0, \quad \mathbf{X} \in \Omega^0, \quad t \in [0, T] \tag{Ap4.56b}$$

where $\mathbf{b}_0$ is the body force vector, $\mathbf{T}$ is the first Piola- Kirchhoff stress tensor and $\mathbf{S}$ is the second Piola-Kirchhoff stress tensor.

A4.2.3 Weak form of equations of motion

The motion of the body system is analyzed using the principle of virtual work abandoning the virtual formulation based on the principle of stationary total potential energy. Thus, by employing a standard variational procedure to the Cauchy's equations of motion in the spatial configuration, its weak form is obtained

$$\int_{\Omega^t} \boldsymbol{\sigma} : \nabla_{\mathbf{x}}(\delta\mathbf{u}) d\Omega = \int_{\Omega^t} \rho(\mathbf{b} - \mathbf{a}) \cdot \delta\mathbf{u} d\Omega + \int_{\Gamma_\sigma^t} \mathbf{t} \cdot \delta\mathbf{u} d\Omega \tag{Ap4.57}$$

where $\mathbf{u}$ is an arbitrary kinematically admissible displacement field and $\delta\mathbf{u}$ is the virtual displacement field. The above equation physically express the principle of virtual work that states as the condition of a dynamic equilibrium equality of the internal and external virtual work. The left hand side integral represents the internal virtual work and the right hand side integrals represents components of the virtual work of external forces including the internal forces. The displacement boundary conditions are included into (*Ap*4.57) by the assumption of the kinematic admissibility of $\delta\mathbf{u}$. The traction boundary conditions are included into (*Ap*4.57) by including the virtual work of the traction forces $\mathbf{t}$ into the external virtual work.

In the same fashion, the variational procedure applied to the equations of motion in the material configuration leads to the equation of virtual work in the material configutarion, in terms of the first Piola-Kirchhoff stress tensor

$$\int_{\Omega^0} \mathbf{T} : \nabla_{\mathbf{X}}(\delta\mathbf{u}) d\Omega = \int_{\Omega^0} \rho_0(\mathbf{b}_0 - \mathbf{A}) \cdot \delta\mathbf{u} d\Omega + \int_{\Gamma_\sigma^0} \bar{\mathbf{T}} \cdot \delta\mathbf{u} d\Omega \tag{Ap4.58}$$

or in terms of the second Piola-Kirchhoff stress tensor

$$\int_{\Omega^0} (\mathbf{S} \cdot \mathbf{F}^T) : \nabla_{\mathbf{X}}(\delta\mathbf{u}) d\Omega = \int_{\Omega^0} \rho_0(\mathbf{b}_0 - \mathbf{A}) \cdot \delta\mathbf{u} d\Omega + \int_{\Gamma_\sigma^0} \bar{\mathbf{T}} \cdot \delta\mathbf{u} d\Omega \tag{Ap4.59}$$

The same set of equations can be rewritten by introducing the corresponding energy conjugate deformation measures: to the Cauchy strain tensor the linear Almansi strain tensor $\boldsymbol{\epsilon}$, to the first Piola-Kirchhoff stress tensor the deformation gradient $\mathbf{F}$ and to the second Piola-Kirchhoff stress tensors the Green-Lagrange strain tensor $\mathbf{E}$ as follows:

$$\int_{\Omega^t} \boldsymbol{\sigma} : \delta\boldsymbol{\epsilon} d\Omega = \int_{\Omega^t} \rho(\mathbf{b} - \mathbf{a}) \cdot \delta\mathbf{u} d\Omega + \int_{\Gamma_\sigma^t} \mathbf{t} \cdot \delta\mathbf{u} d\Omega \qquad (Ap4.60)$$

$$\int_{\Omega^0} \mathbf{T} : \delta\mathbf{F} d\Omega = \int_{\Omega^0} \rho_0(\mathbf{b}_0 - \mathbf{A}) \cdot \delta\mathbf{u} d\Omega + \int_{\Gamma_\sigma^0} \bar{\mathbf{T}} \cdot \delta\mathbf{u} d\Omega \qquad (Ap4.61)$$

$$\int_{\Omega^0} \mathbf{S} : \delta\mathbf{E} d\Omega = \int_{\Omega^0} \rho_0(\mathbf{b}_0 - \mathbf{A}) \cdot \delta\mathbf{u} d\Omega + \int_{\Gamma_\sigma^0} \bar{\mathbf{T}} \cdot \delta\mathbf{u} d\Omega \qquad (Ap4.62)$$

The above set of the weak form of equations of dynamic equilibrium is the base for formulating finite element equations, thus the discretization procedure is applied to this set of equations.

A4.3 CONSTITUTIVE EQUATIONS

As mentioned above, to complete the specification of a problem of the motion of a deformable body a suitable constitutive equation must be specified. The constitutive equations relate stress to strain and/or strain rate that characterize the behaviour of a material under an application of forces or loads. They vary for different materials or even they can differ for the same material in different regimes of deformation, i.e. the response during elastic deformation is different from that during plastic deformation.

A constitutive equation, commonly used to describe an objective physical phenomenon such as material behaviour under applied loads, must obey certain axioms or principles during the occurrence of the physical phenomenon.

A purely mechanical constitutive equation has to fulfil three fundamental principles:

- principle of determination of stress which states that the stress in body is determined by the history of the motion of that body.
- principle of local action which states that in determining the stress at given particle, the motion outside an arbitrary small neighbourhood of it may bee disregarded.
- principle of material frame indifference which introduces the concept of objectivity that is significant in the finite plasticity theory, i.e. constitutive equations must be invariant under the changes of reference frame.

The constitutive models used in the program formulation are presented below.

A4.3.1 Hypoelastic constitutive equations

The behaviour of a hypoelastic material is expressed as

$$\dot{\boldsymbol{\sigma}} = \mathbf{C} : \mathbf{d} \tag{$Ap4.63$}$$

where $\mathbf{C}$ is the rank of constitutive tensor dependent on material properties, deformation and stress quantities, $\mathbf{d}$ is the deformation rate tensor expressed by equation ($Ap4.26$) and $\dot{\boldsymbol{\sigma}}$ represents some rate stress. A stress rate that fulfils the requirement of objectivity must vanish when the body is performing rigid body motion. As the material derivative of the Cauchy stress tensor $\dot{\boldsymbol{\sigma}}$ is not objective, the constitutive equation ($Ap4.63$) is rewritten as

$$\boldsymbol{\sigma}^{\nabla} = \mathbf{C} : \mathbf{d} \tag{$Ap4.64$}$$

where $\boldsymbol{\sigma}^{\nabla}$ is the Jauman-Zaremba rate. The rate constitutive equation ($Ap4.64$) with the Jauman-Zaremba derivative of the Cauchy stress tensor is the base for large strain elastoplastic model implemented in the code. For hypoelastic material, the total stresses and hence the internal force vector come from the integration of the rate equation ($Ap4.63$).

A4.3.2 Hyperelastic constitutive equations

Hyperelastic models are essentially higher order forms of linear elastic models in which the stresses are some functions of the total strains or stresses. The obvious example of a hyperelastic material is rubber. The behaviour of a hyperelastic material is expressed in the spatial description

$$\boldsymbol{\sigma} = \rho \frac{\partial \Psi(\varepsilon)}{\partial \varepsilon} \tag{$Ap4.65$}$$

or in the material description

$$\mathbf{S} = \rho_0 \frac{\partial \bar{\Psi}(\mathbf{E})}{\partial \mathbf{E}}, \quad \mathbf{T} = \rho_0 \frac{\partial \bar{\Psi}(\mathbf{F})}{\partial \mathbf{F}} \tag{$Ap4.66$}$$

where Ψ is an elastic potential function called the strain energy density. It is a scalar function of one of the deformation or strain tensors and $\boldsymbol{\sigma}$ is the stress which is derivable from a strain energy function. The total stress and hence the

internal force vector come directly from ($Ap4.65$) and not from the integration of the rate equation.

Large strain elasto-plastic constitutive model used in the code for continuum elements are based on the expression ($Ap4.65$).

A4.3.3 Constitutive tensor for elastic material

The constitutive tensor for three different materials is presented below.

A4.3.3.1 Anisotropic material

The tensor $\mathbf{C}$ is anisotropic and non-constant 4 rank tensor, with 81 components. Because of symmetry, only 21 of those components can be independent and these elastic constants describe the properties of anisotropic elastic material. It can be presented in matrix form with 21 independent components

$$\mathbf{C} = \begin{bmatrix} C_{1111} & C_{1122} & C_{1133} & C_{1112} & C_{1113} & C_{1123} \\ C_{1122} & C_{2222} & C_{2233} & C_{2212} & C_{2213} & C_{2223} \\ C_{1133} & C_{2233} & C_{3333} & C_{3312} & C_{3313} & C_{3323} \\ C_{1112} & C_{2212} & C_{3312} & C_{1212} & C_{1312} & C_{2312} \\ C_{1113} & C_{2213} & C_{3313} & C_{1312} & C_{1313} & C_{2313} \\ C_{1123} & C_{2223} & C_{3323} & C_{2312} & C_{2313} & C_{2323} \end{bmatrix} \qquad (Ap4.67)$$

A4.3.3.2 Orthotropic material

The matrix $\mathbf{C}$ for the orthotropic material is reduced due to three mutually orthogonal planes of symmetry at each point that possess the material. The number of independent elastic constants is reduced to 9, thus the matrix $\mathbf{C}$ is expressed as

$$\mathbf{C} = \begin{bmatrix} C_{1111} & C_{1122} & C_{1133} & 0 & 0 & 0 \\ C_{1122} & C_{2222} & C_{2233} & 0 & 0 & 0 \\ C_{1133} & C_{2233} & C_{3333} & 0 & 0 & 0 \\ 0 & 0 & 0 & C_{1212} & 0 & 0 \\ 0 & 0 & 0 & 0 & C_{1313} & 0 \\ 0 & 0 & 0 & 0 & 0 & C_{2323} \end{bmatrix} \qquad (Ap4.68)$$

A4.3.3.3 Isotropic material

The material with properties independent of the direction is called isotropic. The elastic properties are defined with 2 independent parameters what leads to the elasticity tensor

$$\mathbf{C} = \lambda \mathbf{1} \otimes \mathbf{1} + 2\mu \mathbf{I} \tag{Ap4.69}$$

where λ and μ are Lamé constants, $\mathbf{I}$ is the fourth order unit tensor and $\mathbf{1}$ is he second order unit tensor. The matrix $\mathbf{C}$ for isotropic material is

$$\mathbf{C} = \begin{bmatrix} \lambda+\mu & \lambda & \lambda & 0 & 0 & 0 \\ \lambda & \lambda+\mu & \lambda & 0 & 0 & 0 \\ \lambda & \lambda & \lambda+\mu & 0 & 0 & 0 \\ 0 & 0 & 0 & \mu & 0 & 0 \\ 0 & 0 & 0 & 0 & \mu & 0 \\ 0 & 0 & 0 & 0 & 0 & \mu \end{bmatrix} \tag{Ap4.70}$$

The Lamé constants are expressed as

$$\mu = \frac{E}{2(1+\nu)} \quad \lambda = \frac{\nu E}{(1+\nu)(1-2\nu)} \tag{Ap4.71}$$

where E is Young's modulus and ν is Poisson's coefficient.

The constant constitutive tensor $\mathbf{C}$ leads to the linear elastic material model where elastic strains are relatively small. For larger elastic strains the stress-strain relation is nonlinear and the model of nonlinear elasticity must be used.

A4.3.4 Decomposition of elasto plastic deformations

The strain $\boldsymbol{\varepsilon}$ in the classical small strain elasto-plastic theory is divided into elastic recoverable $\boldsymbol{\varepsilon}^e$ and plastic non-recoverable $\boldsymbol{\varepsilon}^p$ parts

$$\boldsymbol{\varepsilon} = \boldsymbol{\varepsilon}^e + \boldsymbol{\varepsilon}^p \tag{Ap4.72}$$

Similarly, the strain rate $\dot{\boldsymbol{\varepsilon}}$ is divided into elastic recoverable $\dot{\boldsymbol{\varepsilon}}^e$ and plastic non-recoverable $\dot{\boldsymbol{\varepsilon}}^p$ parts as

$$\dot{\boldsymbol{\varepsilon}} = \dot{\boldsymbol{\varepsilon}}^e + \dot{\boldsymbol{\varepsilon}}^p \tag{Ap4.73}$$

For small strains there are no distinction between strain measures because in this decomposition the plastic part of the strain rate is defined on physical grounds by elastic unloading which should involve no additional plastic flow.

For finite strain elasto-plastic problem, the decomposition of the strain meassures or their rates is not without ambiguity. The difficulty arise due to possibility of choice different measures of strain. Thus, it is necessary to develop some sort of elasto-plastic decomposition that is applicable for the finite strain case.

The additive decomposition of the Green-Lagrange strain tensor into elastic and plastic parts is given as

$$\mathbf{E} = \mathbf{E}^e + \mathbf{E}^p \qquad (Ap4.74)$$

and in hypoelastic models, in the same manner the additive decomposition of the deformation rate tensor $\mathbf{d}$ is

$$\mathbf{d} = \mathbf{d}^e + \mathbf{d}^p \qquad (Ap4.75)$$

The additive decomposition of the deformation rate tensor is postulated for large displacements large strain shell elements with translational degrees of freedom only and is the starting point of the constitutive model implemented in the code. The above decomposition of finite elasto-plastic deformtions is not only decomposition used in literature.

Lee [L-1] assumes that the decomposition of the deformation into an elastic and plastic parts can be written by means of the multiplicative decomposition of the deformation gradient tensor

$$\mathbf{F} = \mathbf{F}^e\mathbf{F}^p \qquad (Ap4.76)$$

where $\mathbf{F}^e$ is the deformation gradient which express the elastic part of the deformation and $\mathbf{F}^p$ is the deformation gradient which express the plastic part of the deformation. The plastic deformation $\mathbf{F}^p$ can be expressed as

$$\mathbf{F}^p = (\mathbf{F}^e)^{-1}\mathbf{F} \qquad (Ap4.77)$$

where $(\mathbf{F}^e)^{-1}$ is the deformation that locally releases the stresses, what means that a local stress-free configuration is assumed. The deformation expressed by equation $(Ap4.77)$ is the deformation between the reference configuration and stress-free configuration. The stress-free configuration is not uniquely defined, all such configurations differ from each other by rigid body rotations only.

The multiplicative factorization (*Ap*4.76) results in the additive decomposition of the rate of deformation tensor $\mathbf{d}$ into elastic part $\mathbf{d}^e$ and plastic part $\mathbf{d}^p$ [G-1] as

$$\mathbf{d} = \mathbf{d}^e + \mathbf{d}^p \tag{Ap4.78}$$

The plastic part is expressed as

$$\mathbf{d}^p = \frac{1}{2}(\mathbf{L}^p + \mathbf{L}^{pT}) \tag{Ap4.79}$$

where the plastic spatial velocity is defined as

$$\mathbf{L}^p = \mathbf{F}^e \bar{\mathbf{L}}^p (\mathbf{F}^e)^{-1} \tag{Ap4.80}$$

and the plastic velocity gradient $\bar{\mathbf{L}}^p$ is defined as

$$\bar{\mathbf{L}}^p = \dot{\mathbf{F}}^p (\mathbf{F}^p)^{-1} \tag{Ap4.81}$$

The additive decomposition expressed by equation (*Ap*4.78) resulting from the multiplicative decomposition expressed by equation (*Ap*4.76) can be developed in different ways (as a consequence of disagreement in the literature). Thus, the equation (*Ap*4.78) can be rewritten [M-3] as

$$\mathbf{d} = \mathbf{d}^e + \bar{\mathbf{d}}^p \tag{Ap4.82}$$

where

$$\bar{\mathbf{d}}^p = \frac{1}{2}(\bar{\mathbf{L}}^p + (\bar{\mathbf{L}}^p)^T) \tag{Ap4.83}$$

The additive terms $\mathbf{d}^e$ and $\bar{\mathbf{d}}^p$ are defined on different configurations, spatial and intermediate, respectively.

There is another way to derive additive relations from the multiplicative decomposition (*Ap*4.77) used as a base of large elasto-plastic continuum elements in the code. The adequate elastic and plastic strain tensors are defined at any of the three configurations in intention to obtain the additive relation for the strain tensors at any of the three configurations. Having this relation in one configuration, the relations in other configurations can be obtained by means of pull-back or push-forward operations.

The derivation in the spatial configuration is presented. The elastic Finger tensor can be presented as

$$\mathbf{b}^{e-1} = (\mathbf{F}^e)^{-T} \cdot (\mathbf{F}^e)^{-1} \qquad (Ap4.84)$$

The elastic Almansi tensor is defined as

$$\mathbf{e}^e = \frac{1}{2}(\mathbf{I} - (\mathbf{b}^e)^{-1}) \qquad (Ap4.85)$$

and the plastic part of Almansi tensor is defined satisfying the additive relation

$$\mathbf{e} = \mathbf{e}^e + \mathbf{e}^p \qquad (Ap4.86)$$

The elastic and plastic parts of the rate of the deformation are defined as the Lie derivatives of the elastic and plastic Almansi strain tensors, respectively

$$\mathbf{d}^e = L_{\mathbf{v}}\mathbf{e}^e \quad \mathbf{d}^p = L_{\mathbf{v}}\mathbf{e}^p \qquad (Ap4.87)$$

The additive relations in the reference and in the intermediate configuration are

$$\mathbf{E} = \mathbf{E}^e + \mathbf{E}^p, \quad \dot{\mathbf{E}} = \dot{\mathbf{E}}^e + \dot{\mathbf{E}}^p \qquad (Ap4.88a)$$

$$\bar{\mathbf{E}} = \bar{\mathbf{E}}^e + \bar{\mathbf{E}}^p, \quad \bar{\mathbf{d}} = \bar{\mathbf{d}}^e + \bar{\mathbf{d}}^p \qquad (Ap4.88b)$$

where

$$\mathbf{E}^p = \frac{1}{2}(\mathbf{C}^p - \mathbf{I}), \quad \mathbf{E}^e = \mathbf{E} - \mathbf{E}^p, \quad \mathbf{C}^p = (\mathbf{F}^p)^T \cdot \mathbf{F}^p \qquad (Ap4.89a)$$

$$\bar{\mathbf{E}}^e = \frac{1}{2}(\bar{\mathbf{C}} - \mathbf{I}), \quad \bar{\mathbf{C}} = (\mathbf{F}^e)^T \cdot \mathbf{F}^e, \quad \bar{\mathbf{E}}^p = \frac{1}{2}(\mathbf{I} - (\mathbf{b}^p)^{-1}) \qquad (Ap4.89b)$$

$$(\mathbf{b}^p)^{-1} = (\mathbf{F}^p)^{-T} \cdot (\mathbf{F}^p)^{-1} \qquad (Ap4.89c)$$

The kinematic relation at any configuration can be derived at this configuration or by applying adequate pull-back or push-forward operations to the relations derived for another of the two other configurations.

A4.3.5 Hypoelastic model of rate-independent plasticity

By extension of the small strain elastoplastic models, a number of hypoelastic models of plasticity are obtained. The hypoelsastic model in the spatial configuration can be presented generally with the following set of equations:

- Additive decomposition of the spatial rate of deformation is expressed as

$$\mathbf{d} = \mathbf{d}^e + \mathbf{d}^p \qquad (Ap4.90)$$

- Hypoelastic rate constitutive equation, is defined as

$$\dot{\boldsymbol{\sigma}} = \mathbf{C} : \mathbf{d}^e \qquad (Ap4.91)$$

  where $\mathbf{C}$ is the spatial elasticity tensor and $\dot{\boldsymbol{\sigma}}$ denotes any objective stress rate.
- The yield condition, is expressed by the function

$$f(\boldsymbol{\sigma}, \mathbf{q}) = 0 \qquad (Ap4.92)$$

  where $\mathbf{q}$ represents a set of internal variables that characterize the hardening of the material. Different yield conditions can be employed.
- Flow rule is expressed as

$$\mathbf{d}^p = \dot{\gamma} \frac{\partial \Phi(\boldsymbol{\sigma}, \mathbf{q})}{\partial \boldsymbol{\sigma}} \qquad (Ap4.93)$$

  For associative flow rule $\Phi = f$.
- Hardening law is expressed as

$$\dot{\mathbf{q}} = -\dot{\gamma} \mathbf{h}(\boldsymbol{\sigma}, \mathbf{q}) \qquad (Ap4.94)$$

- Loading-anloading conditions - Kuhn-Tucker conditions

$$\dot{\gamma} \geq 0 \quad f(\boldsymbol{\sigma}, \mathbf{q}) \leq 0 \quad \dot{\gamma} f(\boldsymbol{\sigma}, \mathbf{q}) = 0 \qquad (Ap4.95)$$

  where the consistency requirement is

$$\dot{\gamma} \dot{f}(\dot{\boldsymbol{\sigma}}, \mathbf{q}) = 0 \qquad (Ap4.96)$$

This model is implemented in the code for large strain axisymmetric shell elements, for large strain shell elements with translational degrees of freedom and large displacement small strain continuum elements. Such kind of model is adequate for metal plasticity but its numerical implementation leads to the special corresponding integration algorithm which preserves objectivity.

A4.3.6 Hyperelastic model of rate-independent plasticity

The hyperelastic model in the spatial configuration is presented with the following set of equations:

- Additive decomposition of the Almansi strain tensor derived assuming multiplicative decomposition of the deformation gradient tensor

$$\mathbf{e} = \mathbf{e}^e + \mathbf{e}^p \tag{Ap4.97}$$

- Free energy function

$$\Psi = \Psi^e(\mathbf{e}^e) + \Psi^p(\mathbf{q}) \tag{Ap4.98}$$

- Hyperelastic constitutive equation

$$\boldsymbol{\sigma} = \rho \frac{\partial \Psi^e(\mathbf{e}^e)}{\partial \mathbf{e}^e} \tag{Ap4.99}$$

- Yield condition

$$f(\boldsymbol{\sigma}, \mathbf{q}) = 0 \tag{Ap4.100}$$

- Flow rule

$$\mathbf{d}^p = L_{\mathbf{v}}\mathbf{e}^p = \dot{\gamma}\frac{\partial f(\boldsymbol{\sigma}, \mathbf{q})}{\partial \boldsymbol{\sigma}} \tag{Ap4.101}$$

- Hardening law

$$L_{\mathbf{v}}\mathbf{q} = -\dot{\gamma}\mathbf{h}(\boldsymbol{\sigma}, \mathbf{q}) \tag{Ap4.102}$$

- Loading/unloading conditions

$$\dot{\gamma} \geq 0 \quad f(\boldsymbol{\sigma}, \mathbf{q}) \leq 0 \quad \dot{\gamma} f(\boldsymbol{\sigma}, \mathbf{q}) = 0 \tag{Ap4.103}$$

where the consistency requirement is $\dot{\gamma}\dot{f}(\boldsymbol{\sigma}, \mathbf{q}) = 0$

For clarity reason, short general view on yield conditions and uniaxial stress-strain relation is given below.

A4.3.7 The mathematical theory of plasticity and yield conditions

The mathematical theory of plasticity has as the object a theoretical description of the relationship between stress and strain for a material which exhibits an elastic-plastic response. Plastic behaviour is characterized by an irreversible straining which is not time dependent and can only be sustained once a certain level of stress has been reached.

A theory which models elasto-plastic material deformation has the following requirements:

- an explicit relationship between stress and strain must be formulated to describe material behaviour under elastic conditions, i.e. before the onset of plastic deformation, when the relationship between stress and strain is given by the standard linear expression $\boldsymbol{\sigma} = \mathbf{C}\boldsymbol{\varepsilon}$.
- a yield criterion indicating the stress level at which plastic flow commences must be postulated. The yield criterion determines the stress level at which plastic deformation begins.
- a relationship between stress and strain must be developed for postyield behaviour, i.e. when the deformation is made up of both elastic and plastic components.

A4.3.8 Yield conditions

The yield condition determines the stress level at which plastic deformation begins and it must be invariant to change of frame reference. All the stress states that cause yielding can be imagined to constitute a continuous surface, called yield surface, that divides the stress space into elastic and plastic domains. The yield surface is the boundary of these two domains and can change during plastic flow. Because the stress strain relationship is different for elastic and plastic deformation, the deformation of the shape and position of the yield surface in the stress space is required. The yielding of material is defined by the yield condition

$$f(\boldsymbol{\sigma}, \mathbf{q}) = 0 \qquad (Ap4.104)$$

and can be presented as the equation defining the surface in the stress space $\boldsymbol{\sigma}$ dependent on the set of internal variables $\mathbf{q}$. The yield function is expressed in terms of 'true' Cauchy stress tensor. In a small strain cases, the Cauchy stress tensor is substituted by the second Piola-Kirchhoff stress tensor

$$f(\mathbf{S}, \mathbf{q}) = 0 \qquad (Ap4.105)$$

In the plasticity models, the internal variables are taken as the plastic strain components ε^p and the hardening variable k. The following options are available:

$f(\boldsymbol{\sigma}, \mathbf{q}) = 0$ the plastic flow is occurring

$f(\boldsymbol{\sigma}, \mathbf{q}) \leq 0$ the stress state is below the yield point and behaviour is elastic

$f(\boldsymbol{\sigma}, \mathbf{q}) \geq 0$ is not admissible in classical plasticity theory

The expansion (contraction), translation and distortion of the yield surface are characteristic of material hardening. Two simple classical models are shown in Figure 4A.3.

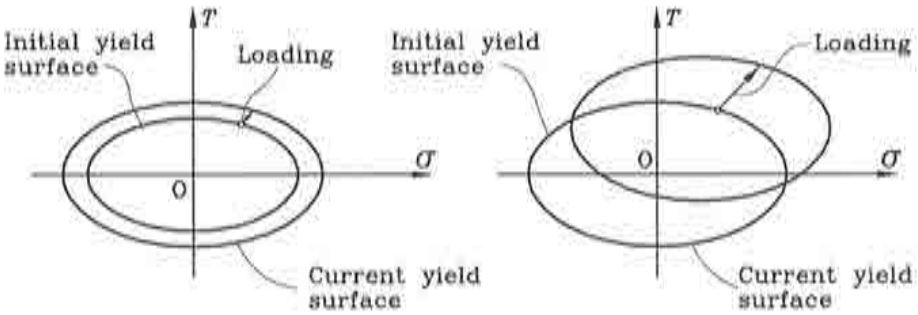

Figure 4A.3 Graphic representation of isotropic and kinematic hardening.

The isotropic hardening assumes that the subsequent yield surface is a uniform expansion of the initial yield surface, as shown in Figure 4A.3 and that the material isotropic response to yielding remains unchanged during plastic deformation what leads to the fact that the contour of initial and subsequent yield surfaces is the same.

The kinematic hardening assumes that the yield surface translate as a rigid body in the stress space during the plastic deformation, as shown in Figure 4A.3. As a consequence, the shape of the subsequent yield surface during plastic deformation remains unchanged. This model is introduced due to calculation of the Bauchinger effect.

Some materials, notably soils have not strain harden but strain soften instead, thus the yield stress level at a point decreases with increasing plastic deformation. Therefore for an isotropic model, the original yield curve contracts progressively without translation. Consequently, yielding implies local failure and the yield surface becomes a failure criterion.

The progressive development of the yield surface is defined relating the yield stress to the plastic deformation by means of the hardening parameter k in two ways. If the degree of work hardening is a function of the total plastic work, then

$$k = W^p = \int dW^p = \int \boldsymbol{\sigma} : \dot{\boldsymbol{\varepsilon}}^p dt \qquad (Ap4.106)$$

where $\dot{\boldsymbol{\varepsilon}}^p$ are the plastic components of strain occurring during a strain increment.

If k is related to a measure of the total plastic deformation, then

$$k = \int d\bar{\varepsilon}^p = \int \sqrt{\frac{2}{3}\dot{\boldsymbol{\varepsilon}}^p : \dot{\boldsymbol{\varepsilon}}^p} dt \qquad (Ap4.107)$$

where $\bar{\varepsilon}^p$ is the effective, generalized or equivalent plastic strain. This behaviour is termed strain hardening. Thus, the yield function expressed by equation $(Ap4.104)$ with the set of hardening parameters $\mathbf{q} = \{\bar{\varepsilon}^p, k\}$ can be written as

$$\int(\boldsymbol{\sigma}, \boldsymbol{\varepsilon}^p, k) = F(\boldsymbol{\sigma} - \boldsymbol{\alpha}(\boldsymbol{\varepsilon}^p)) - \sigma_y(k) \qquad (Ap4.108)$$

where σ_y is the equivalent (uniaxial) yield stress and $\boldsymbol{\alpha}$ represents the shift of the yield surface in the stress space. The equation $(Ap4.104)$ can be used for isotropic as well as for kinematic hardening.

The isotropic hardening is expressed if $\boldsymbol{\alpha} = \mathbf{0}$ and $d\sigma_y/dk > 0$. The equation $(Ap4.108)$ can be rewritten for isotropic yield function as

$$f(\boldsymbol{\sigma}, k) = F(\boldsymbol{\sigma}) - \sigma_y(k) \qquad (Ap4.109)$$

The kinematic hardening is expressed if $\boldsymbol{\alpha} \neq \mathbf{0}$ and the equation (Ap4.109) can be rewritten as

$$f(\boldsymbol{\sigma}, \boldsymbol{\varepsilon}^p) = F(\boldsymbol{\sigma}) - \boldsymbol{\alpha}(\boldsymbol{\varepsilon}^p)) - \sigma_y \qquad (Ap4.110)$$

The shape of the yield surface depends on the yield criterion used. Different hypothesis have been used to establish the yield condition. The most important

yield conditions for metal plasticity are the Mises-Huber, Tresca and Hill criteria. For the materials such as concrete, rock and soil, the best suitable yield criterions are the Mohr-Coulomb and Drucker-Prager criteria.

Generally, the yield criteria for metals does not depend on the first invariant J_1 of the stress tensor. Experimental observations indicate that plastic deformation of metals is essentially independent of hydrostatic pressure. On the contrary, the yield criteria for pressure - sensitive materials (concrete, rock and soil) include the influence of the hydrostatic pressure, i.e. dependence on J_1.

A4.3.9 Stress state and stress space

The yield surface or yield function can be represented mathematically in the stress space by a surface separating the elastic and plastic domains [K-1]. This surface can be determined by its shape, size and orientation. The geometrical representation of any stress state in the stress space are necessary. The stress state at any material point is expressed in terms of 'true' Cauchy stress. For numerical computation it is convenient to rewrite yield function in terms of alternative stress invariants. The components of the stress tensor $\boldsymbol{\sigma}$ in the cartesian coordinate system are presented by a matrix of the second order

$$[\sigma_{ij}] = \begin{bmatrix} \sigma_{xx} & \sigma_{xy} & \sigma_{xz} \\ \sigma_{yx} & \sigma_{yy} & \sigma_{yz} \\ \sigma_{zx} & \sigma_{zy} & \sigma_{zz} \end{bmatrix} \qquad (Ap4.111)$$

and as it is symmetric, only six stress components are independent determinating uniquely a stress state. The three principal stress are calculated from

$$|\sigma_{ij} - \sigma\delta_{ij}| = 0 \qquad (Ap4.112)$$

i.e.

$$\begin{bmatrix} \sigma_{xx} - \sigma & \sigma_{xy} & \sigma_{xz} \\ \sigma_{yx} & \sigma_{yy} - \sigma & \sigma_{yz} \\ \sigma_{zx} & \sigma_{zy} & \sigma_{zz} - \sigma \end{bmatrix} = 0 \qquad (Ap4.113)$$

or in rewritten form

$$\sigma^3 - J_1\sigma^2 + J_2\sigma - J_3 = 0 \qquad (Ap4.114)$$

where J_1, J_2 and J_3 are the invariants of stress tensor, expressed as follows

$$J_1 = tr(\boldsymbol{\sigma}) = \sigma_{ii} = \sigma_{xx} + \sigma_{yy} + \sigma_{zz} \qquad (Ap4.115)$$

$$J_2 = \frac{1}{2}\sigma_{ij}\sigma_{ij} = \sigma_{xx}\sigma_{yy} + \sigma_{yy}\sigma_{zz} + \sigma_{xx}\sigma_{zz} - {\sigma_{xy}}^2 - {\sigma_{yz}}^2 - {\sigma_{zx}}^2 \quad (Ap4.116)$$

$$J_3 = \frac{1}{3}\sigma_{ij}\sigma_{jk}\sigma_{ki} = det[\sigma_{ij}] \quad (Ap4.117)$$

The same invariants expressed in terms of the principal stresses σ_1, σ_2 and σ_3 can be rewritten

$$J_1 = \sigma_1 + \sigma_2 + \sigma_3 \quad (Ap4.118)$$

$$J_2 = \sigma_1\sigma_2 + \sigma_2\sigma_3 + \sigma_3\sigma_1 \quad (Ap4.119)$$

$$J_3 = \sigma_1\sigma_2\sigma_3 \quad (Ap4.120)$$

For each principal stress σ_i, the associated principal direction $\mathbf{n}^{(i)} (i = 1, 2, 3)$ can be obtained as

$$\boldsymbol{\sigma} \cdot \mathbf{n}^{(i)} = \sigma_i \mathbf{n}^{(i)} \quad (Ap4.121)$$

what after some algebra gives

$$\begin{bmatrix} \sigma_{xx} & \sigma_{xy} & \sigma_{xz} \\ \sigma_{yx} & \sigma_{yy} & \sigma_{yz} \\ \sigma_{zx} & \sigma_{zy} & \sigma_{zz} \end{bmatrix} = [R_{ij}] \begin{bmatrix} \sigma_1 & 0 & 0 \\ 0 & \sigma_2 & 0 \\ 0 & 0 & \sigma_3 \end{bmatrix} [R_{ij}]^T \quad (Ap4.122)$$

where

$$[R_{ij}] = [n_j^{(i)}] = \begin{bmatrix} n_1^{(1)} & n_1^{(2)} & n_1^{(3)} \\ n_2^{(1)} & n_2^{(2)} & n_2^{(3)} \\ n_3^{(1)} & n_3^{(2)} & n_3^{(3)} \end{bmatrix} \quad (Ap4.123)$$

Thus, if the principal stresses and their directions are known, the stress state can be determined.

In the plasticity theory, the stress tensor is decomposed as follows

$$\sigma_{ij} = p\delta_{ij} + S_{ij} \quad (Ap4.124)$$

where p is the hydrostatic stress or pressure

$$p = \frac{1}{3}\sigma_{ii} = \frac{1}{3}(\sigma_{xx} + \sigma_{yy} + \sigma_{zz}) = \frac{1}{3}(\sigma_1 + \sigma_2 + \sigma_3) \qquad (Ap4.125)$$

with $p\delta_{ij}$ being the spherical or hydrostatic stress tensor and S_{ij} being the deviatoric stress tensor expressed as

$$S_{ij} = \sigma_{ij} - p\delta_{ij} \qquad (Ap4.126)$$

Thus, the following expressions are given

$$J_1' = tr(\mathbf{S}) = S_{ii} = S_1 + S_2 + S_3 = 0 \qquad (Ap4.127)$$

$$J_2' = \frac{1}{2}S_{ij}S_{ij} = \frac{1}{6}[(\sigma_{xx} - \sigma_{yy})^2 + (\sigma_{yy} - \sigma_{zz})^2 + (\sigma_{zz} - \sigma_{xx})^2] + \sigma_{xy}{}^2 + \sigma_{yz}{}^2 + \sigma_{zx}{}^2$$

$$= \frac{1}{6}[(\sigma_1 - \sigma_2)^2 + (\sigma_2 - \sigma_3)^2 + (\sigma_3 - \sigma_1)^2] = \frac{1}{2}(S_1^2 + S_2^2 + S_3^2) \qquad (Ap4.128)$$

$$J_3' = det(S_{ij}) = \frac{1}{3}S_{ij}S_{jk}S_{ki} = S_1S_2S_3 \qquad (Ap4.129)$$

where $S_i (i = 1, 2, 3)$ are the principal values of the deviatoric tensor $\mathbf{S}$. The use of equations $(Ap4.121)$ and $(Ap4.125)$ leads to

$$\mathbf{S} \cdot \mathbf{n}^{(i)} = (\boldsymbol{\sigma} - p\mathbf{I}) \cdot \mathbf{n}^{(i)} = (\sigma_i - p)n^{(i)} \quad i = 1, 2, 3 \qquad (Ap4.130)$$

what shows that the principal directions of the deviatoric stress $\mathbf{S}$ are the same as those of the stress tensor $\boldsymbol{\sigma}$.

The principal deviatoric stresses $S_i (i = 1, 2, 3)$ are related to the principal stresses $\sigma_i (i = 1, 2, 3)$

$$S_i = \sigma_i - p \qquad (Ap4.131)$$

where

$$S_1 = \frac{2\sigma_1 - \sigma_2 - \sigma_3}{3}$$

$$S_2 = \frac{2\sigma_2 - \sigma_1 - \sigma_3}{3}$$

$$S_3 = \frac{2\sigma_3 - \sigma_1 - \sigma_2}{3}$$

The invariants of the deviatoric stress $\mathbf{S}$ are related to the invariants $J_i (i = 1, 2, 3)$ of the stress tensor $\boldsymbol{\sigma}$ as

$$J_1' = 0 \tag{Ap4.132}$$

$$J_2' = \frac{1}{3}(J_1^2 - 3J_2) \tag{Ap4.133}$$

$$J_3' = \frac{1}{27}(2J_1^3 - 9J_1 J_2 + 27J_3) \tag{Ap4.134}$$

Some additional remarks about octahedral normal and shear stress, σ_{oct} and τ_{oct}, respectively are given below. For clarity reason, first it is necessary to define the octahedral plane as the plane whose normal has the same angles with each of the principal directions of the stress tensor $\boldsymbol{\sigma}$. Thus, the unit normal $\mathbf{n} = (n_1, n_2, n_3)$ must satisfy

$$n_1^2 = n_2^2 = n_3^2 \tag{Ap4.135}$$

and

$$n_1^2 + n_2^2 + n_3^2 = 1 \tag{Ap4.136}$$

what leads to

$$n_1 = n_2 = n_3 = \pm\frac{1}{\sqrt{3}} \tag{Ap4.137}$$

It means that there are eight families of octahedral planes, as follows

$$\pm\sigma_1 \pm \sigma_2 \pm \sigma_3 = \sqrt{3}C \tag{Ap4.138}$$

with C being a constant.

The octahedral normal stresses σ_{oct} is the normal stress on an octahedral plane and is expressed as

$$\sigma_{oct} = \mathbf{n} \cdot \boldsymbol{\sigma} \cdot \mathbf{n} = \sigma_1 n_1^2 + \sigma_2 n_2^2 + \sigma_3 n_3^2 = \frac{1}{3}(\sigma_1 + \sigma_2 + \sigma_3) = \frac{1}{3}J_1 \tag{Ap4.139}$$

The octahedral shear stress τ_{oct} is the shear stress on an octahedral plane expressed as

$$\tau_{oct}{}^2 = |\boldsymbol{\sigma} \cdot \mathbf{n}|^2 - \sigma_{oct}{}^2 = \frac{1}{9}[(\sigma_1 - \sigma_2)^2 + (\sigma_2 - \sigma_3)^2 + (\sigma_3 - \sigma_1)^2] = \frac{2}{3}J_2' \qquad (Ap4.140)$$

The representation of a stress state geometrically requires a six dimensional space with the six independent stress components as its coordinate axes. The yield surface (or failure surface) for anisotropic material needs six-dimensional stress space and the orientation of the principal stresses is as important as the magnitude of the principal stresses, what leads to complex calculation. For the isotropic material, since the material properties are the same in any direction, only the magnitude of the principal stresses are required, thus a three dimensional stress space using the three principal stresses as the coordinate axes are sufficient.

A4.3.9.1 The Mises Huber yield criterion

The Mises Huber yield criterion [K-1], assumes that the plastic yielding will occur only when the second invariant J_2' of the deviatoric stress tensor $\mathbf{S}$ reaches a critical value k^2

$$J_2' - k^2 = 0 \quad \text{for} \quad \text{yielding} \quad \text{or} \quad \text{plastic} \quad \text{deformation}$$

$$J_2' < k^2 \quad \text{for} \quad \text{elastic} \quad \text{deformation}$$

The yield criterion, in terms of stress components has the form

$$\frac{1}{6}[(\sigma_{xx} - \sigma_{yy})^2 + (\sigma_{yy} - \sigma_{zz})^2 + (\sigma_{zz} - \sigma_{xx})^2] + \sigma_{xy}{}^2 + \sigma_{yz}{}^2 + \sigma_{zx}{}^2 = k^2 \qquad (Ap4.141)$$

or in rewritten form

$$\frac{1}{6}[(\sigma_1 - \sigma_2)^2 + (\sigma_2 - \sigma_3)^2 + (\sigma_3 - \sigma_1)^2] = k^2 \qquad (Ap4.142)$$

In principal stress space, this condition gives a circular cylinder surface, whose projection onto π plane is a circle, as it is shown in Figure 4A.4.

The determination of the constant k is performed by a simple tension test

$$\sigma_1 = \sigma_y \quad \sigma_2 = \sigma_3 = 0 \qquad (Ap4.143)$$

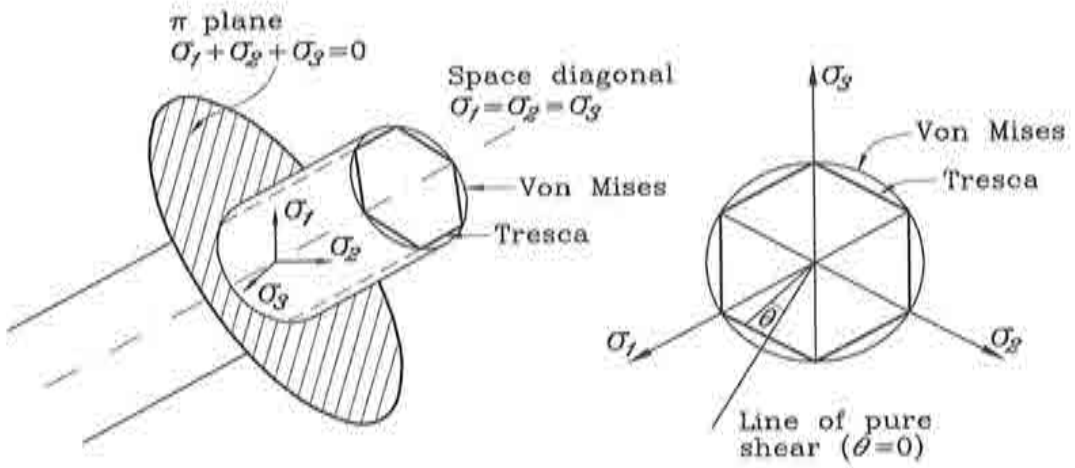

Figure 4A.4 Geometrical representation of the Tresca and von Mises yield surfaces in principal stress space (a) and π plane representation (b).

where σ_y is the yield stress in simple tension. Thus, substituting (*Ap*4.143) into (*Ap*4.142) gives

$$\frac{1}{3}\sigma_y{}^2 = k^2 \qquad (Ap4.144)$$

and finally

$$k = \frac{\sigma_y}{\sqrt{3}} \qquad (Ap4.145)$$

A4.3.9.2 The Tresca yield criterion

The Tresca yield criterion [K-1], assumes that the plastic yielding occurs only when the maximum shear stress reaches the critical value of material k. Mathematically it is expressed as

$$\tau_{max} = k \quad \text{for} \quad \text{yielding} \quad \text{or} \quad \text{plastic} \quad \text{deformation}$$

$$\tau_{max} < k \quad \text{for} \quad \text{plastic} \quad \text{deformation}$$

In terms of principal stresses, the Tresca yield condition is written as

$$max[\frac{1}{2}|\sigma_1 - \sigma_2|, \frac{1}{2}|\sigma_2 - \sigma_3|, \frac{1}{2}|\sigma_3 - \sigma_1|] = k \qquad (Ap4.146)$$

or

$$\frac{1}{2}(\sigma_{max} - \sigma_{min}) = k \qquad (Ap4.147)$$

The constant k, applying the same procedure with the uniaxial test is expressed as

$$k = \frac{\sigma_y}{2} \qquad (Ap4.148)$$

The yield surface has the form of a circular cone. The projection of these surfaces onto π plane is presented in Figure 4A.5.

A4.3.9.3 The Mohr-Coulomb yield criterion

The Mohr-Coulomb yield criterion [K-1], depends on the mean stress, i.e. this criterion includes the influence of the hydrostatic pressure (dependence on J_1) what is necessary in the plasticity applications to soil, rock and concrete. This criterion is a generalization of the Coulomb friction failure law defined by

$$f = \tau + \sigma_n tan\phi - C = 0 \qquad (Ap4.149)$$

where τ is the magnitude of the shearing stress, σ_n is the normal stress, c is the cohesion and ϕ is the angle of internal friction, expressed respectively

$$\tau = \frac{\sigma_1 - \sigma_3}{2} cos\phi \qquad (Ap4.150)$$

$$\sigma_n = \frac{\sigma_1 + \sigma_3}{2} + \frac{\sigma_1 - \sigma_3}{2} sin\phi \qquad (Ap4.151)$$

In terms of principal stresses $\sigma_i, i = 1, 2, 3$, the criterion $(Ap4.150)$ criterion can be rewritten as

$$f = max[|\sigma_i - \sigma_j| + |\sigma_i + \sigma_j| sin\phi] - 2C \quad cos\phi = 0 \qquad (Ap4.152)$$

or

$$(\sigma_1 - \sigma_3) = 2C \quad cos\phi - (\sigma_1 + \sigma_3) sin\phi \qquad (Ap4.153)$$

In principal stress space this gives a conical yield surface as a consequence of the fact that a hydrostatic stress does influence yielding, as it is presented in Figure 4A.5.

A4.3.9.4 The Drucker Prager yield criterion

Mohr-Coulomb and Tresca yield surfaces have hexagonal-shaped corners, what presents difficulties when the classical associated plasticity theory is used to determine the plastic strain increment. An approximation to the Mohr-Coulomb law is introduced by Drucker and Prager [K-1] as a modification of the Mises-Huber yield criterion, to allow hydrostatic stress dependency, considering the surface as a smooth cone by adding a hydrostatic stress term αJ_1 to the Mises-Huber criterion

$$f = \alpha J_1 + \sqrt{J_2'} - k = 0 \qquad (Ap4.154)$$

where J_1 is the first invariant of the stress tensor $\boldsymbol{\sigma}$, $J_1 = \sigma_{11} + \sigma_{22} + \sigma_{33}$ and the values α and k in order to make the Drucker Prager circle coincide with the outer apices of the Mohr-Coulomb hexagon

$$\alpha = \frac{2sin\phi}{\sqrt{3}(3 + sin\phi)} \qquad k = \frac{6Ccos\phi}{\sqrt{3}(3 + sin\phi)} \qquad (Ap4.155)$$

The yield surface has the form of a circular cone. The projection of these surfaces onto π plane is presented in Figure 4A.5.

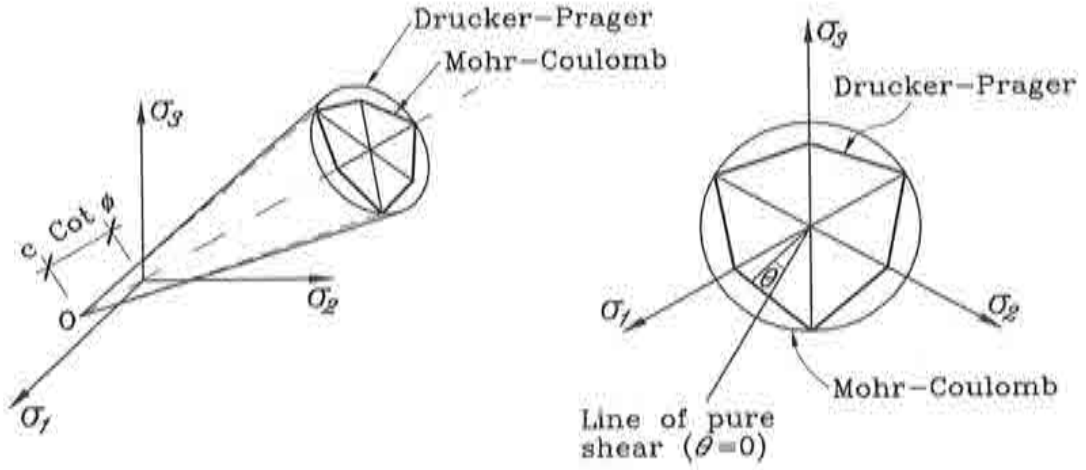

Figure 4A.5 Geometrical representation of the Mohr-Coulomb and Drucker-Prager yield surfaces in principal stress space (a) and π plane representation (b).

A4.3.9.5 The Hill criterion

The Hill yield criterion [H-1], is the modification of the Tresca or Von Mises criterion for isotropic materials, to describe the yielding of anisotropic materials by using additional material constants. With reference to the orthotropic material, the Hill's yield criterion 1948 is based on the following assumptions

- the material is orthotropic, thus exist three mutually orthogonal planes of symmetry at each material point. The principal axes of anisotropy are the intersections of those planes.
- the hydrostatic stress does not affect yielding.
- there is not Bauchinger effect - the phenomenon which occurs when the yield stress obtained in reloading or reversed direction is substantially less than the yield stress in the original direction.

Mathematically, according to the principal axes of anisotropy x, y and z the Hill condition is

$$f(\boldsymbol{\sigma}) =$$

$$\sqrt{F(\sigma_{22}-\sigma_{33})^2) + G(\sigma_{33}-\sigma_{11})^2 + H(\sigma_{11}-\sigma_{22})^2 + 2L{\sigma_{23}}^2 + 2M{\sigma_{13}}^2 + 2N{\sigma_{12}}^2}$$

$$-1 \qquad (Ap4.156)$$

where F, G, H, L, M and N are material constants characterizing the current state of anisotropic yield behaviour, expressed as follows

$$F = \frac{1}{2}\left(\frac{1}{\bar{\sigma}_{22}^2} + \frac{1}{\bar{\sigma}_{33}^2} - \frac{1}{\bar{\sigma}_{11}^2}\right) \qquad (Ap4.157a)$$

$$G = \frac{1}{2}\left(\frac{1}{\bar{\sigma}_{33}^2} + \frac{1}{\bar{\sigma}_{11}^2} - \frac{1}{\bar{\sigma}_{22}^2}\right) \qquad (Ap4.157b)$$

$$H = \frac{1}{2}\left(\frac{1}{\bar{\sigma}_{11}^2} + \frac{1}{\bar{\sigma}_{22}^2} - \frac{1}{\bar{\sigma}_{33}^2}\right) \qquad (Ap4.157c)$$

$$L = \frac{1}{2\bar{\sigma}_{23}^2} \quad M = \frac{1}{2\bar{\sigma}_{13}^2} \quad N = \frac{1}{2\bar{\sigma}_{12}^2} \qquad (Ap4.157d)$$

In the above expressions, $\bar{\sigma}_{11}$, $\bar{\sigma}_{22}$ and $\bar{\sigma}_{33}$ are the tensile yield stress in the principal anisotropic directions and $\bar{\sigma}_{12}$, $\bar{\sigma}_{23}$ and $\bar{\sigma}_{13}$ are the yield stresses in shear with respect to the principal axes of anisotropy.

A4.3.10 Loading and unloading in stress space

Under mechanical loading a material deform elastically or plastically depending on the applied loading level [K-1]. The stress-strain relations for elastic deformation and plastic deformation are different, thus it is important to make difference between elastic and plastic regions to be able to identify whether the deformation is elastic or plastic. The yield surface is used to identify elastic and plastic regions and loading and unloading criteria is used to identify the characteristics of the deformation.

Loading occurs when the stress state point is on the yield surface and remains there, thus the plastic deformation can increase indefinitely. Unloading is caused when the stress point moves to the inside of the yield surface. If the subsequent yield surface is exactly the same at any instant, the material is perfectly plastic. If $F(\boldsymbol{\sigma}) = (\boldsymbol{\sigma}) - k_0$ is the yield function, then the following states are possible

$$F(\boldsymbol{\sigma}) < 0 \quad \text{elastic} \quad \text{deformation}$$

$$F(\boldsymbol{\sigma}) = 0$$

$$dF = f(\boldsymbol{\sigma} + d\boldsymbol{\sigma}) - f(\boldsymbol{\sigma}) = \frac{\partial f}{\partial \boldsymbol{\sigma}} : d\boldsymbol{\sigma} = 0 \quad \text{loading}$$

$$dF = f(\boldsymbol{\sigma} + d\boldsymbol{\sigma}) - f(\boldsymbol{\sigma}) = \frac{\partial f}{\partial \boldsymbol{\sigma}} : d\boldsymbol{\sigma} \leq 0 \quad \text{unloading}$$

The direction of the vector $\partial f / \partial \boldsymbol{\sigma}$ in the stress space has the direction of outer normal $\mathbf{n}$ to the yield surface. For perfect plastic material, the yield surface is fixed and can not expand, thus $d\boldsymbol{\sigma}$ can not point outward, as it is shown in Figure 4A.6.a. The loading and unloading for work-hardening material is shown in Figure 4A.6.b.

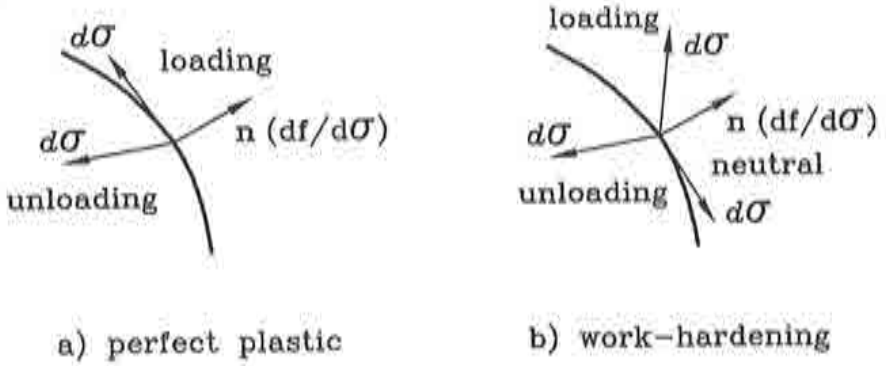

Figure 4A.6 Loading and unloading for (a) perfect plastic and (b) work hardening materials.

For work hardening materials, the above expressions are

$$F(\boldsymbol{\sigma}) < 0 \quad \text{elastic} \quad \text{deformation}$$

$$F(\boldsymbol{\sigma}) = 0, \quad \frac{\partial f}{\partial \boldsymbol{\sigma}} : d\boldsymbol{\sigma} \geq 0 \quad \text{loading}$$

$$F(\boldsymbol{\sigma}) = 0, \quad \frac{\partial f}{\partial \boldsymbol{\sigma}} : d\boldsymbol{\sigma} = 0 \quad \text{neutral} \quad \text{loading}$$

$$F(\boldsymbol{\sigma}) = 0, \quad \frac{\partial f}{\partial \boldsymbol{\sigma}} : d\boldsymbol{\sigma} \leq 0 \quad \text{unloading}$$

It should be emphasized that during plastic deformation, the yield criterion should be satisfied at all times.

A4.3.11 Uniaxial stress-strain relation

The direct result of the standard tensile test are the nominal stress (i.e. the first Piola-Kirchhoff stress)

$$\hat{\boldsymbol{\sigma}} = \frac{P}{A_0} \tag{Ap4.158}$$

and the nominal strain (i.e. engineering strain)

$$\hat{\boldsymbol{\varepsilon}} = \frac{L - L_0}{L_0} \tag{Ap4.159}$$

where A_0 and L_0 are the original area and length, respectively. Thus, nominal stress $\hat{\boldsymbol{\sigma}}$ and nominal strain $\hat{\boldsymbol{\varepsilon}}$ are defined based on the original dimensions.

For a large strain elasto-plastic analysis, the appropriate measures are the 'true' Cauchy stress

$$\sigma = \frac{P}{A} \tag{Ap4.160}$$

and logarithmic natural strain

$$d\varepsilon = \frac{dL}{L} \Rightarrow \varepsilon = \int_{L_0}^{L} \frac{dL}{L} = ln\frac{L}{L_0} \tag{Ap4.161}$$

where A and L are the current area and length, respectively. The logarithmic strain or natural strain is particularly useful in plasticity, since amount of plastic deformation (like equivalent plastic strain $\bar{\varepsilon}_p$) is measured using this strain measure.

The corresponding relation between the logarithmic and engineering strain using equations ($Ap4.159$) and ($Ap4.161$) is expressed as

$$\varepsilon = ln\frac{L}{L_0} = ln\frac{\Delta L + L_0}{L_0} = ln(1+\bar{\varepsilon}) \qquad (Ap4.162)$$

The current area used in calculation of the Cauchy stress requires measurement of the cross section area of the speciman, but in metal plasticity for practical purposes is calculated assuming the constant volume, i.e. the plasticity theory assumed that the material is incompressible

$$A_0 L_0 = AL \qquad (Ap4.163)$$

thus, the relationship between $\bar{\sigma}$ and σ can be expressed as

$$\sigma = \frac{P}{A} = \frac{P}{A_0}\frac{L}{L_0} = \bar{\sigma}(1+\bar{\varepsilon}) \qquad (Ap4.164)$$

The uniaxial stress-strain curve can be approximated by the Ludwik-Nadai formula

$$\sigma = C(\bar{\varepsilon}_o + \bar{\varepsilon}_p)^n \qquad (Ap4.165)$$

where C is the Ludwik constant and n is the hardening exponent with a value between 0.1 and 0.5. The Ludwik-Nadai formula takes into account nonlinear hardening. The maximal nominal stress occurs when the logarithmic strain ε is equal to the hardening exponent n.

A reference yield stress in the yield criteria for a multiaxial stress states is the uniaxial yield stress σ_y. The plastic part of the uniaxial stress-strain relationship $\sigma = \sigma(\varepsilon)$ obtained from a standard tensile test gives the uniaxial yield stress denoted as $\sigma_y(\bar{\varepsilon}^p)$. Thus, if linear hardening is assumed, the uniaxial yield stress $\sigma_y(\bar{\varepsilon}^p)$ is expressed as

$$\sigma_y(\bar{\varepsilon}^p) = \sigma_{yo} + H\bar{\varepsilon}^p \qquad (Ap4.166)$$

where H is the hardening modulus.

CHAPTER 5

NON-LINEAR SHELL

5.1 INTRODUCTION

In the analysis of shells, it is of interest to reduce the number of degrees of freedom per node, thus achieving reduction of the computational effort. As it has been done in the previous chapter, the analysis is accomplished by making explicit use of the Kirchhoff-Love hypothesis on the shell fibre remaining straight and perpendicular to the midsurface of the shell, using the combined FE/FV approach to eliminate the rotational degrees of freedom.

The framework of the mixed Hu-Washizu formulation using the concepts based on the combined FE/FV technique is again used to develop two triangular plate elements without rotational degrees of freedom for linear analysis, called the BPT and BPN elements, Zarate [Z-1]. They are based on the Cell Centered and Cell Vertex schemes, respectively. The rotation-free BPT element was extended by Cendoya [C-1] to nonlinear analysis of shells called the BST element in an explicit dynamic code. As it has been shown that the Cell Vertex scheme has some advantages over the Cell Centered scheme in the previous chapters, the extension of the BPN element for the linear analysis to the nonlinear dynamic analysis of shells is presented in this study.

The layout of the chapter is the following. First, the basic theory for thin plate/shell element is reviewed. The set of the governing equations is developed in integral form in the framework of the mixed Hu-Washizu formulation and the study of stability of the numerical solution is presented.

Two conceptually different triangle elements without rotational degrees of freedom are derived on the basis of the Cell Centered and Cell Vertex schemes. Details on the derivation of the element stiffness matrices and the load vectors as well as the imposition of boundary conditions are given further. The same explicit dynamic code, explained in the previous chapter, is used for the extension of the BPN element for the linear analysis to the BSN element for the nonlinear dynamic analysis.

The efficiency of the new element is checked with several examples of practical application, most notably, sheet metal forming. Finally, some conclusions are given.

5.2 BASIC THEORY

The plate shown in Figure 5.1 is considered. The Kirchhoff thin plate conditions are assumed as

$$\theta_x = \frac{\partial w}{\partial x}, \quad \theta_y = \frac{\partial w}{\partial y} \tag{5.1}$$

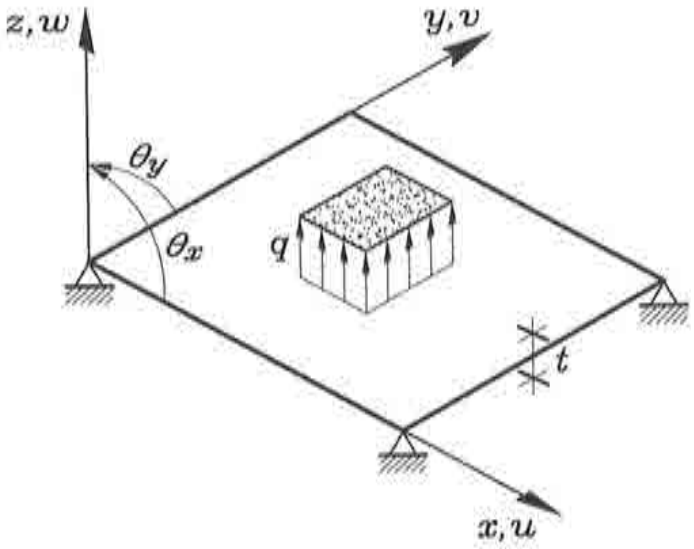

Figure 5.1 Sign convention for the deflections and rotations in a plate.

The set of the governing equations is expressed as follows. The kinematic equation gives the curvature field

$$\boldsymbol{\chi} = [\chi_x, \chi_y, \chi_{xy}]^T = \mathbf{L}w \tag{5.2}$$

where $\mathbf{L}$ is the differential curvature operator defined as

$$\mathbf{L} = [-\frac{\partial^2}{\partial x^2}, -\frac{\partial^2}{\partial y^2}, -\frac{2\partial^2}{\partial x \partial y}]^T \tag{5.3}$$

The constitutive relationship between bending moments and curvatures is expressed as

$$\mathbf{m} = [m_x, m_y, m_{xy}]^T = \mathbf{D}\boldsymbol{\chi} \tag{5.4}$$

where the $\mathbf{D}$ matrix is

$$\mathbf{D} = \frac{Et^3}{12(1-\nu^2)} \begin{bmatrix} 1 & \nu & 0 \\ \nu & 1 & 0 \\ 0 & 0 & \frac{1-\nu}{2} \end{bmatrix} \tag{5.5}$$

with E and ν being the Young's modulus and Poisson's ratio, respectively.

The equilibrium equation is expressed as

$$\mathbf{L}^T \mathbf{m} + q = 0 \tag{5.6}$$

where q is the distributing loading.

The set of the governing equations is obtained in the integral form from the standard Hu-Washizu functional

$$\Pi = \frac{1}{2} \int \int_A \boldsymbol{\chi}^T \mathbf{D} \boldsymbol{\chi} dA + \int \int_A [\mathbf{L}w - \boldsymbol{\chi}]^T \mathbf{m} dA - \int \int_A q w dA \tag{5.7}$$

where A is the area of the plate.

The condition of the minimum potential energy is

$$\delta \Pi = 0 \tag{5.8}$$

and the independent functions subjected to variation are w, $\mathbf{m}$ and $\boldsymbol{\chi}$. The variation of Π with respect to $\mathbf{m}$, $\boldsymbol{\chi}$ and w leads to the following set of kinematic, constitutive and equilibrium equations

$$\int \int_A \delta \mathbf{m}^T [\mathbf{L}w - \boldsymbol{\chi}] dA = 0 \tag{5.9a}$$

$$\int \int_A \delta \boldsymbol{\chi}^T [\mathbf{D}\boldsymbol{\chi} - \mathbf{m}] dA = 0 \tag{5.9b}$$

$$\int \int_A [\mathbf{L}\delta w]^T \mathbf{m} dA - \int \int_A \delta w q dA = 0 \tag{5.9c}$$

Equations (5.9a), (5.9b) and (5.9c) represent the global satisfaction over the plate of the kinematic, constitutive, and equilibrium equations, respectively. They are the basis for the combined FE/FV discretization.

5.3 FINITE ELEMENT - FINITE VOLUME DISCRETIZATION

A discretization of the plate into standard three node triangles is considered. The curvatures $\boldsymbol{\chi}$ and the bending moments $\mathbf{m}$ are described by constant fields within appropriate non-overlapping control domains covering the whole domain as

$$\mathbf{m} = \mathbf{I}_3 \mathbf{m}_p \qquad \delta\mathbf{m} = \mathbf{I}_3 \delta\mathbf{m}_p \tag{5.10a}$$

$$\boldsymbol{\chi} = \mathbf{I}_3 \boldsymbol{\chi} \qquad \delta\boldsymbol{\chi} = \mathbf{I}_3 \delta\boldsymbol{\chi}_p \tag{5.10b}$$

where $(\cdot)_p$ denotes constant values over the p-th control domain and $\mathbf{I}_3$ is the 3×3 unit matrix.

Two kind of control domains are used. The first is the control domain formed by a single triangular element corresponding to the Cell Centered scheme, presented in Figure 5.2.a. The second one, is the control domain formed by $\frac{1}{3}$ of the areas of the elements surrounding a node, corresponding to the Cell Vertex scheme, presented in Figure 5.2.b. The 'patch of elements' associated to the control domain in the Cell Centered scheme is formed by four elements while in the Cell Vertex scheme the number of elements in the patch is variable.

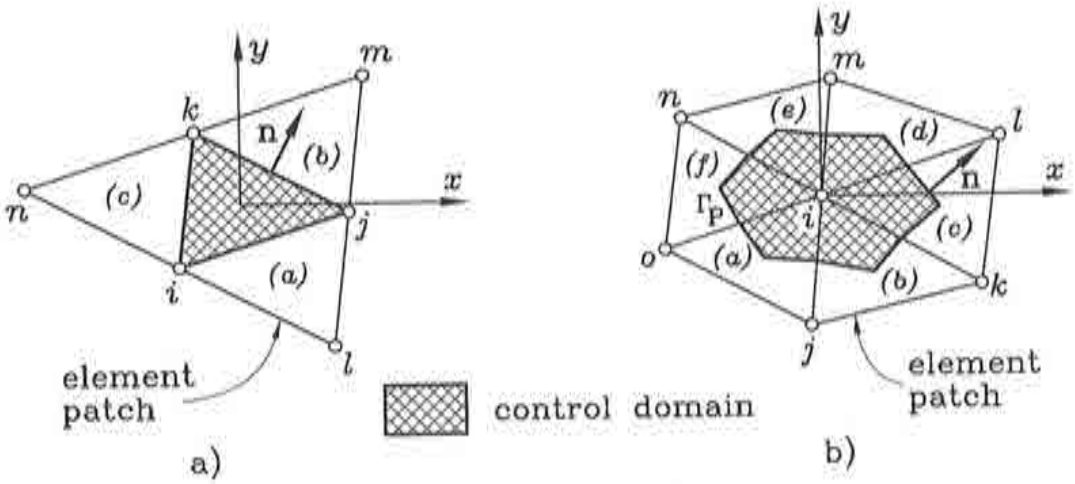

Figure 5.2 (a) Cell Centered triangular patch and (b) Cell Vertex triangular patch.

It should be noted that in the Cell Centered scheme each control domain coincides with an standard three node finite element triangle. In the Cell Vertex scheme an element is formed by contributions from three different control domains, as presented in Figure 5.3.

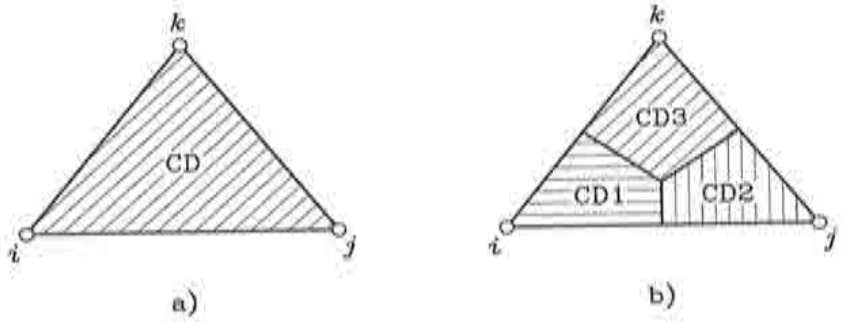

Figure 5.3 (a) Cell Centered element and (b) Cell Vertex element.

Derivation of the curvature and bending moment fields as well as stiffness matrix of each control domain are expressed in terms of the nodal deflections associated to the corresponding element patch. The area integrals in equation (5.9) can be expressed as a sum of contributions over different control domains. The constitutive equation over each patch (5.9b) is rewritten as

$$\sum_p \int\int_{A_p} \delta\boldsymbol{\chi}_p^T [\mathbf{D}\boldsymbol{\chi}_p - \mathbf{m}_p] dA = 0 \tag{5.11}$$

where A_p is the area of the p-th control domain.

Taking into account that the virtual curvatures are arbitrary, gives

$$\boxed{\mathbf{m}_p = \mathbf{D}_p \boldsymbol{\chi}_p} \tag{5.12}$$

Equation (5.12) defines the constant bending moment field over the control domain in terms of the corresponding curvatures, where $\mathbf{D}_p = \frac{1}{A_p}\int\int_{A_p} \mathbf{D} dA$ is the average constitutive matrix over a control domain.

The kinematic equation over the plate surface (5.9a) is rewritten as

$$\sum_p \int\int_{A_p} \delta\mathbf{m}_p^T [\mathbf{L}w - \boldsymbol{\chi}_p] dA = 0 \tag{5.13}$$

Taking into account that the virtual bending moments are arbitrary, the curvature over each control domain $\boldsymbol{\chi}_p$ is expressed as

$$\boxed{\boldsymbol{\chi}_p = \frac{1}{A_p}\int\int_{A_p} \mathbf{L}w dA = \frac{1}{A_p}\oint_{\Gamma_p} \mathbf{T}\boldsymbol{\nabla} w d\Gamma} \tag{5.14}$$

where

$$\mathbf{T} = \begin{bmatrix} n_x & 0 \\ 0 & n_y \\ n_y & n_x \end{bmatrix}, \quad \boldsymbol{\nabla} = \begin{Bmatrix} \frac{\partial}{\partial x} \\ \frac{\partial}{\partial y} \end{Bmatrix} \tag{5.15}$$

and $\mathbf{n} = [n_x, n_y]^T$ is the unit normal vector to the boundary Γ_p surrounding the control domain, Figure 5.2.

The transformation of the area integral into the line integral is typical of the Finite Volume method. Equation (5.14) defines the curvatures for each control domain in terms of the deflection gradients along the boundaries.

The equilibrium equation (5.9c) can be rewritten as

$$\sum_p \int\int_{A_p} [\mathbf{L}\delta w]^T \mathbf{m}_p dA - \int\int_{A_p} \delta w q dA = 0 \tag{5.16}$$

Integrating by parts the first integral in the above equation, gives

$$\sum_p \int\int_{A} [\mathbf{L}\delta w]^T \mathbf{m}_p dA = \sum_p [\oint_{\Gamma_p} \mathbf{T}\boldsymbol{\nabla}\delta w]^T \mathbf{m}_p d\Gamma \tag{5.17}$$

thus, the equilibrium equation can be rewritten as

$$\sum_p [\oint_{\Gamma_p} \mathbf{T}\boldsymbol{\nabla}\delta w]^T \mathbf{m}_p d\Gamma - \sum_p \int\int_{A_p} \delta w q dA = 0 \tag{5.18}$$

Substituting equation (5.14) into (5.12) and replacing the latter into the equilibrium equation (5.18) leads to

$$\boxed{\sum_p \oint_{\Gamma_p} [\mathbf{T}\boldsymbol{\nabla}\delta w]^T \frac{1}{A_p} \mathbf{D}_p \mathbf{T}\boldsymbol{\nabla}\delta w d\Gamma - \sum_p \int\int_{A_p} \delta w q dA = 0} \tag{5.19}$$

Equation (5.19) is the basis for deriving the final set of algebraic equations, after appropriate discretization of the deflection field. The simplest option is to interpolate linearly the deflection within each triangle element in terms of the nodal deflections in the standard finite element manner as

$$w = \sum_{i=1}^{3} N_i w_i = \mathbf{N}^{(e)} \mathbf{w}^{(e)} \tag{5.20}$$

where w_i denote nodal deflection values and N_i are the standard linear shape functions of the three node triangle, $\mathbf{N}^{(e)} = [N_1, N_2, N_3]$ and $\mathbf{w}^{(e)} = [w_1, w_2, w_3]^T$.

Substituting equation (5.20) into (5.19) leads to the final system of algebraic equation as

$$\mathbf{K}\mathbf{w} = \mathbf{f} \tag{5.21}$$

where the vector $\mathbf{w}$ contains the nodal deflections. The stiffness matrix $\mathbf{K}$ is obtained by assembling the contributions from the different control domains given by

$$\mathbf{K}_p = [\mathbf{B}_p]^T \mathbf{D}\mathbf{B}_p A_p \tag{5.22}$$

where $\mathbf{B}_p$ is the curvature matrix relating the constant curvature field within a control domain and the nodal deflections associated to the patch.

Substituting equation (5.20) into (5.14) gives

$$\boldsymbol{\chi}_p = \mathbf{B}_p \mathbf{w}_p \tag{5.23}$$

where the vector $\mathbf{w}_p$ consists the deflections of the nodes linked to the p-th control domain. The computation of the curvature matrix $\mathbf{B}_p$ is different for the Cell Centered and Cell Vertex schemes, presented in detail in the next section.

The nodal force vector $\mathbf{f}$ is obtained as in the standard linear finite element triangles. The components of the nodal force vector $\mathbf{f}$ for a distributed load q are

$$f_i^{(e)} = \int\int_{A^{(e)}} N_i q(x) dA \tag{5.24}$$

where the global nodal force component f_i is obtained by assembling the element contributions $f_i^{(e)}$ in the standard finite element manner. For a constant distributed load q

$$f_i = \sum_e \frac{qA^{(e)}}{3} \tag{5.25}$$

where the sum collects all triangles sharing the $i-th$ node and $A^{(e)}$ is the area of the element e.

A study of stability of the mixed Finite Element - Finite Volume approach used is presented in Annex 5.1.

5.4 COMPUTATION OF THE CURVATURE MATRIX

The computation of the curvature matrix $\mathbf{B}_p$ is different for the Cell Centered and Cell Vertex schemes, so they are presented separately as in the previous chapters. The practical application of the plate/shell element requires the consideration of the various types of boundary conditions: free edges, simply supported edges, fictitious symmetry edges and clamped edges.

5.4.1. Cell Centered scheme - BPT element

The Cell Centered patch for the BPT element is presented in Figure 5.4. It should be noted that the control domain in this case coincides with each triangle. Equations (5.14) and (5.18) require the computation of the deflection gradient along the control domain boundaries. The deflection is linearly interpolated within each element which coincides with control domain, thus the term ∇w is discontinuous at the element edges what causes the difficulties in the Cell Centered scheme.

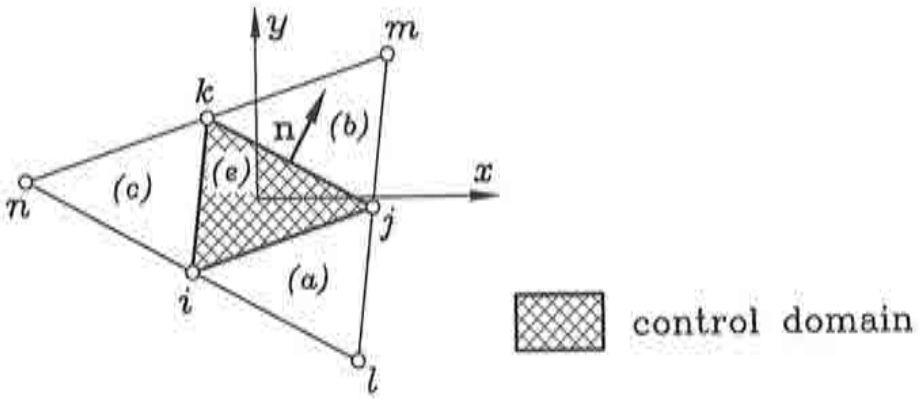

Figure 5.4 BPT element.

Oñate and Cervera [O-2] proposed a method to overcome this problem. The deflection gradients at the triangle sides are calculated as the average value of the gradients contributed by the two elements sharing the side. The constant curvature field for each control domain is expressed as

$$\boldsymbol{\chi}_p = \frac{1}{2A^{(e)}} \oint_{\Gamma_p} \mathbf{T}[\nabla \mathbf{N}^{(p)} \mathbf{w}^{(p)} + \nabla \mathbf{N}^{(i)} \mathbf{w}^{(i)}] d\Gamma = \mathbf{B}_p \mathbf{w}_p \qquad (5.26)$$

where

$$\mathbf{w}_p = [w_i, w_j, w_k, w_l, w_m, w_n]^T \tag{5.27}$$

The indexes p and $i = a, b, c$ denote the p-th element and any of the three elements adjacent to element p, respectively. The curvature matrix $\mathbf{B}_p$ is given by

$$\mathbf{B}_p = [\mathbf{B}_p^i, \mathbf{B}_p^j, \mathbf{B}_p^k, \mathbf{B}_p^l, \mathbf{B}_p^m, \mathbf{B}_p^n] \tag{5.28}$$

where

$$\mathbf{B}_p^i = \frac{1}{2A_p} \oint_{\Gamma_p} \mathbf{T}[\nabla \mathbf{N}_i^{(p)} + \nabla \mathbf{N}_i^{(i)}] d\Gamma \tag{5.29}$$

It should be noted that the $\mathbf{B}_p$ matrix is 3×6 matrix relating the deflections of the six nodes of the four element patch contributing to a control domain and therefore the stiffness matrix $\mathbf{K}_p$ is 6×6 matrix expressed as

$$\mathbf{K}_p = \mathbf{B}_p^T \mathbf{D} \mathbf{B}_p A_p \tag{5.30}$$

5.4.1a Imposition of the boundary conditions

The BPT element with a side along a boundary edge has one of the elements contributing to the patch missing, as shown in Figure 5.5.

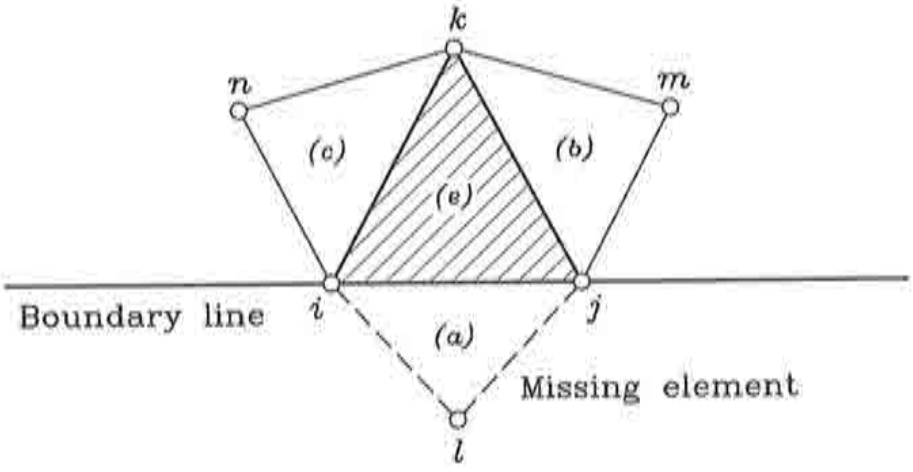

Figure 5.5 Imposition of the boundary conditions - BPT element.

The imposition of the boundary conditions on the prescribed rotations are performed during the construction of $\mathbf{B}_p$ matrix, what makes the main difference with respect to the standard Finite Element method. The contribution from the boundary line edge ij to the patch curvature matrix is

$$\mathbf{B}_p|_{ij} = \frac{1}{A_p} \oint_{\Gamma_{ij}} \mathbf{T} \nabla \mathbf{N}^{(p)} d\Gamma \tag{5.31}$$

The same equation is used for the computation of the contributions from edges jk and ki. Additional conditions must be imposed in the case of boundary edges where the rotations and/or the deflections are constrained. The various types of boundary conditions are considered: simply supported edge, symmetry edge and clamped edge.

5.4.1.1 Simply supported edge

The condition for the simply supported edge is given as

$$w = \frac{\partial w}{\partial s} = 0 \tag{5.32}$$

where the condition $\frac{\partial w}{\partial s} = 0$ is simply imposed by prescribing $w = 0$ in the boundary nodes at the global equation solution level in the standard manner, with s being the boundary direction. The effect of the missing contributing element at the boundary edge is accounted using the expression (5.31)

5.4.1.2 Symmetry edge

The condition for the symmetry edge is given as

$$\frac{\partial w}{\partial x} = 0 \quad \text{or} \quad \frac{\partial w}{\partial y} = 0 \tag{5.33}$$

The condition in the prescribed rotation is imposed by neglecting the contribution from the zero rotation term ($\frac{\partial w}{\partial x}$ or $\frac{\partial w}{\partial y}$) at the symmetry edge when equation (5.31) is computed.

5.4.1.3 Clamped edge

The condition for the clamped edge is given by

$$w = \nabla w = 0 \tag{5.34}$$

what simply implies making zero the integral from equation (5.31) for the corresponding clamped edge. The condition $w = 0$ on the nodes laying on clamped edges is prescribed at the equation solution level in the standard manner. The conditions on the rotations are simply imposed by neglecting the contributions from the clamped edges in the line integral expressed by equation (5.26). For instance, if side ij is clamped this simply implies making zero the integral from equation (5.31).

5.4.2 Cell Vertex scheme - BPN element

The Cell Vertex patch for the BPN element is presented in Figure 5.6. The BPN element combines an standard finite element interpolation with non-standard integration domains.

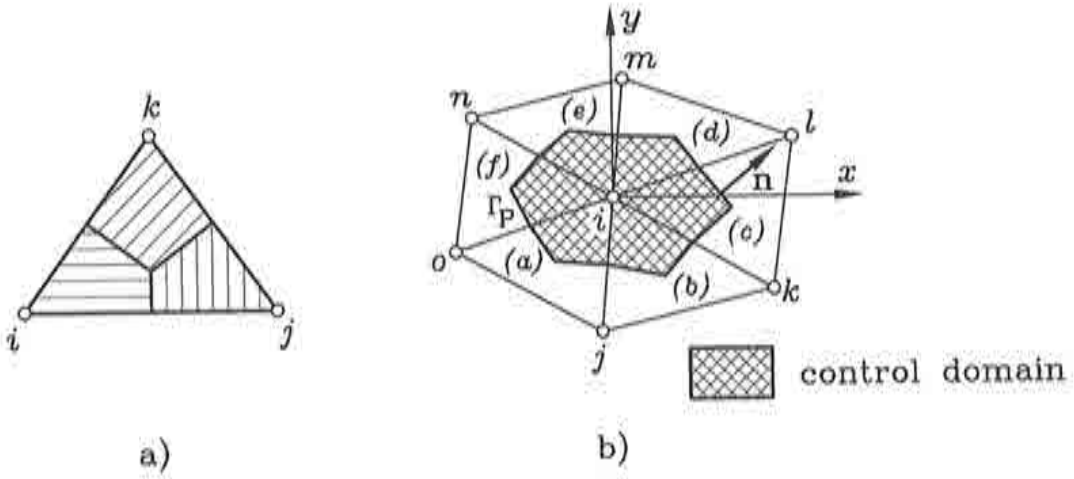

Figure 5.6 (a) BPN element and (b) BPN control domain.

The advantage of the Cell Vertex scheme is that the deflection gradient is continuous along the control domain boundaries. This allows to compute directly the corresponding curvature vector as

$$\boldsymbol{\chi}_p = \frac{1}{A_p} \oint_{\Gamma_p} \mathbf{T} \nabla \mathbf{N}_p \mathbf{w}_p d\Gamma = \mathbf{B}_p \mathbf{w}_p \tag{5.35}$$

where $\mathbf{N}_p$ contains the shape functions of all elements contributing to the p-th control domain. The curvature matrix $\mathbf{B}_p$ is given by

$$\mathbf{B}_p = [\mathbf{B}_p^i, \mathbf{B}_p^j, \mathbf{B}_p^k, \mathbf{B}_p^l, \mathbf{B}_p^m, \mathbf{B}_p^n, \mathbf{B}_p^o] \tag{5.36}$$

where

$$\mathbf{B}_p^i = \frac{1}{A_p} \oint_{\Gamma_p} \mathbf{T} \nabla \mathbf{N}_i d\Gamma \tag{5.37}$$

It is important to note that the curvature matrix $\mathbf{B}_p$ is in this case the global curvature matrix for the central p-th node. As a result, the product $\mathbf{B}_p^T \mathbf{D}_p \mathbf{B}_p A_p$ provides the p-th row of the global stiffness matrix. This fact simplifies the assembly and solution process as the global stiffness equations for a node can be eliminated once they are computed.

The standard element stiffness matrix can also be calculated by adding the contribution of the three internal domains forming an element, as shown in Figure 5.3. This process has not been found useful for practical purposes and the direct assembly of the control domains contributions as explained above is recommended.

5.4.2a Imposition of the boundary conditions

The imposition of the boundary conditions, shown in Figure 5.7, is simpler than for the BPT element as the deflection gradient is continuous along the control domain boundaries in this case.

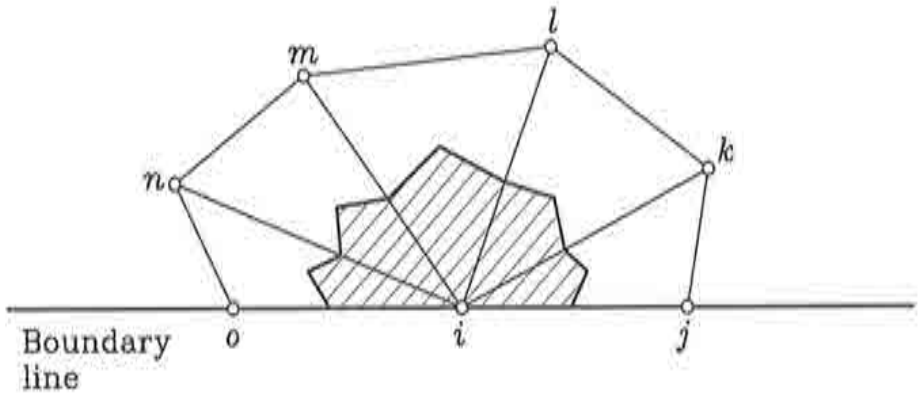

Figure 5.7 Imposition of the boundary conditions - BPN element.

The condition $w = \bar{w}$ is prescribed at the global solution level while the prescribed rotations must be accounted for the construction of the curvature matrix. The various types of boundary conditions are considered: simply supported edges, free edges and clamped and symmetry edges.

5.4.2.1 Simply supported edge

The required condition $\frac{\partial w}{\partial s} = 0$ along the edge direction is fulfil prescribing the vertical deflection to a zero value at the global solution level.

5.4.2.2 Free edge

The free edges boundary condition does not require any special treatment for the rotations at the free edges. The advantage from the mixed formulation can be performed prescribing the edge bending moments M_n and M_{sn} to a zero value. This is achieved by eliminating the contributions from these moments at free edge patches, making zero the appropriate rows in the constitutive matrix **D**.

5.4.2.3 Clamped and symmetry edge

The required zero rotation conditions at clamped and symmetry edges are imposed by eliminating the contributions from these rotations in the line integrals in equation (5.35).

5.5 EXTENSION TO SHELLS - BST AND BSN ELEMENTS

The extension to shells is derived in a similar fashion as in the previous section for plates. The so called BST and BSN elements are based on the Cell Centered and Cell Vertex schemes, respectively.

5.5.1 Cell Centered scheme - BST element

The BST element is the combination of the previous presented Basic Plate Triangle BPT element with the standard Constant Strain Triangle CST used to model the membrane behaviour. The **B**asic **S**hell **T**riangle element is shown in Figure 5.8.

The element curvatures within each control domain are expressed in the local axes. The constant curvatures of the control domain are expressed in terms of the local deflection gradients at the element edges, following the same procedure as in equations (5.14) and (5.18). The local deflection gradients are expressed in terms of the average values of contributions from the adjacent elements sharing the same side. The sign convention is presented in Figure 5.9.

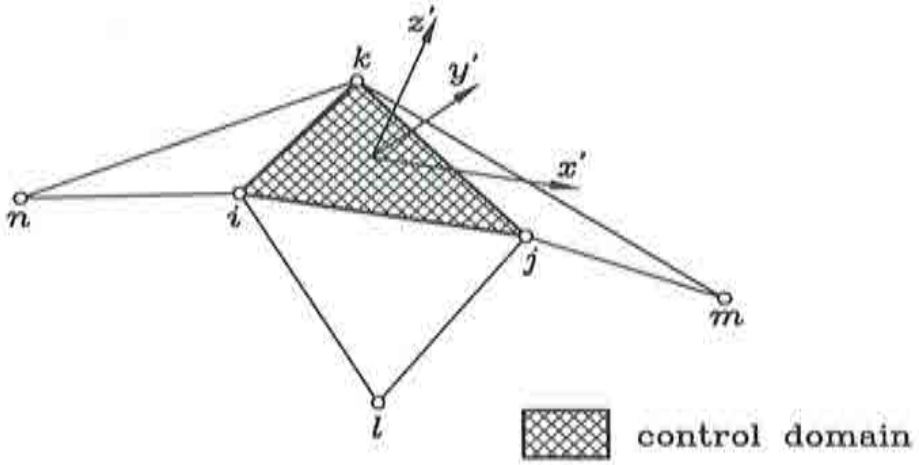

Figure 5.8 BST element.

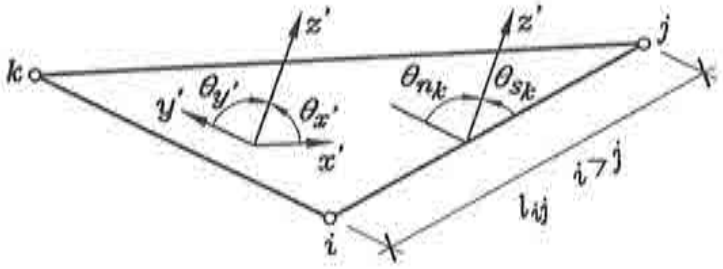

Figure 5.9 Sign convention for BST element.

The curvature $\boldsymbol{\chi}'^{(e)}$ for the element e is expressed as

$$\boldsymbol{\chi}'^{(e)} = \left\{ \begin{array}{c} \chi_{x'} \\ \chi_{y'} \\ \chi_{x'y'} \end{array} \right\}^{(e)} = \frac{1}{A^{(e)}} \oint_{\Gamma^{(e)}} \begin{bmatrix} -n_{y'}n_{x'} & {n_{x'}}^2 \\ n_{y'}n_{x'} & {n_{y'}}^2 \\ {n_{y'}}^2 - {n_{x'}}^2 & 2n_{y'}n_{x'} \end{bmatrix} \left\{ \begin{array}{c} \theta_s \\ \theta_n \end{array} \right\} d\Gamma =$$

$$= \frac{1}{A^{(e)}} \{ \mathbf{n}_{ij}^{(e)} \boldsymbol{\theta}_{ij} l_{ij} + \mathbf{n}_{jk}^{(e)} \boldsymbol{\theta}_{jk} l_{jk} + \mathbf{n}_{ki}^{(e)} \boldsymbol{\theta}_{ki} l_{ki} \} \tag{5.38}$$

where

$$\boldsymbol{\theta}_{ij} = \left\{ \begin{array}{c} \theta_s \\ \theta_n \end{array} \right\}_{ij} \tag{5.39}$$

and θ_s and θ_n are the tangential and normal rotations at the patch edges, Figure 5.9. Using the condition that the shear stresses are zero allows to express the tangential rotations at the edge in terms of the deflection at the end node as

$$\theta_{s_{ij}}{}^{(e)} = \frac{w'_j - w'_i}{l_{ij}} \Rightarrow j > i \tag{5.40}$$

Inside each element, using the assumptions of the Kirchhoff hypothesis gives

$$\frac{\partial w'}{\partial x'} = \theta_{x'}, \quad \frac{\partial w'}{\partial y'} = \theta_{y'} \tag{5.41}$$

The normal rotation of the side ij can be expressed as

$$\theta_{n_{ij}} = n_{x'}(\frac{\partial w'}{\partial x'}) + n_{y'}(\frac{\partial w'}{\partial y'}) \tag{5.42}$$

The normal rotation $\theta_{n_{ij}}$ for two adjacent elements is presented in Figure 5.10.

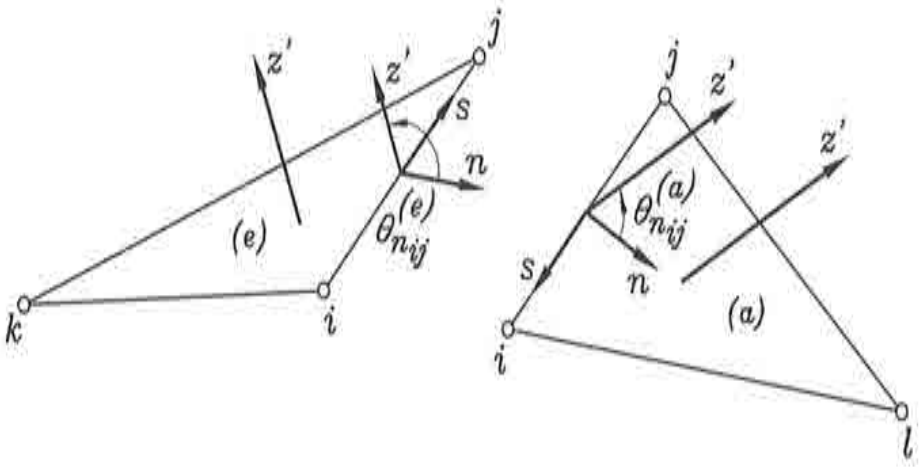

Figure 5.10 The normal rotation $\theta_{n_{ij}}$ for two adjacent elements.

Thus, the rotations $\theta_{n_{ij}}^{(e)}$ and $\theta_{n_{ij}}^{(b)}$ are expressed as

$$\theta_{n_{ij}}^{(e)} = n_{x'}^{(e)}(\frac{\partial w'}{\partial x'})^{(e)} + n_{y'}^{(e)}(\frac{\partial w'}{\partial y'})^{(e)} = \mathbf{n}_{ij}^{(e)} \nabla \mathbf{N}^{(e)} \mathbf{w}'^{(e)} \tag{5.43a}$$

$$\theta_{n_{ij}}^{(a)} = n_{x'}^{(a)}\left(\frac{\partial w'}{\partial x'}\right)^{(a)} + n_{y'}^{(a)}\left(\frac{\partial w'}{\partial y'}\right)^{(a)} = \mathbf{n}_{ij}^{(a)}\nabla\mathbf{N}^{(a)}\mathbf{w}'^{(a)} \tag{5.43b}$$

or in matrix form

$$\theta_{n_{ij}}^{(e)} = [n_{x'}^{(e)}, n_{y'}^{(e)}]\left\{\begin{array}{c}\frac{\partial w'}{\partial x'}\\ \frac{\partial w'}{\partial y'}\end{array}\right\}^{(e)} = [n_{x'}^{(e)}, n_{y'}^{(e)}]\frac{1}{2A^{(e)}}\sum_{i=1}^{3}\left\{\begin{array}{c}b_i^{(e)}\\ c_i^{(e)}\end{array}\right\}w_i'^{(e)} =$$

$$= \mathbf{A}_{ij}^{(e)}\left\{\begin{array}{c}w_1'^{(e)}\\ w_2'^{(e)}\\ w_3'^{(e)}\end{array}\right\} = \mathbf{A}_{ij}^{(e)}\mathbf{w}'^{(e)} \tag{5.44a}$$

$$\theta_{n_{ij}}{}^{(a)} = [n_{x'}^{(a)}, n_{y'}^{(a)}]\left\{\begin{array}{c}\frac{\partial w'}{\partial x'}\\ \frac{\partial w'}{\partial y'}\end{array}\right\}^{(a)} = [n_{x'}^{(a)}, n_{y'}^{(a)}]\frac{1}{2A^{(b)}}\sum_{i=1}^{3}\left\{\begin{array}{c}b_i^{(a)}\\ c_i^{(a)}\end{array}\right\}w_i'^{(a)} =$$

$$= \mathbf{A}_{ij}^{(a)}\left\{\begin{array}{c}w_1'^{(a)}\\ w_2'^{(a)}\\ w_3'^{(a)}\end{array}\right\} = \mathbf{A}_{ij}^{(a)}\mathbf{w}'^{(a)} \tag{5.44b}$$

what finally gives the value $\theta_{n_{ij}}$ as

$$\theta_{n_{ij}} = \frac{1}{2}[\theta_{n_{ij}}^{(e)} + \theta_{n_{ij}}^{(a)}] = \frac{1}{2}[\mathbf{A}_{ij}^{(e)}\mathbf{w}'^{(e)} + \mathbf{A}_{ij}^{(a)}\mathbf{w}'^{(a)}] \tag{5.45}$$

After the expressions for θ_s given by equation (5.40) and for θ_n given by equation (5.45), the expression (5.39) for the curvature can be rewritten as follows

$$\boldsymbol{\chi}'^{(e)} = \frac{1}{A^{(e)}}\{\mathbf{n}_{ij}^{(e)}\boldsymbol{\theta}_{ij}l_{ij} + \mathbf{n}_{jk}^{(e)}\boldsymbol{\theta}_{jk}l_{jk} + \mathbf{n}_{ki}^{(e)}\boldsymbol{\theta}_{ki}l_{ki}\} = \mathbf{B}'^{(e)}_{b}\mathbf{w}'^{(e)} \tag{5.46}$$

where the displacement vector is

$$\mathbf{w}'^{(e)}_{12\times 1} = \left\{\begin{array}{c}\mathbf{w}'^{(e)}\\ \mathbf{w}'^{(a)}\\ \mathbf{w}'^{(b)}\\ \mathbf{w}'^{(c)}\end{array}\right\} \tag{5.47}$$

with

$$\mathbf{w}'^{(e)}_b = \left\{ \begin{array}{c} w'^{(e)}_1 \\ w'^{(e)}_2 \\ w'^{(e)}_3 \end{array} \right\}, \quad \mathbf{w}'^{(a)}_b = \left\{ \begin{array}{c} w'^{(a)}_1 \\ w'^{(a)}_2 \\ w'^{(a)}_3 \end{array} \right\}$$

$$\mathbf{w}'^{(b)}_b = \left\{ \begin{array}{c} w'^{(b)}_1 \\ w'^{(b)}_2 \\ w'^{(b)}_3 \end{array} \right\}, \quad \mathbf{w}'^{(c)}_b = \left\{ \begin{array}{c} w'^{(c)}_1 \\ w'^{(c)}_2 \\ w'^{(c)}_3 \end{array} \right\} \tag{5.48}$$

A simple transformation gives

$$\mathbf{w}'^{(e)} = \mathbf{T}^{(e)} \mathbf{w}^{(e)} \tag{5.49}$$

and the expression for the curvature (5.46) can be rewritten as

$$\boldsymbol{\chi}'^{(e)} = \mathbf{B}'^{(e)}_b \mathbf{T}^{(e)} \mathbf{w}^{(e)} = \mathbf{B}^{(e)}_b \mathbf{w}^{(e)} \tag{5.50}$$

where the curvature matrix is

$$\mathbf{B}^{(e)}_b = \mathbf{B}'^{(e)}_b \mathbf{T}^{(e)} \tag{5.51}$$

with $\mathbf{B}'^{(e)}_b$ being

$$\mathbf{B}'^{(e)}_b = [\mathbf{B}'_{b1}, \mathbf{B}'_{b2}, \mathbf{B}'_{b3}, \mathbf{B}'_{b4}, \mathbf{B}'_{b5}, \mathbf{B}'_{b6}] \tag{5.52}$$

The bending stiffness matrix for the patch is expressed as

$$\mathbf{K}^{(e)}_b = \int\int_A [\mathbf{B}^{(e)}_b]^T \mathbf{D}_b \mathbf{B}^{(e)}_b dA \tag{5.53}$$

The membrane strain matrix is given by the standard expressions for the CST element. It can be easily shown that

$$\mathbf{B}^{(e)}_m = \mathbf{B}'^{(e)}_m \mathbf{T}^{(e)} \tag{5.54}$$

where

$$\mathbf{B}'^{(e)}_{m} = [\mathbf{B}'_{m1}, \mathbf{B}'_{m2}, \mathbf{B}'_{m3}, \mathbf{0}] \tag{5.55}$$

or rewritten in the expanded form

$$\mathbf{B}'^{(e)}_{mi} = \begin{bmatrix} \frac{\partial N_i}{\partial x'} & 0 \\ 0 & \frac{\partial N_i}{\partial y'} \\ \frac{\partial N_i}{\partial y'} & \frac{\partial N_i}{\partial x'} \end{bmatrix} = \frac{1}{2A^{(e)}} \begin{bmatrix} b_i & 0 \\ 0 & c_i \\ c_i & b_i \end{bmatrix}^{(e)} \tag{5.56}$$

The local membrane displacement vector is

$$\mathbf{w}'^{(e)}_{m} = [u'^{(e)}_1, v'^{(e)}_1, u'^{(e)}_2, v'^{(e)}_2, u'^{(e)}_3, v'^{(e)}_3]^T \tag{5.57}$$

The membrane stiffness matrix in global axes is expressed as

$$\mathbf{K}^{(e)}_{m} = \int\int_A [\mathbf{B}^{(e)}_{m}]^T \mathbf{D}_m \mathbf{B}^{(e)}_{m} dA \tag{5.58}$$

Finally, the global stiffness matrix is

$$\mathbf{K}^{(e)}_{18\times 18} = \int\int_A [\mathbf{B}^{(e)}]^T \mathbf{D}\mathbf{B}^{(e)} dA = A^{(e)} [\mathbf{B}^{(e)}]^T \mathbf{D}\mathbf{B}^{(e)} \tag{5.59}$$

where

$$\mathbf{B}^{(e)}_{6\times 18} = \begin{Bmatrix} \mathbf{B}^{(e)}_{m} \\ \mathbf{B}^{(e)}_{b} \end{Bmatrix} \tag{5.60}$$

Thus, the global stiffness matrix for any patch is expressed as

$$\mathbf{K}^{(e)}\mathbf{w}^{(e)} - \mathbf{f}^{(e)} = \mathbf{q}^{(e)} \tag{5.61}$$

where

$$\mathbf{w}^{(e)}_{18\times 1} = \begin{Bmatrix} \mathbf{w}_1 \\ \mathbf{w}_2 \\ \mathbf{w}_3 \\ \mathbf{w}_4 \\ \mathbf{w}_5 \\ \mathbf{w}_6 \end{Bmatrix}, \quad \mathbf{w}_i = \begin{Bmatrix} u_i \\ v_i \\ w_i \end{Bmatrix} \tag{5.62}$$

and the force vector is

$$\mathbf{f}^{(e)} = \left\{ \begin{array}{c} \mathbf{f}_1 \\ \mathbf{f}_2 \\ \mathbf{f}_3 \\ \mathbf{f}_4 \\ \mathbf{f}_5 \\ \mathbf{f}_6 \end{array} \right\}, \quad \mathbf{f}_i = \left\{ \begin{array}{c} f_i^x \\ f_i^y \\ f_i^z \end{array} \right\} \tag{5.63}$$

The force vector $\mathbf{f}_i$ is obtained as a sum over elements sharing node i in the patch. For the self weighting case this gives

$$\mathbf{f}_i = \frac{g}{3} \sum_e (\rho A t)^{(e)} \tag{5.64}$$

The BST element was extended to nonlinear analysis by Cendoya [C-1], using the Updated Lagrangian formulation. More details about this element and its extension to nonlinear analysis with the description of the explicit dynamic formulation, stress computation, material model, thickness updating and contact and friction can be found in [C-1].

5.5.2 Cell Centered scheme - BSN element

The BSN element is the combination of the presented Basic Plate Nodal BPN element with the standard Constant Strain Triangle CST used to model the membrane behaviour. The Basic Shell Nodal element is shown in Figure 5.11.

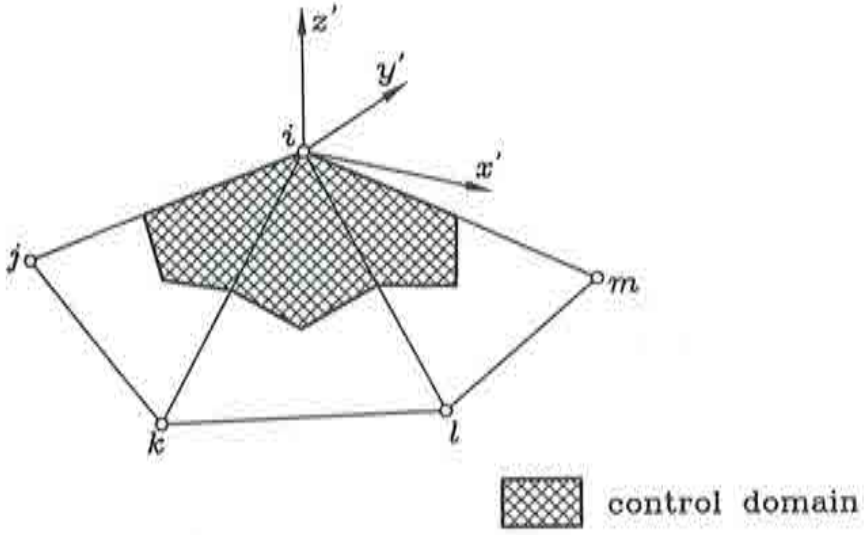

Figure 5.11 Cell Centered scheme for derivation of BSN element.

The constant curvature and bending moment fields are defined in the local nodal axes. A transformation of the rotations from nodal to element axes for each of the elements forming the patch is required. In order to describe the different stress states inside the shell as well as to impose the boundary conditions, the different coordinate systems are introduced in the formulation, as presented in Figure 5.12.

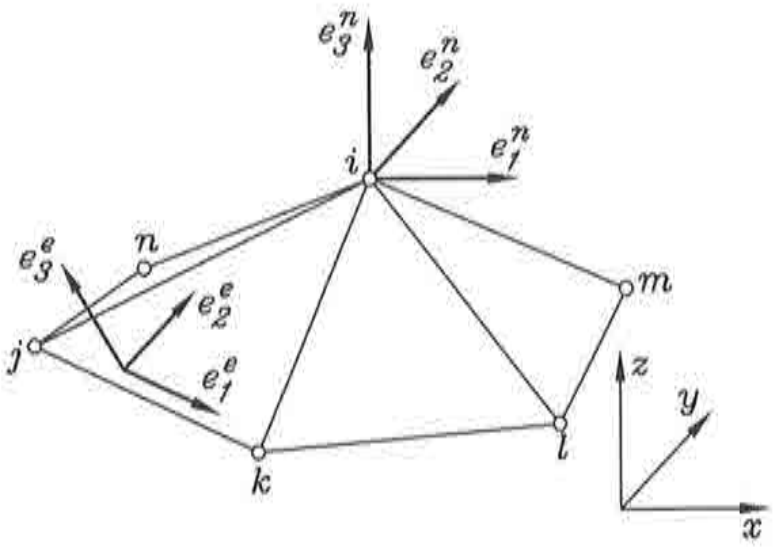

Figure 5.12 Coordinate systems.

- Global axes: x, y, z are used for the definition of the nodal variables and nodal coordinates.
- Elemental axes: $e_1^{(e)}, e_2^{(e)}, e_3^{(e)}$ are connected with the element under the consideration and the node where the stiffness matrix is evaluated; so three coordinate elemental systems exist for each element depending on the node under the consideration i, j or k. The first axis $e_1^{(e)}$ corresponds to the direction of the side jk and the second one $e_2^{(e)}$ is on the plane which is formed by three nodes i, j and k. The third axis $e_3^{(e)}$ is perpendicular to the plane formed by nodes i, j and k.

$$e_1^{(e)} = \begin{Bmatrix} \lambda_{1x}^{(n)} \\ \lambda_{1y}^{(n)} \\ \lambda_{1z}^{(n)} \end{Bmatrix}, \quad e_2^{(e)} = \begin{Bmatrix} \lambda_{2x}^{(n)} \\ \lambda_{2y}^{(n)} \\ \lambda_{2z}^{(n)} \end{Bmatrix}, \quad e_3^{(e)} = \begin{Bmatrix} \lambda_{3x}^{(n)} \\ \lambda_{3y}^{(n)} \\ \lambda_{3z}^{(n)} \end{Bmatrix} \tag{5.65}$$

- Nodal axes: $e_1^{(n)}, e_2^{(n)}, e_3^{(n)}$ are the function of the Euler angles, presented in Figure 5.13, defined as rotations that systematically make rotation of the global axis system.

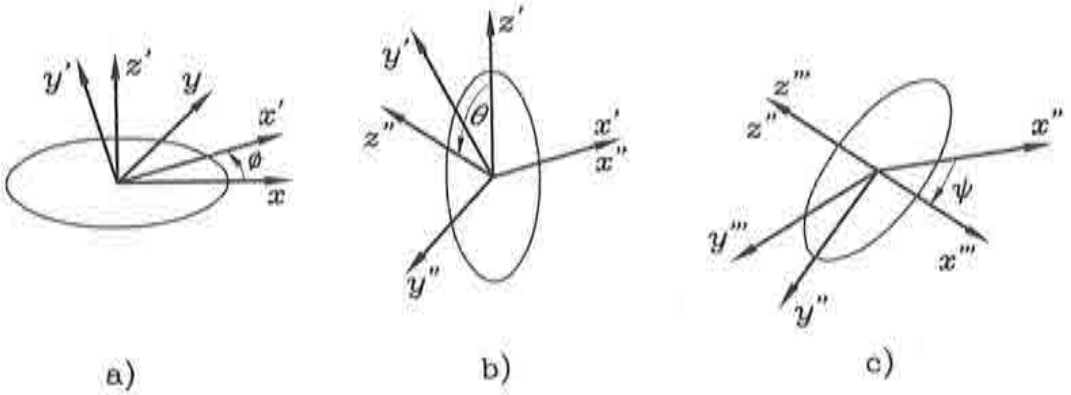

Figure 5.13 Euler angles.

- The first rotation ϕ rotates in anticlockwise direction and the system xy advances into the new position $x'y'$, without changing the position of the axis $z = z'$.
- The second rotation θ rotates in anticlockwise direction and the system $z'y'$ advances into the new position $z''y''$, without changing the position of the axis $x' = x"$ which is a rotate axis.
- The third rotation ψ rotates in anticlockwise direction and the system $x''y''$ advances into the new position $x'''y'''$, without changing the position of the axis $z'' = z'''$.

The transformation of the nodal coordinates to global coordinates is expressed as

$$\mathbf{x}'^{(n)} = \mathbf{C}^{(n)T}\mathbf{x} \tag{5.66}$$

where

$$\mathbf{C}^{(n)T} = \begin{Bmatrix} e_1^{(n)T} \\ e_2^{(n)T} \\ e_3^{(n)T} \end{Bmatrix} = \begin{Bmatrix} \lambda_{1x}^{(n)} & \lambda_{1y}^{(n)} & \lambda_{1z}^{(n)} \\ \lambda_{2x}^{(n)} & \lambda_{2y}^{(n)} & \lambda_{2z}^{(n)} \\ \lambda_{3x}^{(n)} & \lambda_{3y}^{(n)} & \lambda_{3z}^{(n)} \end{Bmatrix} \tag{5.67}$$

The deformation tensor $\boldsymbol{\varepsilon}$ is given as

$$\boldsymbol{\varepsilon} = \begin{Bmatrix} \varepsilon_{xx} & \varepsilon_{xy} & \varepsilon_{xz} \\ \varepsilon_{yx} & \varepsilon_{yy} & \varepsilon_{yz} \\ \varepsilon_{zx} & \varepsilon_{zy} & \varepsilon_{zz} \end{Bmatrix} \tag{5.68}$$

The element can be rotated by the rotation matrix $\mathbf{Q}$

$$\mathbf{Q} = \begin{Bmatrix} \lambda_{1x} & \lambda_{1y} & \lambda_{1z} \\ \lambda_{2x} & \lambda_{2y} & \lambda_{2z} \\ \lambda_{3x} & \lambda_{3y} & \lambda_{3z} \end{Bmatrix} \tag{5.69}$$

The transformation from the local to global system is expressed as

$$\boldsymbol{\varepsilon} = \mathbf{Q}^T \boldsymbol{\varepsilon}' \mathbf{Q}, \quad \boldsymbol{\varepsilon} = \mathbf{S}_{lg} \boldsymbol{\varepsilon}' \tag{5.70}$$

and vice versa

$$\boldsymbol{\varepsilon}' = \mathbf{Q} \boldsymbol{\varepsilon} \mathbf{Q}^T, \quad \boldsymbol{\varepsilon}' = \mathbf{S}_{gn} \boldsymbol{\varepsilon} \tag{5.71}$$

As in the shell theory the local normal deformations $\varepsilon_{z'z'}$ are not used, the matrix of the rotation can be simplified as

$$\boldsymbol{\varepsilon} = \mathbf{R}_{lg} \boldsymbol{\varepsilon}' \tag{5.72a}$$

$$\boldsymbol{\varepsilon}' = \mathbf{R}_{gn} \boldsymbol{\varepsilon} \tag{5.72b}$$

The nodal displacement vector, expressed in global axes is

$$\mathbf{w}^T = [u_1, v_1, w_1, u_2, v_2, w_2, u_3, v_3, w_3] \tag{5.73}$$

The bending displacement vector in local axes is

$$\mathbf{w}'^T_b = [w'_1, w'_2, w'_3] \tag{5.74}$$

and the membrane displacement vector in local axes is

$$\mathbf{w}'^T_m = [u'_1, v'_1, u'_2, v'_2, u'_3, v'_3] \tag{5.75}$$

The transformation which relates the local and global displacement vectors is given as

$$\mathbf{w'}_b = \mathbf{R}_b\mathbf{w}, \quad \mathbf{w'}_m = \mathbf{R}_m\mathbf{w} \tag{5.76}$$

where

$$\mathbf{R}_b = \begin{bmatrix} \lambda_{3x}^{(e)} & \lambda_{3y}^{(e)} & \lambda_{3z}^{(e)} & 0 & 0 & 0 & 0 & 0 & 0 \\ 0 & 0 & 0 & \lambda_{3x}^{(e)} & \lambda_{3y}^{(e)} & \lambda_{3z}^{(e)} & 0 & 0 & 0 \\ 0 & 0 & 0 & 0 & 0 & 0 & \lambda_{3x}^{(e)} & \lambda_{3y}^{(e)} & \lambda_{3z}^{(e)} \end{bmatrix} \tag{5.77}$$

and matrix $\mathbf{R}_m$ is

$$\mathbf{R}_m = \begin{bmatrix} \lambda_{1x}^{(e)} & \lambda_{1y}^{(e)} & \lambda_{1z}^{(e)} & 0 & 0 & 0 & 0 & 0 & 0 \\ \lambda_{2x}^{(e)} & \lambda_{2y}^{(e)} & \lambda_{2z}^{(e)} & 0 & 0 & 0 & 0 & 0 & 0 \\ 0 & 0 & 0 & \lambda_{1x}^{(e)} & \lambda_{1y}^{(e)} & \lambda_{1z}^{(e)} & 0 & 0 & 0 \\ 0 & 0 & 0 & \lambda_{2x}^{(e)} & \lambda_{2y}^{(e)} & \lambda_{2z}^{(e)} & 0 & 0 & 0 \\ 0 & 0 & 0 & 0 & 0 & 0 & \lambda_{1x}^{(e)} & \lambda_{1y}^{(e)} & \lambda_{1z}^{(e)} \\ 0 & 0 & 0 & 0 & 0 & 0 & \lambda_{2x}^{(e)} & \lambda_{2y}^{(e)} & \lambda_{2z}^{(e)} \end{bmatrix} \tag{5.78}$$

It is assumed that the variation of the curvature expressed in the global axis system inside the domain of one node is constant

$$\int_\Omega [\boldsymbol{\chi} - \mathbf{R}_{lg}\boldsymbol{\chi}'] d\Omega = 0 \tag{5.79}$$

or in rewritten form

$$\int_\Omega \boldsymbol{\chi} d\Omega = \int_\Omega \mathbf{R}_{lg} \begin{Bmatrix} -\frac{\partial \theta_{x'}}{\partial x'} \\ -\frac{\partial \theta_{y'}}{\partial y'} \\ -\frac{\partial \theta_{x'}}{\partial y'} - \frac{\partial \theta_{y'}}{\partial x'} \end{Bmatrix} d\Omega \tag{5.80}$$

where Ω is the corresponding domain of the node i

$$\Omega_i = \frac{\sum_e A^{(e)}}{3} \tag{5.81}$$

Substituting equation (5.81) into (5.80), yields

$$\boldsymbol{\chi}\frac{\sum_e A^{(e)}}{3} = \int_\Omega \mathbf{R}_{lg}\boldsymbol{\chi}' d\Omega \tag{5.82}$$

Using the assumptions of the Kirchhoff hypothesis

$$\frac{\partial w'}{\partial x'} = \theta'_x, \quad \frac{\partial w'}{\partial y'} = \theta'_y \tag{5.83}$$

equation (5.82) can be rewritten as

$$\boldsymbol{\chi}\frac{\sum_e A^{(e)}}{3} = \int_\Omega \mathbf{R}_{lg}\left\{\begin{array}{c} -\frac{\partial^2 w'}{\partial x'^2} \\ -\frac{\partial^2 w'}{\partial y'^2} \\ -\frac{2\partial^2 w'}{\partial x'\partial y'} \end{array}\right\} d\Omega \tag{5.84}$$

Using the Green theorem, the above equation can be rewritten as

$$\boldsymbol{\chi} = \frac{3}{\sum_e A^{(e)}}\oint_\Gamma \mathbf{R}_{lg}\begin{bmatrix} -n_{x'} & 0 \\ 0 & -n_{y'} \\ -n_{y'} & -n_{x'} \end{bmatrix}\left\{\begin{array}{c} \partial_{x'}w' \\ \partial_{y'}w' \end{array}\right\} d\Gamma = \frac{3}{\sum_e A^{(e)}}\mathbf{R}_{lg}\mathbf{B'}_p\mathbf{w'}_p \tag{5.85}$$

In order to be able to evaluate the nodal curvature, the transformation from global to nodal coordinate system has to be performed, thus the above expression can be rewritten as

$$\boldsymbol{\chi}^{(i)} = \mathbf{R}_{gn}\frac{3}{\sum_e A^{(e)}}\mathbf{R}_{lg}\mathbf{B'}_p\mathbf{R}_b\mathbf{w}_p \tag{5.86}$$

where the nodal curvature matrix is

$$\mathbf{B}_b^{(i)} = \mathbf{R}_{gn}\frac{3}{\sum_e A^{(e)}}\mathbf{R}_{lg}\mathbf{B}_p \tag{5.87}$$

with $\mathbf{w}_p$ being the global displacements of the patch nodes.

The global bending stiffness matrix for the node i is therefore given by

$$\mathbf{K}_b^{(i)} = \int_\Omega [\mathbf{B}_b^{(i)}]^T \mathbf{D}_b^{(i)}\mathbf{B}_b^{(i)} d\Omega \tag{5.88}$$

The membrane strain matrix is expressed by the formulation of the CST element

$$\mathbf{B}_m = \mathbf{B'}_m \mathbf{R}_m \tag{5.89}$$

where as in the previous BST element

$$\mathbf{B'}_m = [\mathbf{B'}_{m1}, \mathbf{B'}_{m2}, \mathbf{B'}_{m3}, \mathbf{0}] \tag{5.90}$$

with

$$\mathbf{B'}_m^{(e)} = \begin{bmatrix} \frac{\partial N_1^{(e)}}{\partial x'} & 0 & \frac{\partial N_2^{(e)}}{\partial x'} & 0 & \frac{\partial N_3^{(e)}}{\partial x'} & 0 \\ 0 & \frac{\partial N_1^{(e)}}{\partial y'} & 0 & \frac{\partial N_2^{(e)}}{\partial y'} & 0 & \frac{\partial N_3^{(e)}}{\partial y'} \\ \frac{\partial N_1^{(e)}}{\partial y'} & \frac{\partial N_1^{(e)}}{\partial x'} & \frac{\partial N_2^{(e)}}{\partial y'} & \frac{\partial N_2^{(e)}}{\partial x'} & \frac{\partial N_3^{(e)}}{\partial y'} & \frac{\partial N_3^{(e)}}{\partial x'} \end{bmatrix} \tag{5.91}$$

The global membrane stiffness matrix for the element e is

$$\mathbf{K}_m^{(e)} = \int_{A^{(e)}} [\mathbf{B}_m^{(e)}]^T \mathbf{D}_m \mathbf{B}_m^{(e)} dA \tag{5.92}$$

Following the same procedure as for the BPN element, the membrane strain matrix can be developed for node i giving the membrane CSN element. Starting with the assumption that the membrane deformations in global axes are constant or equal to the sum of all contributions from the elements in the patch, the following expression is given

$$\int_\Omega [\boldsymbol{\varepsilon}_m - \mathbf{R}_{lg} \boldsymbol{\varepsilon'}_m] d\Omega = 0 \tag{5.93}$$

or

$$\int_\Omega \boldsymbol{\varepsilon}_m d\Omega = \int_\Omega \mathbf{R}_{lg} \boldsymbol{\varepsilon'}_m d\Omega \tag{5.94}$$

what leads to

$$\boldsymbol{\varepsilon}_m \frac{\sum_e A^{(e)}}{3} = \int_\Omega \mathbf{R}_{lg} \boldsymbol{\varepsilon'}_m \Omega \tag{5.95}$$

On the other side, the variation of membrane deformations over each element from the CST formulation is

$$\varepsilon_m^{(e)} = \mathbf{B}_m'^{(e)} \mathbf{R}_m^{(e)} \mathbf{w}^{(e)} \tag{5.96}$$

or in expanded form, the same for the node i is

$$\varepsilon_m^{(i)} = \mathbf{R}_{gn} \frac{3}{\sum_e A^{(e)}} [\sum_e (\frac{A^{(e)}}{3} \mathbf{R}_{lg} \mathbf{B}_m'^{(e)} \mathbf{R}_m^{(e)} \mathbf{w}^{(e)})] \tag{5.97}$$

where the nodal curvature matrix is

$$\mathbf{B}_m^{(i)} = \mathbf{R}_{gn} \frac{3}{\sum_e A^{(e)}} [\sum_e (\frac{A^{(e)}}{3} \mathbf{R}_{lg} \mathbf{B}_m^{(e)}] \tag{5.98}$$

where $\mathbf{w}_p$ are the global displacements of the patch nodes. The global membrane stiffness matrix is

$$\mathbf{K}_m^{(i)} = \int_\Omega [\mathbf{B}_m^{(i)}]^T \mathbf{D}_m^{(i)} \mathbf{B}_m^{(i)} d\Omega \tag{5.99}$$

More details about the transformation matrices used in above expressions can be found in Zarate [Z-1]. The global stiffness matrix is calculated as

$$\mathbf{K}^{(i)} = \int_\Omega [\mathbf{B}^{(i)}]^T \mathbf{D}^{(i)} \mathbf{B}^{(i)} d\Omega \tag{5.100}$$

5.6 NON-LINEAR BSN ELEMENT

The same element is extended to the nonlinear explicit dynamic analysis using the Updated Lagrangian formulation. The extension of the BSN element to the nonlinear analysis as well as the practical application in the framework of sheet metal forming by some numerical examples are presented further.

5.6.1 Explicit Dynamic Formulation

The dynamic equilibrium equations are written in terms of the principle of the virtual work using the Updated Lagrangian formulation. The discretized form of equilibrium equations is expressed as [Z-4]

$$\mathbf{M}\ddot{\mathbf{a}} + \mathbf{p} = \mathbf{f} \tag{5.101}$$

where $\mathbf{M}$ is the mass matrix and $\mathbf{p}$ and $\mathbf{f}$ are the vectors of internal and external forces, respectively. These forces are calculated by assembling the element contributions

$$\mathbf{p}^e = \int\int_A^e \mathbf{B}^T \hat{\boldsymbol{\sigma}}' dA \tag{5.102}$$

$$\mathbf{f}^e = \int\int_A^e \mathbf{N}^T \mathbf{t} dA \tag{5.103}$$

where $\mathbf{t}$ is the vector of surface forces, i.e. the contact forces acting on the element and the strain matrix $\mathbf{B}$ and the stresses $\boldsymbol{\sigma}$ are divided in the membrane and bending parts

$$\mathbf{B} = \begin{bmatrix} \mathbf{B}_m \\ \mathbf{B}_b \end{bmatrix} \quad \text{and} \quad \hat{\boldsymbol{\sigma}}' = \begin{bmatrix} \boldsymbol{\sigma}_m \\ \boldsymbol{\sigma}_b \end{bmatrix} \tag{5.104}$$

The stresses $\boldsymbol{\sigma}_m$ and $\boldsymbol{\sigma}_b$ are

$$\boldsymbol{\sigma}_m = [N_{x'}, N_{y'}, N_{x'y'}]^T \tag{5.105a}$$

$$\boldsymbol{\sigma}_b = [M_{x'}, M_{y'}, M_{x'y'}]^T \tag{5.105b}$$

Equation (5.104) is integrated in time using the explicit dynamic scheme with a diagonal (lumped) mass matrix.

5.6.2 Computation of stresses

The stresses are computed in the local element system at each time increment using an hypoelastic rate constitutive law

$$\boldsymbol{\sigma}'^{\nabla} = \mathbf{D}\dot{\boldsymbol{\varepsilon}}' \tag{5.106}$$

where $\boldsymbol{\sigma}'^{\nabla}$ is the Jaumann rate of the Cauchy stress, $\dot{\boldsymbol{\epsilon}}' = [\dot{\varepsilon}_{x'}, \dot{\varepsilon}_{y'}, \dot{\gamma}_{x'y'}]^T$ is the rate of the deformation vector and $\mathbf{D}$ is the elasto-plastic matrix.

The stresses at the end of a time increment are obtained by

$$\boldsymbol{\sigma}'^{t+\Delta t} = \boldsymbol{\sigma}'^{t} + \mathbf{D}\Delta\boldsymbol{\varepsilon}'^{\frac{n+1}{2}} \tag{5.107}$$

where the stress $\boldsymbol{\sigma}'^{t}$ has to be rotated before the sum expressed by equation (5.107). The final-resultant stresses are obtained as

$$\hat{\boldsymbol{\sigma}}' = \left\{ \begin{array}{c} \boldsymbol{\sigma}_m \\ \boldsymbol{\sigma}_b \end{array} \right\} = \int_{-\frac{h}{2}}^{\frac{h}{2}} \left\{ \begin{array}{c} \boldsymbol{\sigma}' \\ z'\boldsymbol{\sigma}' \end{array} \right\} dz' \tag{5.108}$$

where h is the thickness of the shell and $\boldsymbol{\sigma}' = [\sigma_{x'}, \sigma_{y'}, \tau_{x'y'}]^T$.

5.6.3 Anisotropic material model

An elasto-plastic material model is used, where the elastic behaviour is assumed to be isotropic and an anisotropic plane model based on Hill's theory is chosen for the plastic part. The yield function used in the analysis is expressed as

$$C_1|\sigma_1 + \sigma_2|^M + C_2|\sigma_1 - \sigma_2|^M = \sigma_l^M \tag{5.109}$$

where

$$C_1 = \frac{1}{2(1+R)}, \quad C_2 = \frac{1+2R}{2(1+R)} \tag{5.110}$$

and R is the Lankford coefficient

$$R = \frac{1}{4}(R_0 + 2R_{45} + R_{90}) \tag{5.111}$$

Equation (5.109) gives the quadratic Hill's yield function for the value $M = 2$ and the isotropic von Mises function for the value $R = 1$ and $M = 2$.

5.6.4 Thickness updating

The element thickness is updated to preserve the constant volume using the following expression

$$h^{t+\Delta t} = \frac{A^0 h^0}{A^{t+\Delta t}} \tag{5.112}$$

where A^0 and h^0 are the initial area and initial thickness.

5.7 NUMERICAL EXAMPLES

5.7.1 Square cup deep drawing

5.7.1.1 Problem description

This example is one of the benchmark tests proposed in NUMISHEET'93 [M-1]. The analysis of the deep drawing process of a square sheet into a square cup is carried out. This test emphasizes the ability to simulate a large amount of material draw-in with a nearly vertical wall. Other numerical results available from [M-1] are compared with the numerical results obtained with the BSN element. To demonstrate the performance of the BSN element, two different element types were used for this problem: 3D hexahedral solid element and new triangular BSN shell element.

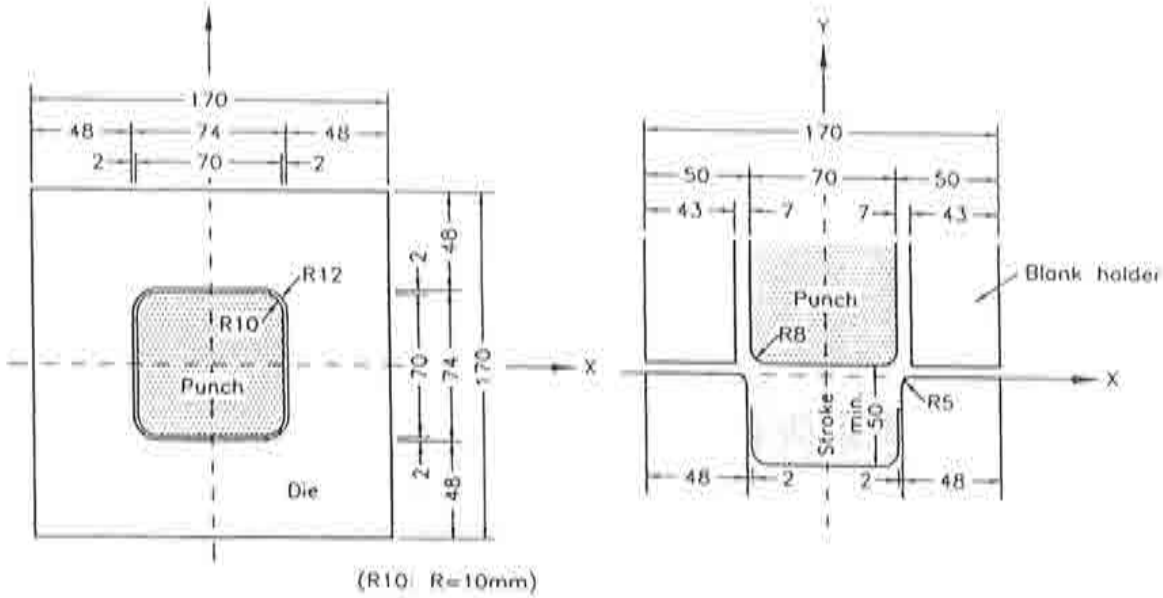

Figure 5.14 Geometry of the Square Cup Deep Drawing.

5.7.1.2 Finite element model

Geometry

The geometry of the punch, die and blankholder is shown in Figure 5.14. Because of symmetry considerations, the simulation was carried out using a quarter of the defined structure. For this deep drawing problem, the punch travel is $40.00mm$.

Mesh

The sheet was modelled using 1800 BSN triangular shell layered elements (3 node) or 900 HEX8R hexahedral solid elements (8 node). The blankholder is modelled using 13 HEX8R hexahedral solid elements (8 node) and the punch and the die using 649 DUMQ rigid elements (4 node). The discretization of the sheet and tools is presented in Figure 5.15 (note that the sheet and tools are translated for clarity).

Materials

The sheet material was mild steel using a nonlinear hardening elasto-plastic model. The following properties were used:

Young's modulus: $= YOUNG = 206GPa$

Poisson's ratio: $= POISS = 0.3$

Mass density: $= MASSD = 7800kg/m^3$

Nonlinear hardening: $= CONSO = 565.3MPa$

$EFREF = 0.007117$

$CONSN = 0.2589$

The blankholder material was steel using a linear elastic model with the following properties:

Young's modulus: $= YOUNG = 210GPa$

Poisson's ratio: $= POISS = 0.3$

Mass density: $= MASSD = 7800kg/m^3$

Nonlinear hardening: $= CONSO =$ very high value to prevent yielding

$EFREF =$ value is unimportant

$CONSN =$ value is unimportant

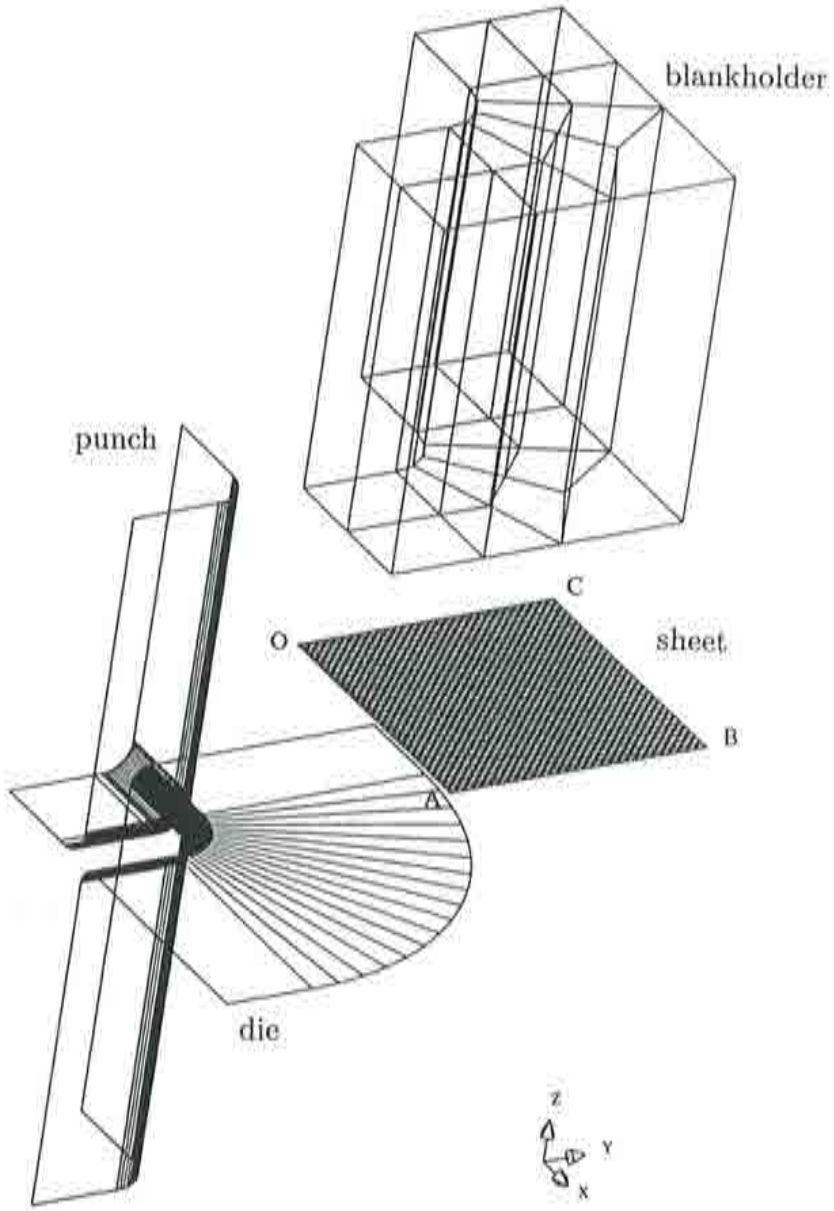

Figure 5.15 Discretization of the sheet and tools.

Boundary Conditions

The die was held in place while the punch was moved vertically. Contact surfaces between all tools and the sheet (punch - sheet, die - sheet and blankholder - sheet contact pairs) were modelled using a friction coefficient of 0.114; the penalty coefficient for both normal and tangential contact forces was 0.3.

Loading

A constant blankholding force of $19.6kN$ was applied to the surface of the blankholder as a surface load on those elements. The punch was moved vertically for $40mm$ by applying a sinusoidal velocity over the total analysis time period.

5.7.1.3 Analysis considerations

The total response time was obtained using an automatic time stepping calculation and was terminated when the punch stroke was completed. Material non-linearities were considered to be rate independent.

5.7.1.4 Results and discussion

Figures 5.17 and 5.18 show the initial geometry layout as well as the final sheet geometry, respectively. The final shape agrees very well with the numerical and experimental solutions in [M-1].

Three different measures for the draw-in were chosen: the draw-in in x direction DX along the symmetry plane, the draw-in in y direction DY along the symmetry plane, (because of symmetry the values DX and DY should coincide) and the diagonal draw-in DD at the sheet corner. The draw-in definitions are shown in Figure 5.16.

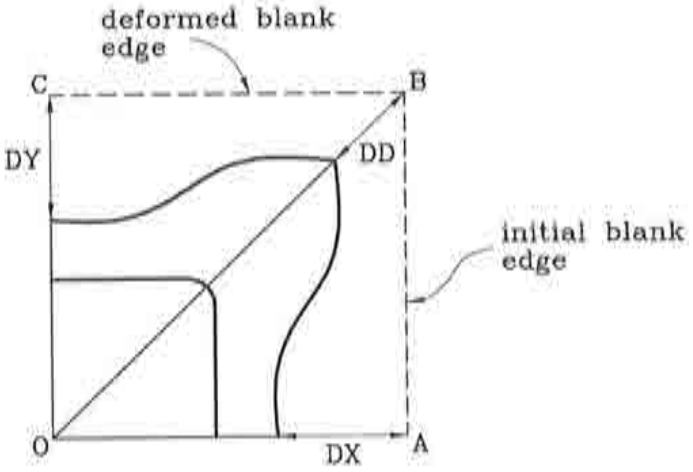

Figure 5.16 Draw-in definitions.

The other primary quantities of interest are the strain distribution produced in the formed product. The strain distributions are presented along the symmetry lines O-A and O-C (because of the symmetry the values of O-A and O-C coincide) and along the line from the center to the corner of the sheet O-B. The side of the sheet that faces the die is used for the presentation of the strain distributions. It should be noted that distances are measured with respect to the deformed length along the sheet.

The minor strain distribution along the lines O-A and O-B are presented in Figures 5.19 and 5.20 respectively. The major strain distribution along the lines O-A and O-B are presented in Figures 5.21 and 5.22 respectively. It can be noted that the largest strains are located in the region of the radii of the punch and die. Thickness strain distributions along the lines O-A and O-B are presented in Figures 5.23 and 5.24 respectively. Values for the average of the experimental results are only available for the thickness strains but not for the minor and major strains; these are also shown in Figures 5.23 and 5.24 and the numerical results compare well.

5.7.1.5 Conclusions

The numerical results obtained by either the hexahedral 3D solid elements, triangular BST or the triangular BSN shell element show good correlation with the available numerical and experimental results from the NUMISHEET'93 conference [M-1].

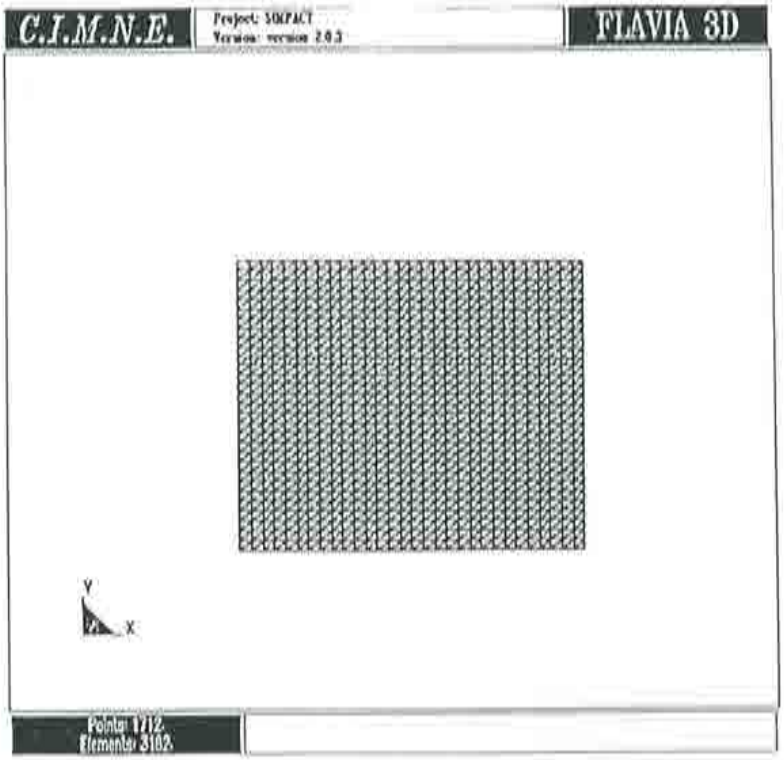

Figure 5.17 Initial geometry of sheet (triangular shell elements).

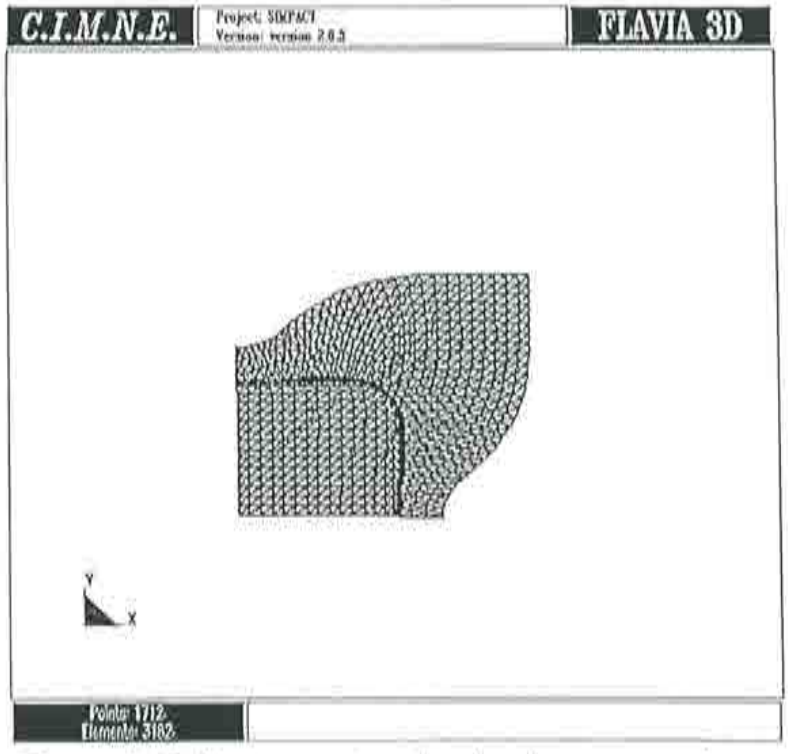

Figure 5.18 Sheet geometry after drawing was complete.

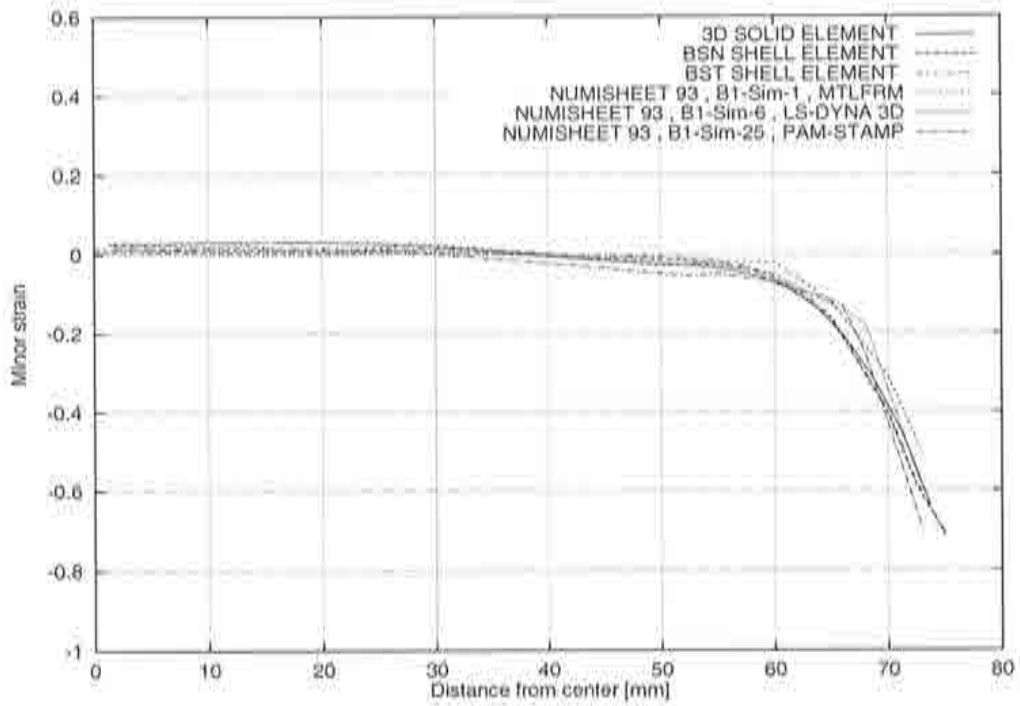

Figure 5.19 Minor strain distribution along the line O-A.

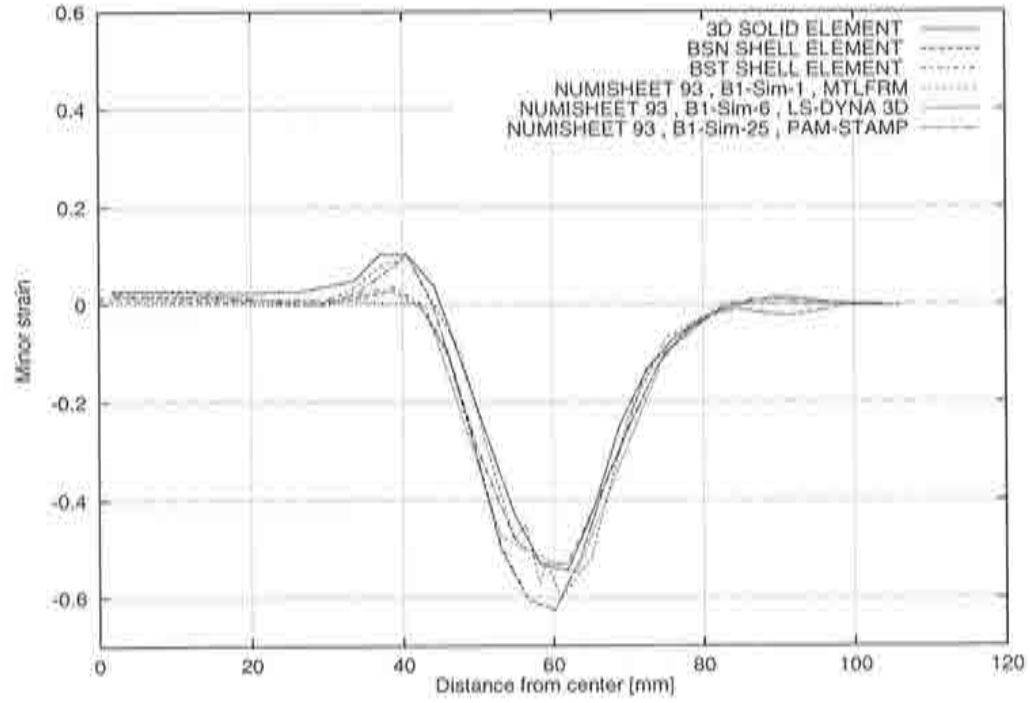

Figure 5.20 Minor strain distribution along the line O-B.

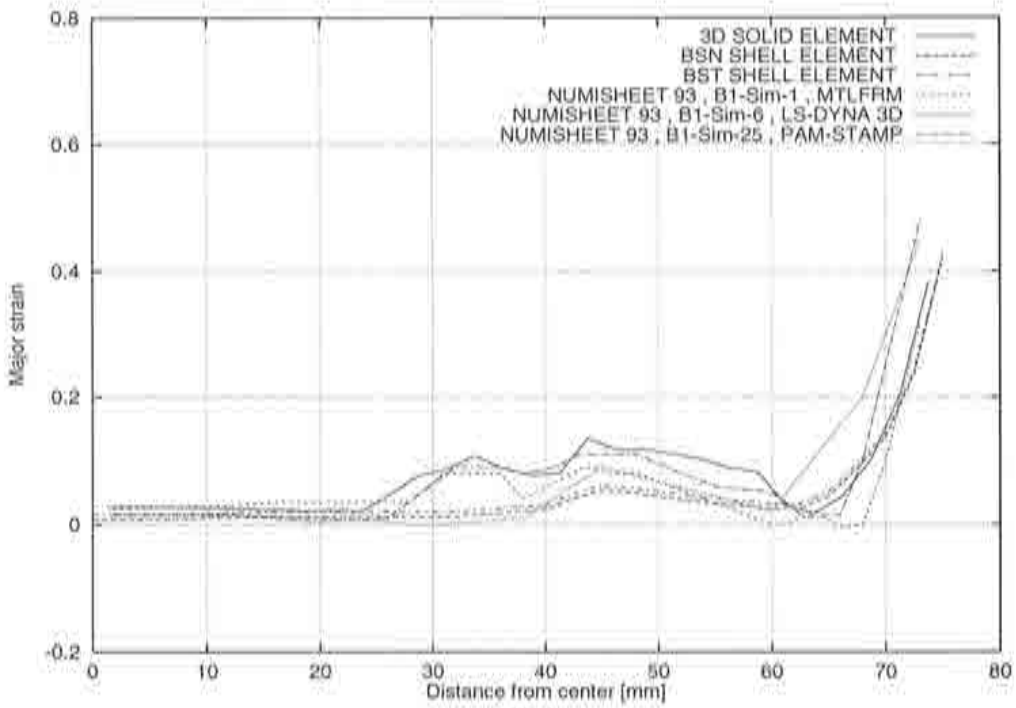

Figure 5.21 Major strain distribution along the line O-A.

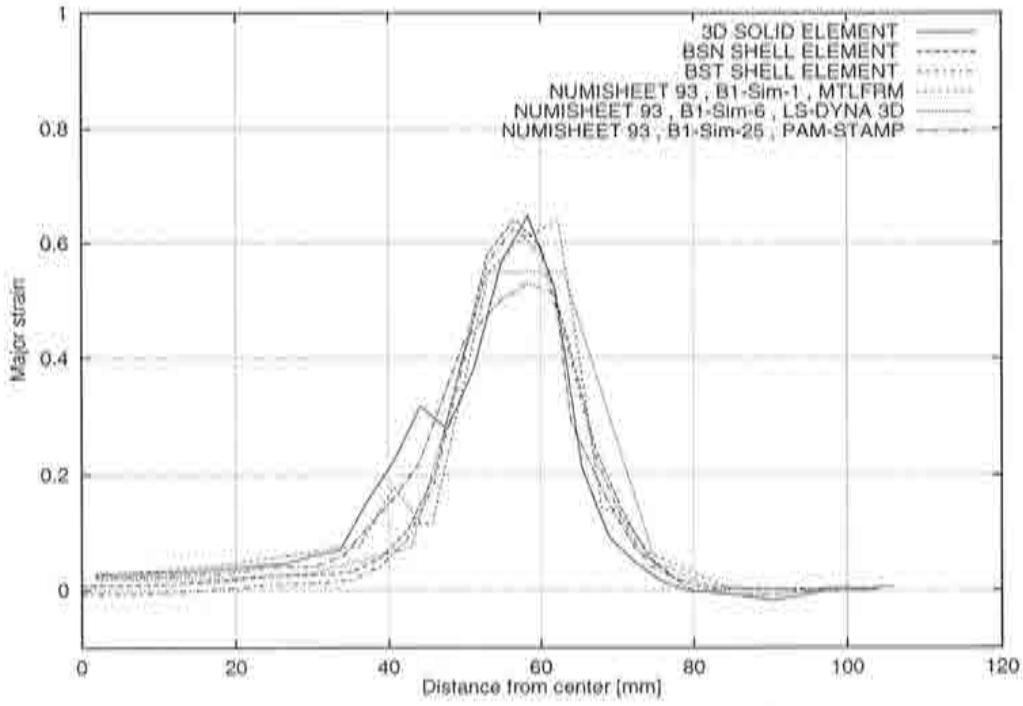

Figure 5.22 Major strain distribution along the line O-B.

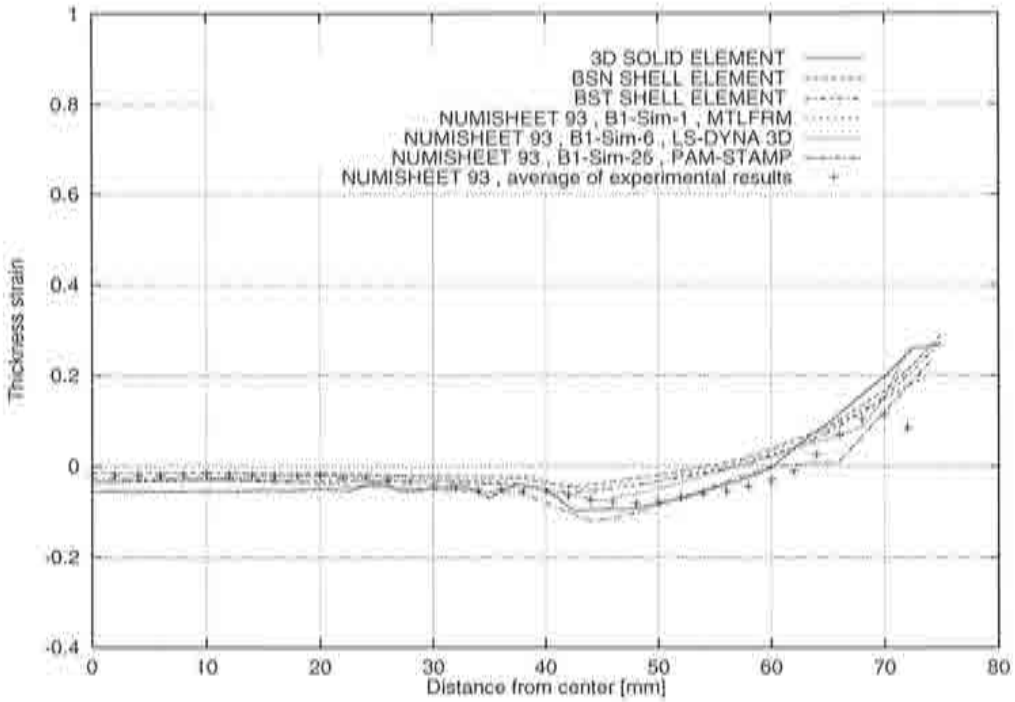

Figure 5.23 Thickness strain distribution along the line O-A.

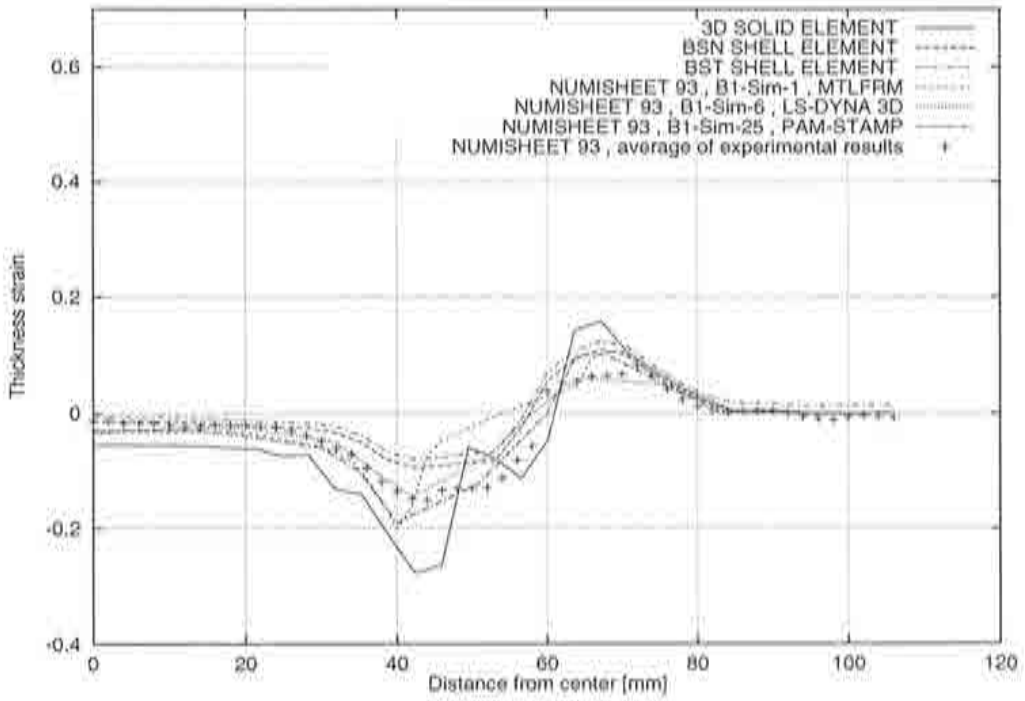

Figure 5.24 Thickness strain distribution along the line O-B.

5.7.2 S-RAIL deep drawing and springback

5.7.2.1 Problem description

The S-rail benchmark problem corresponds to one of the benchmark tests proposed in NUMISHEET'96 [L-2]. The drawn part selected for this benchmark contains combined bending and drawing zones, but the controlling of wrinkling and springback is a key problem. The analysis was carried out in two parts: stamping and then the springback computation once the tools were removed.

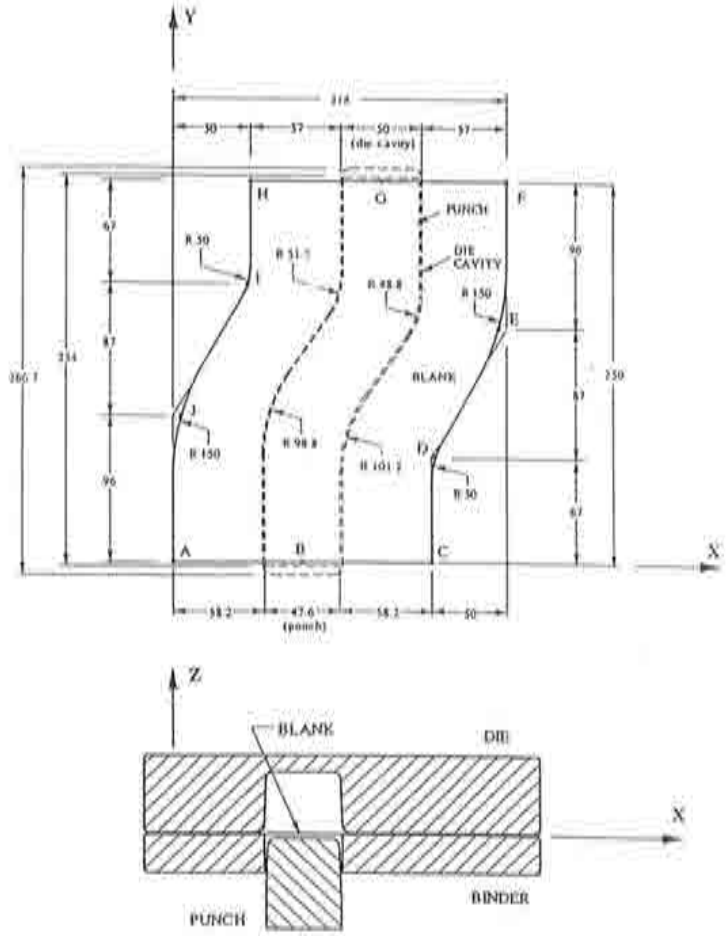

Figure 5.25 Complete geometry of the S-rail Deep Drawing and Springback.

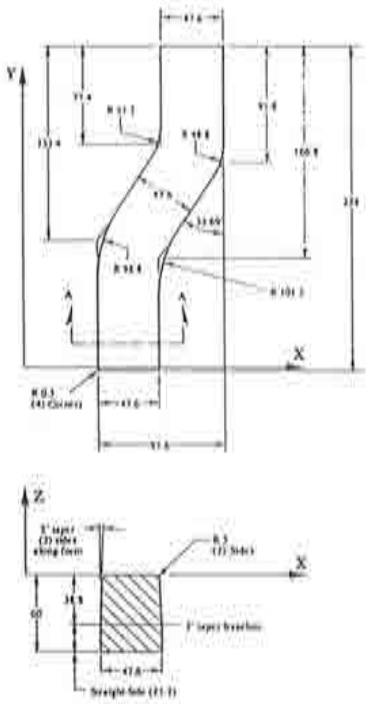

Figure 5.26 Punch geometry.

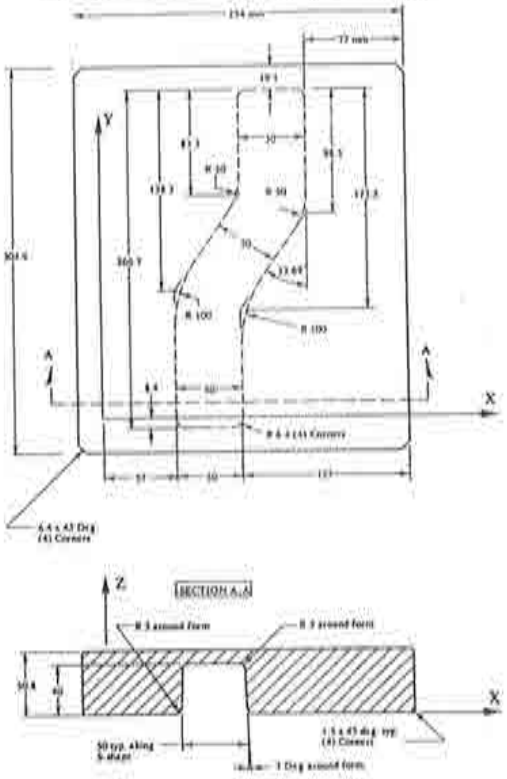

Figure 5.27 Die geometry.

5.7.2.2 Finite element model

Geometry

The geometrical data of the punch, die and blankholder are shown in Figure 5.25, 5.26 and 5.27, respectively. The punch travel is $37.0mm$.

Mesh

The sheet was modelled using 12000 BSN triangular shell layered elements (3 node). The blankholder was modelled using 190 QSS4 quadrilateral shell elements (4 node) to facilitate the application of the blankholder force. The punch and the die were modelled using 968 and 1496 DUMQ rigid elements (4 node) respectively. The discretized sheet is presented in Figure 5.28 as well as discretized tools (blankholder, punch and die) are presented in Figure 5.29. Reference points for comparison purposes before and after the stamping are presented in Figure 5.30.

Materials

The sheet material was mild steel using a nonlinear isotropic hardening elasto-plastic model. The following properties were used:

Young's modulus: $= YOUNG = 206GPa$

Poisson's ratio: $= POISS = 0.3$

Mass density: $= MASSD = 7800kg/m^3$

$EFREF = 0.0058$

$CONSN = 0.233$

The blankholder material was steel using a linear elastic model with the following properties:

Young's modulus: $YOUNG = 210GPa$

Poisson's ratio: $POISS = 0.33$

Mass density: $MASSD = 8700kg/m^3$

Nonlinear hardening: $= CONSO =$ very high value to prevent yielding

$EFREF =$ value is unimportant

$CONSN =$ value is unimportant

Boundary Conditions

The die and the blankholder were held in place while the punch was moved vertically. Contact surfaces between all tools and the sheet (punch - sheet, die - sheet and blankholder - sheet contact pairs) were modelled using a friction coefficient of 0.11; the penalty coefficient for both normal and tangential contact forces was 0.1.

Loading

A constant blankholding force of 10 kN was applied to the surface of the blankholder as a surface load on those elements. The punch was moved vertically for $37.0mm$ by applying a sinusoidal velocity over the total analysis time period.

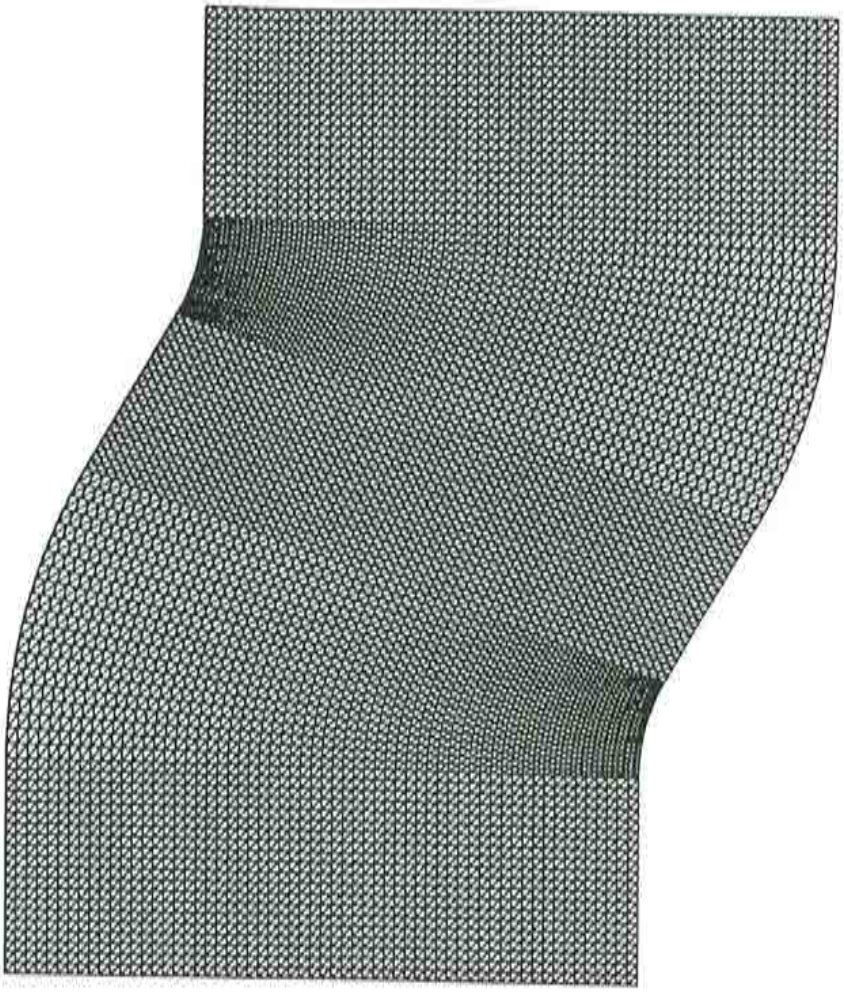

Figure 5.28 Discretized sheet.

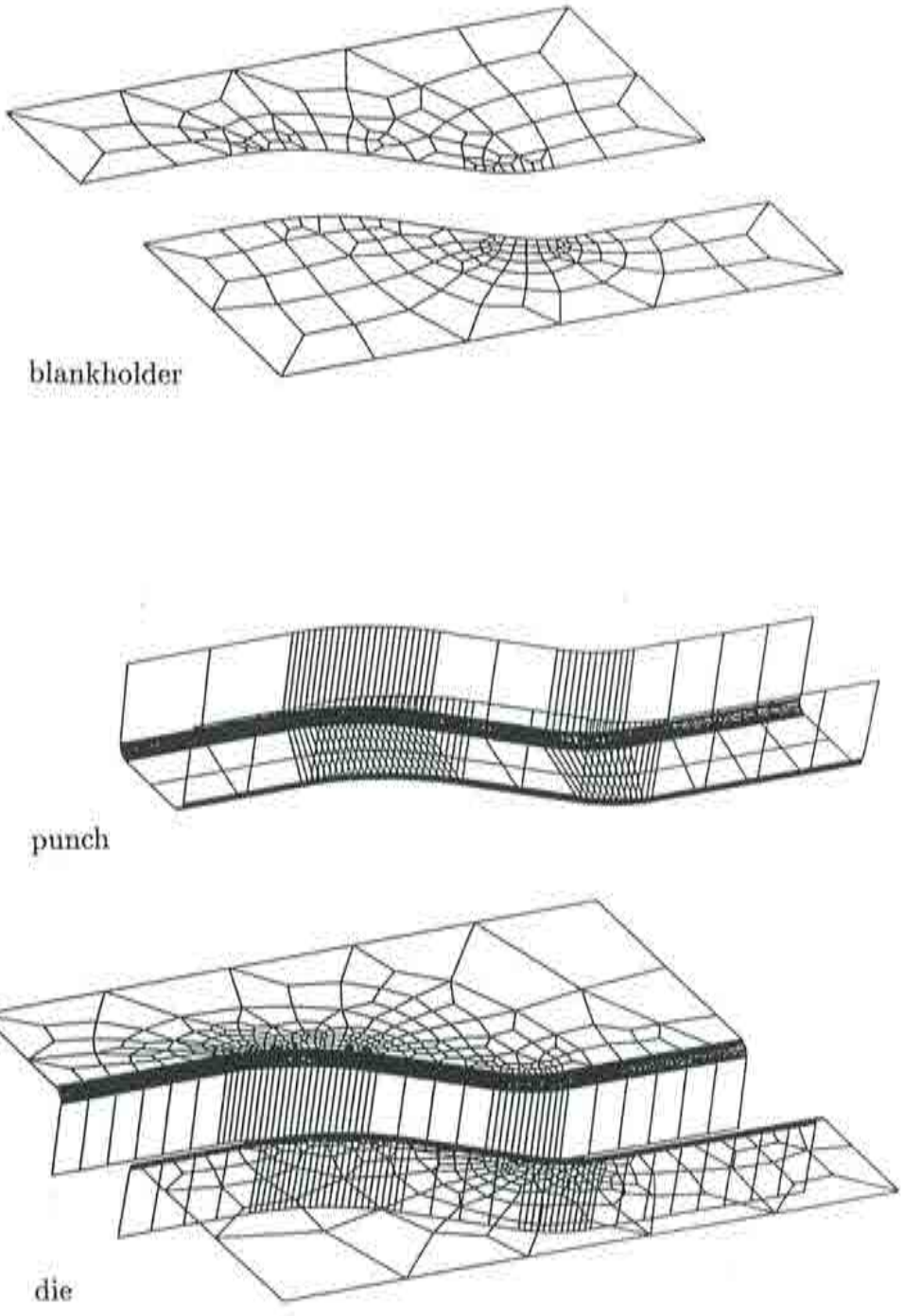

Figure 5.29 Discretized tools.

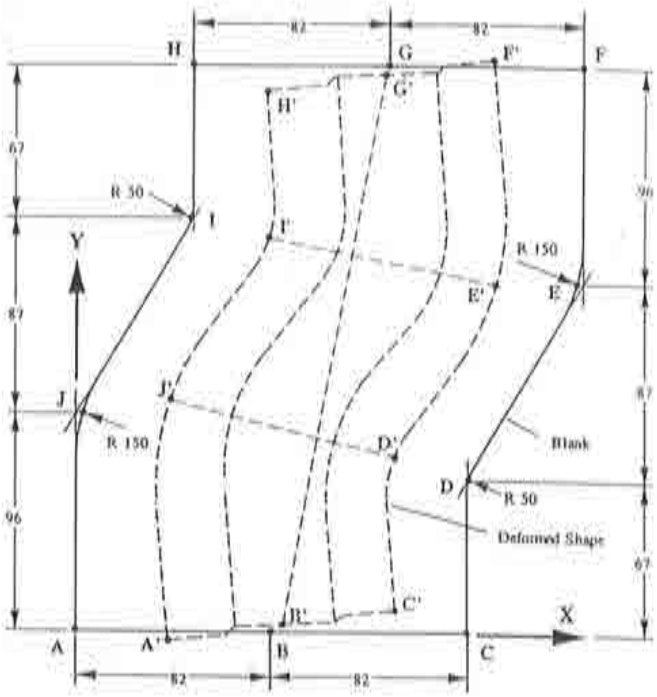

Figure 5.30 Reference points before and after the stamping.

Figure 5.31 Deformed mesh after the stamping stage superimposed on the original mesh.

5.7.2.3 Analysis considerations

The total response time was obtained using a fix time step of $0.1500E-06$ seconds. The simplicity of the formulation is based on avoiding the use of rotational degrees of freedom per node (BSN triangular elements) and the representation of the complex shell deformation in the stamping process is successfully achieved. Material non-linearities were considered by means of the hypoelastic model of elastoplasticity. The springback was achieved using dynamic relaxation with the explicit algorithm - this is inefficient but shows that satisfactory results can be obtained (implicit methods are more efficient for these computations).

5.7.2.4 Results and discussion

The superposition of the final deformed shape on the original sheet is shown in Figure 5.31. The emphasis is on predicting the final deformations after springback. The numerically obtained deformed shape after springback is shown in Figure 5.33 which compares extremely well with the experimental results shown in Figure 5.32. A different view of the numerical result, clearly showing the buckling of the upper surface, is shown in Figure 5.34. Comparison of the experimental and numerical result across section J"D" is given in Figure 5.53 and a Z-coordinate comparison across section B"G" is given in Figure 5.36. These results compare very well given that the maximum error is about 5%. The comparison curves of punch force versus punch height are presented in Figure 5.37; again the results obtained with the BSN element are in good agreement with those presented in [L-2]

5.7.2.5 Conclusions

The radial strain distributions for the solid and shell elements agree reasonably well with the reference solution given in [L-2]. Similar results were obtained for the circumferential and thickness distributions for all elements.

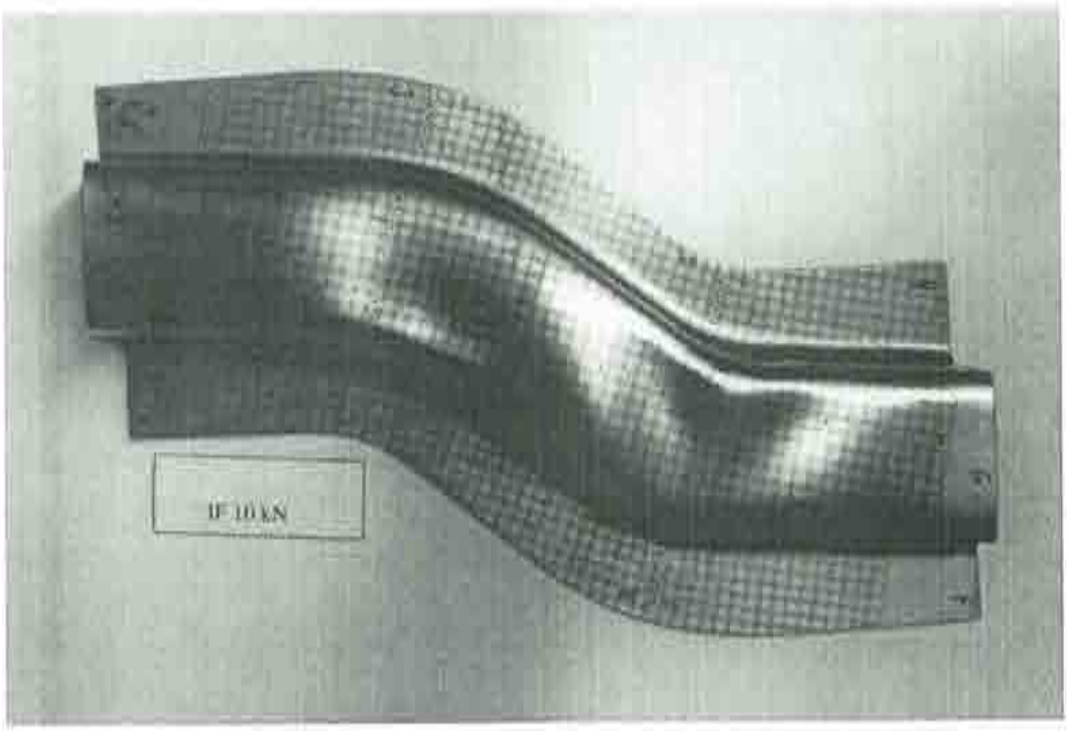

Figure 5.32 Deformed shape obtained in experiment.

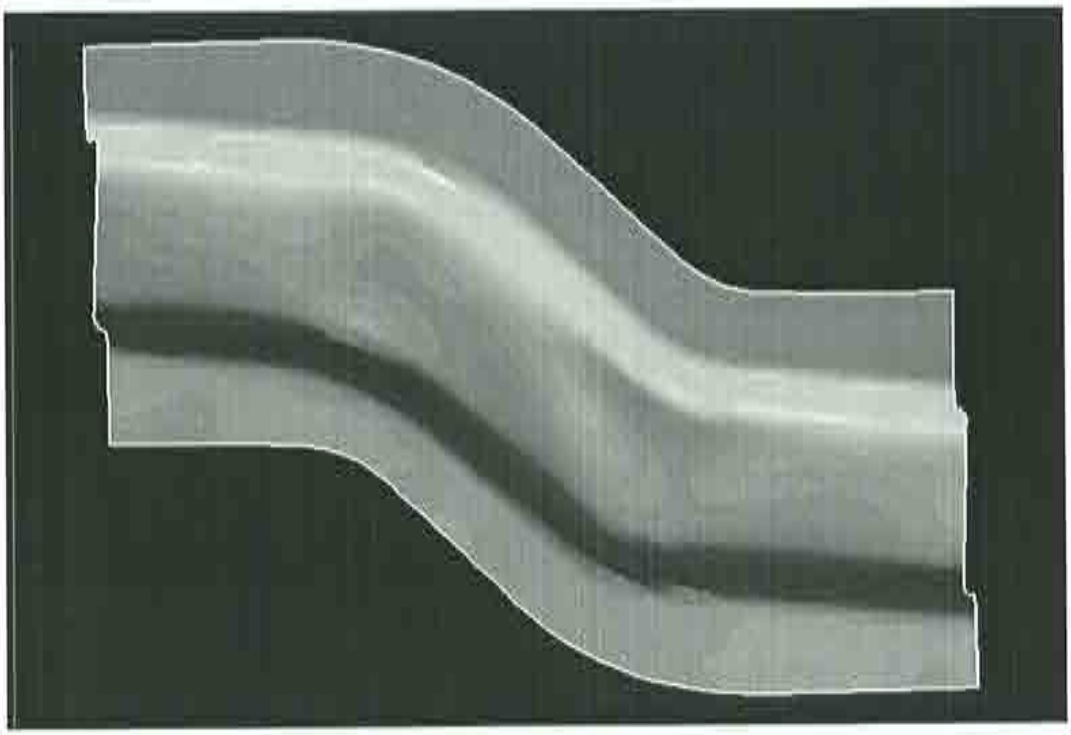

Figure 5.33 Deformed shape obtained in simulation.

Figure 5.34 Deformed shape after springback.

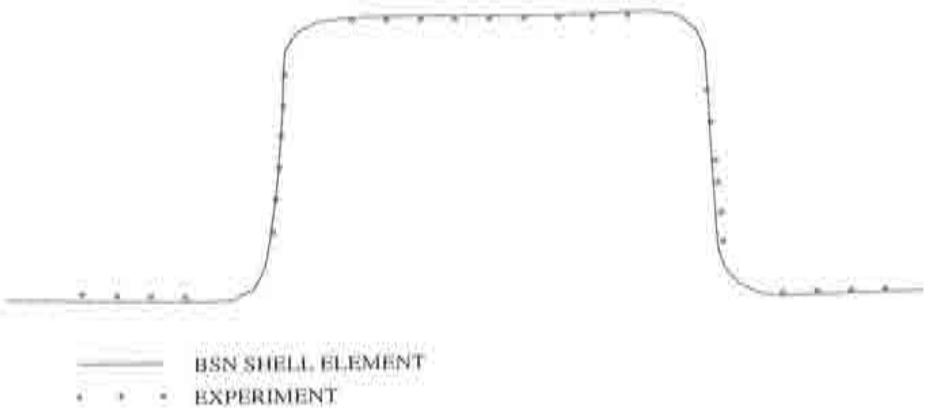

Figure 5.35 Comparison of sections J"-D" obtained in simulation and experiment.

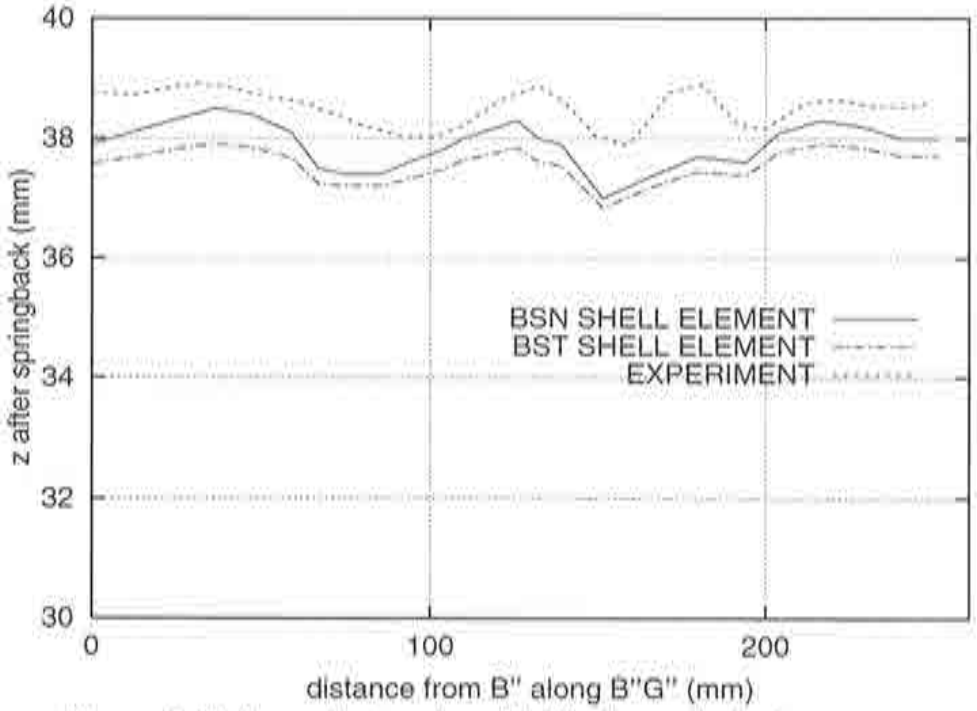

Figure 5.36 Z-coordinates along B"-G" after springback.

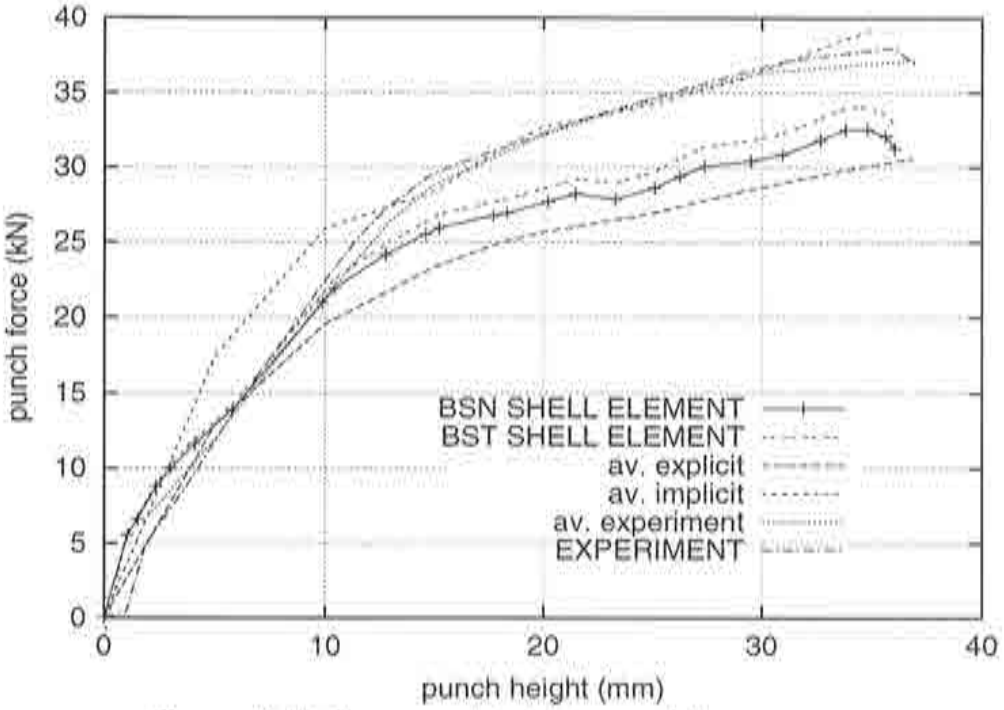

Figure 5.37 Curve punch height - punch force.

ANNEX 5.1

STUDY OF STABILITY

Despite the facility of relaxation, the shape function continuity requirements does not give the satisfactory results for certain choices of the individual shape functions for the mixed formulation. Some additional conditions - namely stability conditions are presented. These conditions have to be satisfied for the total problem as well as for the element patches.

Taking the following approximations

$$\mathbf{w} = \mathbf{N}_w \bar{\mathbf{w}} \qquad (An5.1a)$$

$$\mathbf{m} = \mathbf{N}_m \bar{\mathbf{m}} \qquad (An5.1b)$$

$$\boldsymbol{\chi} = \mathbf{N}_\chi \bar{\boldsymbol{\chi}} \qquad (An5.1c)$$

and replacing them into the equation (5.9), the same set of equations can be rewritten as

$$\int\int_A \mathbf{N}_m{}^T [\mathbf{L}\mathbf{N}_w \bar{\mathbf{w}} - \mathbf{N}_\chi \bar{\boldsymbol{\chi}}] dA = 0 \qquad (An5.2a)$$

$$\int\int_A \mathbf{N}_\chi{}^T [\mathbf{D}\mathbf{N}_\chi \bar{\boldsymbol{\chi}} - \mathbf{N}_m \bar{\mathbf{m}}] dA = 0 \qquad (An5.2b)$$

$$\int\int_A (\mathbf{L}\mathbf{N}_w)^T \mathbf{N}_m \bar{\mathbf{m}} dA - \int\int_A \mathbf{N}_w{}^T q dA = 0 \qquad (An5.2c)$$

Collecting the corresponding approximations and rewriting equation $(An5.2)$ in matrix form, yields

$$\begin{bmatrix} \mathbf{K}_{\chi\chi} & \mathbf{K}_{m\chi} & \mathbf{0} \\ \mathbf{K}_{m\chi}{}^T & \mathbf{0} & \mathbf{K}_{wm} \\ \mathbf{0} & \mathbf{K}_{wm}{}^T & \mathbf{0} \end{bmatrix} \begin{Bmatrix} \bar{\boldsymbol{\chi}} \\ \bar{\mathbf{m}} \\ \bar{\mathbf{w}} \end{Bmatrix} = \begin{Bmatrix} \mathbf{0} \\ \mathbf{0} \\ \mathbf{f} \end{Bmatrix} \qquad (An5.3)$$

where

$$\mathbf{K}_{\chi\chi} = \int\int_A \mathbf{N}_\chi{}^T \mathbf{D} \mathbf{N}_\chi dA \qquad (An5.4a)$$

$$\mathbf{K}_{m\chi} = -\int\int_A \mathbf{N}_m{}^T \mathbf{N}_\chi dA \qquad (An5.4b)$$

$$\mathbf{K}_{wm} = \int\int_A \mathbf{N}_w{}^T \mathbf{N}_m dA \qquad (An5.4c)$$

$$\mathbf{f} = \int\int_A \mathbf{N}_w{}^T q dA \qquad (An5.4d)$$

The criteria of stability for any element assembly and boundary conditions is

$$n_x + n_w \geq n_m \qquad (An5.5a)$$

$$n_m \geq n_w \qquad (An5.5b)$$

where n_x, n_m and n_w are the numbers of degrees of freedom in appropriate variables.

Thus, the stability of the matrix always occurs if the number of the unknowns in the vector $\bar{\boldsymbol{\chi}}$ called n_χ and vector $\bar{\mathbf{w}}$ called n_w is less than the number of the unknowns n_m in the vector $\bar{\mathbf{m}}$, equation $(An5.5a)$. This is necessary but not sufficient condition. The additional condition is that the number of the unknowns in the vector $\bar{\mathbf{m}}$ called n_m is less than the number of the unknowns n_w in the vector $\bar{\mathbf{w}}$, equation $(An5.5b)$. As mentioned before, the condition expressed by equation $(An5.5)$ is to be satisfied for the whole system as well as for the element patches.

The matrix expression by equation $(An5.3)$ can be written as

$$\mathbf{K}_{\chi\chi}\bar{\boldsymbol{\chi}} + \mathbf{K}_{m\chi}\bar{\mathbf{m}} = \mathbf{0} \qquad (An5.6a)$$

$$\mathbf{K}_{m\chi}{}^T\bar{\boldsymbol{\chi}} + \mathbf{K}_{wm}\bar{\mathbf{w}} = \mathbf{0} \qquad (An5.6b)$$

$$\mathbf{K}_{wm}{}^T\bar{\mathbf{m}} = \mathbf{f} \qquad (An5.6c)$$

The first equation gives the curvature $\bar{\boldsymbol{\chi}}$ as

$$\bar{\boldsymbol{\chi}} = -\mathbf{K}_{\chi\chi}{}^{-1}\mathbf{K}_{m\chi}\bar{\mathbf{m}} \qquad (An5.7)$$

then, replacing $\bar{\boldsymbol{\chi}}$ into equation $(An5.6b)$ gives

$$\mathbf{K}_{wm}\bar{\mathbf{w}} - [\mathbf{K}_{m\chi}{}^{T}\mathbf{K}_{\chi\chi}{}^{-1}\mathbf{K}_{m\chi}]\bar{\mathbf{m}} = \mathbf{0} \qquad (An5.8)$$

where $\mathbf{K}_{mm} = [\mathbf{K}_{m\chi}{}^{T}\mathbf{K}_{\chi\chi}{}^{-1}\mathbf{K}_{m\chi}]$, so the $\bar{\mathbf{m}}$ is

$$\bar{\mathbf{m}} = \mathbf{K}_{mm}{}^{-1}\mathbf{K}_{wm}\bar{\mathbf{w}} \qquad (An5.9)$$

The last equation $(An5.6c)$ gives

$$[\mathbf{K}_{wm}{}^{T}\mathbf{K}_{mm}{}^{-1}\mathbf{K}_{wm}]\bar{\mathbf{w}} = \mathbf{f} \qquad (An5.10)$$

what leads to the stiffness matrix $\mathbf{K}$ expressed by equation (5.21) as

$$\mathbf{K}\bar{\mathbf{w}} = \mathbf{f} \qquad (An5.11)$$

where $\mathbf{K} = [\mathbf{K}_{wm}{}^{T}\mathbf{K}_{mm}{}^{-1}\mathbf{K}_{wm}]$.

Assuming that the constant curvature and moment field within each element patch are

$$n_{\chi} = n_{m} \qquad (An5.12a)$$

$$\mathbf{N}_{\chi} = \mathbf{N}_{m} = \mathbf{I}_{m} \qquad (An5.12b)$$

the first stability condition is rewritten as

$$n_{\chi} + n_{w} \geq n_{m} \Rightarrow n_{w} = 0 \qquad (An5.13a)$$

and the second stability condition as

$$n_{m} = n_{\chi} \geq n_{w} \qquad (An5.13b)$$

Implemented simplified form of the terms involving the curvature operator expressed by equations (5.10), the matrices in equation $(An5.4)$ are

$$\mathbf{K}_{\chi\chi} = \int\int_{A} \mathbf{I}_{m}{}^{T}\mathbf{D}\mathbf{I}_{m}dA = \mathbf{D}A \qquad (An5.14a)$$

$$\mathbf{K}_{m\chi} = -\int\int_{A} \mathbf{I}_{m}^{T}\mathbf{I}_{m}dA = -\mathbf{I}_{m} - A \qquad (An5.14b)$$

$$\mathbf{K}_{wm} = -\int\int_{A} \mathbf{I}_m^T \mathbf{N}_w dA = \oint_{\Gamma} [\mathbf{T}\mathbf{N}_w]^T \mathbf{I}_m d\Gamma \qquad (An5.14c)$$

Replacing the corresponding matrices into $\mathbf{K}_{mm}$ leads to

$$\mathbf{K}_{mm} = [\mathbf{K}_{m\chi}{}^T \mathbf{K}_{\chi\lambda}{}^{-1} \mathbf{K}_{m\chi}] = -A\mathbf{I}_m{}^T A^{-1} \mathbf{D}^{-1} - A\mathbf{I}_m = A\mathbf{D}^{-1} \qquad (An5.15)$$

and substituting equation $(An5.15)$ into $(An5.11)$ yields

$$[\mathbf{K}_{wm}{}^T \mathbf{K}_{mm}{}^{-1} \mathbf{K}_{wm}]\bar{\mathbf{w}} = \mathbf{f} \qquad (An5.16)$$

where

$$\boxed{\mathbf{K} = \left[\oint_{\Gamma} [\mathbf{T}\mathbf{N}_w]^T \mathbf{I}_m d\Gamma\right]^T \frac{1}{A} \mathbf{D} \left[\oint_{\Gamma} [\mathbf{T}\mathbf{N}_w]^T \mathbf{I}_m d\Gamma\right]} \qquad (An5.17)$$

The global stiffness matrix $\mathbf{K}$ is constructed by assembling the contributions of the different control domains using the Cell Centered and Cell Vertex schemes, as explained in the previous sections.

CHAPTER 6

CONCLUSIONS

6.1 INTRODUCTION

The objective of the thesis is the development of efficient solution procedures for large industrial problems in nonlinear shell analysis typical of metal forming and crash worthiness situation. The efficiency of the formulation has been achieved by the new combined FE/FV based approximations allowing for the rotational-free formulations of the typical structure elements (beams, plates and shells). The development of elements has been carried out in the framework of linear analysis and then extended to nonlinear by means of Updated Lagrangian formulation and an explicit dynamic analysis. The procedure has been selected in the spirit of a sound approach to solve nonlinear problems which should not be started at the outset with the most complicated model. It is recommended to start with the appropriate linear analysis to become aware of the particular problem at hand and to introduce different nonlinearity effects progressively. The structural elements developed in this thesis provide the basis for respectable solution for nonlinear problems.

The efficiency of this new approach has been achieved by the new combined FE/FV technique for constructing structural finite elements (beams, plates and shells) which do not carry rotational degrees of freedom. This naturally means that the computational efforts for solving these problems can be significantly reduced due to the reduction of a number of degrees of freedom.

All the elements developed in this thesis exhibit very satisfying and robust performance which is primarily the consequence of solid theoretical foundation of the combined FE/FV technique developed in this study using the Hu-Washizu mixed variational formulation.

6.2 PRINCIPAL CONTRIBUTIONS OF THE THESIS

The main contributions of the thesis are the following:

- A rigorous theoretical basis of combined FE/FV approximations is constructed by making use of the mixed Hu-Washizu variational formulation. This kind of formulation allows for more freedom in choosing appropriate interpolations in order to accommodate various constraints appearing in discrete approximations of structural theories.
- Two combined FE/FV techniques are developed: Cell Centered scheme which considers the complete domain of the particular element and its neighbours for which FE/FV approximations is being constructing, and Cell Vertex scheme which focuses upon the particular node defining the corresponding domain of each patch as the appropriate subdomains of the elements attached to the node.
- The development of FE/FV approximations has been carried out for beam, axisymmetric and arbitrary shape shell elements with displacement degrees of freedom only. For all these elements it has been found that the Cell Vertex scheme exhibits a superior performance.
- Taking into account the last observation it is only the Cell Vertex scheme that has been chosen as the basis for constructing the extension to nonlinear analysis of axisymmetric and arbitrary shape shells. The whole procedure has been accomplished by means of Updated Lagrangian formulation and an explicit dynamic analysis.
- It has been demonstrated with several numerical simulations, of very complex sheet stamping problems including frictional contact situations, that the BSN element developed in this thesis is a very versatile tool for practical sheet stamping analysis.

6.3 FUTURE LINES OF RESEARCH

Future developments of this research can be carried out in order to increase the efficiency of computation at more advanced level.

- More precisely, the modern computer equipment can be valuable to achieve better results, by using the developed FE/FV elements with parallel computing procedures.
- In addition, the developed elements can be used in combination with adaptive mesh refinement which would be of the particular interest for capturing stress and strain concentrations.
- The thermomechanical coupling can also be considered in order to increase applicability of the developed shell elements to different forming procedures - hot versus cold forming.

REFERENCES

[B-1] Bathe, K.J., *"Finite Element Procedures in Engineering Analysis"*, Prentice-Hall International Editions, 1992.

[B-2] Bathe, K.J., Ramm, E. and Wilson, E.L., "Finite Element Formulations for Large Deformation Dynamic Analysis", *International Journal for Numerical Method in Engineering*, Vol. **9**, pp. 353-386, 1975.

[B-3] Bathe, K.J. and Ozdemir. H., "Elastic-Plastic Large Deformation Static and Dynamic Analysis", *Computers and Structures*, Vol. **6**, pp. 81-92, 1976.

[B-4] Barnes, M.R., *"Form finding and analysis of tension space structure by dynamic relaxation"*, Ph.D. Thesis, Department of civil Engineering, The City University, London, 1977.

[B-5] Batoz, J.L., Bathe, K.J. and Ho, L.W., "A study of three-node triangular plate bending elements", *International Journal for Numerical Methods in Engineering*, Vol. **15**, pp. 1771-1812, 1980.

[B-6] Brunet, M. and Sabourin, F., "Prediction of Necking and Wrinkles with a Simplified Shell Element in Sheet Forming", *International Conference of Metal Forming Simulation in Industry*, Vol. **II**, pp. 27-48, B. Kröplin (Ed.), 1994.

[C-1] Cendoya, P.H., *"Non linear explicit analysis of shells using a shell triangle with translational degrees of freedom"*, (in Spanish), Ph.D. Thesis, Universitat Politécnica de Catalunya, Barcelona, 1996.

[C-2] Crisfield, M.A., *"Non-linear Finite Element Analysis of Solids and Structures"*, John Wiley & Sons Ltd., 1991.

[G-1] Garino, C.G., *"A Numerical Model for the Anlaysis of Large Elasto Plastic Deformations of Solids"*, Ph.D. Thesis, Universitat Politecnica de Catalunya, Barcelona, 1993.

[H-1] Hampshire, J.K., Topping, B.H.V. and Chan, H.C., "Three node triangular elements with one degree fredom per node", *Engineering Computation*, Vol **9**, pp. 49-62, 1992.

[H-2] Hill, R., "A theory of the yielding and plastic flow of anisotropic metals", *Proceedings Royal Soc. London*, pp. 281-297, 1948.

[H-3] Hirch, C., *"Numerical computation of internal and external flow"*, Vol. **I**, J. Wiley & Sons Ltd., 1989.

[H-4] Honnor, M.E., *"Non-linear Finite Element Analysis of Axisymmetric Shells applied to Sheet Metal Forming"*, Ph.D. Thesis, University College of Swansea, 1985.

[H-5] Hughes, T.R.J., *"The Finite Element Method, Linear Static and Dynamic analysis"*, Prentice-Hall International Editions, 1987.

[I-1] Idelson., S. and Oñate, E., "Finite elements and finite volumes for CFD. Two good friends", *Publication CIMNE N^o* 26, Barcelona 1993.

[Y-1] Yang, D.J., Jung, D.W., Song, L.S., Yoo, D.J. and Lee, J.H., *NUMISHEET '93*, Eds. Makinouchi, A., Nakamachi, E., Oñate, E. and Wagoner, R.H., RIKEN, Tokyo, 1993.

[K-1] Khan, A.S. and Huang S., *"Continuum Theory of Plasticity"*, John Wiley & Sons, Inc. 1995.

[L-1] Lee, E.H., "Finite deformation effects in plasticity analysis", *International Conference on Numerical Methods in Industrial Forming Processes*, Swansea, Pittman, 1982.

[L-2] Lee, E.H., Kinzel, G.L., and Wagoner, R.H., "Numerical Simulation of 3D Sheet Metal Forming Processes - Verification of Simulations with Experiments", *NUMISHEET'96*, Dearborn, Michigan, September 29 - October 3, 1996.

[L-3] Lee, E.H., Wagoner, R. and Nakamachi, E., "A benchmark test for sheet metal forming analysis", *Technical Report*, Ohio State University, 1990.

[M-1] Makinouchi, A., Nakamachi, E., Oñate, E., and Wagoner, R., "Numerical Simulation of 3D Sheet Metal Forming Processes - Verification of simulation with Experiment", *NUMISHEET'93*, Isehara, Japan, 31 August - 2 September 1993.

[M-2] Malvern, L.E., *"Introduction to the Mechanics of a Continuous Medium"*, Prentice-Hall, Englewood Cliffs, 1969.

[M-3] Marsden, J.E. and Hughes, T.J.R., *"Mathematical Foundations of Elasticity"*, Prentice-Hall, 1983.

[M-4] Matiasson, K., "Continuum Mechanics Principles for Large Deformation Problems in Solid and Structural Mechanics", *Publication 81-86*, Department of Structural Mechanics, Chalmers University of Technology, 1981.

[M-5] Morley, L.S.D., "The triangular equilibrium element in the solution of plate bending problems", *Aero Quart*, Vol. **19**, pp.149-169, 1968.

[N-1] Nay, R.A. and Utku, S., "An alternative for the finite element method", *Variat. Meth. Engng.*, Vol **1**, 1972.

[O-1] Oñate, E., *"Calculo de Estructuras por el Metodo de Elementos Finitos"*, CIMNE, Barcelona, 1992.

[O-2] Oñate, E. and Cervera, M., "Derivation of Thin Plate Bending Elements with One Degree of Freedom per Node. A Simple Three Node Triangle", *Engng. Comput.*, Vol **10**, pp. 543-561, 1993.

[O-3] Oñate, E., Cervera, M. and Zienkiewicz, O.C., "A Study of the Finite Volume Methods for Structural Mechanics", *Publication CIMNE N^o* 15, 1992.

[O-4] Oñate, E., Rojek, J. and Cendoya, P., "SB-2:LDH Rail Simulation Benchmark Results", *NUMISHEET'96* Dearborn, Michigan, September 29 - October 3, 1996.

[O-5] Owen, D.R. and Hinton, E., *"Finite Elements in Plasticity - Theory and Practice"*, Prineridge Press Limited, 1980.

[P-1] Papadopoulos, P. and Taylor, R.L., "A simple algorithm for three-dimensional finite element analysis of contact problems", *Computational Struct.*, Vol **46**, pp. 1107-1118, 1993.

[P-2] Phaal, R. and Calladine, C.R., "A simple class of finite elements for plate and shell problems. I: Elements for beams and thin plates",*International Journal for Numerical Method in Engineering*, Vol. **35**, pp. 955-977, 1992.

[P-3] Phaal, R. and Calladine, C.R., "A simple class of finite elements for plate and shell problems. II: An element for thin shells with only translational degrees of freedom", *International Journal for Numerical Method in Engineering*, Vol. **35**, pp. 979-996, 1992.

[R-1] Rio, G., Tathi, B. and Laurent, H., "A New Efficient Finite Element Model of Shell with Only Three Degrees of Freedom per Node. Applications to Industrial Deep Drawing Test", *Recent Development in Sheet Metal Forming Technology, Ed. M.J.M. Barata Marques, 18-th IDDRG Biennal Congress*, Lisbon, 1994.

[R-2] Rojek, J., Jovicevic, J. and Oñate, E., "Industrial applications of sheet stamping simulation using new explicit finite element models", *Research Report CIMNE, N^o* 97, Barcelona, 1996.

[R-3] Rojek, J. and Oñate, E., "Sheet springback analysis using simple 3 node shell triangles with translation degrees of freedom", *Research Report CIMNE, N^o* **124**, Barcelona, 1997.

[S-1] Saracibar, C.A. and Oñate, E., *"Modelado Numérico de Procesos de Conformado de Láminas Métalicas"*, Monografia CIMNE *N^o* 8, 1991.

[S-2] Saran, M., Schedin, E., Samuelson, A., Melander, A. and C.Gustaffson., "Nuemrical and Experimental Investigations of Deep Drawing of Metal Sheets",*Publication 89, Department of Structural Mechanics, Chalmers University of Technology,* Goteborg, Sweden, 1989.

[T-1] Timoshenko, S., *"Theory of plates and shells"*, Mc. Graw Hill, 1979.

[U-1] Uguraz, A.C., *"Stresses in plates and shells"*, Mc. Graw Hill, 1981.

[W-1] Washizu, K., *"Variational Methods in Elasticity & Plasticity"*, Pergamon Press, 1975.

[Z-1] Zarate., F., *"New finite element for plate and shell analysis"*, Ph.D. Thesis, (in Spanish), Universitat Politécnica de Catalunya, Barcelona, 1996.

[Z-2] Zarate, F. and Oñate, E., "Nuevos elementos de placa y lámina con variables de desplazamientos nodales", *III Congresos de Métodos Numéricos en Ingenieria, SEMNI,* Zaragoza, June 1996.

[Z-3] Zarate., H.F. and Oñate, E., "New thin plate and shell triangles with translational degrees of freedom only", *IUTAM/IACM Symposium on Discretization Methods in Structural Mechanics,* Viena, June 1997.

[Z-4] Zienkiewicz, O.C. and Taylor, R.L., *"The Finite Element Method"*, -4^{th}. Ed., Mc Graw Hill, Vol. **I**, 1989, Vol. **II**, 1991.

[Z-5] Zienkiewicz, O.C. and Oñate, E., "Finite Volumes vs Finite Elements. Is there really a choice?", *Publication CIMNE N^o* 8, Barcelona, 1990.